Biochemical and structural characterization of chronophin

Die biochemische und strukturelle Charakterisierung von Chronophin

Dissertation for a doctoral degree

at the Graduate School of Life Sciences,

Julius-Maximilian-Universität Würzburg

(Section Biomedicine)

submitted by

Gunnar Knobloch

from Bogotá, Columbia

Würzburg, November 2014

Submitted on: ……..

Office stamp

Members of the *Promotionskomitee*:

Chairperson:	Prof. Dr. Jörg Schultz
Primary Supervisor:	Prof. Dr. Antje Gohla
Supervisor (Second):	Prof. Dr. Hermann Schindelin
Supervisor (Third):	Dr. Katrin Heinze

Date of Public Defence: ……..

Date of Receipt of Certificates: ……

Table of contents

A Summary

The haloacid dehalogenase (HAD) family of phosphatases is an ancient, ubiquitous group of enzymes, and their emerging role in human health and disease make them attractive targets for detailed analyses. This thesis comprises the biochemical and structural characterization of chronophin, an HAD-type phosphatase, which has been shown to act on Ser^3-phosphorylated cofiln-1, a key regulator of actin dynamics, and on the Ser/Thr-phosphorylated steroid receptor co-activator 3 (SRC-3). Besides being a specific phosphoprotein phosphatase, chronophin also acts on the small molecule pyridoxal 5'-phosphate (PLP, vitamin B_6), implying that chronophin serves as a regulator of a variety important physiological pathways. The analysis of chronophin was performed on different levels, ranging from intrinsic regulatory mechanisms, such as the allosteric regulation via dimerization or the characterization of specificity determinants, to modes of extrinsic modulation, including the association with putative interacting proteins or the generation of chronophin-specific inhibitors.

The association of the previously identified putative chronophin interactors calcium- and integrin-binding protein 1 (CIB1) and calmodulin was investigated using recombinantly expressed and purified proteins. These studies revealed that the interaction of chronophin with CIB1 or calmodulin is mutually exclusive and regulated by calcium. Neither CIB1 nor calmodulin had an effect on the *in vitro* chronophin phosphatase activity towards PLP or phospho-cofilin-1, but might regulate other functions of this important phosphatase.

The role of chronophin dimerization was studied by generating a constitutively monomeric variant, which showed reduced PLP hydrolyzing activity. X-ray crystallographic studies revealed that dimerization is essential for the positioning of the substrate specificity loop in chronophin, unraveling a previously unknown mechanism of allosteric regulation through a homophilic interaction. This mechanism potentially applies to other enzymes of the C2a subfamily of HAD-type phosphatases, as all structurally characterized members show a conserved mode of dimerization.

The general determinants of substrate specificity in the C2a subfamily of HAD phosphatases were investigated by performing domain swapping experiments with chronophin and its paralog AUM and subsequent biochemical analyses of the hybrid proteins. The X-ray crystallographic structure determination of the chronophin catalytic domain equipped with the AUM capping domain revealed the

first partial structure of AUM. This structural information was then used in subsequent studies that analyzed the divergent substrate specificities of AUM and chronophin in an evolutionary context.

Finally, a set of four chronophin inhibitors were generated based on the structure of PLP and characterized biochemically, showing moderate inhibitory effects with IC_{50}-values in the micromolar range. These compounds nevertheless constitute valuable tools for future *in vitro* experiments, such as studies concerning the structure-function relationship of chronophin as a PLP phosphatase. In addition, the crystal structure of one inhibitor bound to chronophin could be solved. These results provide the basis for the further development of competitive chronophin inhibitors with increased specificity and potency.

B Zusammenfassung

HAD Phosphatasen gehören zu einer phylogenetisch alten Proteinfamilie, die in allen drei Domänen des Lebens vertreten ist. Enzyme dieser vergleichsweise wenig charakterisierten Familie von Phosphatasen erweisen sich zunehmend als biomedizinisch interessante Zielmoleküle, da immer mehr Krankheiten identifiziert werden, bei denen HAD Phosphatasen eine Rolle spielen. In der hier vorliegenden Doktorarbeit wurde die HAD Phosphatase Chronophin biochemisch und strukturell charakterisiert. Bisher konnte gezeigt werden, dass Chronophin die Proteine Cofilin-1, ein Schlüsselprotein in der Regulation des Aktin-Zytoskeletts, und den Steroidrezeptor Coaktivator 3 (SRC-3) dephosphoryliert. Darüberhinaus ist bekannt, dass Chronophin eine spezifische Pyridoxal 5'-Phosphat (PLP, Vitamin B_6) Phosphatase ist, und somit an der Regulation verschiedenster Signalwege beteiligt ist. Die hier beschriebene Analyse von Chronophin beinhaltet die Untersuchung intrinsischer Regulationsmechanismen, wie z.B. Determinanten der Substratspezifität, die allosterische Regulation über Dimerisierung, bis hin zur Kontrolle durch extrinsische Faktoren wie interagierende Proteine oder Inhibitoren.

Die Interaktion von Chronophin mit den kürzlich in unserer Arbeitsgruppe identifizierten Interaktionspartnern CIB1 (Kalzium- und Integrin-bindendes Protein 1) und Calmodulin wurde mit Hilfe rekombinant exprimierter und gereinigter Proteine untersucht. Dabei kam heraus, dass sich die Assoziation von CIB1 und Calmodulin an Chronophin gegenseitig ausschließt, und dass dieser Prozess durch Kalzium reguliert wird. Dabei beeinflusst weder die Bindung an CIB1 noch an Calmodulin die Phosphataseaktivität von Chronophin gegenüber den Substraten PLP oder phosphoryliertem Cofilin-1. Möglicherweise regulieren die beiden interagierenden Proteine die Funktion von Chronophin auf eine andere, hier nicht weiter untersuchte Art und Weise.

Der Einfluss der Chronophin-Dimerisierung wurde untersucht, indem wir eine konstitutiv monomere Variante des üblicherweise dimeren Chronophins geschaffen haben. Diese monomere Variante des Enzyms wies eine deutlich reduzierte Aktivität gegenüber PLP auf. Durch röntgenkristallographische Analysen des wild-typischen Proteins und der monomeren Variante konnten wir zeigen, dass die Dimerisierung von Chronophin notwendig ist, um ein Strukturelement, welches wichtig für die Substratspezifität ist, in einer korrekten Position zu halten. Dieser allosterische Mechanismus zur Aufrechterhaltung der Substratspezifität war bisher unbekannt, und trifft möglicherweise auf alle Proteine der C2a Unterfamilie von HAD Phosphatasen zu, die strukturell mit Chronophin verwandt sind.

Die Faktoren, welche auf die Substratspezifität von Chronophin Einfluss nehmen wurden untersucht, indem einzelne Proteindomänen mit dem paralogen Protein AUM ausgetauscht, und die so geschaffenen Protein-Hybride biochemisch untersucht wurden. Durch das Lösen der röntgenkristallographischen Struktur eines Protein-Hybrids, bestehend aus der katalytischen Domäne von Chronophin und der *capping*-Domäne von AUM, konnte die die erste partielle Struktur von AUM untersucht werden. Mit Hilfe dieser strukturellen Information und durch bioinformatische Analysen konnten anschließend die unterschiedliche Substratspezifitäten der beiden paralogen Phosphatasen Chronophin und AUM in einem evolutionsbiologischen Kontext untersucht werden.

Zusätzlich wurden vier mögliche Chronophin-Inhibitoren auf der Basis der PLP-Struktur synthetisiert. Die biochemische Analyse der Substanzen als Chronophin-Hemmer ergab moderate inhibitorische Eigenschaften mit IC_{50}-Werten im micromolaren Bereich. Jedoch stellen die hier charakterisierten Inhibitoren nützliche Werkzeuge für die Untersuchung der Struktur-Wirkungsbeziehungen von Chronophin als PLP-Phosphatase dar. Die röntgenkristallographische Struktur von Chronophin mit einem der Inhibitoren liefert außerdem eine wichtge Grundlage für die zukünfitige Verbesserung der Inhibitoren bezüglich Effektivität und Spezifität.

1 Introduction

1.1 Kinases and phosphatases

Phosphorylation is the reversible attachment of a phosphate group to macromolecules like proteins and DNA or to small organic molecules, such as lipids, carbohydrates and other metabolites. This modification dramatically changes the chemical properties of the respective substrate by adding or removing the bulky, highly polar phosphate group with two negative charges that can undergo several hydrogen bonds, making phosphorylation a versatile tool used to trap metabolites within cells, regulate enzyme activities, protein interactions or influence the binding of cofactors.

The addition of a phosphate moiety to a substrate is either catalyzed by phosphorylases that transfer inorganic phosphate onto acceptors, such as glucans or nucleosides, or by kinases that instead utilize phosphate groups from high-energy donor molecules, such as ATP, to transfer the terminal γ-phosphate to their macromolecular or small molecule substrates. The removal of phosphate, on the other hand, is accomplished by the action of phosphatases. The interplay of these antagonistically acting enzymes is involved in the regulation of virtually all cellular processes in living organisms.

The phospho-regulation of proteins is of particular importance, since it represents the most widespread eukaryotic post-translational modification and it is crucial for a vast amount of cellular functions, including DNA-repair [8], transcriptional control [9], apoptosis [10], immune response [11], metabolism [12] and cellular differentiation [13]. Estimates assume that approximately 30% of all cellular proteins are phosphorylated on at least one residue [14]. Thus, many kinases and phosphatases have already been associated to human disease [7, 15-17]. To date, 518 putative human protein kinase genes have been identified ([5], 538 according to kinase.com), making kinases one of the largest protein families constituting ~2% of the human genome [5]. The estimated number of human protein phosphatases, in contrast, is lower and ranges around 199 genes [4]. The amount of putative human kinases and phosphatases is greatly outnumbered by the abundance of phosphorylation sites that have been identified. To date, more than 70,400 phosphorylated serine, threonine and tyrosine residues of the potential ~700,000 phosphorylation sites in a cell have been characterized *in vivo* using mass spectrometry [18, 19]. The relative abundances of typical phosphorylation sites of amino acids containing hydroxyl groups (O-phosphorylation) have been shown to be typically ~90% serine, ~10% threonine and ~1%

threonine residues [20, 21], whereas the unusual phosphorylation sites, such as N-phosphorylation (histidine, arginine and lysine), S-phosphorylation (cysteine) or acylphosphorylation (aspartic acid and glutamic acid) are less well-characterized, and will therefore not be described in detail.

The vast amount of experimentally found phosphorylation sites, opposed by the comparatively low number of kinase and phosphatase genes, brings up the question how the exquisite specificity of the respective kinases and phosphatases towards their substrates can be achieved, leading to precise signaling events needed for cellular functions. Concerning kinases this seems especially challenging, since most eukaryotic protein kinases belong to a single superfamily and exhibit a structurally highly conserved catalytic domain of ~250 residues, composed of an N-terminal lobe of β-sheets and a bigger α-helical lobe at the C-terminus [22, 23]. ATP binds in the cleft between the two lobes and the γ-phosphate gets transferred by conserved residues within the catalytic domain to a serine, threonine or tyrosine hydroxyl oxygen of the substrate that binds along the cleft of the two catalytic domain lobes. Sequence variations of this catalytic domain led to the classification into 10 groups of human kinases that were subdivided into families and subfamilies of highly homologous enzymes. A small number of kinases that display a completely different catalytic fold and mechanism, mostly acting on small molecule substrates, have been combined into the 11th group of atypical kinases. A classification overview of the complete set of human kinases, the kinome, is given in Figure 1.

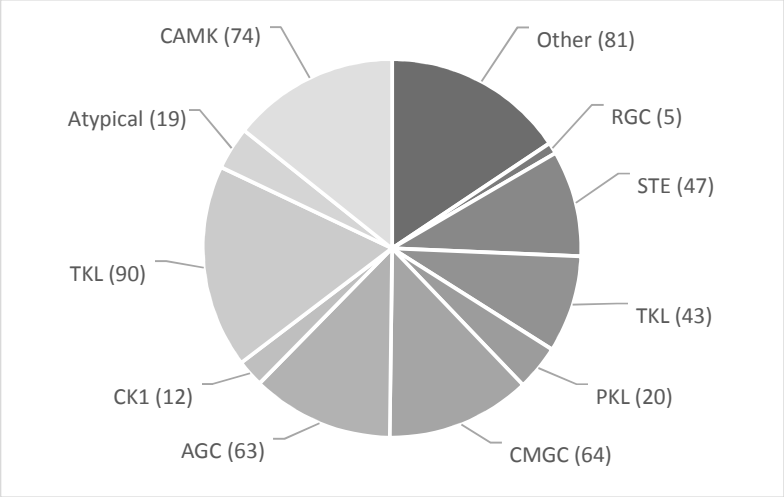

Figure 1. Classification of the human kinome. The 518 human kinases were grouped based on the sequence similarity of the catalytic domain, evolutionary conservation and known function [5]. The 11 groups consist of 133 homologous families that are subdivided into various subfamilies (not shown). This classification into groups does not apply for the atypical kinases that have different catalytic domain folds and mechanisms. The size of a group or family is shown in parentheses. AGC, named after protein kinase A, G and C (PKA, PKG, PKC). STE, homologs of the yeast STE7, STE11 and STE20 genes. CMGC, named after the kinases CDK, MAPK, GSK3 and CLK. TKL, tyrosine kinase like. CAMK, similar to calcium/calmodulin regulated kinases. RGC, receptor guanylate cyclases. CK1, homologs of cell kinase 1. TK, tyrosine kinases. PKL, protein kinase like. Other, group consists of several families that do not fit into other eukaryotic protein kinase (ePK) groups. Atypical, diverse group with no structural similarity to ePKs.

Protein kinase specificity is mediated by a variety of mechanisms such as the depth of the catalytic site that either accommodates the bulky tyrosine or the smaller serine/threonine substrate side chains [24, 25]. Also, the charge or hydrophobicity of residues surrounding the active site help the protein kinase to discriminate between consensus sequences of their substrates and

non-substrate sequences [26]. Distal docking sites can further increase the affinity towards the substrate leading to increased local concentrations of the substrate [27, 28]. The interplay of catalytic subunits with scaffolding and adaptor proteins adds another level of specificity determination, allowing a single kinase to target different substrates by dynamically interacting with a variety of scaffolding/adaptor molecules, depending on the cellular requirements [29-31]. Finally, kinase specificities can be regulated spatially, by localization of the enzyme into distinct subcellular compartments (i.e. by adaptor subunits) leading to locally increased concentrations of the reactants [32-34]. Taken together, these diverse modes of specificity control and substrate recognition lead to a huge variation in phosphorylation sites a kinase can phosphorylate, ranging from very dedicated enzymes as the phosphorylase kinase or the myosin light chain kinase (MLCK) that are only known to phosphorylate a single substrate [35, 36], to promiscuous kinases, such as some calcium-calmodulin dependent protein kinases (CAMK) or cyclin-dependent kinases (CDK) that phosphorylate a wide range of target proteins [37-43].

Protein phosphatases are equally tightly regulated as their enzymatic counterparts, the protein kinases. However, the comparatively low number of genes encoding for phosphatases and the promiscuity some isolated phosphatase catalytic domains show *in vitro* led to the misconception that protein phosphatases were less specific than protein kinases [44]. However, subsequent studies have shown that protein phosphatases are indeed very specific and nonredundant enzymes [45]. The human genome sequencing finally has shown that the human phosphatase complement, the phosphatome, is composed of ~200 phosphatases [4] that are traditionally grouped into six superfamilies according to their substrate specificity, catalytic signature motifs and domain structures [4, 46]. Newer studies suggest the classification into 18 subfamilies based on structural data [47]. An overview of the widely accepted classical division into six subfamilies of the human phosphatase complement is depicted in Figure 2.

The phosphoprotein phosphatase (PPP) and metallo-dependent protein phosphatase (PPM) families account for the majority of phospho-serine and phospho-threonine dephosphorylation reactions. Although they are unrelated in sequence and overall structure, these two families share a structurally similar catalytic center [48] that probably evolved independently from two unique ancestral genes. The PPP superfamily uses a bimetal (Fe^{3+} and Zn^{2+})- dependent catalytic mechanism [49, 50] for protein dephosphorylation and the catalytic domains are highly conserved across species [46]. This superfamily's substrate specificity and function is tightly regulated by interacting with a plethora of regulatory, scaffolding and targeting subunits, allowing a small number of catalytic subunits - 13 in *H. sapiens* - to target a vast amount of substrates and to fulfill many different functions, as extensively shown for protein phosphatases 1 (PP1) and 2A (PP2A) [51-54].

Phosphatases of the PPM superfamily are Mg^{2+}/Mn^{2+}-dependent and share 11 highly conserved signature motifs that constitute structural and functional elements needed for catalysis and metal ion cofactor binding. Here, substrate specificity and regulation is mediated by a variety of additional domains that are fused to the catalytic domain [55, 56]. The most prominent members of the superfamily PPM phosphatases belong to the protein phosphatase 2C (PP2C) subfamily [48, 57, 58].

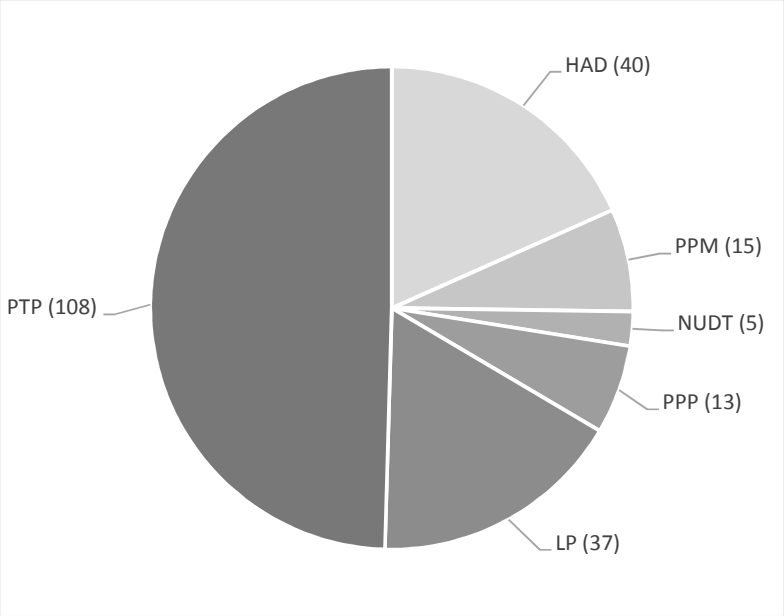

Figure 2. The human phosphatome according to [4] and [7]. The ~200 phosphatases found in the human genome are grouped into six superfamilies in terms of substrate specificities, signature motifs and domain structures. The size of each superfamily is shown in parentheses. HAD, haloacid dehalogenase-like phosphatases. PPM, metallo-dependent phosphoprotein phosphatases. NUDT, or Nudix; nucleoside diphosphate linked to moiety X phosphatases. PPP, phosphoprotein phosphatases. LP, lipid phosphatases. PTP, phospho-tyrosine phosphatases.

The protein tyrosine phosphatases (PTPs) represent the biggest superfamily of phosphatases, with 108 genes found in humans. The members share the common catalytic signature motif CX_5R (C, cysteine; X, any amino acid; R, arginine) but are unrelated in their domain structure and substrate preferences, suggesting that this catalytic mechanism evolved independently three times [46]. Therefore, PTPs have been subdivided into three classes, the class I, II and III of Cys-based PTPs. Class I can be further divided into classical PTPs that exclusively act on phospho-tyrosine phosphorylated proteins, and dual specificity protein phosphatases (DSPs), acting on both, phospho-serine/threonine and phospho-tyrosine residues. The other two classes are represented by the unique low-molecular-mass PTP (LMPTP) and three isoforms of CDC25. Some of the human PTPs have been shown to dephosphorylate non-protein substrates, such as mRNA or phosphoinositides [59-61]. Phospho-tyrosine selectivity of the PTP superfamily is assured by a catalytic cleft deep enough to accommodate bulky phospho-tyrosine residues, whereas phospho-serine/phospho-threonine and dual specificity phosphatases exhibit a relatively shallow active site [62-64]. Similar to the PPM superfamily, PTPs acquired additional substrate specificity and functionality by fusion of a large variety of modular domains to the catalytic domains. These additional domains include transmembrane receptors, protein-protein-interaction modules or membrane targeting domains, as reviewed in [65].

The fourth, and most recently identified superfamily of phosphatases whose members can act on phosphorylated proteins, metabolites or nucleic acids are the aspartate-based phosphatases. They share a haloacid dehalogenase-like hydrolase (HAD) Rossmann-fold with the conserved active site signature motif DXDXT/V (D, aspartate; X, any amino acid; T, threonine; V, valine), and are termed HAD phosphatases. To date, 40 human enzymes have been identified [7], but according to the Structure-Function Linkage Database many more potential sequences exist in the human genome [66]. This ancient family of phosphatases perform catalysis using a mechanism based on an aspartate residue as a nucleophile [67-69], rather than a serine or cysteine residue used by the other protein phosphatase superfamilies [16, 50, 54]. The substrate preferences range from small molecules, such as pyridoxal 5'-phosphate, to serine-/threonine- and tyrosine-phosphorylated protein substrates [70-72]. Specificity and chemical diversification is mediated by domain insertions into defined sites of the catalytic core. Based on these inserts, the HAD phosphatase superfamily is subdivided into five subfamilies. Additional domains, e.g. for membrane-targeting or DNA binding, can be present to further diversify the functionality of this phosphatase superfamily [7, 73-75]. Chronophin, the phosphatase characterized in this work, belongs to this superfamily of phosphatases, therefore this class of enzymes will be described in more detail in the next section.

The remaining two phosphatase superfamilies of lipid phosphatases (LP) and NUDT phosphatases (nucleoside diphosphate linked to moiety X, also termed Nudix) exclusively dephosphorylate small molecules. The heterogeneous LP superfamily is grouped into three subfamilies that act on a variety of phosphorylated lipids, such as sphingosines, inositides and lysophosphatidic acids [76-79], and often show a broad substrate specificity *in vitro* [80, 81]. Members of this superfamily often are integral membrane proteins or exhibit membrane targeting domains and can additionally be equipped with protein-protein-interaction interfaces [82-84].

The NUDT or Nudix superfamily of phosphohydrolases acts on a wide range of pyrophosphates, including nucleoside di- and triphosphates, nucleotide sugars, dinucleoside and diphosphoinositol polyphosphates and RNA caps. The members share the signature motif $GX_5EX_7REUXEEXGU$ (G, glycine; E, glutamate; R, arginine; X, any amino acid; U, aliphatic, hydrophobic residue) that plays an important role in catalysis and binding of the essential divalent cation (mostly Mg^{2+}), while specificity is mediated by residues and motifs in distinct locations of the structure [85-87].

Taken together, phosphoprotein phosphatase specificity is regulated by a variety of mechanisms, similar to the ones regulating protein kinase substrate discrimination. In contrast to many protein kinases that phosphorylate a characteristic consensus sequence, making respective target phosphorylation sites

readily predictable by bioinformatic tools, the target sequences in protein phosphatase substrates often vary greatly [88, 89]. The mechanisms by which the different protein phosphatase families achieve their remarkable substrate specificity differ significantly between the superfamilies: while most catalytic domains of the PPP family form substrate- and function-specific dimeric or trimeric holoenzymes with regulatory, scaffolding and targeting subunits, other protein phosphatase families, such as the PTPs, PPMs or the HAD phosphatases, acquired substrate specificity by fusing regulatory, scaffolding or targeting subunits to the catalytic domains on the genetic level, yielding multidomain proteins. This modular architecture permits a high degree of diversification in terms of specificity and functionality, making phosphatases nonredundant and specialized regulators of physiological processes.

1.2 Haloacid dehalogenase (HAD) hydrolases

The haloacid dehalogenase (HAD)-type superfamily of hydrolases is an ancient, ubiquitous class of enzymes present in all three kingdoms of life. According to the Structure-Function Linkage Database [66], almost 80.000 putative unique protein sequences have been identified, including 536 entries for *H. sapiens*, making HAD hydrolases one of the biggest enzyme superfamilies. The majority (~74%) of these enzymes are phosphatases that hydrolyze phosphate mono-esters, while the second biggest group (~25%) consists of ATPases that act as phosphoanhydride hydrolases. Enzymes facilitating phosphonate hydrolysis (phosphonatases), haloalkane hydrolysis (haloalkane dehalogenases) or transfer reactions of phosphoryl groups between hexose hydroxyl substituents (phosphomutases) are found much less frequently. The following description refers exclusively to HAD phosphatases.

All members of this superfamily share a common Rossmann-fold that contains a three-layered α/β-sandwich comprised of repeating β-α units, forming a central parallel β-sheet that is typically composed of at least five strands in a '54123'-orientation. This fold orients four loops containing the conserved HAD signature motifs that are critical for catalysis and binding of the divalent metal cofactor Mg^{2+} [69]. Motif I has the consensus sequence hhhDXDX(T/V)(L/V)h, with h indicating hydrophobic residues, and X any residue. This motif is located immediately downstream of the Rossmann-fold β-strand 1 in the so called 'squiggle', a conserved structural element composed of six amino acids, starting from the first aspartate in the motif, folding into an almost complete single α-helical turn. During catalysis, the first aspartate in this sequence performs the nucleophilic attack with its carboxylate group, while the backbone carbonyl group

of the second aspartate (Asp + 2) coordinates the cofactor. Downstream of the squiggle a conserved β-hairpin, termed 'flap', protrudes from the Rossmann-fold, partially occluding the binding cleft of the protein.

The consensus sequence of motif II is hhhhhh(S/T) and contains a conserved serine or threonine residue that helps to orient the substrate for the nucleophilic attack and to stabilize the phosphoaspartate intermediate that is formed during catalysis. This motif is located directly downstream of β-strand 2 of the Rossmann-fold.

The HAD consensus motif III is represented by a conserved lysine residue that together with motif II helps to coordinate the substrate and to stabilize the reaction intermediate. This lysine is located upstream of an α-helix that is followed by β-strand 4 of the central β-sheet in the Rossmann-fold.

Finally, motif IV is located downstream of β-strand 4 in the Rossmann-fold. It exhibits the consensus sequence (G/S)(D/S)X_{3-4}(D/E)hhhh and mediates the coordination of the cofactor Mg^{2+} through its aspartate/glutamate residues [7, 68, 69]. Variations of this motif have been found that lack the variable amino acids between the aspartates [90]. Since the Rossmann-fold contains all residues required for catalysis, it is often referred to as the catalytic core or catalytic domain.

The catalytic mechanisms of HAD-type phosphatases is a biphasic reaction. In the first step, the aspartate nucleophile of HAD signature motif I performs a nucleophilic attack on the phosphoryl group of the substrate, resulting in the formation of a phosphoaspartyl intermediate and the dissociation of the substrate's leaving group, which is protonated by the second aspartate of motif I. In the following, step a water molecule initiates a nucleophilic attack on the phosphoaspartyl intermediate to regenerate the catalytic aspartate and to release the phosphate group. Here, the second aspartate of motif I deprotonates the nucleophilic water, thus serving as a general acid/base

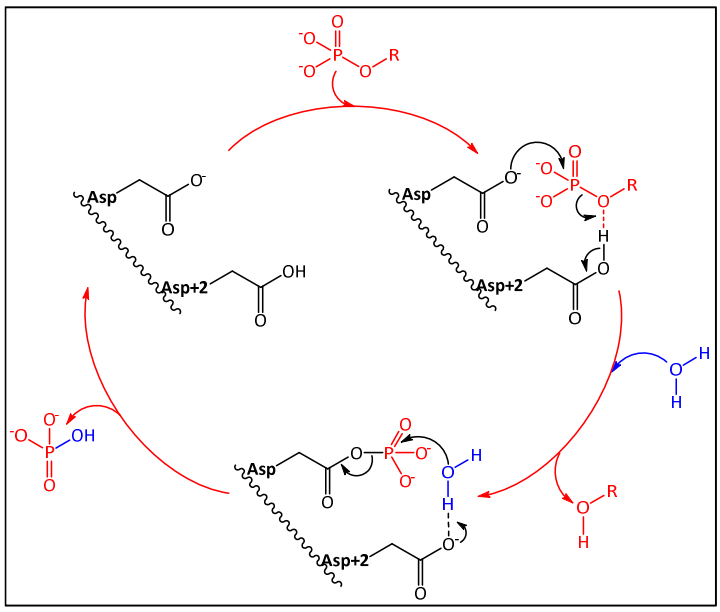

Figure 3. Simplified catalytic mechanism of HAD phosphatases. The two aspartates of conserved motif I are shown as Asp (nucleophile) and Asp+2 (general acid/base). The phosphorylated substrate and the respective leaving groups are shown in red and the water nucleophile in blue. For details, see text.

during the catalytic cycle. A simplified reaction mechanism is depicted in Figure 3. The cofactor Mg^{2+} is absolutely essential for this catalytic mechanism, as it helps to correctly coordinate the substrate's phosphoryl group for the nucleophilic attack and allows close approximation of the substrate phosphomonoester dianion to the catalytic aspartate. The positively charged metal ion additionally stabilizes and neutralizes the negative charge of the phosphoryl oxygens, thereby increasing their dipole moments and the partial positive charge of the phosphorous, making it a better electrophile for the active site aspartate nucleophile. Furthermore, the Mg^{2+} ion, together with the HAD signature motif II and III residues, neutralizes and therefore stabilizes the negative charge of the trigonal bipyramidal transition state [68].

The Rossmann-fold catalytic core is accessorized with additional inserts termed cap domains that control solvent accessibility to the active site, contribute to substrate specificity and selectivity, and in some cases mediate oligomerization. Based on the insertion point and the topology of the cap, HAD phosphatases can be classified into five different subfamilies of highly homologous enzymes [69]. The structurally simplest representative is the C0 cap, consisting of only small inserts at either one of two possible cap insertion sites. Members of this subfamily have been shown to act on macromolecules by utilizing the substrate itself to exclude bulk solvent [90, 91], while other members oligomerize via the capping domain allowing them to process small molecules by 'pseudocapping' [92].

Members of the C1 subfamily of HAD phosphatases are defined by an α-helical insert between the two β-strands of the flap structure, while members of the C2 subfamily possess inserts following β-strand 3 of the catalytic domain and are subdivided into C2a and C2b, depending on the topology of their α/β-fold. C1- and C2-type HAD phosphatases typically process low molecular weight substrates, as the extended capping domains allow bulk solvent exclusion during catalysis, while fully sequestering the substrate within the active site by cap closure. Additionally, the caps have been shown to provide domains that define specificity by directly interacting with the substrate leaving group [93-96]. A few exceptional C1- and C2-capped enzymes have been shown to act on macromolecular substrates, such as the Eyes absent family members (Eya) that dephosphorylate phospho-tyrosine phosphorylated proteins and chronophin that, besides being a pyridoxal 5'-phosphate phosphatase, targets the N-terminal serine phosphorylation site of the protein cofilin-1 [71, 72, 97]. Finally, the C1 + C2 members of the HAD phosphatase superfamily feature inserts in both positions, between the β-strands of the flap and following β-strand 3 of the catalytic core [69]. The crystal structures of some capped HAD phosphatases show extensive movements between the catalytic domain and the capping domain, suggesting a transition between an opened conformation

that allows substrate binding to a closed conformation that excludes bulk solvent for catalysis [98-100]. Representatives of each HAD-type hydrolase subfamily are shown in Figure 4.

The presence of all cap-types in the three kingdoms of life and similar taxonomic distributions of the subfamilies suggests that at least one member of each structural subtype was present in the last universal common ancestor (LUCA), from which genetic radiation led to the vast amount of sequences found today. Interestingly, chemical functionality is not associated with structure, as different cap-types are capable of catalyzing the same reaction, indicating a convergent chemical evolution following an initial diversion due to cap insertion into the Rossmann-fold [7, 69, 101].

Besides the cap-domains, some HAD-type phosphatases acquired additional domains that allowed further diversification and specialization. These include DNA kinase and epoxide hydrolase domains, protein-protein-interaction interfaces, membrane targeting domains and ubiquitin-like folds [73, 102-105]. The regulation of HAD phosphatases through interactions with other proteins, such as regulatory subunits and targeting or scaffolding domains have so far only been described for very few HAD phosphatases [106, 107].

The emerging role of HAD phosphatases in health and disease is displayed by the growing number of enzymes that are linked to human diseases such as cancer, cardio-vascular, metabolic and neurological disorders [7]. This makes the superfamily of HAD-type phosphatases interesting targets for future studies that aim to better understand their regulation and physiological relevance. An improved understanding of structure-function relationships in this enzyme family might also lead to the development of compounds that can be used to modulate their activities *in vivo*.

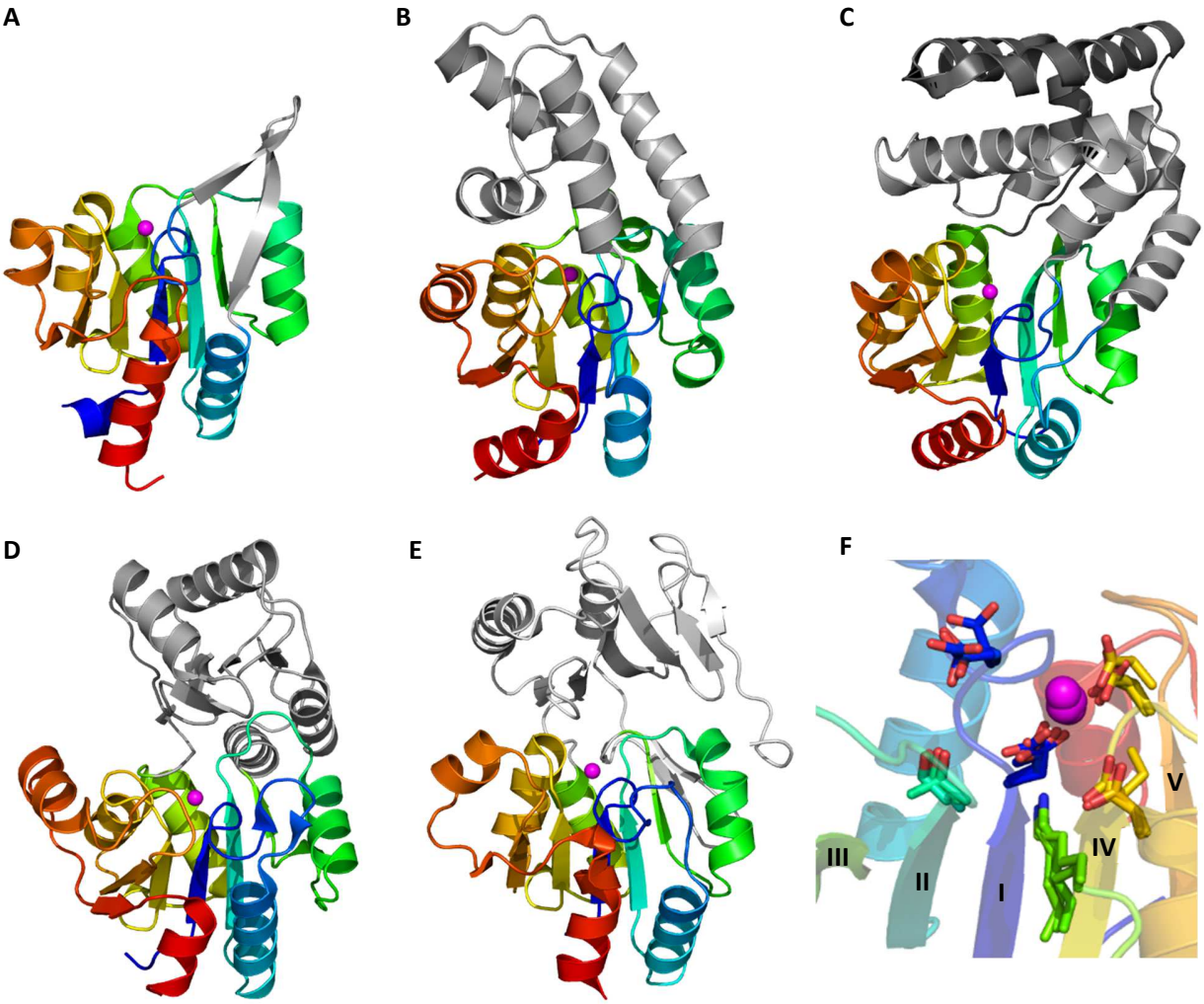

Figure 4. Representative structures of the five HAD phosphatase subfamilies. The conserved Rossman-fold catalytic domains are rainbow-colored from the N-terminus (blue) to the C-terminus (red), the capping domain insertions are colored in gray. The position of the essential cofactor Mg^{2+} in the active site is indicated by a magenta sphere. A, C0 subfamily member 3-deoxy-D-manno-octulosonate 8-phosphate phosphatase KdsC from Haemophilus influenza (PDB code 1K1E). The minimal β-hairpin cap is inserted between β-strand 1 (blue) and β-strand 2 (cyan) of the catalytic core. The C-terminal 21 residues are not shown for better visualization. B, Uncharacterized HAD-type hydrolase (PDB code 2FDR) from Agrobacterium tumefaciens as a representative of the C1 subfamily. The α-helical cap is inserted between β-strand 1 (blue) and β-strand 2 (cyan) of the catalytic core. C, Uncharacterized protein from Archaeoglobus fulgidus (PDB code 1Y8A) as a member of the C1+C2 subfamily of HAD-type hydrolases. This subfamily features cap-insertions in the C0/C1 position (between β-strand 1 and β-strand 2) and between β-strand 3 (green) and β-strand 4 (yellow) of the catalytic domain, shown in light gray and dark gray, respectively. The C-terminal 51 residues are not shown for better visualization. Members of the C2a (D) and C2b (E) possess cap-domain inserts between β-strand 3 (green) and β-strand 4 (yellow) of the catalytic domain, which differ in the topology of their α/β-fold. Shown are p-nitrophenyl phosphatase from Archaeoglobus fulgidus (D, PDB code 3QGM) and an uncharacterized HAD-type hydrolase from Klebsiella pneumoniae subsp. pneumoniae (E, PDB code 3PGV). F, Alignment of all HAD-motifs of the depicted HAD subfamily members (A-E), emphasizing the extreme positional conservation of the active site machinery. Motif I: blue, motif II: cyan, motif III: green, motif IV: orange. The conserved Rossmann-fold of 3QGM (D) is shown for better orientation as a rainbow colored transparent cartoon representation. The central β-sheets in '54123'-orientation are indicated with roman numbers I-V.

1.3 The HAD phosphatase chronophin

Human chronophin is a haloacid dehalogenase-type phosphatase of 296 amino acids (292 in the murine ortholog) that is highly conserved in mammals, showing more than 85% sequence identity on the amino acid level when the proteins of *Mus musculus*, *Rattus norvegicus*, *Bos taurus* and *Canis familiaris* are compared to the human protein. The comparison to hypothetical orthologs in species from more distant taxa, such as *Danio rerio*, *Arabidopsis thaliana* or *Saccharomyces cerevisiae* typically show amino acid sequence identities around 30% and similarities above 60% [108], still indicating a high degree of evolutionary conservation. The enzyme has been shown to be broadly expressed in human and murine tissues, with the highest levels in the central nervous system, particularly the brain, but also in the liver, heart, kidney, testes and skeletal muscle [71, 108].

	motif I	motif II	SSL	motif III	motif IV
HUMAN|Q96GD0	^{21}GVLFDCDGVL^{30}	^{56}FVSNN^{60}	^{180}PW**H**PLSDGSRTP^{191}	^{211}VGKPS^{215}	^{236}VGDRLETDIL^{245}
MOUSE|P60487	^{21}GVLFDCDGVL^{30}	^{56}FVSNN^{60}	^{176}PW**H**PLSDGSRTP^{187}	^{207}VGKPS^{211}	^{232}VGDRLETDIL^{241}
RAT|B2GV79	^{21}GVLFDCDGVL^{30}	^{56}FVSNN^{60}	^{176}PW**H**PLTDGSRTP^{187}	^{207}VGKPS^{211}	^{232}VGDRLETDIL^{241}
DOG|J9NUR4	^{21}GVLFDCDGVL^{30}	^{56}FVSNN^{60}	^{180}PW**H**PLSDGSRTP^{191}	^{211}VGKPS^{215}	^{236}VGDRLETDIL^{245}
SQUIRREL|I3N3H3	^{21}GVLFDCDGVL^{30}	^{56}FVSNN^{60}	^{184}PW**H**PLSDGSRTP^{195}	^{215}VGKPS^{219}	^{240}VGDRLETDIL^{249}
COW|F1MW60	^{21}GVLFDCDGVL^{30}	^{56}FVSNN^{60}	^{180}PW**H**PLSDGSRTP^{191}	^{211}VGKPS^{215}	^{236}VGDRLETDIL^{245}
CHICK|F1NC58	^{29}GLLFDCDGVL^{38}	^{64}FVSNN^{68}	^{187}PW**H**PLSDGQRTP^{199}	^{218}VGKPN^{222}	^{245}VGDRLETDIL^{254}
ZEBRAFISH|B3DI21	^{25}NVLFDCDGVI^{35}	^{60}FVTNN^{64}	^{186}PW**H**PLRGGRITP^{197}	^{217}IGKPS^{221}	^{244}IGDRLETDIL^{253}
	:*******	**.**	***** * **	:***.	:*********

Figure 5. Sequence alignment of chronophin orthologs from different vertebrates. Shown are the four conserved HAD-motifs (I-IV) and the substrate specificity loop (SSL). The residues of the catalytic site are highlighted in gray, the histidine residue of the substrate specificity loop, which is important for the coordination of pyridoxal 5'-phosphate is shown in bold font. The species and Uniprot protein identifiers are given on the left. Fully conserved residues are indicated with an asterisk (*), conserved residues with highly similar properties are indicated with a colon (:) and a period (.) shows conserved positions with only weakly similar properties.

The crystal structure of human chronophin has been solved in 2007 [94], showing that the protein is a member of the C2a subfamily of HAD-type phosphatases. As such, chronophin is composed of two distinct domains, namely the catalytic core and the capping domain. The larger catalytic domain spans amino acids 1-87 and 212-296 and consists of a Rossmann-fold that typically shows a relatively high structural conservation among all members belonging to the HAD superfamily of phosphatases. This domain harbors the four HAD signature motifs that together form the active site and help to orient the catalytically essential cofactor Mg^{2+}. In human chronophin, the characteristic central β-sheet of the Rossman-fold is expanded by two additional short β-strands originating from the N- and C-terminus of the polypeptide, and are here termed 0 and 6. Thus, this central element of the catalytic core can be described as a parallel β-sheet in '0654123'-orientation, whose strands are connected by α-helices (Figure 6B).

HAD signature motif I is located in the squiggle, directly following β-strand 1 of the catalytic core, and contains the two conserved aspartates, of which Asp^{25} serves as the nucleophile in the first step of the hydrolysis reaction. The flap element of human chronophin, located downstream of the squiggle, is a short β-hairpin composed of six amino acids (Trp^{31}-Ala^{36}) that partially roofs the active site. Motif II (Ser^{58}) and III (Lys^{213}) are located directly after β-strand 2 and upstream of β-strand 4, whereas motif IV (Asp^{238} and Asp^{243}) is located downstream of β-strand 4.

The smaller capping domain that stretches from amino acid 88 to 211 in human chronophin is inserted between β-strands 3 and 4 of the catalytic core and largely occludes the active site. It consists of five central parallel β-strands in a '21345'-orientation that are connected by helices. Following β-strand 3 of the capping domain an extended β-hairpin (Pro^{176}-Pro^{187}) is inserted that has been shown to be involved in coordination of chronophin's small molecular weight substrate pyridoxal 5'-phosphate (PLP) by π-electron stacking of the imidazole ring in His^{182} and the pyridine ring of PLP [94]. This structural element, referred to as the 'substrate specificity loop', roofs the entrance of the active site in addition to the flap, thus helping to shield the active site and to exclude bulk solvent, while at the same time contributing to the substrate specificity of chronophin (Figure 6C). An alignment of the human chronophin HAD motifs and the substrate specificity loop with the putative orthologs from several different organisms is shown in Figure 5. The structure of human chronophin is displayed in Figure 6.

Another function of the capping domain is to provide the protein with an interface for homodimerization. This interaction is mainly mediated by the α-helix following β-strand 2 of the capping domain and the α-helix downstream of the substrate specificity loop, which also takes part in the interaction. The dimerization interface largely consists of hydrophobic and polar interactions.

The existence of a disulfide bond between the catalytic domain (Cys^{91}) and the capping domain (Cys^{221}) in several, but not all published structures, led to the speculation that a redox-sensitive mechanism may control the inter-domain movement [109]. Domain movements have been reported for other HAD-type phosphatases [98-100], and a disulfide bridge between the two domains would impede the domain movement and possibly render the phosphatase inactive by inhibiting the opening of the catalytic pocket for substrate binding. However, no differences between the chronophin structures exhibiting a disulfide between Cys^{91} and Cys^{221} (PDB code 2CFS) and the chronophin structure with reduced cysteines (PDB code 2OYC) could be detected by X-ray crystallography [109] and, so far, no domain movement in chronophin or other C2a-type HAD phosphatases has ever been reported, irrespective of the oxidation state of cysteines or ligand binding.

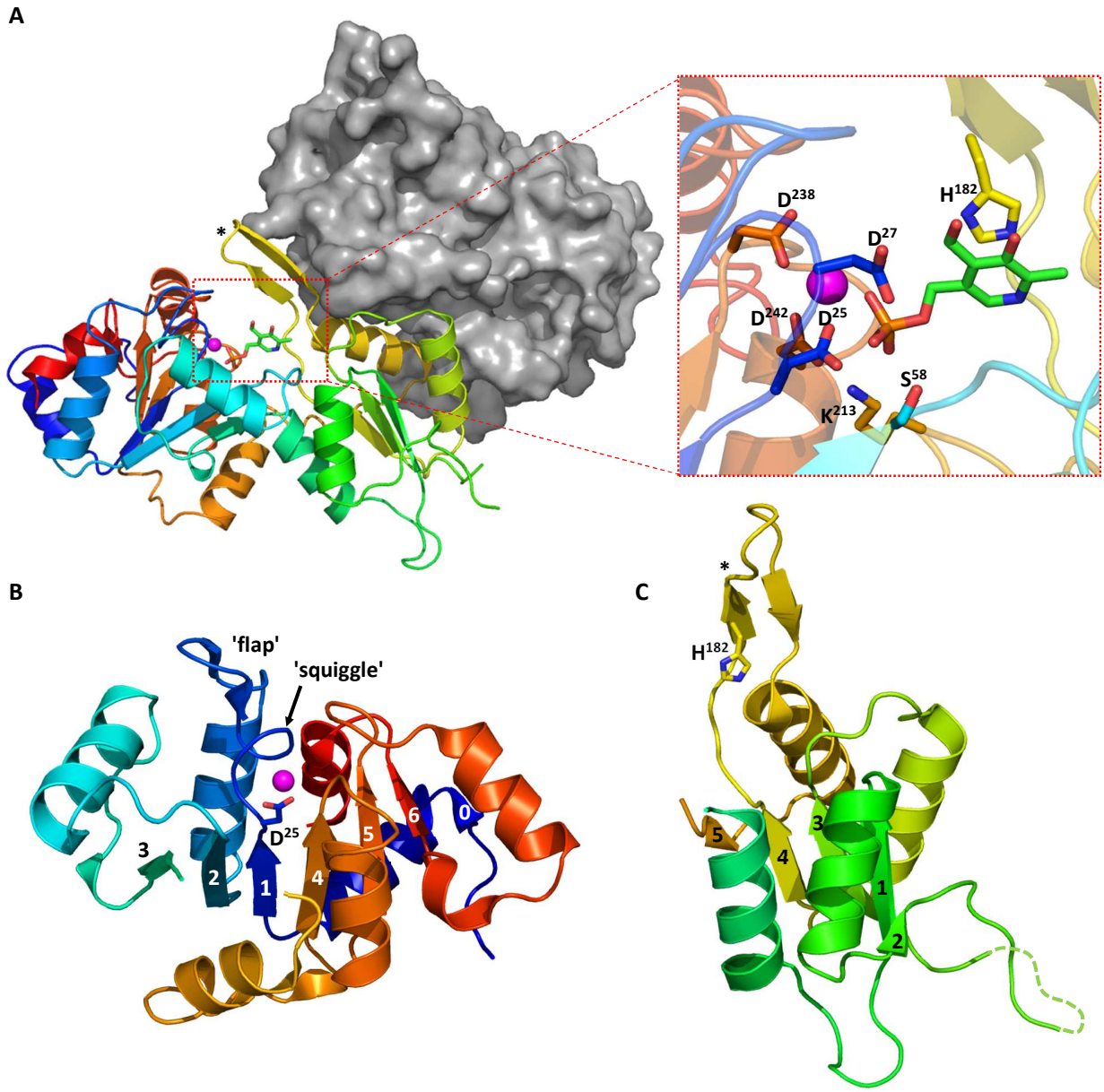

Figure 6. Crystal structure of human chronophin. A (left), Structure of the dimeric holo-enzyme with bound pyridoxal 5'-phosphate (PLP, red box). One protomer is shown as cartoon representation and rainbow-colored from the N-terminus (blue) to the C-terminus (red), the other protomer is shown as surface representation (gray). The catalytic domain in the cartoon representation is colored blue-cyan and orange-red, the capping domain is colored green-yellow. The substrate specificity loop is indicated by an asterisk (, yellow β-hairpin). The catalytically inert Ca^{2+}-ion used for co-crystallization with the substrate PLP is shown as a magenta sphere and marks the position of the cofactor Mg^{2+}. Right, detailed view of the active site with bound PLP. The catalytic residues from the HAD-motifs I-IV and the histidine, which coordinates the pyridine ring in PLP, are shown as sticks. Motif I: blue, motif II: cyan, motif III: light orange, motif IV: dark orange. B, interior view of the chronophin catalytic core. The color-code is according to A, and the central β-sheet in '0654123'-orientation is indicated by numbers. The catalytic nucleophile Asp^{25} is shown as sticks, the cofactor Mg^{2+} is represented by a magenta sphere. The position of the 'squiggle' and 'flap' are given in the figure. C, interior view of the chronophin capping domain. The central β-sheet in '21345'-orientation of this domain is indicated by numbers, and the substrate specificity loop harboring His^{182}, which is critical for the coordination of PLP, is indicated by an asterisk (*). The color-code is according to A. PDB codes: 2P69, 2OYC.*

1.4 Substrates of chronophin

1.4.1 Pyridoxal 5'-phosphate

The HAD phosphatase chronophin was initially identified as a specific phosphatase for phosphorylated B_6 vitamers, with the highest affinity for pyridoxal 5'-phosphate (PLP, K_m 1.5µM), and was therefore termed pyridoxal 5'-phosphate phosphatase (PDXP/PLPP) [70]. PLP is the biologically active form of the vitamin B_6 vitamers that comprise pyridoxal (PL), pyridoxamine (PM), pyridoxine (PN) and the phosphorylated derivatives (PLP, PMP, PNP) of these compounds (Figure 7).

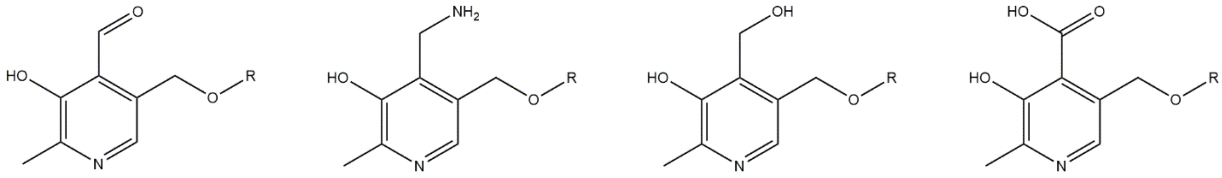

Figure 7. Structures of the vitamin B_6 vitamers. From left to right: pyridoxal (PL), pyridoxamine (PM), pyridoxine (PN) and pyridoxic acid (PA). R = H or PO_3^{2-}. In vertebrates, PL, PM and PN are converted enzymatically into the bioactive form PLP, while PA and PAP represent the end-products of the vitamin B_6 metabolism and are excreted.

PLP is one of the most versatile cofactors and participates as a cofactor in more than 140 reactions, such as transaminations, decarboxylations, deamininations, racemizations, aldol cleavage reactions, as well as eliminations and substitutions at the β and γ atoms of amino acid side chains [110]. The PLP-dependent processes include crucial reactions in the synthesis of neurotransmitters [111, 112], amino acid metabolism [113-115], glycogen breakdown [116], heme synthesis [117] and lipid metabolism [118]. A dysbalance in the metabolism of PLP can have dramatic effects, and many diseases are associated with PLP deficiencies, such as epilepsy, depression, cardiovascular diseases and cancer [119-122].

These characteristics make PLP an essential cofactor for all living organisms, but unlike microorganisms and plants, animals are not able to synthesize PLP *de novo*. Therefore, PLP or its vitamers have to be ingested, as they can all be interconverted enzymatically into the bioactive form of vitamin B_6. The only exceptions constitute 4-pyridoxic acid and 4-pyridoxic acid 5'-phosphate, which are the end-products of the vitamin B_6 metabolism that are excreted in the urine.

Upon ingestion, the vitamin B_6 derivatives get dephosphorylated by a membrane-bound tissue non-specific alkaline phosphatase (TNAP), if needed, and absorbed in the jejunum and ileum by passive

diffusion [123]. This process is driven by trapping the vitamers in the intestinal epithelium through pyridoxal kinase (PDXK)-mediated phosphorylation. It is thought that these intestinal cells directly convert the vitamers into PL by the action of the pyridox(am)ine phosphate oxidase (PNPO) and a pyridoxal 5'-phosphatase phosphatase, and subsequently release PL into the blood stream for the transport into the distant tissues of the organism, where PL is phosphorylated by PDXK to become the bioactive form of vitamin B_6, PLP. B_6 vitamer concentrations that exceed the capacity of the intestinal PLP metabolism to convert PN and PM into PL, supposedly lead to an additional release of the unaltered PN and PM into the blood. The conversion of these B_6 vitamers into PL might then take place in the liver, as this organ has been shown to possess all enzymes and functionalities of the vitamin B_6 metabolism [1, 124]. The role of chronophin as a physiological PLP phosphatase has not yet been demonstrated directly. However, we recently established a chronophin knock-out mouse line and are currently investigating the effects of chronophin loss on a biochemical and a physiological level using this mouse model. Importantly, we were able to show that PLP levels are dramatically increased in organs of chronophin knock-out mice, establishing that chronophin indeed functions as a physiological and non-redundant PLP phosphatase *in vivo* (data not published). The putative PLP metabolism is illustrated in Figure 8.

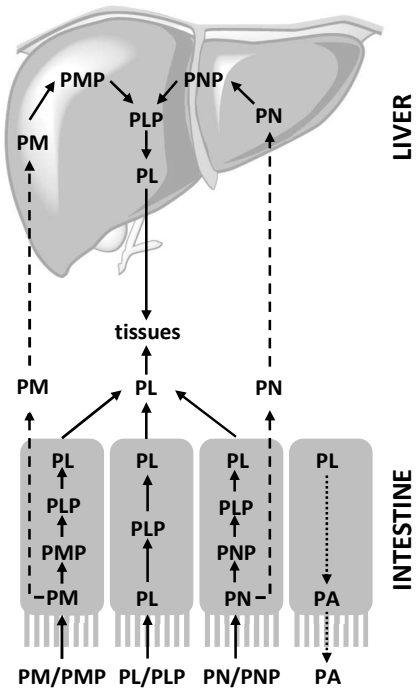

Figure 8. Hypothetical human PLP metabolism (modified from [1]). PM(P), pyridoxamine (5'-phosphate). PL(P), pyridoxal (5'-phosphate). PN(P), pyridoxine (5'-phosphate). PA, pyridoxic acid. For details, see text.

All structurally characterized PLP-dependent enzymes belong to one of five distinct protein folds: the aspartate aminotransferase (AspAT or type I) fold, the β-subunit of tryptophan synthase (TrpSβ or type II) fold, the alanine racemase (AlaR or type III) fold, the D-amino acid aminotransferase (D-AAT or type IV) fold and the glycogen phosphorylase (GP or type V) fold [125]. The catalyzed reactions of all five protein folds involve the formation of a covalent Schiff base intermediate with the 4'-aldehyde of PLP and the ε-amino group of a lysine side chain in the active site of the respective enzyme. This linkage is termed internal aldimine and represents the resting state of the enzyme. The Schiff base linkage then gets replaced by the amino group of an incoming substrate, forming the so called external aldimine intermediate composed of PLP and the substrate, while the active site lysine is released. The external aldimine is the common intermediate from which the different reaction types are catalyzed (see Figure 9).

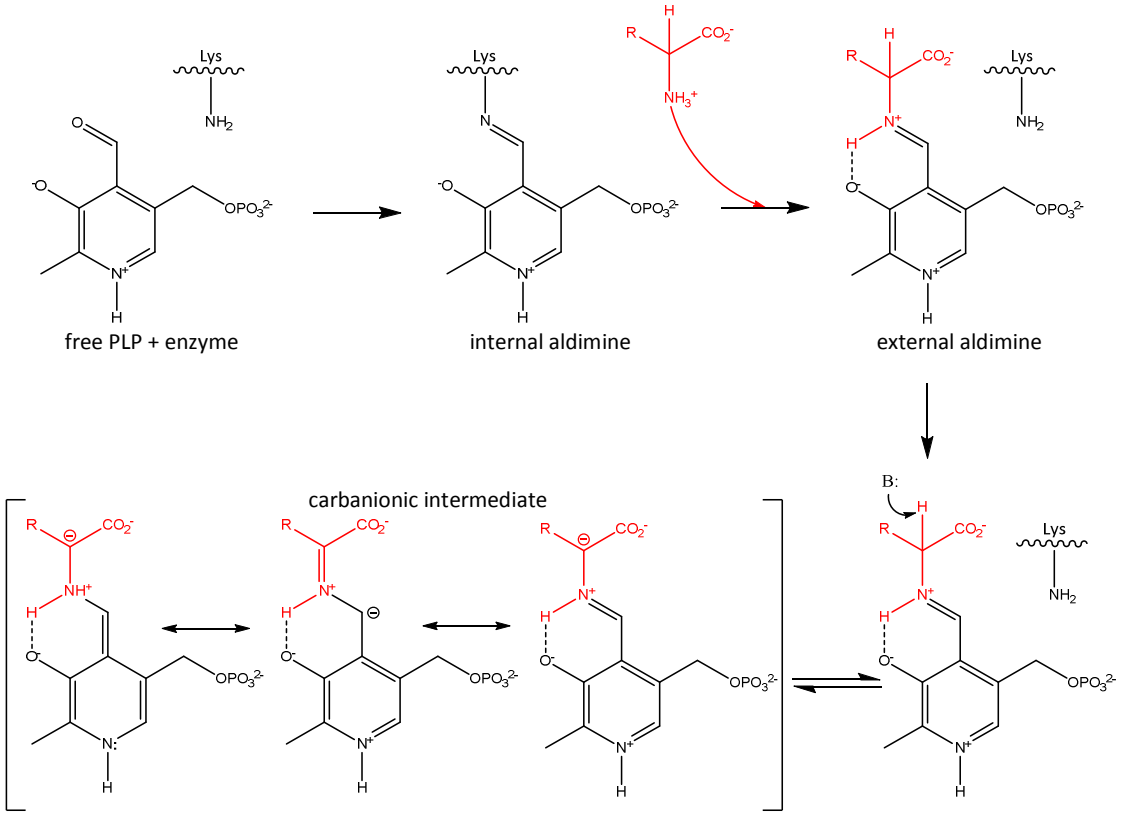

Figure 9. General mechanism of PLP-dependent enzymes. PLP and the active site lysine of the respective enzyme form a Schiff base linkage (internal aldimine) that gets exchanged by the substrate's (red) amino group to form the external aldimine. The following deprotonation (B: = base) of the substrate and the stabilization of the resulting carbanionic intermediate is facilitated by PLP. The carbanionic intermediate (shown as resonance structures) is then converted in one of the various reactions, including transaminations, decarboxylations, deaminations, racemizations, aldol cleavage and other reactions, catalyzed by PLP-dependent enzymes.

During catalysis, PLP serves as an electron sink, facilitating the deprotonation of the carbon attached to the Schiff base nitrogen of the external aldimine. This results in the formation of a carbanionic intermediate that is stabilized by PLP for the subsequent conversion of the substrate [126]. During catalysis, the phosphate group of PLP is always located near the N-terminus of an α-helix, the so called anchoring α-helix. Thus, the relative orientation and location of PLP within the enzyme are determined by the position of the anchoring helix and the active site lysine [125]. The only exception of the aforementioned general mechanism is the PLP-mediated phosphorolytic cleavage of α-glucanes catalyzed by glycogen phosphorylase and maltodextrin phosphorylase. Here, the internal aldimine stays covalently linked to the enzyme, while the 5'-phosphate of PLP acts as a general acid-base during catalysis.

1.4.2 Cofilin-1

Besides being a PLP-specific phosphatase, chronophin has also been shown to directly dephosphorylate the serine-phosphorylated protein cofilin-1 and the serine/threonine-phosphorylated steroid receptor co-activator 3 (SRC-3). Thus, chronophin is able to act on low molecular weight substrates and macromolecules. This section describes the role of the chronophin substrate cofilin-1, while the next section (1.4.3) focuses on the functions of SRC-3.

Cofilin-1 belongs to the members of low molecular mass (15-21kDa) actin-binding proteins and is an ubiquitous, essential regulator of actin dynamics in virtually all eukaryotic cells. Actin is a globular structural protein (G-actin) that polymerizes into right-handed, double helical microfilaments (F-actin), an important component of the cytoskeleton, and additionally forms part of the contractile apparatus of muscle cells. Hence, actin is essential for important cellular functions including cell motility, cytokinesis, endo- and exocytosis, organelle trafficking and muscle contraction [127-132].

During all these processes, the dynamics of actin-filament assembly and disassembly have to be tightly regulated by a plethora of actin binding proteins, among them the family of actin depolymerizing factors (ADFs), which includes the chronophin phosphatase substrate cofilin-1. Being regulators of essential actin-dependent processes, the ADF/cofilin family has been associated with various human diseases, such as neurodegenerative disorders, kidney malfunctions and the invasiveness and metastasis of cancer [133-135]. Other functions of ADFs that are unrelated to the regulation of cytosolic actin dynamics include chaperoning actin to the nucleus where actin is involved in transcriptional control, chromatin remodeling and mRNA export and the release of cytochrome c during apoptosis [136, 137], and will not be described in detail. Furthermore, ADF/cofilin has been shown to activate phospholipase D1 (PLD1), a protein that regulates the actin cytoskeleton in a lipase activity-independent manner [138, 139].

Vertebrates express three isoforms of these actin remodeling proteins, termed ADF (also known as destrin), cofilin-1 and cofilin-2 (hereafter collectively referred to as ADF/cofilin). The most abundant member of this family is cofilin-1, which is expressed in non-muscle tissue, whereas ADF is also present in non-muscle tissue, but only up to a level of 5-10% of cofilin-1 [140]. Cofilin-2, in contrast, is the predominant species in muscle cells. All three actin binding proteins are highly homologous on amino acid sequence level and share related biochemical functions in regulating actin dynamics. However, different physiological and developmental processes have been shown to be dependent on specific ADF/cofilin isoforms [141, 142]. The knock-out of either ADF or cofilin-1 could be rescued by expression of the other

protein, indicating significant functional redundancy. However, cofilin-1 is the only isoform that has been shown to be embryonically lethal in knock-out mice [143, 144].

The actin-remodeling action of ADF/cofilin is on the one hand mediated by actin-filament severing, a process creating new nucleation sites from which additional filaments can polymerize. This function is mechanistically achieved through binding of ADF/cofilin to the actin filaments, leading to increased torsional dynamics that finally break the non-covalent bonds in the longitudinal interface of F-actin [145, 146]. On the other hand, ADF/cofilin can bind to G-actin monomers and thereby promote actin-filament nucleation or sequestration of G-actin monomers. The balance between the actin severing and polymerizing activities of ADF/cofilin have been shown to be concentration-dependent: while high concentration of ADF/cofilin induce actin nucleation, medium concentrations have been shown to stabilize filamentous actin. Low concentrations, in contrast, favor F-actin severing [147]. Although the functions of ADF and cofilin-1 are redundant, they differ quantitatively, with ADF being more efficient in sequestering G-actin and cofilin-1 showing increased nucleation and severing properties [148].

The ADF/cofilin-mediated actin-remodeling is subjected to a complex regulation by a variety of mechanisms, including pH-responsive inactivation through phosphatidylinositol 4,5-bisphosphate (PtdIns(4,5)P_2, PIP_2)-binding at plasma membranes, phosphorylation that targets cofilin for proteasomal degradation in a ubiquitin-dependent manner, inactivating oxidation, and most importantly in the context of chronophin, the activity regulation through phosphorylation on serine^3 [149-158]. This particular phosphorylation site is the target of numerous kinases downstream of various signaling pathways, such as the LIM kinases (Lin-11, Isl1, and Mec-3, LIMK) that are targets of kinases downstream of Rho GTPase signaling, and the testicular kinases (TESK), acting downstream of cell-adhesion regulation [159, 160]. Phosphorylation of serine^3 interferes with binding to G- and F-actin, therefore preventing the nucleation and severing activities of ADF/cofilin. Thus, activation is mediated through phosphatases, including members of the slingshot (SSH) family, protein phosphatase 1 (PP1), protein phosphatase 2A (PP2A) and chronophin [71, 161, 162]. The SSH phosphatase activity itself is mainly regulated by phosphorylation [163], while the association of chronophin, PP1 and PP2A with its substrate phospho-cofilin is mediated by protein-protein-interactions (for details on chronophin, see below) [106, 164]. The complexity of the ADF/cofilin phosphoregulation is enhanced by the fact that the cofilin regulators LIMK1 and SSH1 are both regulated differently by the p21-activated kinase 4 (PAK4) downstream of the Rho GTPases Rac/CDC42 [165, 166], while SSH additionally directly targets LIMK1 for dephosphorylation [165]. A simplified regulatory mechanism of cofilin phosphocycling is summarized in Figure 10.

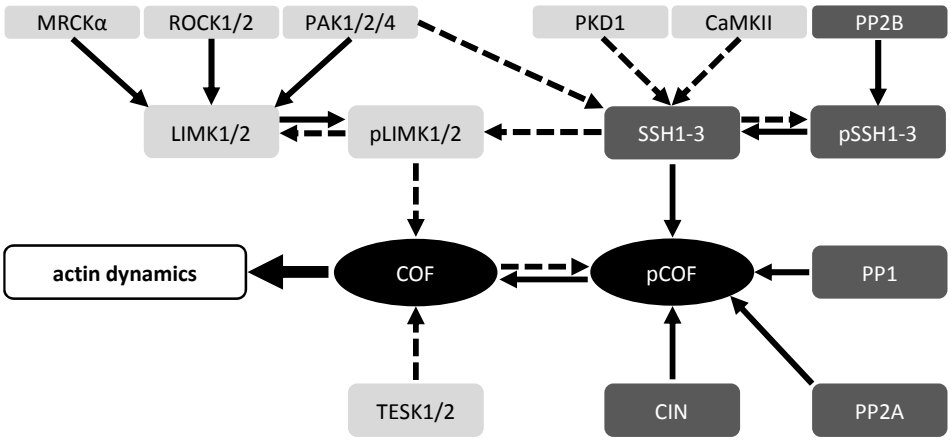

Figure 10. Simplified phosphoregulation of ADF/cofilin. Kinases are shown in light gray with black font, phosphatases in dark gray with white font. ADF/cofilin (COF) is shown in black with white font. Activating phosphoregulation is represented by solid arrows, whereas phosphoregulation leading to inhibition of the respective protein is depicted as dashed arrows. Phosphorylated isoforms of proteins are indicated by a lower case 'p'. The myotonic dystrophy kinase-related Cdc42-binding kinase α (MRCKα), the Rho-associated protein kinases 1 and 2 (ROCK1/2) and the p21-activated kinases 1, 2 and 4 (PAK1/2/4) are targets of Rho-GTPase signaling (not shown) and specifically activate LIM kinases 1 and/or 2 (LIMK1/2). PAK 4 additionally inhibits Slingshot 1 (SSH1). TES kinases 1 and 2 (TESK1/2) are regulated downstream of integrin signaling (not shown). Chronophin (CIN), protein phosphatase 2A (PP2A) and protein phosphatase 1 (PP1) are regulated by protein-protein-interactions (not shown), while the slingshot family of phosphatases (SSH1-3) are phosphoregulated by the Ca^{2+}/calmodulin-dependent protein kinase II (CaMKII), protein kinase D1 (PKD1) and the serine/threonine protein phosphatase calcineurin/PP2B.

Chronophin was identified as a specific and direct cofilin-specific phosphatase by employing an activity based screen. In motile and dividing cells, chronophin co-localizes with cofilin to regions of high actin dynamics, such as membrane ruffles, lamellipodia or the cleavage furrow and the contractile ring during cell division. Overexpression of chronophin in cells showed decreased steady-state phospho-cofilin-1 levels, concomitant dissolution of cortical actin and reduced F-actin stress fibers. The loss of chronophin activity, in contrast, reduced cofilin-1 phosphocycling, stabilized F-actin and led to cell division defects, clearly showing the role of chronophin as a physiological cofilin-1 phosphatase [71]. The distinct subcellular localizations of SSH and chronophin during mitosis indicates that these two cofilin-specific phosphatases might be regulated differentially in a spatiotemporal manner [71, 167].

1.4.3 SRC-3

The second protein substrate that has been identified to be targeted for dephosphorylation by the HAD phosphatase chronophin is the steroid receptor coactivator 3 (SRC-3) [168], one of the three SRC/p160 steroid receptor coactivator family members. SRC-3 acts as a transcriptional coactivator for nuclear receptors (NR), which comprise a conserved superfamily of transcription factors that are activated by steroid, thyroid, retinoid and other lipophilic endocrine hormone ligands [169], thereby specifically regulating gene expression during development, homeostasis and metabolism. Upon ligand binding, NRs undergo conformational changes enabling the recruitment of coactivators, such as SRC-3, that directly enhance the NR-mediated gene expression [170].

SRC-3 was initially identified to be amplified in breast cancer and was therefore named amplified in breast cancer 1 (AIB1) [171]. Other frequent names of SRC-3 are nuclear receptor coactivator-3 (NCoA-3), thyroid hormone receptor activating molecule-1 (TRAM1), activator of thyroid hormone and retinoid receptor (ACTR), receptor associated coactivator-3 (RAC3) and p300/CBP interacting protein (p/CIP). The ~160kDa protein consists of three structural domains: the N-terminal basic helix-loop-helix-Per/ARNT/Sim domain (bHLH-PAS) that mediates the interaction of SRC-3 with other DNA-binding proteins, the receptor-interaction domain (RID), by which SRC-3 binds to the ligand-activated nuclear receptors and, finally, the C-terminal domain harboring histone acetyltransferase activity. Additionally, this domain contains two intrinsic transcriptional activation domains, AD1 and AD2, by which SRC-3 recruits histone acetyltransferases and histone methyltransferases, respectively [172].

Transcriptional analyses in human tissues revealed that SRC-3 shows specific expression patterns with high abundance in uterus, mammary gland, hypophysis, testis, heart, and skeletal muscle whereas only low levels were detected in bone marrow, liver, lung, brain, kidney, stomach, and adrenal gland [173].

SRC-3 has been implicated to be important in the steroid receptor-mediated regulation of normal growth, puberty, female reproductive function, and mammary gland development [174]. Besides its role as a nuclear receptor coactivator, SRC-3 has been shown to be a transcriptional coactivator for other transcription factors, including NF-κB, AP-1, E2F1, STAT6 and PEA3. Additionally, SRC-3 acts as a translational repressor regulating proinflammatory cytokine mRNA translation [175-180]. The oncogenic potential of SRC-3 has been shown in mouse models [181], and many other cancer types besides breast cancer have been associated so far with SRC-3 dysregulations [182].

The function of SRC-3 is regulated by post-translational modification, including ubiquitination, acetylation, methylation and phosphorylation [183-186]. Ubiquitinitation targets SRC-3 for degradation, methylation and acetylation inhibit the SRC-3 function as a NR coactivator by promoting dissociation of the nuclear receptor protein complexes. Phosphorylation, in contrast, leads to an activation by allowing coactivator complex assembly, for instance with the histone acetyltransferase p300/CBP and the coactivator arginine methyltransferase 1 (CARM1) that induce chromatin remodeling in order to facilitate transcription of the nuclear receptor target gene [183, 187, 188]. SRC-3 phosphorylation has so far been shown to involve kinases downstream of distinct cellular signaling pathways, such as the mitogen-activated protein kinase (MAPK), IκB kinase (IKK) and receptor tyrosine kinase HER2/neu [189-191]. It is thought that different cellular kinase-mediated signaling events lead to specific phosphorylation patterns of SRC-3, resulting in differential transcription factor dependent activation of target genes [192], or even the regulation of coactivator turnover by phosphorylation-dependent ubiquitination and subsequent proteasomal degradation [184]. Therefore, phosphatases play a decisive role in the control of transcriptional coactivators. A model of SRC-3 coactivator complex regulation is shown in Figure 11.

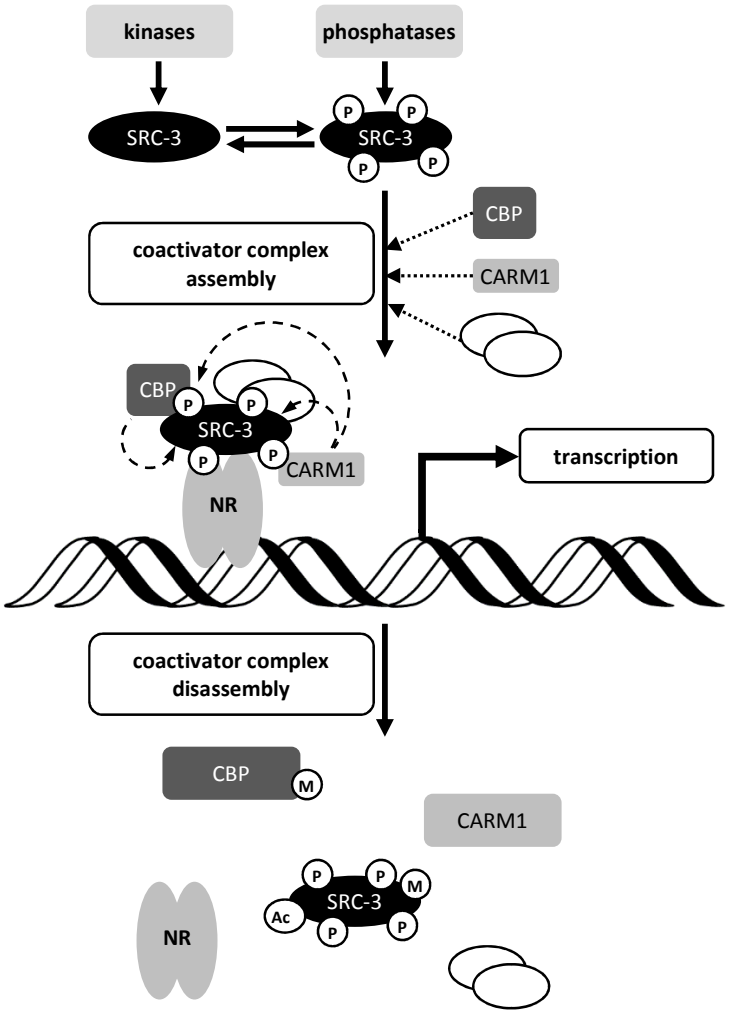

Figure 11. Model of SRC-3 coactivator complex regulation. SRC-3 is activated by kinase-mediated phosphorylation (indicated by a circled 'P') downstream of various signaling pathways. This process is antagonized by phosphatases, such as chronophin. Phosphorylation of SRC-3 leads to coactivator complex assembly, including histone acetyltransferase CBP and coactivator arginine methyltransferase 1 (CARM1), and possibly other coactivators (white circles). The interaction of this coactivator complex with nuclear receptors (NR), such as the estrogen receptor, leads to target gene transcription. Subsequently, SRC-3 and other components of the coactivator complex get methylated and acetylated through the action of CARM1 and CBP, leading to coactivator complex disassembly.

Chronophin has been found to be involved in the phosphoregulation of SRC-3 by employing a functional genomic screen. Subsequently, it could be shown that chronophin is a negative regulator of SRC-3 activity in cells, by dephosphorylating six known serine/threonine phosphorylation sites in SRC-3, and therefore inhibiting the ligand-dependent interaction of SRC-3 and the estrogen receptor (ER) [168]. This indicates that chronophin might play a direct role in the transcriptional co-regulatory activity of SRC-3 in steroid receptor signaling.

Taken together, chronophin has so far been shown to target very different substrates for dephosphorylation, ranging from small molecular weight compounds, such as phosphorylated vitamin B_6 derivatives, to serine/threonine phosphorylated proteins like cofilin-1 and SRC-3. This implies that chronophin plays a role in very different physiological processes, namely the vitamin B_6 metabolism, where this phosphatase might be crucial for the release of unphosphorylated B_6 vitamers from cells, the regulation of actin dynamics through activating dephosphorylation of serine^3-phosphorylated ADF/cofilin and inhibiting transcriptional co-regulatory activity of SRC-3 in steroid receptor signaling. The association of all these processes with human health and disease make chronophin a highly interesting target for further studies, aiming to better understand the role and regulation of this phosphatase in the various pathways.

To date, chronophin has already been implicated in some pathological conditions. A potential role of chronophin in epilepsy was found, suggesting that chronophin-mediated actin dynamics might play a role in the changes of morphological properties and excitability of the epileptic hippocampus in rat brains [193]. A subsequent study could additionally provide evidence for a role of chronophin in inducing apoptosis in astrocytes via ADF/cofilin in a rat brain epilepsy model [194]. The same group furthermore found indications that chronophin inhibits the induction of long term potentiation in rat brains, a process that changes the synaptic efficacy in response to neuronal activity, which is important in learning and memory [195].

1.5 Interaction partners of chronophin

1.5.1 β-Arrestin-1

Information about the regulation of chronophin, and HAD-type phosphatases in general, is very limited. To date, only two interaction partners of chronophin have been identified, one of which is β-arrestin-1. Arrestins are best known for their functions in G-protein coupled receptor (GPCR) desensitization and internalization [196, 197], but they also serve as signaling scaffolds by interacting with distinct elements of signaling pathways, bringing them into close proximity and therefore activating signaling cascades independently of G-proteins [198]. According to recent studies, protease-activated receptor-2 (PAR-2) activation promotes cofilin dephosphorylation and actin-filament severing in a β-arrestin-dependent process without engaging G-proteins. This process has been shown to be dependent on chronophin activity, while LIM kinase (LIMK) action is antagonized by an unknown mechanism involving β-arrestins. Finally, it could be shown that all three proteins, cofilin, chronophin and LIMK associate with β-arrestins upon PAR-2 stimulation, followed by a redistribution to membrane protrusions [107, 199]. These results suggest that β-arrestins might serve as a scaffold for a complex composed of cofilin, chronophin and inhibited LIMK, facilitating actin filament severing locally restricted to membrane protrusions.

1.5.2 Heat-shock protein 90β

The other chronophin interactor that has been described so far is heat-shock protein 90β (Hsp90β) [106]. The family of Hsp90 proteins are ubiquitous molecular chaperones found in all kingdoms of life, and are essential for the viability of eukaryotic cells [200]. Vertebrates exhibit several isoforms: the inducible Hsp90α, the constitutively expressed Hsp90β and two additional homologs in mitochondria and the endoplasmatic reticulum [201]. Hsp90s selectively assist 'client' proteins, which differ structurally and functionally, including telomerase, nitric oxide synthase, nuclear hormone receptors and protein kinases, in correct folding and maturation [202-205]. This mechanism is ATP-driven, however the molecular basis for specificity and precise function is largely unknown.

According to Huang et al. [106], Hsp90β directly interacts with chronophin. The association of the proteins has been shown to be significantly enhanced in the presence of ATP. Binding of chronophin to Hsp90 leads to an attenuation of cofilin dephosphorylation *in vitro* and in cells. The authors suggest that

the Hsp90-chronophin interaction constitutes an energy status sensing mechanism leading to cofilin dephosphorylation upon ATP-depletion. Furthermore, they found evidence for the formation of ADF/cofilin-actin rods, pathological aggregates that are often present in neurodegenerative diseases [133], as a consequence of the Hsp90/chronophin-dependent energy depletion response mechanism in cultured murine hippocampal and cortical neurons.

1.5.3 The Ca^{2+} and integrin binding protein 1 (CIB1)

Recently, our group identified two additional putative interaction partners of chronophin, which will be discussed in greater detail since their association with chronophin and their role in chronophin regulation were investigated as part of this thesis. All discussed results and detailed information regarding material and methods presented in the following section are unpublished data of Dr. E. Jeanclos (our lab) or can be found in the doctoral thesis of A. Hoffmann (Heinrich Heine University/Düsseldorf, 2009).

One of the novel, putative interaction partners of chronophin is the Ca^{2+}- and integrin-binding protein 1 (CIB1). It is also commonly named calmyrin, DNA-PKcs interacting protein, SNK-interacting protein 2-28 (SIP2-28) or kinase interacting protein (KIP), and it belongs to the EF-hand containing family of calcium-binding proteins (CBPs). Associated family members are generally characterized by the possession of one or more EF-hand domains, structural helix-loop-helix elements that bind Ca^{2+}-ions with high specificity, leading to a conformational change within the CBP and thereby allowing the protein to bind its target effector proteins. Ca^{2+}-ions are important signaling molecules that control a wide range of physiological processes, and CBPs are essential mediators of second messenger effects during Ca^{2+}-signaling.

In the human genome, four CIB homologs denominated CIB1-4 are found [206]. Highly homologous sequences are also present in the genomes of other organisms, such as *Drosophila melanogaster*, indicating evolutionary conservation. Two splice variants of human CIB1, termed CIB1 and CIB1a, are known [207], of which the shorter, 191 amino acid long (22kDa) isoform CIB1 is regarded as the canonical sequence (according to UniProt). CIB1 is broadly expressed in human and murine tissues, whereas CIB1a expression has so far only been analyzed in cancer cells [207-209]. The protein is monomeric *in vivo* and *in vitro*, and the *in vitro* formation of stable dimers and insoluble aggregates has also been reported [210, 211].

Initially, CIB1 was identified as an interaction partner of the cytoplasmatic tail of the platelet specific integrin subunit α_{IIb} [212], and has since then been shown to regulate and interact with a plethora of

different effector proteins, including the transcription factor PAX3 [213], the inositol 1, 4, 5-trisphosphate receptor [214], polo-like kinases [215, 216], the small GTPase Rac3 [217], the focal adhesion kinase (FAK) [218] and the Alzheimer's disease-related presenilin-2 [219]. This implies numerous cellular processes that comprise regulation by CIB1, of which integrin $\alpha_{IIb}\beta_3$ mediated cell adhesion and spreading, cell cycle progression and others have already been delineated to be directly CIB1-associated [217, 220, 221]. Importantly, CIB1 has been shown to be involved in cofilin-mediated actin reorganizations during cell migration, by binding and activating the p21-activated kinase 1 (PAK1), leading to a GTPase independent LIMK1 phosphorylation [220], suggesting that CIB1 and chronophin both play a role in regulating cofilin.

Despite the many processes involving CIB1, knock-out of CIB1 in mice is not lethal, but causes spermatogenesis defects leading to sterility in males, as well as impaired angiogenesis after ischemia and during tumor growth [222-224]. The absence of more severe defects might be due to compensatory effects by other CIB family members [225]. However, several specific roles of CIB1 in health and disease have been described, such as regulation of calcineurin-NFAT signaling during cardiac hypertrophy, involvement in spermatogenesis/development of oligoasthenozoospermia, and a potential role in Alzheimer's disease [226-228].

The crystal structure of CIB1 has been solved in 2004 [206], showing that this protein structurally resembles other EF-hand containing CBPs, such as calmodulin and calcineurin B, which additionally share remarkably high amino acid sequence similarities of more than 50% with CIB1. The protein is predominantly α-helical and contains four EF-hand motifs denoted as EF1-4, of which only the C-terminal two domains (EF3 and EF4) bind Ca^{2+}-ions with dissociation constants (K_d) of 1.9 and 0.54µM, respectively [229]. EF3 is capable of binding Mg^{2+} as well, but with ~60-fold lower K_d (120µM) than Ca^{2+} [229]. Binding of either Ca^{2+}- or Mg^{2+}-ions significantly increases the stability of CIB1, compared to the unliganded apo-CIB1 [230]. Thus, the magnesium-bound form of CIB1 (Mg^{2+}-CIB1) is considered the physiologically relevant form of CIB1 in resting cells, where Mg^{2+}-concentrations usually range from 0.5-3mM [231]. Interestingly, both, Ca^{2+}-CIB1 and Mg^{2+}-CIB1 have been shown to bind effector proteins with high affinity, suggesting that both forms play a role in Ca^{2+}-dependent and -independent cellular processes [232]. EF1 and EF2 are incapable of binding divalent metal ions due to mutations and small insertions in the metal binding loop [206].

CIB1 additionally exhibits an N-terminal extension that can be myristoylated for Ca^{2+}-independent membrane targeting, allowing CIB1 to translocate effector proteins, such as the sphingosine kinase 1 (SK1), to the plasma membrane [219, 233]. The α-helical C-terminal extension of CIB1 folds back into a

hydrophobic channel formed mainly by EF3 and EF4 and shields it from solvent. Displacement of this helix to fully expose the proposed hydrophobic effector protein binding pocket plays an important role in the binding specificity of CIB1 [234]. The structure of CIB1 is displayed in Figure 12.

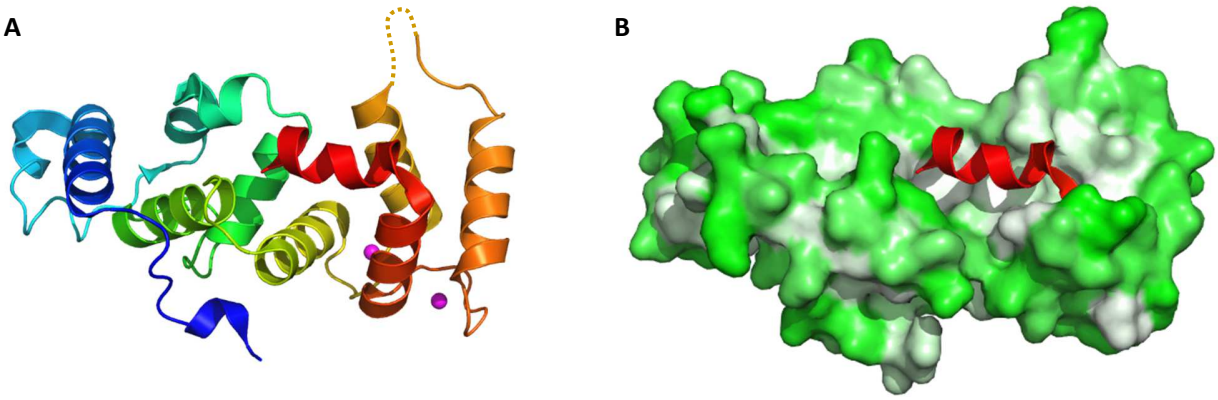

Figure 12. Crystal structure of Ca^{2+}-CIB1. A, Cartoon representation of Ca^{2+}-CIB1, rainbow-colored from the N-terminus (blue) to the C-terminus (red). The flexible N-terminal eight residues including the myristoylation site were removed for crystallization. The functional Ca^{2+}-binding sites EF3 and EF4 are represented in yellow/light orange and dark orange/red, respectively. Two bound Ca^{2+}-ions at EF3 and EF4 are indicated as magenta spheres. B, Surface representation of Ca^{2+}-CIB1, color-coded according to the Eisenberg hydrophobicity scale [3] with green being hydrophilic residues and white being hydrophobic residues. The α-helical C-terminal extension is shown in red as cartoon representation to emphasize its role in shielding the hydrophobic cleft formed by EF3 and EF4. Both representations of Ca^{2+}-CIB1 are oriented equally. PDB code: 1XO5.

The interaction of chronophin and CIB1 was found by screening a mouse brain cDNA library using the yeast two-hybrid system, and was shown to be independent of the chronophin phosphatase activity, as CIB1 likewise associates with the phosphatase-inactive chronophin^{D25N} mutant. Furthermore, the CIB1/chronophin binding interface could be mapped by additional yeast two-hybrid screens. The C-terminal residues 173-178 of CIB1 and residues 75-85 of chronophin seem to be of particular importance for the interaction.

The interaction was additionally confirmed biochemically in solid-phase assays using recombinantly expressed proteins, indicating that chronophin binds directly to CIB1 in a dose-dependent and saturable manner. In support of the yeast two-hybrid mapping, a version of CIB1 C-terminally truncated after residue 173 showed decreased binding to chronophin in solid phase binding assays compared to wild-type CIB1. To further verify this direct interaction, pull-down assays were performed with glutathione-sepharose bound GST-CIB1 as a bait and recombinantly expressed chronophin, lysates from HeLa cells overexpressing chronophin or mouse brain lysates as input. In all three experiments chronophin could be co-precipitated by GST-CIB1 but not GST alone, affirming the bimolecular interaction. The association of CIB1 with chronophin was not increased when pull-down assays were performed at elevated cellular calcium

concentrations, using lysates from HEK293 cell treated with the Ca^{2+}-ionophore A23187, indicating that Ca^{2+}-CIB1 and Mg^{2+}-CIB1 bind equally well to chronophin.

1.5.4 Calmodulin

Based on the homology of CIB1 to calcineurin B (CnB), we hypothesized that calmodulin (CaM) might be another player in a potential chronophin-regulatory complex, as calmodulin and CnB together play a decisive role in the regulation of the Ca^{2+}-dependent serine/threonine phosphatase calcineurin/PP2B (for a review on calcineurin, see [235]).

Calmodulin is a ~17kDa EF-hand containing Ca^{2+}-binding protein structurally similar to CIB1. It is highly conserved, expressed in all eukaryotic cells and represents one of the most important and best characterized mediators of calcium-signaling [236]. Calmodulin targets dozens of effector proteins, including numerous kinases and phosphatases, that are involved in virtually all cellular processes ranging from signaling, metabolism, inflammation to ion channel regulation and many others [237-240]. Ca^{2+}-dependent cytoskeletal regulation is mediated through calmodulin via the Ca^{2+}/calmodulin-dependent protein kinase II (CaMKII) and calcineurin/PP2B, two antagonistic phospho-regulators of the cofilin-specific phosphatase slingshot (SSH, see above) [241, 242]. This indicates that calmodulin, CIB1 and chronophin play important roles in the phosphocycling of ADF/cofilin, the key regulator of cytoskeletal actin dynamics.

Owing to the many pathways involving calmodulin, it is obvious that genetic knock-out of this important Ca^{2+}-signaling molecule is lethal for the respective model organism [243]. However, various human pathological conditions could be associated to mutations of calmodulin, many of them concerning cardiac disorders, such as ventricular tachycardia, idiopathic ventricular fibrillation and recurrent cardiac arrest in infants [244-246].

The structure of Ca^{2+}-free (or apo-) calmodulin is elongated, with two terminal Ca^{2+}-binding lobes that are connected by a flexible linker, each composed of two EF-hands. Thus, calmodulin has four EF-hands, numbered I-IV starting from the N-terminus, which are all involved in calcium-binding. Upon Ca^{2+}-binding to the four EF-hands, (holo-) calmodulin undergoes large conformational changes, opening hydrophobic pockets in each of the lobes and forcing the connecting linker into an α-helical conformation, inducing a dumbbell-shaped overall structure. The binding pockets harbor several methionines that accommodate hydrophobic side chains of the target's protein calmodulin binding domain (CBD), which is generally α-helical. Calmodulin typically wraps around its effector protein's CBD, with the two globular domains

gripping both sides of it. The central lobe-connecting helix collapses during this process, supposedly due to formation of salt-bridges with the target CBD [247]. Structures of apo-calmodulin, holo-calmodulin and holo-calmodulin binding a target peptide are shown in Figure 13.

The hydrophobic binding pockets are generic in shape, and the target CBDs are not required to possess any specific amino acid sequence or structural binding motifs, but rather conserved positions of hydrophobic residues, making calmodulin a highly versatile regulatory protein. Furthermore, calmodulin is not restricted to the aforementioned common mechanism: while most interactions of calmodulin have been shown to be Ca^{2+}-dependent, some have been revealed to be independent of calcium [248, 249], or to follow a distinct, non-canonical Ca^{2+}-dependent binding-mechanism [250-253]. Finally, it is hypothesized that the sequential binding of Ca^{2+}-ions to the four EF-hands I-IV, following a III-IV-I-II order, allows specific effector protein binding dependent on the number of Ca^{2+}-ions bound to calmodulin [254, 255], yet increasing the remarkable plasticity of this protein. Interaction with calmodulin can lead to activation (e.g. by displacing an autoinhibitory domain), inactivation, as seen in voltage dependent Ca^{2+}-channels, or calmodulin-mediated tethering of proteins [256-259].

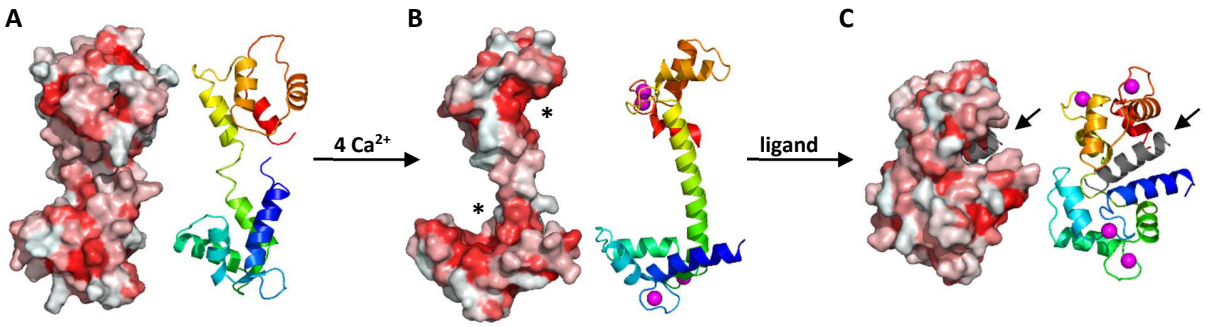

Figure 13. Structural changes of calmodulin induced upon Ca^{2+}- and ligand-binding. Surface representations are colorcoded according to the Eisenberg hydrophobicity scale [3] with white being hydrophilic residues and red being hydrophobic residues. Cartoon representations are rainbow-colored from the N-terminus (blue) to the C-terminus (red). Both representations are oriented in the same way. A, Apo-calmodulin is almost globular. The two lobes (blue-green and yellow-red in the cartoon representation) are connected by a flexible linker. B, Holo-calmodulin. Upon binding of four Ca^{2+}-ions, calmodulin undergoes large conformational changes, opening hydrophobic pockets (indicated with asterisks in the surface representation) for effector protein binding. The bound Ca^{2+}-ions are shown as magenta spheres. C, Holo-calmodulin with bound peptide shown in gray (arrow) of an effector protein (CaMKIIα) buried deeply inside the protein. The bound Ca^{2+}-ions are shown as magenta spheres. PDB codes: 1CFD, 1CLL, 1CM1.

The analysis of the human and murine chronophin sequences using the Calmodulin Target Database (http://calcium.uhnres.utoronto.ca/ctdb/ctdb/home.html) revealed that both orthologs possess potential calmodulin binding domains. Interestingly, these predicted interaction sites partially overlap with the interaction site of CIB1 on chronophin mapped by yeast two-hybrid assay (Figure 14). Importantly, the

predicted calmodulin binding sites of chronophin are partially located on the surface of the protein and contain α-helical elements, suggesting that chronophin indeed might be an effector protein of calmodulin. An analysis of the human and murine CIB1 sequences additionally predicted putative calmodulin binding sites on this protein, implying the possibility of a ternary complex formed by chronophin, calmodulin and CIB1.

H.s. chronophin	[41]PELLERLA**RA GKAALFVSNN SRRARPEL**AL RFARLGFG**GL RAEQL**F**SSAL CAARLLR**QRL
Q96GD0	1234556789 9999999999 8777787654 4444444567 8877766666 6666666543
M.m. chronophin	[41]PELLQRLARA GKNTLFVSNN SRRARPELAL RFARLGFAGL RAEQLFSSAL CAARLLRQRL
P60487	3333334444 4444444321 1123464444 4444444678 9988877777 7777777643

Figure 14. Putative CIB1 and calmodulin binding sites on human and murine chronophin. The CIB1-binding site (gray) on human chronophin was mapped by yeast two-hybrid, the putative calmodulin binding sites (bold font) were found using the Calmodulin Target Database. The values (0-9) below the protein sequences are normalized scores to evaluate the probability of calmodulin-binding, based on criteria such as hydropathy, α-helical propensity and residue charge. Highest probabilities are indicated as series of 9s. The respective sequence of murine chronophin is shown for comparison, Uniprot protein identifiers are given below the species name.

The interactions were then assessed experimentally by employing a calmodulin-sepharose pulldown assay, showing that both, chronophin and CIB1, bind to calmodulin-sepharose but not to the sepharose alone. The same results were achieved by repeating the experiment with endogenous CIB1 and chronophin using murine testis lysates. The interaction of CIB1 and calmodulin with chronophin is mutually exclusive, as a 10-fold molar excess of CIB1 could significantly reduce the amount of chronophin binding to calmodulin-sepharose, substantiating an overlap of the calmodulin and CIB1 interaction sites on chronophin. Interestingly, the calmodulin/chronophin association increased at elevated Ca^{2+}-levels, while the CIB1/calmodulin interaction was concomitantly reduced.

Taken together, these preliminary results indicate that chronophin interacts with both, CIB1 and calmodulin in a mutually exclusive manner. Furthermore, CIB1 and calmodulin were shown to interact with each other. The interactions appear to be regulated by Ca^{2+}, as the presence of Ca^{2+}-ions increases the binding of chronophin to calmodulin-sepharose, while the interaction of CIB1 is diminished. The binding of CIB1 to chronophin seems not to be affected by Ca^{2+}. The interactions are summarized in Figure 15.

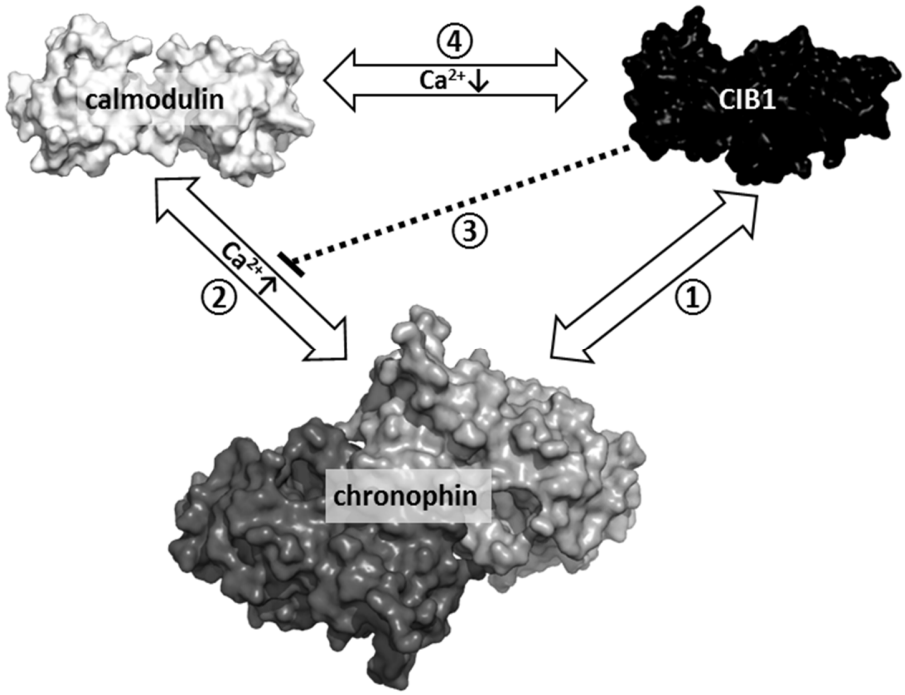

Figure 15. Summary of the previously described interactions between chronophin, calmodulin and CIB1. The CIB1/chronophin-interaction was found employing a yeast two-hybrid screen, and confirmed by pulldown-assays and solid-phase binding assays. Calcium has no effect on the interaction (1). The calmodulin/chronophin-interaction was found by screening the chronophin sequence for putative calmodulin binding sites using the Calmodulin Target Database. The interaction was confirmed by calmodulin-sepharose pulldown-assays, showing that Ca^{2+} increases the interaction (2). The presence of CIB1, in contrast, decreases the binding of chronophin to calmodulin-sepharose, indicating mutually exclusive binding of calmodulin and CIB1 to chronophin (3). According to the Calmodulin Target Database, CIB1 contains a putative calmodulin binding site, which was confirmed by calmodulin-sepharose pulldown-assays. This interaction was shown to decrease in the presence of Ca^{2+}.

2 Materials

2.1 Bacterial strains

Table 1. Bacterial strains.

Strain	Genotype	Supplier
BL21-CodonPlus(DE3)-RIL	F⁻ *ompT hsdS* (r_B^- m_B^-) *dcm*⁺ Tet^r gal λ (DE3) *end*A Hte [*argU ileY leuW* Cam^r]	Stratagene
DH5α	F– Φ80*lac*ZΔM15 Δ(*lac*ZYA-*arg*F) U169 *rec*A1 *end*A1 *hsd*R17 (rK–, mK+) *pho*A *sup*E44 λ– *thi*-1 *gyr*A96 *rel*A1	Invitrogen

2.2 Media and antibiotics

Table 2. Media.

Medium	Composition	Supplier
LB-medium (Luria/Miller)	Tryptone (10g/L) Yeast extract (5g/L) NaCl (10g/L)	Roth
LB-agar (Luria/Miller)	Tryptone (10g/L) Yeast extract (5g/L) NaCl (10g/L) Agar-agar (15g/L)	Roth

Table 3. Antibiotics.

Antibiotics	Final concentration	Supplier
Ampicillin	100µg/mL	Roth
Chloramphenicol	30µg/mL	Applichem
Kanamycin	50µg/mL	Roth

2.3 Enzymes and proteins

Table 4. Enzymes and proteins.

Name	EC number	Supplier
Calf intestinal alkaline phosphatase (CIP)	EC 3.1.3.1	New England Biolabs
Cofilin-1	-	Cytoskeleton Inc.
Desoxyribonuclease I	EC 3.1.21.1	Applichem
DpnI	EC 3.1.21.4	New England Biolabs
LIM kinase 1	EC 2.7.11.1	Merck Millipore
Lysozyme	EC 3.2.1.17	Carl Roth GmbH
NcoI	EC 3.1.21.4	New England Biolabs
NotI	EC 3.1.21.4	New England Biolabs
Pfx polymerase	EC 2.7.7.7	Invitrogen
T4 DNA ligase	EC 6.5.1.1	New England Biolabs
Taq polymerase	EC 2.7.7.7	New England Biolabs
Thrombin	EC 3.4.21.5	GE Healthcare
Tobacco Etch Virus (TEV) protease	EC 3.4.22.44	EMBL Hamburg

2.4 Antibodies

Table 5. Antibodies.

Antibody	Dilution	Species	Product number	Supplier
Anti-rabbit	1:10000	goat	31463	Thermo Scientific
Anti-mouse	1:10000	goat	31437	Thermo Scientific
Calmodulin (mAB)	1:2000	mouse	05-173	Upstate
Chronophin/PDXP (mAB)	1:1000	rabbit	4686	Cell Signaling
CIB1	1:1000	rabbit	-	Homemade (A. Hoffmann)
Cofilin	1:1000	rabbit	3312	Cell Signaling

* mAB, monoclonal antibodies.

2.5 Primers

Table 6. Primers. All primers were purchased from Eurofins Genomics.

Name	Sequence
mCIN (fwd)	5'-CATGCCATGGGA**ATG**GCGCGCTGCGAGC
mCIN (rev)	5'-TAAGAATGCGGCCGC**TCA**GTCCTCCAGCCCCTCCAT
Δ8CIB1 (fwd)	5'-CATGCCATGGGA**ATG**AAGCAGCTGATTGACAATATCCTG
Δ8CIB1 (rev)	5'- TAAGAATGCGGCCGC**TCA**CAGGACAATCTTAAAGGAGCTGG
Δ148CIB1 (fwd)	5'- CATGCCATGGGA**ATG**AAGCAGCTGATTGACAATATCCTG

CAC hybrid 1	5'-GCCGGCCAGCCGCTGGCGCAGGAGGCG
CAC hybrid 2	5'-CGCCTCCTGCGCCAGCGGCTGGCCGGC
CAC hybrid 3	5’-TGTGATGCACTGGAACATGTAAGGGCTAGGCTTCCCGATGATGTCCGCCTGG
CAC hybrid 4	5’-CCAGGCGGACATCATCGGGAAGCCTAGCCCTTACATGTTCCAGTGCATCACA

* All forward (fwd) primers contain a NcoI restriction site, reverse (rev) primers a NotI restriction site. Restriction sites are underlined, START and STOP codons are highlighted in bold.

2.6 Plasmids

Table 7. Plasmids.

Insert (organism)	Vector	Tag (cleavage site)	Source
CAC hybrid (mouse)	pETM-11	N-terminal His_6 (TEV)	Knobloch G.
Calmodulin (Xenopus)	pET3a	-	Krasel C.
Chronophin (mouse)	pETM-11	N-terminal His_6 (TEV)	Knobloch G.
Chronophin^{KK} (mouse)	pETM-11	N-terminal His_6 (TEV)	Kestler C.
CIB1 (mouse)	pGEX-4T-1	N-terminal GST (thrombin)	Hoffmann A.
GroES-GroEL-tig	pG-Tf2	-	Takara Bio Inc.
Δ148CIB1 (mouse)	pETM-11	N-terminal His_6 (TEV)	Knobloch G.
Δ8CIB1 (mouse)	pETM-11	N-terminal His_6 (TEV)	Knobloch G.

2.7 Chemicals

Table 8. Chemicals.

Name	Catalogue ID	Supplier
1,3-bis(tris(hydroxymethyl)methylamino) propane (Bis-Tris-propane)	B6755	Sigma-Aldrich
1,4-Dithiothreitol (DTT)	6908	Roth
1,4-Piperazinediethanesulfonic acid (PIPES)	A1074	Applichem
2-(Cyclohexylamino)ethanesulfonic acid (CHES)	C2885	Sigma-Aldrich
3-(Cyclohexylamino)-1-propanesulfonic acid (CAPS)	C2632	Sigma-Aldrich
4-Morpholinepropanesulfonic acid (MOPS)	M1254	Sigma-Aldrich
Acetic acid (glacial)	7332	Roth
Agarose GTQ	6352	Roth
Ammonium peroxydisulfate (APS)	9178	Roth
Biomol Green	BML-AK111	Enzo Life Sciences
Bis(2-hydroxyethyl)amino-tris(hydroxymethyl)methane (Bis-Tris)	B9754	Sigma-Aldrich
Bromophenol Blue	B0126	Sigma-Aldrich

Calcium chloride	21108	Sigma-Aldrich
Coomassie Brilliant Blue R-250	3862	Roth
Dimethyl sulfoxide (DMSO)	A3672	Applichem
Ethanol (70%)	T913	Roth
Ethanol (p.a.)	32205	Sigma-Aldrich
Ethidium bromide (10mg/mL)	2218	Roth
Ethylene glycol-bis(2-aminoethylether)-*N,N,N',N'*-tetraacetic acid (EGTA)	03777	Sigma-Aldrich
Ethylenedinitrilotetraacetic acid (EDTA)	E9884	Sigma-Aldrich
Formaldehyde (37%)	7398	Roth
Glycerol	A3552	AppliChem
Glycine	3908	Roth
Hydrochloric acid	A0659	AppliChem
Imidazole	S6750	Fluka
Isopropyl-β-D-thiogalactopyranoside (IPTG)	CN08	Roth
L-glutathione (reduced)	6382	Roth
Magnesium chloride	A1036	AppliChem
Manganese chloride	M8054	Sigma-Aldrich
Methanol	32213	Sigma-Aldrich
N,N-Bis(2-hydroxyethyl)glycine (Bicine)	B8660	Sigma-Aldrich
Nonidet P-40	74385	Sigma-Aldrich
Orange G	0318	Roth
PEG 3350	202444	Sigma-Aldrich
PEG MME 550	202487	Sigma-Aldrich
Phos-tag™	304-93521	Wako Pure Chemicals Industries, Ltd.
Potassium hydroxide	6751	Roth
Potassium phosphate monobasic	P5379	Sigma-Aldrich
Pyridoxal 5'-phosphate	82870	Fluka
Rotiphorese Gel 30 (37.5:1) 30 %	3029	Roth
Rotiphorese Gel A (30% acrylamide)	3037	Roth
Rotiphorese Gel B (2% bisacrylamide)	3039.1	Roth
Sodium acetate	S8750	Sigma-Aldrich
Sodium azide	K305	Roth
Sodium cacodylate	C4945	Sigma-Aldrich
Sodium chloride	0962	Roth
Sodium citrate	71497	Sigma-Aldrich
Sodium dodecyl sulfate (SDS)	2326	Roth
Sodium hydroxide	A1551	AppliChem
Sodium phosphate dibasic heptahydrate	S9390	Sigma-Aldrich
SYPRO Orange	S5692	Sigma-Aldrich
Tetracycline	87128	Sigma-Aldrich
Tetramethylethylenediamine (TEMED)	2307	Roth
Tricine	A1085	AppliChem
Triethanolamine	A1423	AppliChem
Tris(hydroxymethyl)aminomethane base	4855	Roth
Tris(hydroxymethyl)aminomethane-HCl	A1087	AppliChem
Triton X-100	648466	Merck
β-Mercaptoethanol	M7522	Sigma-Aldrich

2.8 Crystallization screens

Table 9. Crystallization screens.

Name	Supplier
Crystal screen I + II	Hampton Research
Index Screen	Hampton Research
Nextal PEG Suite	Qiagen
Nextal pH Clear	Qiagen
Nucleix Suite	Qiagen
Optimix 1 - 5	Topaz
Protein Complex Screen	Qiagen
Wizard Screen 1 + 2	Emerald BioSystems

2.9 Equipment

Table 10. Equipment.

Type	Model	Company
Agarose gel system	Mini-Sub Cell GT	BioRad
Autoclave	Systec V-150	Systec
Balance 0.1-2200g	SBA 52	ScalTec
Balance 0.1mg-60g	AT261 DeltaRange	Mettler
Balance 10mg-120g	ACJ 120-4M	Kern
Blotting system (semi-dry)	Trans-blot SD	BioRad
Blotting system (wet tank)	Genie blotter	Idea scientific
CD-Spectropolarimeter	J-810	Jasco
Cell disruptors	M-110P	Microfluidics
	E615	Constant Systems LTD
Centrifuge	Avanti J-26 XP	Beckmann Coulter
Centrifuge ≤2mL	5424, 5424 R	Eppendorf
Chemoluminescence imaging system	FluorChem Q	Alpha Innotech
Column body (gravity flow)	Econo-Column 2.5 × 20cm	BioRad
	Econo-Column 1.5 × 15cm	BioRad
Crystal mounting loop	CryoLoop	Hampton Research
Crystallization robot	HoneyBee 963	Zinsser Analytic
FPLC columns	HiLoad 16/60 Superdex 200 pg	GE Healthcare
	HisTrap HP 1mL	GE Healthcare
	HisTrap HP 5mL	GE Healthcare
	Mono Q 5/50 GL	GE Healthcare
	Resource PHE 1mL	GE Healthcare
	Superdex 200 10/300 GL	GE Healthcare
FPLC system	Äkta purifier 10	GE Healthcare
Glutathione Sepharose	Glutathione Sepharose 4B	GE Healthcare

Ice machine	ZBE 150	Ziegra
Incubator	BB 6220	Heraeus Instruments
Isothermal titration calorimeter	ITC_{200}	Microcal, GE Healthcare
Liquid culture incubator	ISF-1-V, ISF-1-W, ISF-1-X	Kühner
Liquid handling robot	Lissy	Zinsser Analytic
Magnet stirrer	MR Hei-Mix L	Heidolph
Microplate reader	Envision 2104	PerkinElmer Life Sciences
Microscope	SteREO Discovery.V12	Zeiss
Microscope camera	AxioCam MRC	Zeiss
Microscope light source	KL 2500 LCD	Zeiss
Multichannel pipettes	Research Plus 0.5-10µL, 30-300µL	Eppendorf
PCR Thermocycler	C1000	BioRad
	MJ Mini	BioRad
pH-Electrode	BlueLine 14pH	Schott
Pipettes	Research	Eppendorf
Pipetting aid	Pipetus	Hirschmann Laborgeräte
Platform shaker	Unimax 1010	Heidolph
Polyacrylamide gel system	Mini-PROTEAN Tetra Cell	BioRad
Power supply	PowerPac Basic, PowerPac HC	BioRad
Real-Time PCR thermocycler	MX3005P	Stratagene
Spectrophotometer	BioPhotometer	Eppendorf
	NanoDrop 2000c	Thermo Scientific
Thermomixer	Comfort	Eppendorf
	MB-102	BIOER
Tumbling roller mixer	RM5	Hartenstein
X-ray cryosystem	X-Stream 2000	Rigaku
X-ray detector	R-AXIS HTC	Rigaku
X-ray generator	MicroMax-007HF	Rigaku
X-ray optics	VariMax HF	Osmic Inc.

2.10 Consumables

Table 11. Consumables.

Type	**Model**	**Company**
24-well plate (crystallography)	SuperClear	Crystalgen
96-well PCR plate	PP-PCR plate, 96-well	Greiner
96-well plate (assay)	Nunclon delta surface	Thermo Scientific
96-well plate (crystallography)	ClearPlate Halfarea MB	Greiner
Chromatography cellulose	Whatman 3MM	Sigma-Aldrich
Concentrator	Centrifugal Filter Units, MWCO 30kDa	Millipore
	Microcon YM-10, MWCO 10kDa	Millipore
Cover slides	Circular, 22mm diameter	Jena Bioscience
Dialysis cassettes	Slide-A-Lyzer	Pierce Biotechnology
Micro reaction tubes (0.2mL)	Reaction tube, 0.2mL	Hartenstein

Micro reaction tubes (1.5mL)	Microtube 1.5mL	Sarstedt
Nitrocellulose membrane	Hybond-C Extra	Amersham Biosciences
Pipette tips	epT.I.P.S.	Eppendorf
PVDF membrane	Hybond™-P	GE Healthcare
Reaction tubes	Greiner tube, 15mL|50mL	Greiner
Sterile filter	Nylon membrane filter, 0.2µm	Hartenstein
UV/Vis cuvettes	UVette	Eppendorf

2.11 Kits

Table 12. Kits.

Kit	Supplier
Enhanced chemo-luminescence (ECL) Western blotting substrate	Thermo Scientific
Gel Filtration LMW Calibration kit	GE Healthcare
Phosphatase substrate set	JPT Peptide Technologies
Qiagen Plasmid Midi Kit	Qiagen
Qiagen Plasmid Plus Kit	Qiagen
QIAprep Spin Miniprep Kit	Qiagen

2.12 Software and databases

Table 13. Software and databases.

Software/database	Author/Reference
Calmodulin Target Database	calcium.uhnres.utoronto.ca/ctdb/ctdb/home.html
CCP4i	[260]
Coot	[261]
CrystalClear	Rigaku
DALI server	[262]
ImageJ 1.44	http://rsb.info.nih.gov/ij/
iMosFlm	[263]
Origin 7 ITC	Microcal
PDB	www.pdb.org
PDBePISA	www.ebi.ac.uk/pdbe/pisa/; [264]
Phenix.refine	[265]
Prism 4.01	GraphPad
ProtParam	web.expasy.org/protparam/
PubMed	www.ncbi.nlm.nih.gov/pubmed/
PyMol	The PyMOL Molecular Graphics System, Schrödinger, LLC.
Scala	[266]

SEDFIT	[267]
Spectra manager	Jasco
Unicorn 5.0	GE Healthcare
UniProt	www.uniprot.org

3 Methods

3.1 Polymerase chain reaction (PCR)

The polymerase chain reaction (PCR) is a standard technique used to amplify nucleic acid sequences, enabling the detection, quantification and manipulation of these macromolecules. This makes the PCR a powerful tool for a variety of applications in research, forensics and medicine. The method relies on an *in vitro*, polymerase catalyzed, semi-conservative replication of deoxyribonucleic acid (DNA) or ribonucleic acid (RNA) and is generally conducted in three steps: the initial generation of single stranded nucleic acid templates by thermal melting at around 95°C, followed by a hybridization with short, specific stretches of DNA – called primers – that are complementary to the termini of the nucleic acid sequences to be amplified. This so-called annealing step is performed at temperatures below the melting point (T_m) of the primer/template hybrids. The primers serve as starting points from which the polymerase extends a complementary DNA strand by incorporating deoxynucleotide triphosphates (dNTPs), resulting in a double stranded version of the initial template. This last extension step is executed at temperatures ideally suited for the polymerase catalysis. By iteration of melting, annealing and extension the nucleic acid sequence that is located between the two primers, gets amplified.

For all PCR reactions employed in cloning procedures the Platinum® Pfx DNA polymerase was used according to the manufacturer's instructions. All primers were purchased from Eurofins Genomics and designed including a restriction site for insertion into the multiple cloning site of the pETM-11 vector. The forward primers contained a NcoI restriction site and a start codon, the reverse primers a NotI restriction site and a stop codon. The used primers are listed in Table 6.

The cloning of the CAC hybrid was conducted in three steps. First, the DNA coding for the N-terminal residues 1 to 100 of murine chronophin, the murine AUM capping domain (residues 109 to 237) and the C-terminal murine chronophin residues 208 to 292 were amplified independently. Next, the PCR-products of the chronophin N-terminus together with the AUM cap and the AUM cap together with the chronophin C-terminus were used for overhang PCR, since all three PCR-products were designed to overlap at the N- and C-terminal ends of the AUM capping domain. Finally, the two PCR-products of the previous step, composed of the chronophin N-terminus fused to the AUM cap and the AUM cap fused to the chronophin C-terminus, were used for overhang PCR yielding the final construct.

The size of all PCR-products was confirmed by agarose gel electrophoresis (see 3.3) before continuation of the cloning procedure. For this, 1-2µL of the PCR reaction mixture were separated on a 1% agarose gel together with a 1kB DNA ladder.

Table 14. PCR reaction components.

Compound	Volume per 50µL reaction	Final concentration
ddH_2O (sterile)	34-Xµl	to 50µL final volume
Pfx buffer (10×)	5µL	1×
$MgSO_4$ (50mM)	1µL	1mM
primer (10µM)	1.5µL each	0.3µM
dNTPs (10mM)	1.5µL	0.3mM
enhancer (10×)	5µL	1×
template	XµL	10pg – 200ng
polymerase	0.5µL	~1U

Table 15. Thermocycling conditions for standard PCR reactions using the Pfx polymerase.

Step	Temperature	Time	
initial denaturation	94°C	30sec	
melting	94°C	15sec	35×
annealing	T_m – 5°C*	15sec	
extension	72°C	1min/kb	
final extension	72°C	300sec	
hold	4-12°C	∞	

* The annealing temperature depends on the lower melting temperature (T_m) of the respective primer pair.

3.2 Restriction digestion

Restriction endonucleases are proteins that cut duplex DNA by cleaving the sugar-phosphate backbone of each strand at a target restriction sequence, which is highly specific for each enzyme. This makes endonucleases a useful tool for molecular cloning, as sequences cut with the same endonuclease can be specifically ligated (see 3.5). For the generation of expression vectors, the respective plasmids and PCR amplified inserts were digested with a set of two restriction endonucleases for 3-4h at 37°C in buffer conditions according to the Double Digest Finder (https://www.neb.com/tools-and-resources/interactive-tools/double-digest-finder). Digested plasmids were subsequently treated for 1h at 37°C with Calf Intestine Phosphatase (CIP) to prevent re-ligation. The DNA products of the digestions were separated

from contaminants and restriction endonucleases by agarose gel electrophoresis (see 3.3) followed by a purification from the agarose gel (see 3.4).

3.3 Agarose gel electrophoresis

Agarose gel electrophoresis allows the separation of macromolecules according to their migration behavior through an agarose matrix when an electric field is applied. Therefore, this method is frequently used for the analysis and/or purification of nucleic acids.

Agarose gels were prepared by boiling 1% (w/v) genetic quality tested (GQT) agarose in Tris-acetic acid-EDTA (TAE)-buffer until it was fully dissolved, and letting it solidify in a comb-equipped casting tray sealed with tape. For sample analysis, the gel was submersed with TAE buffer in a running chamber and the DNA sample, supplied with an appropriate amount of 5× DNA loading buffer, was separated by applying 80V until the sample buffer dye reached the bottom of the gel. In order to detect and visualize the DNA, the gel was then soaked for 15 minutes in an ethidium bromide bath (0.5µg/mL in ddH_2O) and exposed to UV-light. Ethidium bromide intercalates into double stranded DNA, leading to an increased fluorescence when excited with UV-light, thus indicating the presence of DNA in the gel by emitting orange light. A DNA ladder was used as a size standard.

Table 16. Components of Tris-acetic acid-EDTA (TAE) buffer.

TEA buffer	**5× DNA loading buffer**
40mM Tris, pH 7.6	15% (v/v) glycerol
20mM acetic acid	0.2% (w/v) Orange G dye
1mM EDTA	ddH_2O (sterile)

3.4 Gel extraction

DNA separated from contaminants using agarose gel electrophoresis was extracted from the gel using the QIAquick Gel Extraction Kit according to the manufacturer's instructions. The principle of this

procedure is based on the excision of the agarose containing the DNA of interest, dissolving it in a buffer containing high salt concentrations, which allow the DNA to bind to the silica membrane inside the provided spin column. After binding of the DNA to the column, the sample is washed with ethanol to remove remnant primers, nucleotides, proteins and other impurities such as ethidium bromide and agarose. The purified DNA can finally be eluted in small volumes (30-50µL) of low-salt buffer (e.g. 10mM Tris, pH 8.5) or water. The DNA concentration after the gel extraction was determined photometrically by measuring the absorption at 260nm.

3.5 Ligation

Ligation is the process of covalently linking the ends of two or more DNA/RNA fragments, either specifically in the case of complementary overhangs, or unspecifically when the DNA/RNA is blunt ended. The covalent linkage between DNA fragments is catalyzed by the DNA ligase which synthesizes phosphodiester bonds between adjacent 5'-phosphoryl and 3'-hydroxyl groups of nicked DNA helices in an ATP-driven reaction [268].

The use of two different restriction endonucleases (see 3.2), resulting in two different, non-complementary overhangs, ensures the correct orientation of the insert when ligated with the digested expression plasmid. The ligation was conducted with T4 DNA ligase using a ~5-fold molar excess of insert over plasmid (usually ~100ng plasmid) and letting the reaction proceed for 10 minutes at room temperature. Finally, 5 and 15µL of the ligation were used for transformation into *E. coli* DH5α. The absolute amounts of insert DNA to be used for a certain amount of vector DNA can be calculated by the following equation:

Equation 1

$$\text{ng insert} = \frac{\text{ng vector} \times \text{kb insert}}{\text{kb vector}} \times \text{ratio}\ \frac{\text{insert}}{\text{vector}}$$

with kb being the length of the DNA fragment in kilobases.

Table 17. Ligation reaction components.

Component	Volume
10× T4 DNA ligase buffer	2µL
insert	XµL*
vector	YµL*
sterile ddH_2O	add to 20µL final volume
T4 DNA ligase	1µL

*volumes of digested vector and insert were dependent on the concentration of the purified DNA.

3.6 Transformation of *E. coli* DH5α for molecular cloning

Transformation describes the uptake and incorporation of exogenous genetic material into prokaryotes, fungae and plants, whereas the same process is called transfection in case of animal cells. For molecular cloning, transformation is used to bring genetic material such as plasmids into competent bacteria (see 2.1) that were genetically optimized to amplify the DNA of interest. Here, two 100µL aliquots of chemically competent *E. coli* DH5α were thawed on ice and incubated for 10 minutes with 5µL and 15µL of the ligation reaction, respectively, followed by a 45 second heat shock at 42°C to enable the uptake of DNA through the bacterial cell wall. After that, the bacteria were re-transferred to the ice bath and immediately mixed with 900µL of 4°C cold, sterile LB-medium. Subsequently, the bacteria were allowed to grow for 45 minutes at 37°C while shaking (600-900rpm). The cells were then centrifuged for 2min at 2000 × *g*, the pellet was resuspended in 100µL supernatant and applied to an LB-agar plate containing the appropriate antibiotic to select for positive transformants. The agar plates were incubated over night at 37°C.

3.7 Colony PCR

Colony PCR is a qualitative method used to screen for bacteria transformed with successfully ligated plasmids. It is based on a standard PCR reaction, but rather than using purified nucleic acids as a template for the reaction, it uses bacteria from single colonies containing the DNA. The employed primers are the same as in the PCR reaction used to synthesize the insert. This allows fast discrimination of false positive

clones that contain an empty vector and clones transfected with the plasmid containing the sequence of interest.

For each colony PCR screen, bacteria from a single colony were transferred into a PCR tube containing 10µL of colony PCR master mix using a sterile pipet tip, and were mixed thoroughly. As a positive control, 50ng of the template that was initially used to amplify the insert was included. Here, the *Taq* DNA polymerase was employed.

Table 18. Colony PCR reaction components.

Compound	Volume per 10µL reaction	Final concentration
ddH_2O (sterile)	8.3µL	to 10µL final volume
standard *Taq* reaction buffer (10×)	1µL	1×
primer (10µM)	0.3µL each	0.3µM
dNTPs (10mM)	0.3µL	0.3mM
template	bacteria	variable
Taq polymerase	0.1µL	2.5U

Table 19. Thermocycling conditions for colony PCR.

Step	Temperature	Time	
initial denaturation	95°C	30sec	
melting	95°C	15sec	
annealing	T_m – 5°C*	15sec	35×
extension	68°C	1min/kb	
final extension	68°C	300sec	
hold	4-12°C	∞	

* The annealing temperature depends on the lower melting temperature (T_m) of the respective primer pair.

3.8 Plasmid preparation

Plasmid DNA was purified from *E. coli* DH5α using the QIAprep Spin Miniprep Kit for bacterial cultures of up to 5mL or the Qiagen Plasmid Midi Kit or with the Qiagen Plasmid Plus Kit for cultures of up to 100mL. All kits were used according to the manufacturer's instructions.

Briefly, a single colony was picked with a sterile pipette tip and used to inoculate LB-medium supplemented with the appropriate antibiotic. The culture was grown over night at 37°C, the cells were harvested by centrifugation (15 minutes, 6000 × *g*) and the supernatant was discarded. The cells were resuspended in the provided buffer and then subjected to alkaline lysis by the addition of sodium hydroxide (NaOH) and sodium dodecyl sulfate (SDS), a process by which the cell contents are released and macromolecules such as proteins and DNA are denatured. The subsequent addition of potassium acetate neutralizes the pH of the lysate while at the same time removing the detergent by precipitation as potassium dodecyl sulfate. This allows the plasmidic DNA to renature, while the cell-wall bound genomic DNA precipitates in insoluble complexes with proteins, salt and detergent that can be removed by centrifugation or filtration. RNA is removed during alkaline lysis by RNase A treatment. The cleared lysate is then mixed with binding buffer and loaded onto a resin that specifically binds plasmid DNA, while proteins, degraded RNA and metabolites remain in the flow-through. Subsequent washing with a medium-salt buffer removes residual contaminants, and an additional washing step with 80% ethanol removes salts and leads to the disruption of non-specific hydrophobic interactions. The plasmid DNA was then eluted in low-salt buffer (e.g. 10mM Tris, pH 8.5) or ddH_2O. The DNA concentration was determined photometrically by measuring the absorption at 260nm.

3.9 Sequencing

Cloned constructs that were positively tested by colony PCR (see 3.7) were additionally verified by sequencing (Seqlab Göttingen and MWG Eurofins Operon Ebersberg).

3.10 Preparation of chemically competent *E. coli*

The following protocol was used to prepare chemically competent cells from *E. coli* DH5α, *E. coli* BL21(DE3) and *E. coli* BL21(DE3) transformed with plasmids for chaperone co-expression. A single colony of the respective strain was grown over night at 37°C on an LB-agar plate supplemented with appropriate antibiotic/s and used to inoculate 25mL LB-medium, also supplemented with the appropriate antibiotic/s.

This culture was incubated for 6 to 8 hours at 37°C while vigorously shaking (250-300rpm). Finally a 1:50 dilution was used to inoculate 250mL LB-medium supplemented with appropriate antibiotic/s. This culture was grown over night at 18-22°C while moderately shaking (150-200rpm) until an OD_{600} of 0.55 was reached. The culture was then transferred to an ice bath for 10 minutes. Subsequently, the cells were harvested by centrifugation at 2,500 × *g* for 10 minutes at 4°C. The supernatant was discarded, and remaining medium was removed by inverting the centrifuge flask on a paper towel. The cells were then gently resuspended in 80mL of ice-cold TB-buffer and harvested again by centrifugation at 2,500 × *g* for 10 minutes at 4°C. The supernatant was discarded and remaining buffer was removed by inverting the centrifuge flask on a paper towel. The cells were then gently resuspended in a final volume of 18.6mL ice-cold TB-buffer, and mixed with 1.4mL of sterile 100% DMSO, resulting in a final concentration of 7% DMSO. The bacterial suspension was then stored for 10 minutes on ice, before aliquoting 100µL of the chemically competent cells into chilled, sterile microcentrifuge tubes. The aliquots were immediately snap-frozen in liquid nitrogen and stored at -80°C.

Table 20. TB-buffer for the preparation of chemically competent E.coli.

TB-buffer*
10mM PIPES
250mM KCl
15mM $CaCl_2$
55mM $MnCl_2$

* For the preparation of 1L TB-buffer, all components except for $MnCl_2$ are dissolved in 800mL ddH_2O, the pH is then adjusted to 6.7 with 1M KOH. Afterwards, $MnCl_2$ is gradually added and the volume is brought to 1L. Finally, the buffer is sterile filtered and stored at 4°C.

3.11 Transformation of *E. coli* for protein expression

Chemically competent *E. coli* BL21(DE3) were transformed with the respective plasmid by thawing an 100µL aliquot of cells on ice, incubating it on ice for additional 10 minutes with 50-100ng of plasmid DNA, followed by a heat shock at 42°C for 45-60 seconds to enable the uptake of the DNA by the bacteria. The cells were then immediately transferred back on ice and 900µL of ice-cold LB-medium were added. Finally, the cells were incubated for 45 minutes at 37°C while shaking at 600-900rpm in a thermomixer. These cell suspensions were directly used to inoculate starting cultures (LB-medium supplemented with the appropriate antibiotic/s) that were grown over night at 37°C under shaking at 200rpm.

3.12 Protein expression

Starting cultures were used at a 1:50 dilution to inoculate expression cultures (LB-medium supplemented with the appropriate antibiotic/s). Chronophin^{KK} and the CAC mutant were co-expressed with chaperones encoded by the pG-Tf2 plasmid and chaperone expression was induced with 10ng/mL tetracycline. Cultures were grown at 37°C and 200rpm until reaching an OD_{600} of 0.6 – 0.8 before protein expression was induced with 0.5mM isopropyl β-D-1 thiogalactopyranoside (IPTG). After induction, protein expression was allowed to proceed for 18h at 20°C until the cells were harvested by centrifugation at 8,000 × *g* for 10min. Bacterial pellets were either directly used for protein purification or stored at -80°C.

3.13 Cell lysis

Bacterial pellets were resuspended in the respective lysis buffer (5mL/g pellet) supplemented with protease inhibitors (EDTA-free protease inhibitor tablets) and 150U/mL DNaseI. Sample volumes of up to 50mL were pre-incubated with 1mg/mL lysozyme for 30 minutes at room temperature before sonication for 3 × 45 seconds at pulse rates of 0.7 seconds and an amplitude of 40% with pauses of 1 minute between sonication intervals. The samples were kept on ice during the whole process.

Sample volumes of more than 50mL were lysed by two passages through an e616 cell disruptor or the M-110P microfluidizer at a pressure of 1.5kbar. Lysates were centrifuged for 30 minutes at 35,000 × *g* and 4°C to remove insoluble components and cell debris from the soluble fraction. The resulting cleared supernatants were then used for protein purification.

Table 21. Lysis buffers.

IMAC lysis	**GST lysis**	**HIC lysis**
100mM TEA, pH 7.4 500mM NaCl 5mM $MgCl_2$ 20mM imidazole	100mM TEA, pH 7.4 500mM NaCl	100mM TEA, pH 7.4 1M NaCl 5mM $CaCl_2$

3.14 Protein purification

Generally, proteins were purified in two steps, comprising a first step to isolate the protein of interest from bulk contaminants such as other proteins, nucleic acids and metabolites contained in the *E.coli* lysates, and a second step to achieve a high degree of purity by removing remnant impurities.

Briefly, as the first step, affinity chromatography and hydrophobic interaction chromatography was employed to enrich tagged proteins of interest or untagged calmodulin, respectively. The affinity tag was then cleaved off, the tagged and untagged isoforms of the proteins were separated by inverse affinity chromatography. Finally, size exclusion chromatography was used to achieve final purity (second step). All purification procedures were performed on an ÄKTA liquid chromatography system, unless stated otherwise.

3.14.1 Immobilized metal ion affinity chromatography of His_6-tagged proteins

Hexahistidine (His_6)-tagged proteins were purified by immobilized metal ion affinity chromatography (IMAC), a method based on the affinity that His_6-tags exhibit towards metal ions, such as nickel (Ni^{2+}), cobalt (Co^{2+}) or copper (Cu^{2+}). Thus, resins functionalized with iminodiacetic acid (IDA) or nitrilotriacetic acid (NTA) that chelate these metal ions can be used to purify His_6-tagged proteins.

For the purification of His_6-tagged proteins derived from the pETM-11 expression vector, cleared supernatants were loaded on a HisTrap HP column followed by washing 12 column volumes (CV) with IMAC buffer A. His_6-tagged proteins were then eluted using a linear gradient over 15 CV up to 50% IMAC buffer B. The fractions containing the protein of interest were pooled, and the His_6-tag was cleaved with tobacco etch virus (TEV) protease for 2 days at 4°C. Subsequently, cleaved protein was separated from uncleaved and His-tagged TEV-protease on a HisTrap HP column. Untagged proteins were further purified by size exclusion chromatography (see 3.14.5).

Table 22. Immobilized metal affinity chromatography (IMAC) buffers.

IMAC A	**IMAC B**
50mM TAE, pH 7.4	50mM TEA, pH 7.4
250mM NaCl	250mM NaCl
5mM $MgCl_2$	5mM $MgCl_2$
20mM imidazole	500mM imidazole

3.14.2 Ion exchange chromatography

Ion exchange chromatography (IEX) is based on the reversible interaction of charged molecules with a chromatography medium that has the opposite charge. Usually, the sample is bound to the chromatography medium at low ionic strength and then eluted at increasing ionic strengths. This method can be used for protein purification, since proteins carry a charge in solution that is dependent on their amino acid composition and the pH of the solvent. Here, IEX was used as an intermediate purification step to remove impurities from chronophin^{KK}, which often co-eluted with the target protein during IMAC. For this, the IMAC fractions containing chronophin^{KK} were pooled, concentrated and subsequently diluted 1:10 with IEX buffer A. The sample was then loaded on a Mono Q 5/50 column. At the given buffer conditions, chronophin^{KK} remains in the flow-through of the column, while the impurities bind to the column and can be eluted with IEX buffer B. After adjusting the NaCl concentration of the flow-through containing chronophin^{KK} to ~250mM, the protein was concentrated and TEV cleavage was performed as described in 3.14.1.

Table 23. Ion exchange chromatography (IEX) buffers.

IEX A	**IEX B**
50mM TEA pH 7.4	50mM TEA pH 7.4
5mM $MgCl_2$	5mM $MgCl_2$
	1M NaCl

3.14.3 Affinity purification of GST-tagged proteins

Glutathion S-transferases (GSTs) are enzymes that catalyze the conjugation of reduced glutathione (GSH) to substrates. The high affinity of these proteins towards GSH enables the application of this system in affinity chromatography by expressing a target protein fused to a GST domain (~24kDa) and purifying it using GSH-coated beads. The protein of interest can then be eluted in buffer containing excess GSH.

CIB1, expressed as an N-terminally GST-tagged fusion protein from the pGEX-4T-1 vector, was gravity flow-purified using glutathione sepharose 4B, a resin consisting of cross-linked agarose coupled to GSH via a 10-carbon linker. For each purification, the GSH-sepharose was transferred into a gravity flow column and pre-equilibrated with >5CV GST buffer A. After draining the column, the cleared lysate was added and incubated with the GSH-sepharose for 30 minutes at room temperature while rotating in a tumbling roller

mixer. After the incubation, the column was drained by gravity flow, subsequently washed with >25CV GST buffer A and drained again. The affinity tag was cleaved from the resin-bound GST-CIB1 with thrombin (10U thrombin/mL GSH-sepharose) for 20 hours at room temperature, and untagged CIB1 was eluted with wash buffer. To remove traces of remaining GST, the eluate was run through a gravity column containing unused, pre-equilibrated GSH-sepharose. For the elution of GST-tagged CIB1, 0.5mL elution buffer/mL resin were added and incubated for 10 minutes before the GST-CIB1-containing eluate was collected. All CIB1 variants were further purified by size exclusion chromatography as described in 3.14.5.

Table 24. Buffers used for affinity purification of GST-tagged proteins.

GST A	**GST B**
50mM TEA, pH 7.4 500mM NaCl	50mM TEA, pH 7.4 250mM NaCl 10mM L-glutathione (reduced)

3.14.4 Hydrophobic interaction chromatography purification of calmodulin

Calmodulin undergoes conformational changes upon calcium binding, exposing hydrophobic regions. This behavior can be used for purification using hydrophobic interaction chromatography (HIC), a method based on the reversible interaction of proteins with hydrophobic ligands bound to a chromatography matrix. Buffers with high ionic strength enhance the interaction, thus allowing the elution of calmodulin at low ionic strength and in the presence of Ca^{2+}-chelating agents such as EGTA.

Prior to HIC, the cleared lysates were heat-denatured for 10 minutes at 80°C followed by centrifugation for 30 minutes at 30,000 × *g* to pellet denatured insoluble material. This step reduces the amount of contaminant proteins, while Ca^{2+}-calmodulin remains unaffected due to its extreme thermal stability. Supernatants were applied to a phenylsepharose column (Resource PHE) in HIC buffer A and eluted with HIC buffer B. Calmodulin was further purified by size exclusion chromatography, pure fractions were concentrated to ~20mg/mL and flash-frozen in liquid nitrogen for storage at -80°C.

Table 25. Hydrophobic interaction chromatography (HIC) buffers.

HIC A	HIC B
50mM TEA, pH 7.4	50mM TEA, pH 7.4
1M NaCl	100mM NaCl
5mM $CaCl_2$	10mM EGTA

3.14.5 Size exclusion chromatography

Size exclusion chromatography (SEC) separates molecules according to their hydrodynamic volume, which correlates with a protein's molecular mass/size/form. The separation capacity relies on the differential penetration of the inner volume of a porous stationary phase, with small molecules having access to a larger pore volume in addition to the interparticle volume, thus eluting later than bigger molecules. This method was used as the final purification step for all proteins.

Small protein samples ≤10mg were purified using a Superdex 200 10/300 GL (24mL CV), larger samples using a HiLoad 16/60 Superdex 200 prep grade column (120mL CV). Both columns contain a matrix composed of dextran that is covalently bound to highly cross-linked agarose, allowing the separation of proteins between 10 and 600kDa. The columns were pre-equilibrated with the respective buffer before usage. All protein samples were centrifuged for 15 minutes at 20,000 × *g* to remove precipitates prior to injection into the sample loop (1mL or 5mL loop volume). The elution of the proteins of interest was monitored by recording the absorptions at 280nm and 260nm.

Table 26. Size exclusion chromatography (SEC) buffers.

SEC A	SEC B	SEC C
50mM TEA, pH 7.4	50mM TEA, pH 7.4	10mM TEA, pH 7.4
250mM NaCl	250mM NaCl	100mM NaCl
5mM $MgCl_2$	5mM $MgCl_2$	1mM $MgCl_2$
	5% (w/v) glycerol	

3.15 UV/Vis-Spectroscopy

Protein and DNA concentrations were quantified by absorption measurements using a UV/Vis-spectrophotometer (NanoDrop 2000). The absorption (A) at a wavelength λ is directly proportional to the molar concentration (c) of a sample, as expressed in Lambert-Beer's law:

Equation 2

$$c = \frac{A_\lambda}{\varepsilon_\lambda \cdot d}$$

with ε_λ being the molar extinction coefficient (M^{-1} cm^{-1}) at the measured wavelength, and d the path length of the sample (cm). Protein concentrations were measured using the absorption of tyrosine, tryptophan, cystine (two cysteines linked via a disulfide bond) and phenylalanine residues at 280nm. The ε_{280} of the respective protein was calculated using the ExPASy online tool ProtParam (http://web.expasy.org/protparam/). DNA quantifications were performed at 260nm, the absorption maximum of nucleic acids. At this wavelength the average extinction coefficient of double stranded DNA is 50 (ng·cm)·μL^{-1}. All samples were blank-corrected and measured in triplicates.

3.16 PAGE

Polyacrylamide gel electrophoresis (PAGE) separates macromolecules according to their electrophoretic mobility in a matrix consisting of polymerized monomeric acrylamide cross-linked with N,N'-methylene-bis-acrylamide. The pore size of the matrix can be controlled by varying the concentration and ratio of the acrylamide components. The mobility of the molecule is dependent on its size, charge and conformation.

3.16.1 SDS-PAGE

Sodium dodecyl sulfate polyacrylamide gel electrophoresis (SDS-PAGE) is used to separate proteins under denaturing conditions according to their molecular mass. SDS is an anionic detergent that disrupts the tertiary structure of proteins by binding to their peptide-backbone, providing the protein with negative

charges that are proportional to the length of the polypeptide, and thus to the molecular mass of the protein. The linearized SDS-protein complexes are then separated by PAGE independently of their conformation or native charge. If needed, agents such as dithiothreitol or β-mercaptoethanol can be added to reduce disulfide bonds.

SDS-PAGE was performed as described by Laemmli *et al.* [269] using the Mini PROTEAN Tetra Cell system equipped with 1mm gels. Samples were mixed with 5× sample buffer, heated for 5 minutes at 95°C for further denaturation of the proteins and subsequently subjected to electrophoresis at a constant current until the dye of the sample buffer reached the bottom of the gel. Precision Plus Protein™ Dual Color Standards were used as size standards. Proteins in the gel were either visualized by Coomassie Blue staining (see 3.18) or transferred to a membrane for immunoblotting (see 3.17).

Table 27. Buffers used for SDS-PAGE. AA: acrylamide, BAA: bisacrylamide.

Stacking gel (4%)	**Resolving gel**	**Running buffer**	**Loading buffer (4×)**
4% AA/BAA (w/v, 37.5:1)	8-15% AA/BAA (w/v, 37.5:1)	200mM glycine	50mM Tris, pH 6.8
125mM Tris, pH 6.8	375mM Tris, pH 8.8	0.1% (w/v) SDS	10mM DTT
0.1% (w/v) SDS	0.1% (w/v) SDS	25mM Tris	2% (w/v) SDS
0.25% (w/v) APS	0.25% (w/v) APS		20% (v/v) glycerol
0.15% (w/v) TEMED	0.05% (w/v) TEMED		0.1% (w/v) Bromophenol Blue

3.16.2 Tricine SDS-PAGE

Tricine SDS-PAGE is a variation of the aforementioned SDS-PAGE and used for separating low molecular mass proteins in the range of 1-100kDa, such as the N-terminally truncated version of CIB1, Δ148CIB1, studied in this work. Instead of using a glycine-Tris buffer system, a tricine-Tris buffer system was employed. Tricine has a lower pK, a higher negative charge and a higher ionic strength compared to glycine. This leads to a faster migration during SDS-PAGE conducted at the usual pH values between 6.8 and 8.8, resulting in a shift of the stacking limit towards a lower molecular mass range [270].

Table 28. Buffers used for Tricine SDS-PAGE. AA: acrylamide, BAA: bisacrylamide.

Stacking gel (4%)	**Resolving gel**	**Cathode buffer**	**Loading buffer (4×)**
4% AA/BAA (w/v, 37.5:1)	16% AA/BAA (w/v, 37.5:1)	0.1M Tris, pH 8.25	50mM Tris, pH 6.8
0.1M Tris, pH 8.45	0.1M Tris, pH 8.45	0.1M Tricine	10mM DTT
0.1% (w/v) SDS	0.1% (w/v) SDS	0.1% (w/v) SDS	2% (w/v) SDS
0.25% (w/v) APS	0.25% (w/v) APS	**Anode buffer**	20% (v/v) glycerol
0.15% (w/v) TEMED	0.05% (w/v) TEMED	0.1M Tris, pH 8.9	0.1% (w/v) Bromophenol Blue

3.16.3 Phos-tag SDS-PAGE

SDS-PAGE can be used to determine the phosphorylation state of proteins by adding derivatives of dinuclear metal complexes, such as the 1,3-bis[bis(pyridin-2-ylmethyl)amino]propan-2-olato dizinc(II) complex to the polyacrylamide gel. These complexes selectively bind phosphate moieties of proteins, leading to a retention of the molecules during electrophoresis, and therefore to a separation of phosphorylated and un-phosphorylated versions of the protein in the gel. This allows the detection of both isoforms using the same antibody during immunoblotting, circumventing the disadvantages (such as differing binding affinities) that may occur when of using two separate antibodies.

Buffers and gels for Phos-tag SDS-PAGE gels were prepared according to the standard SDS-PAGE protocol, and the running gels were supplemented with 25µM Phos-tag and 50µM $MnCl_2$. Samples were treated as reported for SDS-PAGE, subjected to electrophoresis for 1 hour at a constant current of 30mA and then used for Western blot analysis (see 0).

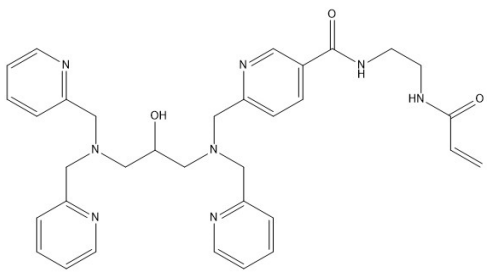

Figure 16. Chemical structure of the employed Phos-tag compound. The molecular weight is 595g/mol.

3.17 Immunoblot/Western blot

The immunoblot, or Western blot, is an analytical technique to specifically detect proteins by antibodies. For this, a protein sample is separated by SDS-PAGE, followed by an electroblotting onto a nitrocellulose or polyvinylidene difluoride (PVDF) membrane that binds proteins non-specifically. The membrane-bound target protein is then detected by a specific antibody and the signal is subsequently amplified by a second antibody that is directed against a species-specific epitope of the first antibody. The secondary antibody is additionally linked to a reporter enzyme, such as alkaline phosphatase (AP) or horseradish peroxidase (HRP), which allows the visualization of the target protein on the membrane.

3.17.1 Standard Western blot

For Western blot analysis, proteins were separated by SDS-PAGE according to the aforementioned protocol. The gel was incubated in anode buffer 2 while the blotting apparatus was assembled with two layers of chromatography paper moistened in cathode buffer on the cathode. The gel was positioned on these papers, followed by the blotting membrane, one chromatography paper moistened in anode buffer 2, and an additional one on top that was equilibrated in anode buffer 1. While assembling the blotting set-up, it is important to make sure that no bubbles are trapped in between the different layers, since they interfere with the electroblotting procedure. The transfer was performed for 30 minutes at 70mA/gel. The success of the blotting was monitored by reversible Ponceau S staining of the membrane-bound proteins, followed by 3×5 minutes washing with water. The membrane was then blocked for at least 30 minutes in blocking solution to prevent unspecific binding of the antibodies to the membrane, followed by rinsing the membrane 3× with water. Hereafter, the membrane was incubated overnight at 4°C in the primary antibody. After thoroughly removing unbound primary antibody by washing the membrane several times with water, the HRP-conjugated secondary antibody was added for 2 hours at room temperature as a 1:10,000 dilution in blocking solution. After this, the membrane was washed several times in water, carefully drained of excess fluid, incubated for 2 minutes with ECL Western blotting substrate for HRP and finally developed using a FluorChem Q chemoluminescence imaging system after removing the ECL solution.

Table 29. Buffers and solutions used for standard Western blot procedure.

Cathode buffer 1	**Anode buffer 1**	**Anode buffer 2**	**Blocking solution**
25mM Tris*	0.3M Tris*	25mM Tris*	50mM Tris HCl, pH 8.0
40mM glycine	40% (v/v) methanol	40% (v/v) methanol	80mM NaCl
10% (v/v) methanol			2mM $CaCl_2$
			0.2% (w/v) NP-40
			5% (w/v) nonfat dry milk
Ponceau staining solution		**Antibody diluent**	
0.2% (w/v) Ponceau S		10mM HEPES (pH 7.4)	
5% (v/v) glacial acetic acid		0.5M NaCl	
		1% (w/v) bovine serum albumin (BSA)	
		0.2% (w/v) Tween 20	
		0.02% (w/v) NaN_3	

**The pH of the buffers is not adjusted*

3.17.2 Blotting of cofilin-1 samples separated by Phos-tag SDS-PAGE

Proteins separated by Phos-tag SDS-PAGE were transferred to polyvinylidene difluoride (PVDF)-membranes for antibody detection by wet-tank blotting using a Genie® blotter. Prior to blotting, the gel was incubated for 10 minutes in Phos-tag transfer buffer supplemented with 1mM EDTA to remove the manganese ions and subsequently washed 3× for 5 minutes with Phos-tag transfer buffer. The blotting apparatus was assembled according to the manufacturer's instructions and the gel was submerged in Phos-tag transfer buffer. The electroblotting of cofilin-1 samples was performed for 1 hour at 12V. The detection of cofilin-1 by antibodies was performed as described in the standard blotting section.

Table 30. Buffer used for electroblotting of Phos-tag SDS-PAGEs. The pH of the buffer was not adjusted.

Phos-tag transfer buffer
25mM Tris-base
192mM glycine
20% (v/v) methanol

3.18 Coomassie Blue-staining of polyacrylamide gels

Polyacrylamide gels were Coomassie Blue-stained for protein visualization. For this, the gels were submerged in Coomassie Blue staining solution until the gel was completely stained. After that, the staining solution was removed, the gel was washed twice with water and then placed in destaining solution until the polyacrylamide background was clear while the protein bands remained blue. Staining and destaining processes can be accelerated by heating in the microwave for 30 seconds. Stained gels were either digitized by scanning or air-dried in a frame between two cellophane sheets.

Table 31. Solutions used for Coomassie Blue-staining and -destaining of SDS-PAGE gels.

Staining solution	**Destaining solution**
40% (v/v) ethanol	40% (v/v) ethanol
10% (v/v) acetic acid	10% (v/v) acetic acid
0.1% (w/v) Coomassie Brilliant Blue R-250	

3.19 Analytical ultracentrifugation

Analytical ultracentrifugation is a method that monitors the sedimentation of macromolecules in a centrifugal field, allowing the study of their hydrodynamic and thermodynamic behavior in solution, without interfering surface or matrix interactions. The deduced information can be used for molar mass determination, the characterization of self-association or heterogeneous binding, such as protein-protein and protein-DNA interactions. Here, the method was used to determine the oligomeric states of chronophin^{WT} and chronophin^{KK}.

Sedimentation velocity analytical ultracentrifugation was carried out using a Beckman Optima XL-I analytical ultracentrifuge with an eight-hole An-50 Ti rotor at 40,000rpm at 20 °C. Four hundred microliters of purified recombinant protein dialyzed against SEC buffer A and reference buffer solution were loaded in standard double-sector charcoal-filled Epon centerpieces equipped with sapphire windows. Protein concentration corresponded to an absorption at 280nm of 0.5–0.8. Data were collected in continuous mode at a step size of 0.003cm using absorption optical detection at a wavelength of 280nm. Data were analyzed using the NIH software SEDFIT to determine continuous distributions for solutions to the Lamm

equation *c*(*s*) as described previously [267]. Analysis was performed with regularization at confidence levels of 0.68 and floating frictional ratio (*f*/*f*0 ~1.32 ± 0.02 for both chronophin wild type and mutant, suggesting a globular conformation), time-independent noise, baseline, and meniscus position to root mean square deviation (r.m.s.d.) values between 0.007 and 0.012.

3.20 Analytical size exclusion chromatography

Size exclusion chromatography, as described in 3.14.5, can be employed for the quantitative analysis of protein complex formation, as the elution volume of a protein or a protein complex can be used to calculate its apparent molecular mass. For this, globular proteins of known molecular mass (Gel Filtration LMW Calibration kit) were used to calibrate a Superdex 200 10/300 GL column, and blue dextran was used to determine the column void volume. Protein elution volumes were measured by monitoring the absorption at 280 nm. The elution volumes were used to calculate the partition coefficient (K_{av}) with the equation:

Equation 3

$$K_{av} = \frac{V_e - V_0}{V_t - V_0}$$

where V_e is the elution volume,V_0 is the void volume, and V_t is the total volume of the column. The apparent molecular mass was then derived from the inverse logarithm of the partition coefficient.

3.21 Thermofluor

Fluorescence-based thermal shift (thermofluor) assays are used as high throughput screens to determine temperature-dependent protein unfolding in solution, with the purpose of increasing the stability of the proteins of interest by optimizing buffer conditions with respect to pH, salt concentrations and additives. The environmentally sensitive dye SYPRO Orange specifically interacts with hydrophobic regions of the unfolded proteins. This leads to a change in its fluorescence behavior, which can be monitored by an increase in absorption and emission at 492/610nm. The derived melting curves are used

to determine the melting temperature (T_m), defined as the temperature that results in half-maximal protein unfolding.

All experiments were conducted using a MX3005P Real-Time PCR thermocycler. Five µL of the protein (final concentration 5-10µM) were mixed with 10µL of the respective buffer (to yield a 1× final concentration) and 5µL of 5× SYPRO Orange dye in ddH_2O. The results are shown in the supplements of this thesis.

3.22 Cross-linking

Chemical cross-linking allows the identification of transient protein-protein interactions by the introduction of a covalent linkage between adjacent molecules using a bifunctional reagent that specifically interacts with functional groups of amino acids. The stably linked protein complex can then be analyzed by suited methods, such as SDS-PAGE or analytical size exclusion chromatography. In this work, the short span (~2-3Å) cross-linker formaldehyde was used to confirm the complex formation of chronophin with CIB1 and calmodulin.

For this, 5 µM of chronophin was incubated for 2h at 37°C with 10µM of CIB1 and/or 10µM of calmodulin (all proteins were untagged) in a total volume of 15µL in SEC buffer A supplemented with 50µM EGTA ± different concentrations of $CaCl_2$ and 0.67% formaldehyde. Cross-linking was stopped by the addition of SDS-PAGE loading buffer, and proteins were resolved by SDS-PAGE and stained with Coomassie Brilliant Blue. Band intensities were analyzed densitometrically using the software ImageJ.

3.23 Isothermal titration calorimetry

Isothermal titration calorimetry (ITC) is a quantitative technique used to directly characterize the thermodynamics of a bimolecular interaction by measuring the temperature changes during binding events as a function of the interactor's concentrations. This allows direct determination of the enthalpic change (ΔH), binding affinty (K_a) and binding stoichiometry (N). From these values, the changes in Gibbs free energy (ΔG) and entropy (ΔS) can be calculated using the equation:

Equation 4

$$\Delta G = -RT\ln K_a = \Delta H - T\Delta S$$

with R being the gas constant and T the absolute temperature.

All ITC experiments were performed on a MicroCal ITC_{200} microcalorimeter at 25°C and were analyzed using MicroCal Origin software. Prior to all ITC experiments, protein samples were extensively dialyzed overnight at 4 °C against filtered and degassed SEC buffer B. Each titration experiment consisted of 2.5µL injections of 300–600µM BeF_3^- diluted in SEC buffer B into the 280µL sample cell containing 25–75µM chronophin. Heat of dilution measurements were carried out as mentioned above by injecting BeF_3^- into SEC buffer B. For each experiment, the binding enthalpy was directly measured, whereas the stoichiometry (*N*) and the dissociation constant (K_d) were obtained using the analysis software, assuming a single site binding model.

3.24 Malachite green assay

The malachite green assay was used for the detection of free inorganic phosphate (P_i) released in a phosphatase catalyzed phosphate monoester hydrolysis reaction. The assay is based on the complex formation of malachite green with ammonium molybdate and P_i under acidic conditions. The resulting malachite green phosphomolybdate complex can be detected by absorbance measurements at 620-650nm.

Generally, the assays were conducted in 96-well microtiter plates by mixing the phosphatase with its substrate in a total volume of 50µL. After a predefined time, the reaction was stopped by the addition of 100µL Biomol Green, and the color development was allowed to proceed for a consistent time of 10-15 minutes. Finally, the absorption of the phosphomolybdate complex was read at 620nm on an Envision 2104 multilabel microplate reader. If needed, free phosphate release was quantitated using phosphate standard curves. Kinetic constants, such as v_{max} and K_m were calculated using GraphPad Prism.

For analysis of the effects of CIB1 and calmodulin on the chronophin pyridoxal 5'-phosphate (PLP)-phosphatase activity, 100nM of chronophin were pre-incubated in the absence or presence of 1µM CIB1 or 1µM calmodulin (all proteins were untagged) for 10min at 22°C in SEC buffer A supplemented with 0.001% (v/v) Triton X-100 and 1mM EGTA or 100µM $CaCl_2$ at pH 7.4. The reactions were started by the

addition of PLP (final concentrations ranging from 0 – 500µM), and stopped after 2min by the addition of Biomol Green. Color was allowed to develop for 10min before the absorbance was read on an Envision 2104 multilabel microplate reader.

For comparisons of chronophin^{WT} and chronophin^{KK}, 100nM of the respective protein was preincubated for 10min at 22°C in SEC buffer B supplemented with 0.001% (v/v) Triton X-100. The reactions were started by the addition of PLP (final concentrations ranging from 0 to 1000µM) and stopped after 2min by the addition of 100µL Biomol Green. Color was allowed to develop for 10min before the absorbance was read on an Envision 2104 multilabel microplate reader.

Inhibitor studies were conducted by pre-incubating 100nM chronophin 10min in SEC buffer B supplemented with 0.001% (v/v) Triton X-100, followed by an incubation time of four minutes with the inhibitor (final concentrations ranging from 0 to 2mM). The reactions were started by the addition of PLP. The final PLP concentrations were ranging from 0 to 500µM in the kinetic assays or set to 20µM in the dose-response assays, respectively. The final volume of each reaction was 50µL. Kinetic measurements were stopped after two minutes, dose-response assays after five minutes by the addition of 100µL Biomol Green. Color was allowed to develop for 15-20min before the absorbance was read on an Envision 2104 multilabel microplate reader.

3.25 *Para*-nitrophenylphosphate (*p*NPP) assays

*P*NPP is an artificial chromogenic substrate that is frequently used to probe the activity of various phosphatases. The enzyme-catalyzed hydrolysis of the phosphate monoester yields *para*-nitrophenol (and inorganic phosphate) that is converted into the *para*-nitrophenolate anion under alkaline conditions, resulting in a shift of the absorbance maximum from 318nm to ~400nm, at which it is usually detected.

The enzymatic activities of chronophin, the CAC hybrid and AUM towards *p*NPP were tested by incubating 100nM of the respective enzyme in 96-well microtiter plates with 1mM *p*NPP in a final volume of 100µL SEC buffer A. Before starting the reactions by the addition of the substrate, the proteins were pre-incubated for 10 minutes at room temperature. The generation of *para*-nitrophenolate was monitored by absorption measurements at 405nm using an Envision 2104 multilabel microplate reader.

3.26 Phospho-cofilin-1 dephosphorylation assays

Cofilin-1 is a key regulator of actin dynamics. The actin depolymerizing activity of cofilin is inhibited by the kinase-catalyzed phosphorylation of Ser^3, activation is mediated by phosphatases, such as chronophin or slingshot that specifically target this phosphorylation site. In order to investigate the roles of CIB1 and calmodulin in the chronophin-mediated phospho-cofilin-1 dephosphorylation, *in vitro* assays using recombinantly expressed and purified chronophin, CIB1 and calmodulin were performed. For this, human cofilin-1 was phosphorylated using the activated catalytic domain (residues 285 to 638) of human LIM kinase 1, by incubating 15µg cofilin-1 with 2ng of the kinase in a final volume of 50µL phosphorylation buffer for 30 minutes at 30°C. Subsequently, the sample was diluted >1:200 in phosphorylation buffer devoid of ATP to reduce the ATP concentration and prevent further phosphorylation reactions. The sample was then concentrated to 100-150µL using a Microcon YM-10 centrifugal filter unit.

For dephosphorylation assays, ~200-300ng of phospho-cofilin-1 were incubated with 50µM chronophin ± ~300µM CIB1 and/or calmodulin in a final volume of 10µL phosphatase buffer supplemented with 1mM EGTA or 100µM Ca^{2+}. A positive control using 1µL calf intestine alkaline phosphatase was included to show successful but unspecific dephosphorylation of phospho-cofilin-1. The reactions were conducted for 1.5 hours at 37°C and stopped by the addition of 5µL SDS-PAGE loading buffer. The samples were then separated by Phos-tag SDS-PAGE, electroblotted onto a nitrocellulose membrane and immunoblotted with cofilin-1-specific antibodies.

Table 32. Buffers used for phospho-cofilin-1 dephosphorylation assays.

Phosphorylation buffer	**Phosphatase buffer**
50mM TEA, pH 7.4	10mM HEPES pH 7.4
250mM NaCl	150mM NaCl
1mM $MgCl_2$	10mM $MgCl_2$
1mM DTT	5% (v/v) glycerol
200µM ATP	1% (w/v) Nonidet P-40
1µM glutathione S-transferase (GST)	

3.27 Circular dichroism (CD) spectroscopy

Right and left handed circularly polarized light is absorbed to different extents by chiral molecules in solution, leading to ellipticity of the polarized light, which can be measured using a CD spectropolarimeter. This effect is used to determine secondary structure elements or to analyze the folding of proteins by measuring the changes in ellipticity over a spectrum of wavelengths in the far UV range (~190-260nm). Here, the method was employed to monitor the conformational changes of the calcium sensing proteins CIB1 and calmodulin in order to determine the buffer conditions needed to fully load the proteins with or to deplete them of calcium. All measurements were performed at 20°C using a J-810 CD spectropolarimeter equipped with a 0.1cm quartz cuvette. CIB1 was measured at a final concentration of 30µM in a buffer containing 25mM TEA (pH7.4) and 50mM NaCl, supplemented with different concentrations of $CaCl_2$, $MgCl_2$, EDTA or EGTA. Calmodulin was measured at a concentration of 10µM in a buffer containing 50mM TEA (pH 7.4), 250mM NaCl and 5mM $MgCl_2$, supplemented with 50µM EGTA or 25µM CaCl2, respectively. The scans were performed continuously at a scan speed of 30nm/minute at a bandwidth of 2nm. Each sample was scanned five consecutive times. The results are shown in the supplement of this thesis.

3.28 Protein crystallization

The self-assembly of a protein into a periodic crystal lattice, finally forming a single crystal, is crucial for X-ray-based structure determination of proteins. A common method to achieve this is the crystallization by vapor diffusion in a sealed system. It relies on the diffusion of solvent from a small droplet containing protein, solvent and precipitant, into a much larger volume of the concentrated precipitant solution alone. This process thus increases the concentration of both precipitant and protein in the droplet, generating a metastable supersaturated solution of the protein that, under favorable conditions, might lead to crystal growth from a nucleation site.

The sitting drop vapor diffusion method using a HoneyBee 963 crystallization robot was employed for initial standardized crystallizations screens in a 96-well format. Here, the droplet consisting of 0.3µL protein solution mixed with 0.3µL of crystallization solution sits on an elevated shelf and is equilibrated against 40µL reservoir solution. Promising crystallization experiments were subsequently optimized in fine

screens using the hanging drop vapor diffusion method, by manually mixing 0.5-2µL with 0.5-2µL crystallization solution on a cover slide. The cover slide is then utilized to seal the well containing 0.5-1mL reservoir solution, with the drop hanging above the reservoir. The respective crystallization conditions are given in Table 33. Prior to X-ray diffraction experiments, all crystals were cryoprotected for flash cooling in liquid nitrogen by soaking in the respective crystallization buffer supplemented with 30% (v/v) glycerol.

Table 33. Crystallization buffers.

Protein	Protein buffer	Crystallization buffer
chronophin^{WT}	10mM TEA pH 7.4 0.1M NaCl 1mM $MgCl_2$	0.1M imidazole, pH 8.0 0.2M NaCl 1M sodium tartrate
chronophin^{WT}•BeF_3^-	10mM TEA pH 7.4 0.1M NaCl 1mM $MgCl_2$	0.1M imidazole, pH 8.0 0.2M NaCl 1M sodium tartrate 1mM BeF_3^-
chronophin^{WT}•inhibitor 3	10mM TEA pH 7.4 0.1M NaCl 1mM $MgCl_2$	0.1M imidazole, pH 8.0 0.2M NaCl 1M sodium tartrate 5mM inhibitor 3
chronophin^{KK}	50mM TEA pH 7.4 0.25M NaCl 5mM $MgCl_2$	0.1M MES pH 6.5 25% PEG MME 550
CAC hybrid	10mM TEA pH 7.4 0.1M NaCl 1mM $MgCl_2$	15% PEG 3350 0.2M $Mg(NO_3^-)_2$

3.29 Data collection

X-rays scattered by electrons of atoms arranged in a periodic crystal lattice are interpreted as reflections on sets of lattice planes. Interference of the scattered X-rays is directly related to the scattering angle θ and the interplanar distance (d) of the reflecting planes. According to Bragg's law

Equation 5

$$n\lambda = 2d \cdot sin\theta$$

constructive interference is maximized when the path length difference, calculated as *2d·sinϑ*, becomes an integer multiple (n) of the incident X-rays wavelength λ. The sum of positive interference produced by scattering events generates a diffraction pattern that is recorded during X-ray crystallography. The intensities and the positions of the reflections relative to the crystal position are then used to calculate the three-dimensional arrangement of electron densities within the crystal.

Initial diffraction experiments were conducted at the in-house X-ray system of the Rudolf Virchow Center using a MicroMax-007HF X-ray generator (Cu anode, 1.5418Å) with an R-AXIS HTC image plate detector. The standard settings for crystal evaluation are given in Table 34, the information about crystal symmetry and diffraction limits retrieved from these initial images was used to set up a strategy for data set collection. Complete data sets were either recorded at the in-house system or at the "Berlin Electron Storage Ring Society for Synchrotron Radiation" (BESSY, Berlin). Data collection statistics tables are given in the respective result sections of this thesis.

Table 34. Parameters for crystal evaluation at the in-house X-ray system.

Parameter	**Setting**
Detector distance	200mm
Number of images	2
ϕ angle	0.5°
Interval angle	90°
Exposure time	5-10minutes

3.30 Data processing and evaluation

The collected X-ray diffraction images were processed using iMosFlm [263] and Scala [266] from the CCP4i program suite [260]. First, during indexing the positional information of the spots is used to determine the unit cell dimensions and lowest symmetry space group of the crystal. Additionally, the position of each spot in reciprocal space is assigned by its Miller indices *hkl*. Next, intensity values (I) and the respective standard uncertainty (σI) of the reflections are determined by integration and corrected for

background intensities. Finally, during merging and scaling, the integrated values of partial reflections dispersed over multiple images collected in the diffraction experiment and symmetry equivalents are combined into one set of structure factor amplitudes and normalized to have a consistent intensity scale.

The quality of the diffraction data can be evaluated using R_{sym} as a measure of the deviation of symmetry related reflections from their average:

Equation 6

$$R_{sym} = \frac{\sum_{hkl} \sum_j |I_{hkl,j} - \langle I_{hkl} \rangle|}{\sum_{hkl} \sum_j I_{hkl,j}}$$

$\langle I_{hkl} \rangle$ is the average intensity of symmetry related observations of a unique reflection $I_{hkl,j}$. R_{sym} values <5% indicate good quality data, whereas 5-10%, 10-20% and >20% represent usable, marginal and questionable quality data, respectively [271]. A version of R_{sym} that is independent of the data set redundancy is R_{meas} :

Equation 7

$$R_{meas} = \frac{\sum_{hkl} \sqrt{\frac{n}{n-1}} \sum_{j=1}^{n} |I_{hkl,j} - \langle I_{hkl} \rangle|}{\sum_{hkl} \sum_j I_{hkl,j}}$$

where n is the multiplicity of the observed reflection. Calculation of the R_{meas} results in higher, but more realistic values than R_{sym} [271]. Another variant to report the expected precision of the reflections intensities is $R_{p.i.m.}$, suggestested by Weiss et al. [272]:

Equation 8

$$R_{p.i.m.} = \frac{\sum_{hkl} \sqrt{\frac{1}{n-1}} \sum_{j=1}^{n} |I_{hkl,j} - \langle I_{hkl} \rangle|}{\sum_{hkl} \sum_j I_{hkl,j}}$$

Typically, diffraction data are truncated at a resolution before R_{sym} and R_{meas} exceed ~0.6 to 0.8, respectively, or before the signal-to-noise (I/σI) drops below ~2.

3.31 Molecular replacement

In order to determine the electron density ρ at position (xyz) in the crystal it is crucial to know the structure factor F(hkl):

Equation 9

$$\rho(\mathrm{xyz}) = \frac{1}{V}\sum_{hkl} F(hkl)e^{-2\pi i(hx+ky+lz)}$$

F(hkl) is a function of the amplitude |F(hkl)| and phase angle ϕ(hkl):

Equation 10

$$F(hkl) = |F(hkl)|e^{i\cdot\varphi(hkl)}$$

The information of the phase angle ϕ(hkl) is lost during X-ray diffraction experiments, a fact known as the phase problem in crystallography. The structure factor amplitude |F(hkl)| however can be calculated, since it is proportional to the measured intensities I(hkl) of the reflections:

Equation 11

$$I(hkl) \propto |F(hkl)|^2$$

The phase problem can be solved by molecular replacement, given that a homologous structure is available. During molecular replacement, the homologous model is repositioned in the unit cell until the best agreement with the experimental data is found. The phases of the search model are then used to calculate an electron density map for the experimental X-ray data.

All structures were solved by molecular replacement with the program Phaser [273] employing the structure of the human pyridoxal 5'-phosphatate phosphatase/chronophin (PDB code 2OYC) as a search model. The structure of chronophin in complex with inhibitor 3 was solved using the murine chronophin^{WT} structure (PDB code 4BX3).

3.32 Model building and refinement

The electron density obtained from molecular replacement is utilized for building an initial model of the crystallized molecule. This model is then subjected to refinement, a process that serves to adjust the model parameters, including atom coordinates, B-factors and occupancies to the experimental data, ideally yielding more accurate electron density that is used to improve the model. During refinement, *a priori* knowledge about protein structures is introduced, such as restraints (bond lengths and angles, planarity of peptide bonds and aromatic components) and constraints (atom occupancy, hydrogen bond lengths and angles) to compensate for the deficiencies of the experimental data. Alternating rounds of refinement and subsequent model improvement are performed until the correlation between experimental diffraction data and model parameters are maximized, as monitored by the reliability factor R_{work}. This factor serves as a measure for the agreement between calculated structure factor amplitudes $|F_c(hkl)|$ and observed structure factor amplitudes $|F_o(hkl)|$.

Equation 12

$$R = \frac{\sum_{hkl} ||F_o(hkl)| - |F_c(hkl)||}{\sum_{hkl} |F_o(hkl)|}$$

In order to avoid over-interpretation of the data, an additional unbiased R-factor, the R_{free}, is calculated using Equation 12 with 5-10% of randomly chosen data that are not included during the refinement process [274].

All initial structure models were built and improved in Coot [261], and subsequently refined using Phenix [265], incorporating torsion angle non-crystallographic symmetry restraints. Ligand restraints for the refinement of inhibitor 3 were generated using the electronic Ligand Builder and Optimization Workbench (eLBOW) and the Restraints Editor Especially Ligands (REEL) of the Phenix program suite [265, 275, 276]. Structural representations were generated with the 3D molecular visualization software PyMol (The PyMOL Molecular Graphics System, Version 1.5.0.4 Schrödinger, LLC).

4 Results

4.1 Protein purification

This section comprises the purification and characterization of proteins used in this work. All proteins were recombinantly expressed in *E. coli* and purified by enriching the protein of interest from cell lysates, followed by cleavage and removal of the affinity tag (if needed), and finally by removing residual contaminants using size exclusion chromatography. All columns were operated on an ÄKTA liquid chromatography system unless stated otherwise. The purified proteins were used for subsequent biochemical and structural analyses.

4.1.1 Immobilized metal affinity chromatography (IMAC)

N-terminally hexahistidine tagged proteins, such as chronophin^{WT}, chronophin^{KK}, Δ8CIB1, Δ148CIB1 and the CAC-mutant were expressed in *E. coli* using the pETM-11 vector system. The isolation of the protein of interest from cleared cell lysates was conducted using immobilized metal ion affinity chromatography (IMAC) by employing a HisTrap HP column (1mL or 5mL). Figure 17A shows the chromatogram of an IMAC purification of chronophin^{WT} to exemplify the applied purification protocol. The fractions containing the protein of interest, as determined by SDS-PAGE, were pooled and concentrated for TEV-cleavage for 48 hours at 4°C. To separate cleaved from uncleaved protein of interest and His-tagged TEV protease, the sample was again loaded on a HisTrap HP column, as shown in Figure 17B for chronophin^{WT}. The cleaved target protein was collected in the flow-through, whereas the uncleaved protein and the TEV protease remained bound to the column. The untagged proteins were concentrated and further purified using size exclusion chromatography.

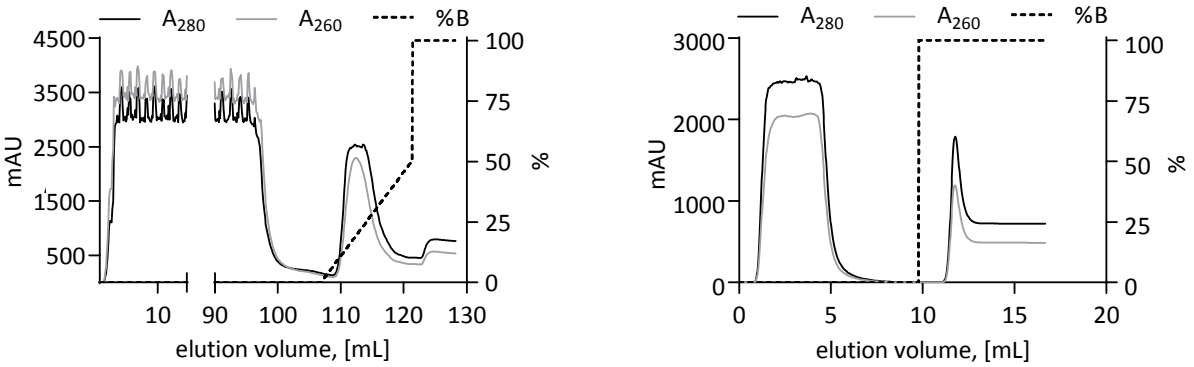

Figure 17. IMAC purification of N-terminally His_6-tagged proteins. A. Chromatogram of His_6-chronophin^{WT} using a 1mL HisTrap HP column. The cleared lysate was loaded on the column (0-95mL), washed with 12CV IMAC buffer A (95-107mL) and finally eluted using a linear gradient over 15CV up to 50% IMAC buffer B (107-122mL). The last step at 100% IMAC buffer B elutes all remaining proteins from the column. B. After TEV cleavage, untagged chronophin^{WT} was separated from uncleaved His_6-chronophin^{WT} and His-tagged TEV protease by applying the sample on a 1mL HisTrap HP column. Untagged chronophin^{WT} elutes in the flow-through (0-10mL), His-tagged proteins are eluted at 100% IMAC buffer B (~12mL).

4.1.2 Hydrophobic interaction chromatography (HIC) of calmodulin

Untagged calmodulin expressed in *E. coli* using the pET-3a vector was purified by hydrophobic interaction chromatography. For this, 1mL of the heat precipitated and cleared lysate was loaded on a Resource PHE column (1mL), washed with 2mL HIC buffer A and finally eluted with 100% HIC buffer B. Calmodulin elutes as a single peak of pure protein. One milliliter of the lysate was sufficient to saturate the column with protein, thus this protocol had to be repeated several times until all calmodulin was extracted from the lysate. A representative chromatogram of the procedure is shown in Figure 18. The fractions containing calmodulin were pooled and concentrated for size exclusion chromatography.

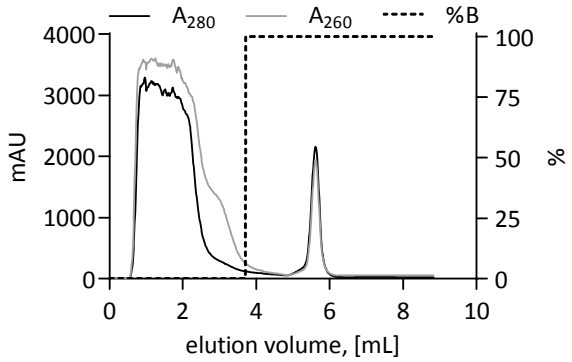

Figure 18. HIC purification of calmodulin. After loading 1mL of lysate (0-1mL), the Resource PHE column was washed with 2mL HIC buffer A (1-3mL) and calmodulin was eluted with 100% HIC buffer B as a single peak (5-6mL).

4.1.3 Ion exchange chromatography of chronophin^{KK}

IMAC purified chronophin^{KK} in some cases co-eluted with high amounts of impurities, presumably representing chaperones that were co-expressed with chronophin^{KK} to increase the protein's solubility. These could be removed by ion exchange chromatography using a 1mL MonoQ 5/50 GL column, as described in 3.14.2. Chronophin^{KK} elutes in the flow-through, whereas the impurities bind to the column and elute with increasing salt concentrations (Figure 19). Interestingly, chronophin^{WT} binds to the column material under the same buffer conditions (not shown), suggesting that monomerization dramatically changes the surface properties of chronophin. The flow-through containing chronophin^{KK} was pooled, concentrated for TEV cleavage and further purified by size exclusion chromatography after removal of the TEV protease and of uncleaved chronophin^{KK}.

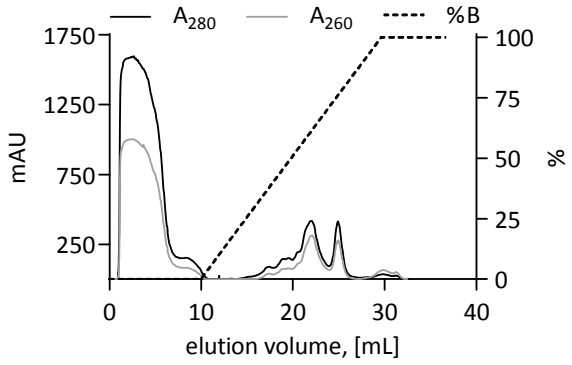

Figure 19. Ion exchange chromatography of chronophin^{KK}. Chronophin^{KK} remains in the flow-through (0-10mL), whereas the impurities bind to the MonoQ column material and elute at the increased salt concentrations of IEX buffer B (10-30mL).

4.1.4 Affinity chromatography of GST-CIB1

N-terminally GST-tagged CIB1 was batch-purified using glutathione sepharose (see 3.14.3). The fusion protein was cleaved on the column and untagged CIB1 was eluted. A representative SDS-PAGE of the already highly pure elution fractions is shown in Figure 20.

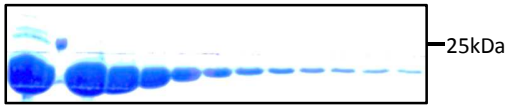

Figure 20. Coomassie Blue-stained 15% SDS-PAGE gel of GSH-Sepharose purified CIB1. The untagged protein was eluted after on-column cleavage, shown are the elution fractions 1-12 and a 25kDa size standard (lane 2).

4.1.5 Size exclusion chromatography

Size exclusion chromatography (SEC) was the final step in the purification protocol of each protein described in this work. SEC served to remove residual contaminants and yield proteins of high purity. The purest fractions were pooled and concentrated, and either snap-frozen in liquid nitrogen for storage at -80°C, or directly used for subsequent biochemical analyses and/or crystallography. Figure 21 shows representative SEC chromatograms of the respective proteins with corresponding SDS-PAGE gels of the pooled fractions.

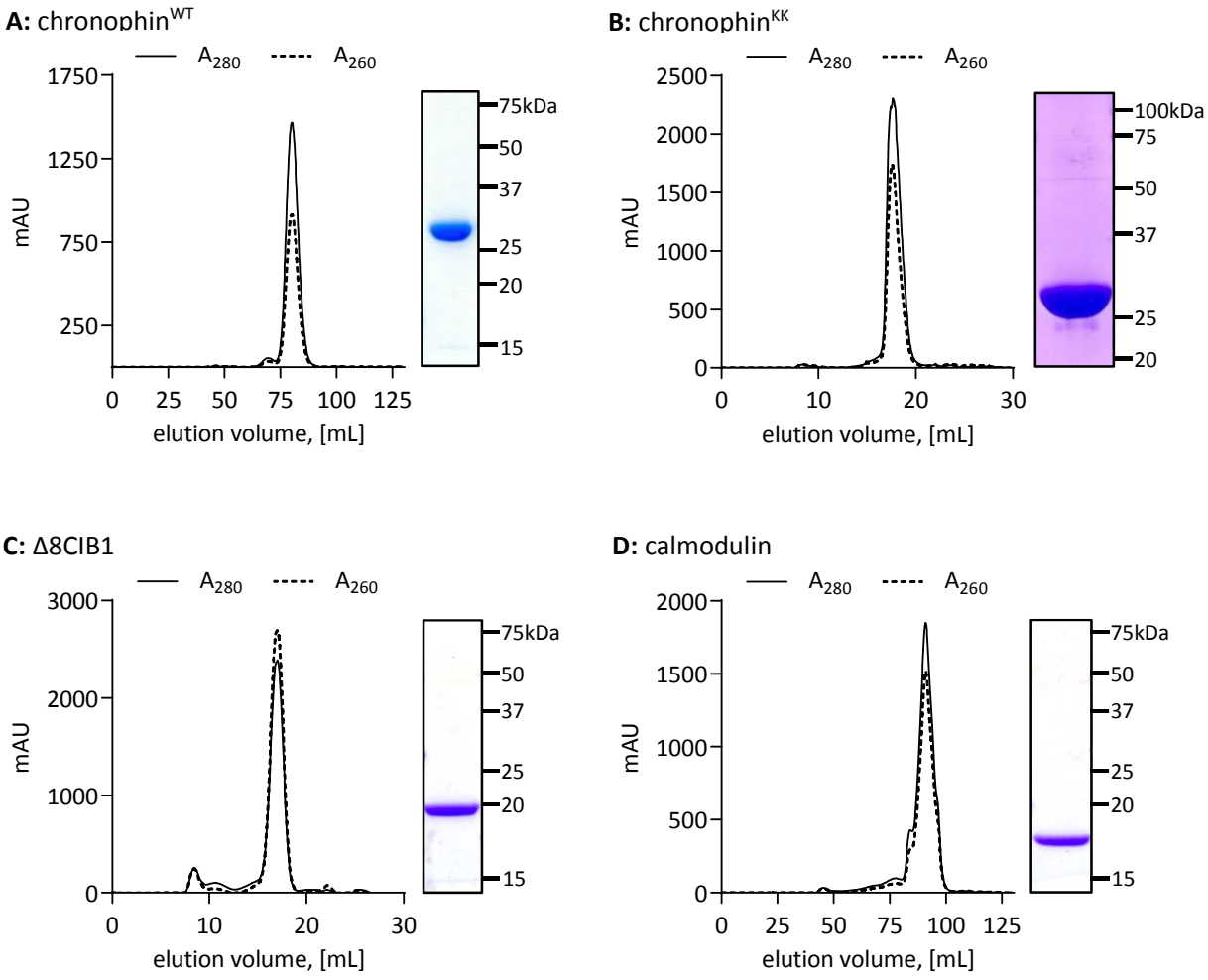

*Figure legend on the next page.

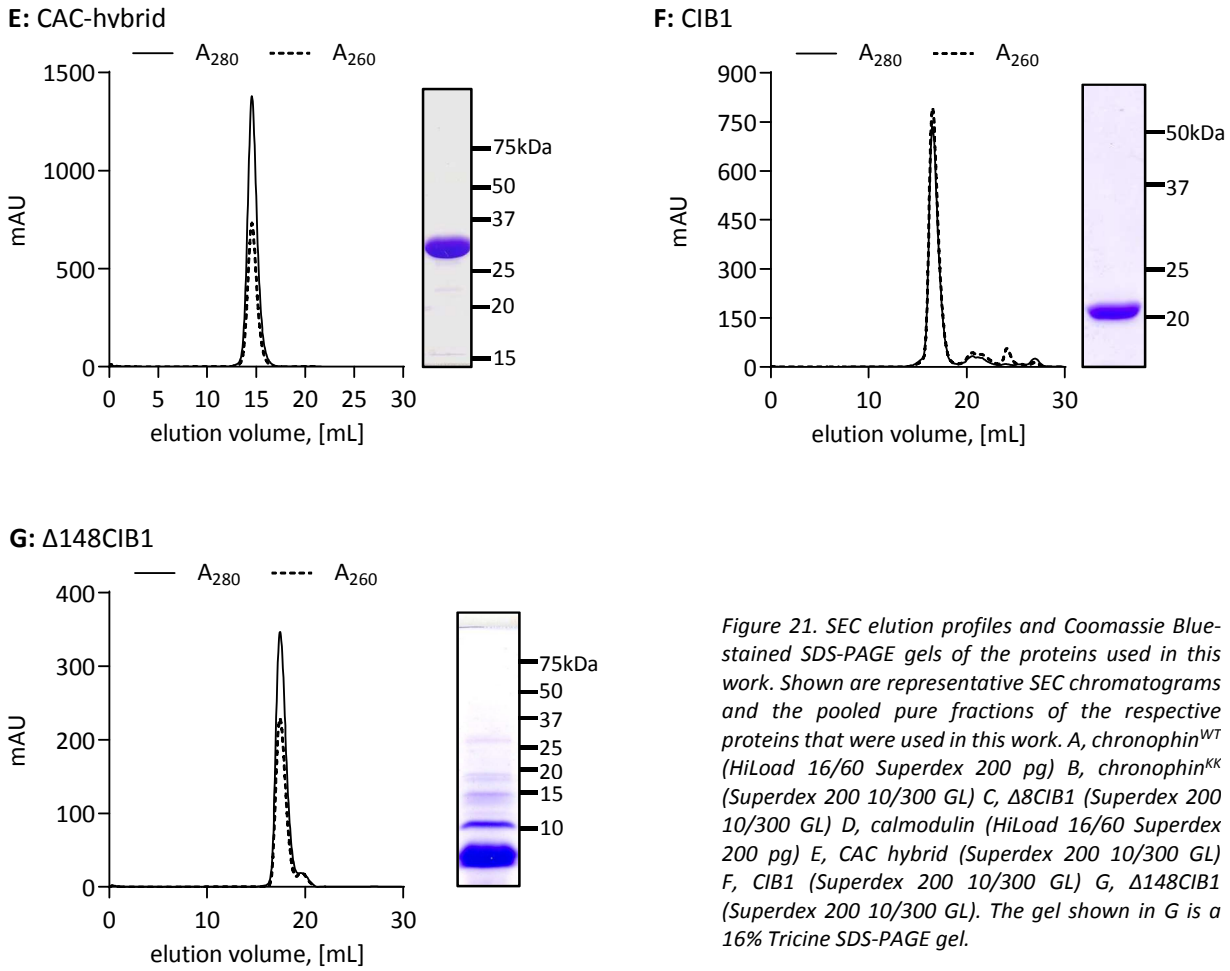

Figure 21. SEC elution profiles and Coomassie Blue-stained SDS-PAGE gels of the proteins used in this work. Shown are representative SEC chromatograms and the pooled pure fractions of the respective proteins that were used in this work. A, chronophin^{WT} (HiLoad 16/60 Superdex 200 pg) B, chronophin^{KK} (Superdex 200 10/300 GL) C, Δ8CIB1 (Superdex 200 10/300 GL) D, calmodulin (HiLoad 16/60 Superdex 200 pg) E, CAC hybrid (Superdex 200 10/300 GL) F, CIB1 (Superdex 200 10/300 GL) G, Δ148CIB1 (Superdex 200 10/300 GL). The gel shown in G is a 16% Tricine SDS-PAGE gel.

4.2 CIB1 and calmodulin as competing interactors of chronophin

This section describes the experiments conducted to further characterize the interaction of chronophin with the Ca^{2+}- and integrin-binding protein 1 (CIB1) and calmodulin. As explicitly described in the introduction, CIB1 was recently identified by our group to be a putative interaction partner of chronophin by screening a mouse brain cDNA library using the yeast two-hybrid system. The interaction could be confirmed biochemically by solid-phase binding assays, as well as in pull-down assays. Additionally, the binding interfaces on CIB1 and chronophin were narrowed down by yeast two-hybrid screens, with residues 173-178 in the C-terminus of CIB1 and residues 75-85 in chronophin being of particular importance.

Given the resemblance of the CIB1/chronophin interaction with the calcineurin A/B complex, calmodulin was hypothesized to be another potential chronophin interaction partner. Bioinformatic analyses using the Calmodulin Target Database predicted a calmodulin binding motif in chronophin that partially overlaps with the mapped CIB1 binding interface. Interestingly, CIB1 also contains a predicted calmodulin binding site. The interactions of calmodulin with CIB1 and chronophin were then confirmed biochemically by pull-down assays, indicating that CIB1 and calmodulin indeed compete for binding to chronophin and that Ca^{2+} modulates the interactions. While elevated Ca^{2+} levels increased the calmodulin/chronophin interaction, the absence of Ca^{2+} seemingly strengthened the CIB1/calmodulin binding. The association of CIB1 and chronophin showed no sensitivity for Ca^{2+}.

4.2.1 Ca^{2+} triggers complex formation with calmodulin

Based on the results previously obtained in our laboratory, further studies were conducted to gain more detailed information on how the interaction of chronophin with CIB1 and calmodulin may be regulated. Unfortunately, direct measurements of binding constants employing isothermal titration calorimetry (ITC) failed to yield reproducible data, making an accurate interpretation of the binding isotherms impossible. In these experiments, I tested binding of chronophin with CIB1 and calmodulin; prior to ITC experiments, all proteins were dialyzed for 24 hours against SEC buffer A supplemented with 1mM EGTA or 1mM $CaCl_2$ to produce Ca^{2+}-depleted or completely Ca^{2+}-bound CIB1 and calmodulin. However, no significant heat change and/or saturation could be measured when chronophin (~100µM) present in the sample cell was titrated with CIB1 or calmodulin at concentrations of up to 1mM (data not shown). Further binding studies, typically performed at lower protein concentrations, using analytical size exclusion chromatography, native PAGE analysis, native agarose gel analysis and analytical ultracentrifugation experiments in the aforementioned buffer conditions also failed to show any interaction of the proteins (data not shown). Taken together, these results led to the assumption that the association of chronophin with CIB1 and calmodulin is of transient nature and/or low binding affinity under the tested conditions.

In order to circumvent this issue and to be able to study the interaction in more detail, chemical crosslinking experiments with formaldehyde were performed. Formaldehyde is a short-span crosslinker (~2-3Å), and is therefore considered to stabilize protein-protein interactions with high specificity, given that suitable residues are present and accessible in the interaction interface [277]. In line with the previously performed protein-protein interaction studies, Figure 22B shows that chronophin can be readily crosslinked to CIB1 or calmodulin respectively, using formaldehyde to stabilize the interaction. The

molecular masses of the complexes detected by Coomassie-stained SDS-PAGE indicate a 1:1 stoichiometry of CIB1 or calmodulin with a chronophin monomer. CIB1/calmodulin-complexes could not be detected. Control experiments conducted under the same conditions including the same total protein concentrations (15µM) did not show nonspecific protein aggregation or stabilization of chronophin dimers (Figure 22A).

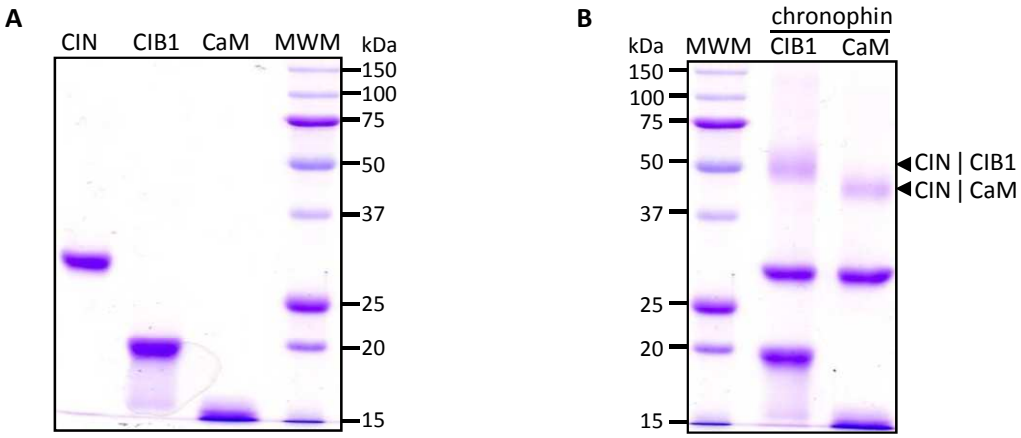

Figure 22. Formaldehyde crosslinking of chronophin (CIN) with CIB1 or calmodulin (CaM). Recombinantly expressed and purified proteins were used for formaldehyde crosslinking. The experiments were conducted using 5µM chronophin, 10µM CIB1 and/or 10µM calmodulin in the presence of 0.67% formaldehyde. Complex formation was subsequently analyzed by 12% SDS-PAGE (MWM, molecular weight marker). A, no unspecific crosslinking is detected when the experiments are conducted using the single proteins at the same total protein concentration (15µM). B, chronophin readily forms complexes with CIB1 and calmodulin in the presence of formaldehyde. The molecular weights of the complexes (arrows) indicate a 1:1 ratio of chronophin and its putative interactors.

In order to analyze the effect of Ca^{2+} on the CIB1/chronophin- and calmodulin/chronophin-complex formation, the formaldehyde crosslinking experiments were repeated in SEC buffer A supplemented with 50µM EGTA in the absence or presence of different concentrations of $CaCl_2$. Figure 23A shows that compared to calcium-free conditions, the CIB1/chronophin interaction was only moderately enhanced in the presence of 25µM Ca^{2+} (lanes 2 and 5). In contrast, the formation calmodulin/chronophin-complexes was barely detectable in the absence of added Ca^{2+} (lane 3), but increased strongly at elevated Ca^{2+}-concentrations (lane 6). Densitometric quantitation of the Coomassie Blue-stained SDS-PAGE gels (Figure 23B) indicate that the calmodulin/chronophin-complex formation increased significantly by 7-fold ($p<0.02$) under elevated Ca^{2+}-concentrations, while the CIB1/chronophin interaction was apparently independent of Ca^{2+}.

When all three proteins were simultaneously subjected to formaldehyde crosslinking, CIB1/chronophin-complexes were the predominant species in the absence of added Ca^{2+} (Figure 23A,

lane 4), whereas calmodulin/chronophin-complexes were prevalent in the presence of 25µM Ca^{2+} (Figure 23A, lane 7).

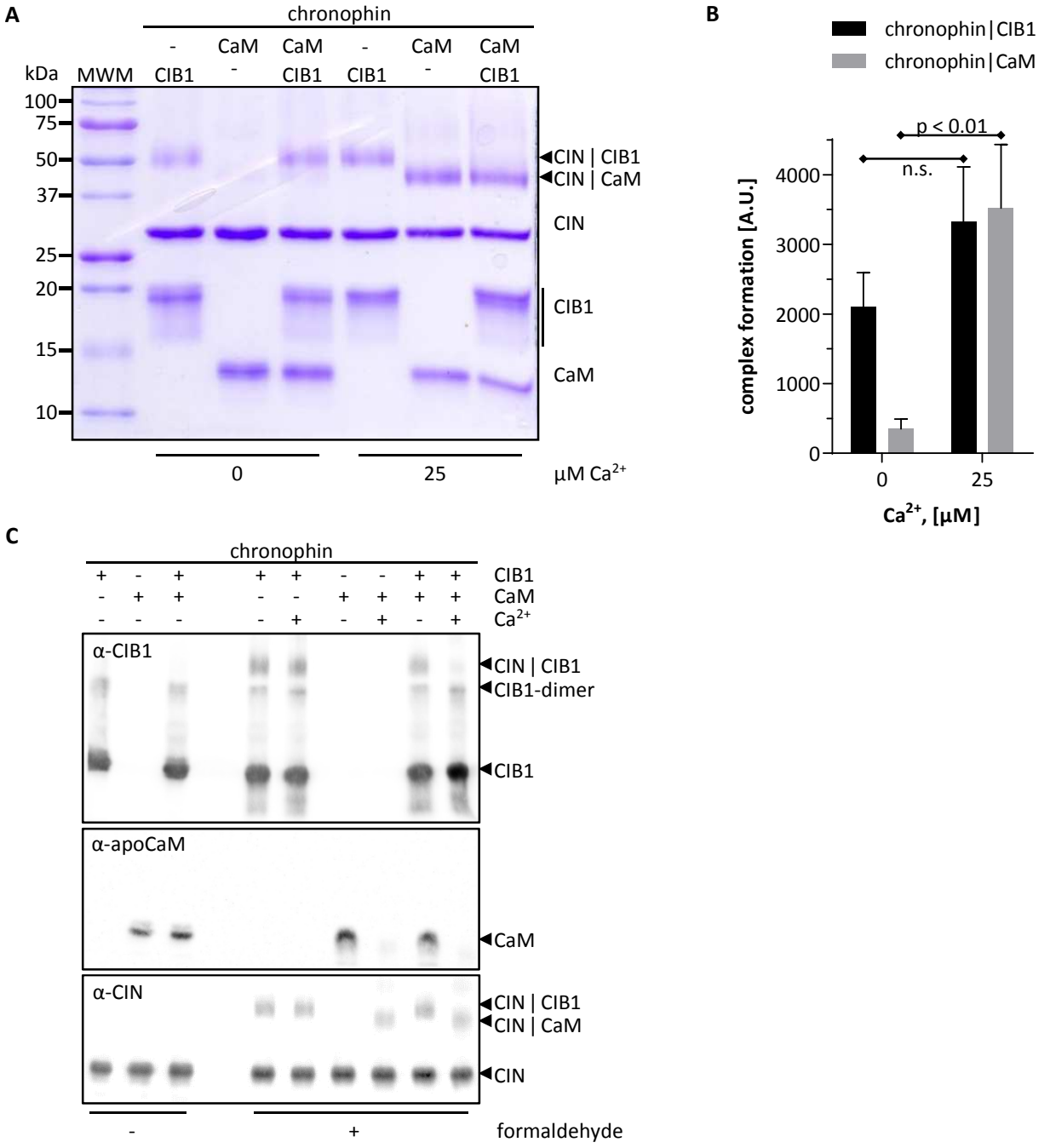

Figure 23. The effect of Ca^{2+} on the formaldehyde crosslinking of chronophin (CIN) with CIB1 and calmodulin (CaM). The experiments were conducted as described in the legend of Figure 22. A, crosslinking experiments in the absence or presence of 25µM Ca^{2+}. B, densitometric analysis of experiments performed as shown in (A). The data represent mean values ± S.E.M. of n=6. The differences of complex formation were analyzed using an unpaired, two-tailed t-test (n.s., not significant). C, the identity of the complexes could be confirmed by immunoblotting using antibodies directed against chronophin (α-CIN), CIB1 (α-CIB1) and apo-calmodulin (α-apoCaM).

The identity of the complexes could additionally be confirmed by Western blot using anti-CIB1, anti-calmodulin and anti-chronophin antibodies, as seen in Figure 23C. The employed calmodulin antibody is specific for apo-calmodulin, thus it shows no signals in crosslinking experiments conducted in the presence of Ca^{2+} (Figure 23C, lanes 7 and 9). Nevertheless, the Ca^{2+}-calmodulin/chronophin-complexes could be detected using the chronophin specific antibody. Interestingly, the chronophin dimerization was not stabilized by formaldehyde crosslinking, whereas CIB1 dimers are visible in the western blot even in the absence of crosslinker (Figure 23C, lanes 1 and 3), an observation that has been reported before [210, 211].

To analyze the Ca^{2+}-modulated complex formation between CIB1, calmodulin and chronophin of in greater detail, formaldehyde crosslinking was performed in the presence of all three proteins over a variety of Ca^{2+}-concentrations ranging from 0 (=50µM EGTA) to 25µM added $CaCl_2$. Figure 24A shows that in the absence of Ca^{2+}, a predominant CIB1/chronophin-complex formation is observable that decreases with increasing amounts of Ca^{2+}, while the calmodulin/chronophin association increases concomitantly. This result is quantified in Figure 24B, also confirming that the overall complex formation stays about the same throughout the experiment.

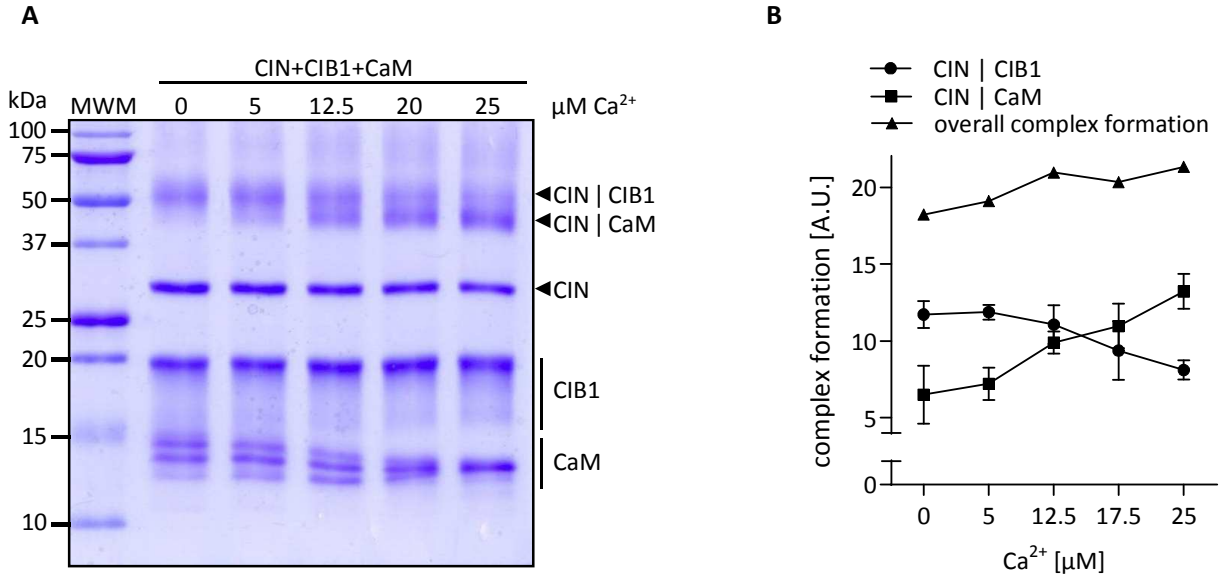

Figure 24. Calcium modulates the complex formation of chronophin, CIB1 and calmodulin. Recombinantly expressed and purified chronophin (CIN), CIB1 and calmodulin (CaM) were used together for formaldehyde crosslinking. The experiments were conducted using 5µM chronophin, 10µM CIB1 and 10µM calmodulin in the presence of 0.67% formaldehyde at different Ca^{2+}-concentrations. Complex formation was subsequently analyzed by 15% SDS-PAGE (MWM, molecular weight marker). A, Coomassie Blue-stained SDS-PAGE gel showing the effect of Ca^{2+} on the crosslinking between chronophin, CIB1 and calmodulin. At low Ca^{2+}-concentrations, calmodulin migrates as multiple bands. B, Densitometric analysis of experiments performed as shown in (A). The data represent mean values ± S.E.M. of n=3. The overall complex formation represents the sum of the chronophin-CIB1 complexes and the chronophin-calmodulin complexes at each Ca^{2+}-concentration.

Summing up, these findings are in line with the previously performed pull-down assays, indicating that CIB1 and calmodulin compete for an overlapping or even the same binding site on chronophin. Furthermore, the results suggest that Ca^{2+} may modulate the interaction between CIB1, calmodulin and chronophin by switching between a CIB1/chronophin-complex found in the absence of Ca^{2+} and a calmodulin/chronophin-complex observed at elevated Ca^{2+}-concentrations.

Finally, a CIB1 construct lacking the N-terminal 148 amino acids (Δ148CIB1) was cloned into the bacterial expression vector pETM-11 and purified in order to test whether the interaction site on CIB1, mapped by the aforementioned yeast two-hybrid screen, was sufficient to detect the interaction with chronophin by formaldehyde crosslinking. As depicted in the CIB1 crystal structure shown in Figure 25A, the Δ148CIB1 construct contains EF-hand 4 of CIB1 and the C-terminal helix of the protein. Figure 25B shows that the interaction of Δ148CIB1 with chronophin can be stabilized by formaldehyde crosslinking in a concentration-dependent manner, indicating that the C-terminus indeed contributes to the binding of chronophin. However, the crosslinking efficiency seems to be reduced, compared to full-length CIB1 or Δ8CIB1 (not shown), suggesting that additional parts of the protein might be involved in the interaction with chronophin.

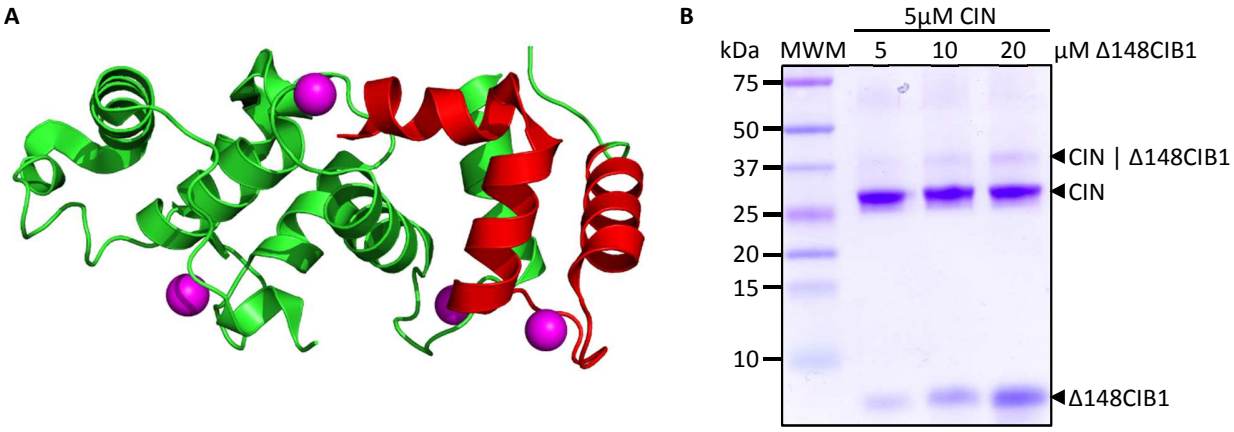

Figure 25. The C-terminal 42 residues of CIB1 are sufficient for formaldehyde crosslinking with chronophin. A, structure of CIB1 (PDB code 1XO5) highlighting residues 149 to 191 (red) that were recombinantly expressed and purified for formaldehyde crosslinking with chronophin. Ca^{2+}-ions are shown as magenta spheres. B, the crosslinking experiments were conducted using 5µM chronophin (CIN) and the indicated concentrations of Δ148CIB1 (5-20µM) in the presence of 0.67% formaldehyde. Complex formation was subsequently analyzed by 16% Tricine SDS-PAGE (MWM, molecular weight marker).

4.2.2 The chronophin-catalyzed PLP hydrolysis is not regulated by CIB1 or calmodulin

CIB1 and calmodulin mediate the regulation of a large number of enzymes, among them various kinases and phosphatases [220, 226, 235]. Therefore, the effect of CIB1 or calmodulin on the chronophin catalyzed PLP hydrolysis was studied by performing steady-state enzyme kinetic measurements using recombinantly expressed and purified proteins in an *in vitro* malachite-green based phosphatase assay. Figure 26 and Table 35 show that CIB1 or calmodulin, used in a 10-fold molar excess over chronophin, have no effect on the catalytic constants of the chronophin mediated PLP hydrolysis, irrespective of the absence or the presence of Ca^{2+}. The general increase of K_m, decrease of v_{max} and, correspondingly, k_{cat} at 100µM Ca^{2+} compared to the Ca^{2+}-free conditions is most likely due to the partial substitution of the essential cofactor Mg^{2+} with catalytically inert Ca^{2+}-ions [94, 278], leading to an inactivation of Ca^{2+}-bound chronophin.

The determined catalytic constants of murine chronophin deviate from the ones that have been previously reported for the human ortholog. According to Fonda *et al.* [70], the K_m of human chronophin towards PLP is ~1.5µM, thus ~36 times lower than the K_m determined for murine chronophin (~54µM), whereas the v_{max} values are comparable for both orthologs (~3µmol/min/mg). This might be the result of differing experimental conditions: while the experiments shown here were conducted at 22°C in a buffer (TEA, pH 7.4) containing 250mM NaCl and 5mM $MgCl_2$, the human protein was tested at 37°C in the same buffer containing no salts other than 4mM $MgCl_2$ [70] and might therefore indicate that the binding and/or hydrolysis of PLP by chronophin is salt-sensitive. The differing kinetic constants might as well reflect the adaptation of enzymatic parameters to the physiological needs of the respective species. It has been shown that vitamin B_6 vitamer plasma levels strongly vary in different animal species [279], suggesting characteristic dietary intake and metabolism of vitamin B_6. According to this publication, the plasma PLP levels range from 29nM in pigs to 2443nM in cats. Human PLP plasma concentrations have been shown to range around 55nmol/L [280], while mice exhibit PLP concentrations of ~200nmol/L in the plasma (unpublished data, Dr. E. Jeanclos).

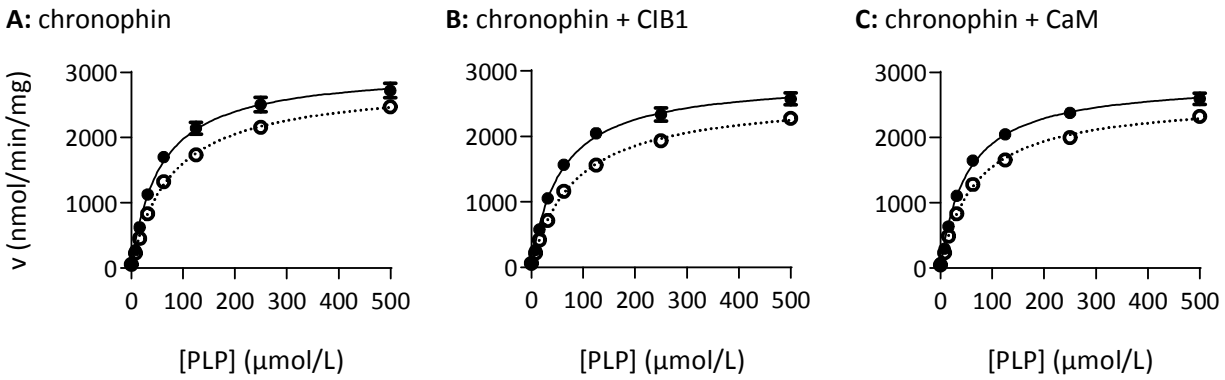

Figure 26: Effect of CIB1 or calmodulin on the chronophin-catalyzed PLP hydrolysis. The PLP dephosphorylation velocities (v) were determined as a function of substrate concentration. For this, 100nM chronophin ± 1µM CIB1 or calmodulin (CaM) were incubated with the indicated concentrations of PLP (ranging from 0-500µM) in a total volume of 50µL in the absence (solid lines) or presence of 100µM Ca^{2+} (dotted lines). The reactions were stopped after 2min by addition of 100µL malachite green, the kinetics of inorganic phosphate release were measured at 620nm and quantified using a phosphate standard. The results represent mean values ± S.E.M. of triplicates performed with three independently purified batches of protein. Most error bars are masked by the symbols.

Table 35. Effect of CIB1 and calmodulin on the kinetic constants of the chronophin catalyzed PLP hydrolysis. Kinetic measurements were conducted as shown in Figure 26. The results represent mean values ± S.E.M. of triplicates performed with three independently purified batches of protein; numbers in parentheses indicate the relative change of the kinetic constants compared to chronophin alone. K_m, Michaelis-Menten constant; v_{max}, maximum enzyme velocity; k_{cat}, turnover number; k_{cat}/K_m, specificity constant; CaM, calmodulin.

		K_m (µM)	v_{max} (µmol/min/mg)	k_{cat} (s^{-1})	k_{cat}/K_m (s^{-1} M^{-1})
1mM EGTA	chronophin	54.35 ± 4.72	3.05 ± 0.08	1.62 ± 0.04	2.98×10^4
	chronophin + CIB1	55.45 ± 4.38	2.88 ± 0.07	1.53 ± 0.04	2.76×10^4
		(102%)	(94.5%)	(94.6%)	(92.6%)
	chronophin + CaM	50.86 ± 3.17	2.88 ± 0.05	1.53 ± 0.03	3.00×10^4
		(93.6%)	(94.3%)	(94.4%)	(100.7%)
100µM Ca^{2+}	chronophin	76.35 ± 2.96	2.84 ± 0.04	1.51 ± 0.02	1.97×10^4
	chronophin + CIB1	82.12 ± 5.02	2.62 ± 0.05	1.39 ± 0.03	1.69×10^4
		(107.6%)	(92.3%)	(92.3%)	(85.8%)
	chronophin + CaM	67.55 ± 4.28	2.60 ± 0.05	1.38 ± 0.03	2.04×10^4
		(88.5%)	(91.6%)	(91.6%)	(103.6%)

4.2.3 CIB1 and calmodulin have no effect on the chronophin mediated phospho-cofilin-1 dephosphorylation

Since CIB1 and calmodulin failed to show an effect on the chronophin activity towards PLP, we hypothesized that the phospho-protein phosphatase activity of chronophin regarding phospho-cofilin-1 might be modulated by these interactors. Both proteins, CIB1 and calmodulin, have already been shown to be indirectly involved in the regulation of cofilin. CIB1 activates the p21-activated kinase 1 (PAK1) leading to an LIM-kinase 1 (LIMK1) mediated phosphorylation of cofilin-1 [220]. Calmodulin in contrast is able to promote activating dephosphorylation and deactivating phosphorylation of the cofilin-specific phosphatase slingshot 1 (SSH1) via calcineurin and the Ca^{2+}/calmodulin dependent kinase II (CaMKII), respectively [241].

In order to test the potential role of CIB1 and calmodulin in the chronophin mediated phospho-cofilin-1 dephosphorylation, recombinantly expressed and purified proteins were used for phospho-cofilin-1 dephosphorylation assays, monitored by Phos-tag SDS-PAGE. As shown in Figure 27A, no dephosphorylation of phospho-cofilin-1 could be shown with chronophin alone, and no change was observed in the presence of CIB1 and/or calmodulin under Ca^{2+}-free conditions or in the presence of 100µM Ca^{2+}. Similar experiments were conducted using different buffer conditions, yielding the same result (not shown). In contrast to this, unspecific dephosphorylation of phospho-cofilin-1 could be shown using calf intestinal alkaline phosphatase (CIP), as shown in Figure 27B.

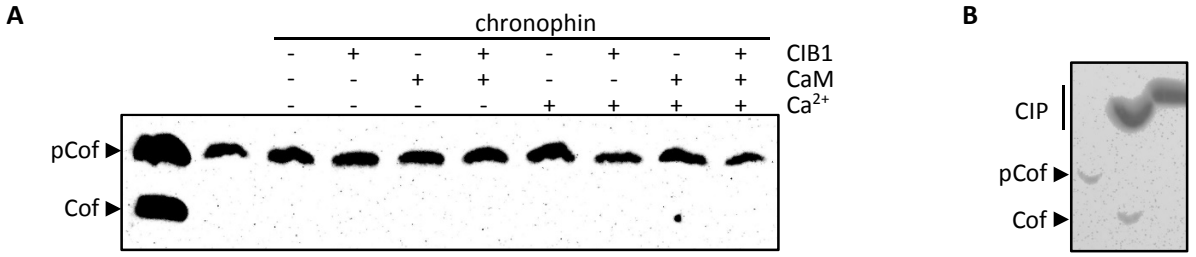

Figure 27. Effect of CIB1 and calmodulin on the chronophin mediated phospho-cofilin-1 dephosphorylation. 200-300ng phospho-cofilin-1 were used for dephosphorylation assays with 50µM chronophin ± ~300µM CIB1 and/or calmodulin in the absence or the presence of 100µM Ca^{2+} (final volume 10µL). The samples were then subjected Phos-tag SDS-PAGE and immunoblotting using a cofilin specific antibody. A, no dephosphorylation could be detected in any of the samples. As a negative control a mixture of phospho-cofilin-1 (pCof) and cofilin-1 (Cof, lane 1) and an untreated phospho-cofilin sample (lane 2) are loaded. B, calf intestine alkaline phosphatase (CIP) was used as a positive control to show unspecific dephosphorylation of phospho-cofilin-1.

4.2.4 CIB1 and calmodulin do not influence the phosphopeptide preferences of chronophin

Phosphoprotein phosphatases, such as the serine/threonine phosphoprotein phosphatase PP2A, are well known to be composed of a catalytic subunit that interacts with a variety of structurally diverse regulatory subunits via a scaffolding subunit. The regulatory subunits are thought to modulate substrate specificities of the catalytic subunit towards different substrates in spatiotemporal manner [51-54]. In order to test whether the putative chronophin interactors CIB1 and calmodulin trigger the chronophin phosphatase activity towards different protein substrates, we employed a malachite green based screen, composed of 360 phosphopeptides derived from established human phosphorylation sites (JPT Peptide Technologies GmbH). Chronophin alone showed no activity towards any of the included peptidic substrates. The presence of a 5-fold molar excess of CIB1 in the absence of Ca^{2+} or calmodulin in the presence of 100µM Ca^{2+} did not induce any preferences of chronophin towards any of the tested phosphopeptide substrates. The screen includes a peptide of human cofilin-2, an actin depolymerizing protein that is predominantly found in skeletal muscles and the heart, and that is highly homologous to the chronophin substrate cofilin-1 (~81% sequence identity). As the peptide is derived from residues 19 to 29 in cofilin-2, with the phosphorylation site being Ser^{24}, and not the chronophin target site Ser^{3}, no activity was expected here.

4.3 The role of chronophin dimerization

This section comprises the biochemical and structural analysis of the potential functional importance of chronophin dimerization. For this, C. Kestler introduced an $A^{194}K/A^{195}K$ double mutation in the dimerization interface of murine chronophin using site-directed mutagenesis. This mutant variant of chronophin, termed $chronophin^{KK}$, was subsequently confirmed to be monomeric *in vitro* and in mammalian cells using a variety of biochemical and biophysical methods. Finally, we were able to crystallize and solve the structure of the wild-type and the monomeric mutant protein, showing that the dimerization is mediated by two helices of the capping domain, which involve interactions with the substrate specificity loop. Monomerization leads to a misplacement of this loop, resulting in significantly reduced PLP-phosphatase activity and decreased binding affinities, as measured by BeF_3^--binding in isothermal titration calorimetry experiments. The results of this section have been published in [281].

4.3.1 Homo-oligomerization is a common feature among haloacid dehalogenase hydrolases

The structure of human chronophin was published in 2007 [94] showing that the protein is a homodimer. In order to analyze, whether other members of the haloacid dehalogenase (HAD) superfamily, and particularly enzymes of the C2a subfamily, tend to form homo-oligomers, the Protein Data Bank was searched for members of the HAD protein family using the Pfam entries PF13419, PF00702, PF13344, PF13242, PF08282 and PF12710. To exclude multiple entries or mutated versions of single proteins, the sequence cutoff was set to 90% identity, yielding 177 unique entries that were additionally verified by assigning the UniProt sequence identifier. The respective HAD cap-type was determined manually and cross-validated with a recent publication [282], and finally, the oligomeric state was determined using the PDBePISA online tool, which allows the calculation of probable quaternary structures, including structural and chemical properties of the macromolecular interfaces. Table 36 summarizes the results of this analysis, indicating that 104 (~59%) of the 177 structurally characterized HAD hydrolases are likely to form oligomers, as opposed to 72 monomeric structures (~41%) and a single hetero-oligomeric entry. Remarkably, only one HAD subfamily is predicted to exist exclusively as oligomers, namely the C2a subfamily that includes the phosphatase chronophin. In this subfamily, homo-dimers are the predominant oligomeric state (~71%), the residual structures are predicted to exist as homo-tetramers (~29%), formed by dimers of dimers.

Table 36. Oligomeric state of structurally characterized HAD hydrolases. The table indicates the number of structures per oligomeric state as determined by PDBePISA analysis, subdivided by structural subfamilies.

	Structural HAD subfamily					
	C0	**C1**	**C1+C2**	**C2a**	**C2b**	**Structures/oligomeric state**
Monomers	11	40	6	-	15	72
Dimers	3	43	6	12	11	75
Trimers	-	2	-	-	-	2
Tetramers	10	4	-	5	1	20
Hexamers	-	1	-	-	-	1
Octamers	4	1	-	-	-	5
Dodecamers	-	1	-	-	-	1
Heterodimers	-	1	-	-	-	1
Structures/Subfamily	**28**	**93**	**12**	**17**	**27**	**177**

4.3.2 Generation of a monomeric chronophin variant

Chronophin^{WT} and the chronophin^{KK} were recombinantly expressed in *E. coli*, purified to homogeneity and used for subsequent determination of the oligomeric state of the two proteins. Among other methods, analytical size exclusion was employed (aSEC, Figure 28), showing that chronophin^{WT} (molecular mass: 31.8kDa) has a peak elution volume of 14.9mL, corresponding to a calculated molecular mass of 60.7kDa, confirming that the protein forms stable dimers in solution. In contrast to this, chronophin^{KK} elutes at a retention volume of 16.1mL that corresponds to a calculated molecular mass of 33.7kDa, indicating that the protein is monomeric. Remarkably, the single mutations (A194K or A195K) had no influence on the oligomeric state of the protein in aSEC experiments (data not shown), emphasizing the stability of the homo-bimolecular interaction of the two protomers in the dimer.

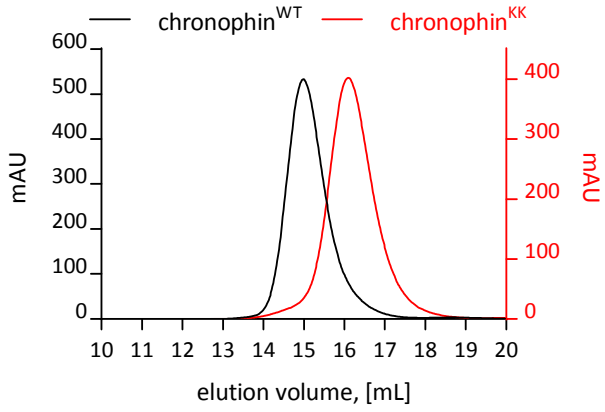

Figure 28: Analytical size exclusion chromatography of chronophin^{WT} and chronophin^{KK}. The superposed chromatograms show that chronophin^{WT} has a peak elution volume of 14.9mL corresponding to a calculated molecular mass of 60.7kDa, while the retention volume of chronophin^{KK} (16.1mL) corresponds to 33.7kDa. The theoretical molecular mass of chronophin is 31.8kDa.

To further confirm the monomeric state of chronophin^{KK}, C. Kestler performed analytical ultracentrifugation (AUC) sedimentation velocity experiments with the help of Dr. I. Tessmer, clearly demonstrating a monomeric molecular mass for the chronophin^{KK} mutant (~32kDa), while the wild-type protein showed sedimentation behavior corresponding to a dimeric state (~56kDa, Figure 29). Finally, Dr. I. Tessmer conducted atomic force microscopy (AFM) imaging studies using chronophin^{WT} and chronophin^{KK}, consistently showing considerably larger AFM volumes for the wild-type protein than for the mutant (for the procedure, see [281]). The measured AFM volumes translate into apparent molecular masses that support the predominantly dimeric state of chronophin^{WT} and monomeric state of chronophin^{KK} with molecular masses of approximately 63±18kDa or 30±13kDa, respectively (Figure 29).

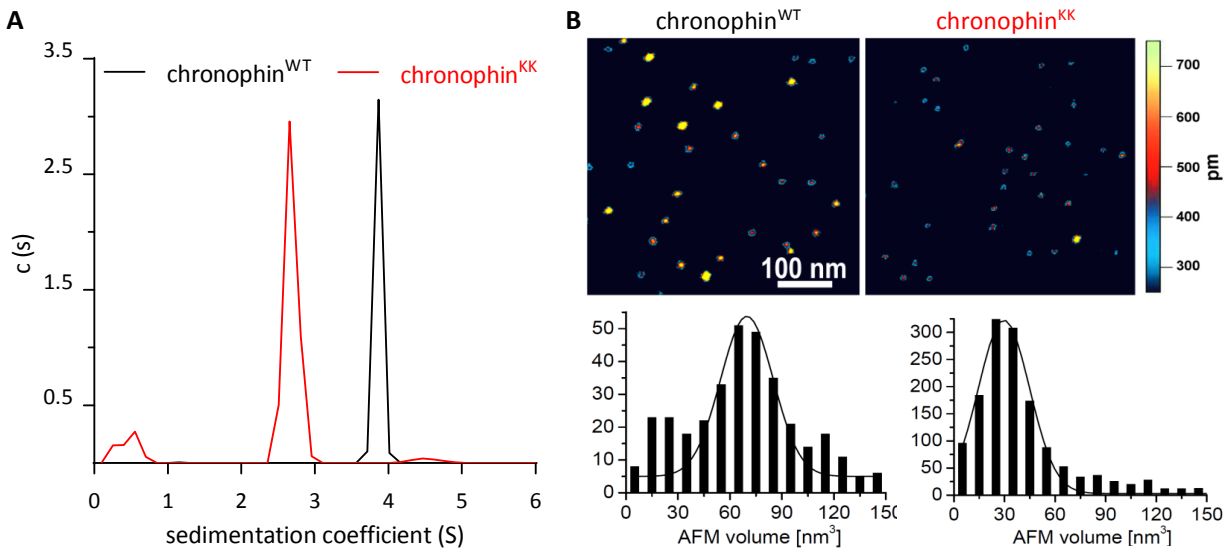

Figure 29. Analytical ultracentrifugation analysis (AUC) and atomic force microscopic (AFM) imaging of chronophin^{WT} and chronophin^{KK}. A, AUC sedimentation velocity experiments demonstrate sedimentation coefficients that correspond to calculated molecular masses of ~56kDa (dimer) for chronophin^{WT} and 32kDa (monomer) for chronophin^{KK}. Consistent results were obtained in three independent experiments. B, AFM images (top) are 500 × 500nm with a height scale of 0.75nm. Bottom, Gaussian fits to statistical volume distributions for chronophin^{WT} or chronophin^{KK} give maxima of 70 nm^3 (337 particles) or 30 nm^3 (1409 particles), respectively, which translate into molecular masses of 63 kDa or 30 kDa. A fraction of chronophin^{WT} also shows protein volumes consistent with a monomeric state.

Taken together, the three independent methods used to determine the oligomeric state of murine chronophin^{WT} and the chronophin^{KK} double mutant indicate that the wild-type protein indeed forms a homodimer in solution, as already implied by the crystal structure of the human (and murine) protein. The replacement of two adjacent small, uncharged alanines for bulky, positively charged lysines at position 194 and 195 in the murine chronophin dimer interface was necessary to create a monomeric variant of this phosphatase, while the single mutations were not sufficient to interfere with the homodimeric interaction.

4.3.3 Chronophin^{KK} is a monomer in mammalian cells

The analysis of the oligomeric states of chronophin^{WT} and chronophin^{KK} in mammalian cells was performed by C. Kestler. For this, HEK293-AD cells were co-transfected with GST-tagged and untagged variants of chronophin^{WT} and chronophin^{KK}, respectively. The cell lysates were used for pull-down assays with glutathione-sepharose, the proteins bound to the beads were separated by SDS-PAGE and subsequently analyzed by Western blotting using a chronophin-specific antibody [281]. As shown in Figure 30A, GST-chronophin^{WT} is able to co-precipitate untagged chronophin^{WT} from cell lysates of HEK293-AD

cells transfected with both proteins, whereas no association of GST-chronophin^{KK} with untagged chronophin^{KK} is detectable in the pull-down. The whole cell lysates are shown in Figure 30B, demonstrating that the amounts of protein in GST-chronophin^{WT}/chronophin^{WT}- and GST-chronophin^{KK}/chronophin^{KK}-expressing cells were comparable. The quantification of four independently performed pull-down experiments is depicted in Figure 30C, and the statistical analysis revealed that the amount of untagged chronophin pulled down by GST-chronophin is significantly smaller for chronophin^{KK} ($p<0.01$). This result is in line with the *in vitro* studies, clearly showing that chronophin^{KK} is monomeric, not only *in vitro* as a recombinantly expressed and purified protein, but also in mammalian cells.

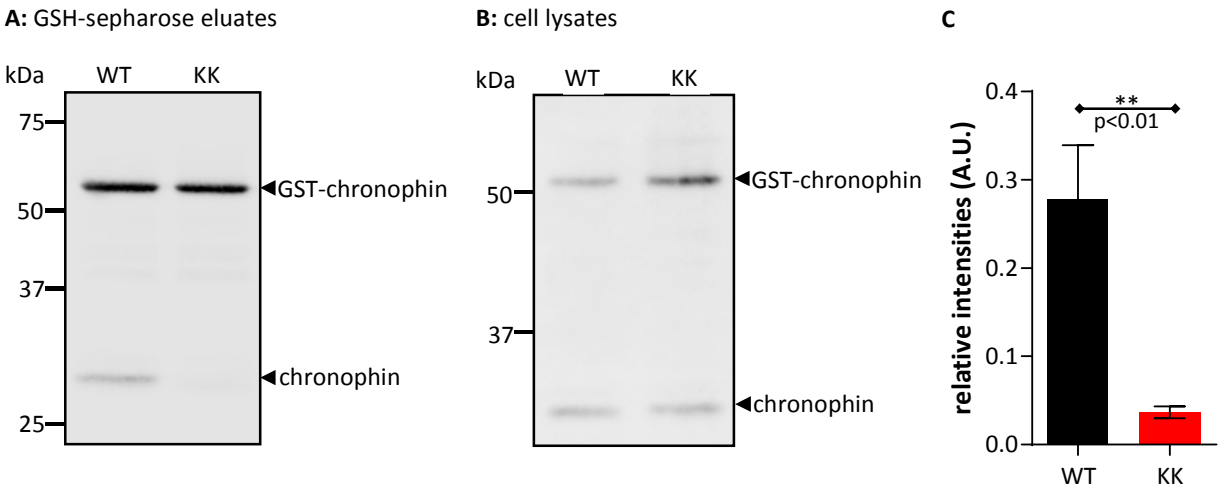

Figure 30. GST pull-down experiments. GST-tagged and untagged versions of chronophin^{WT} or chronophin^{KK} were co-expressed in HEK293-AD cells, and the lysates were used for glutathione-sepharose co-precipitation experiments. Bead-associated proteins were separated by SDS-PAGE and blotted for detection with chronophin-specific antibodies, showing that (A) GST-chronophin^{WT} is able to co-precipitate untagged chronophin^{WT}, while GST-chronophin^{KK} does not bind to untagged chronophin^{KK} in cells. B, representative Western-blot of the cell lysates shows that the protein expression levels are comparable in chronophin^{WT} and chronophin^{KK} expressing cells. C, Densitometric quantification of the Western-blots. The untagged chronophin signals were normalized to the respective GST-chronophin signal. The relative intensities of 4 independent experiments are shown as mean values ± S.E.M., indicating that significantly more untagged chronophin^{WT} can be co-precipitated with GST-chronophin^{WT}, than untagged chronophin^{KK} with GST-chronophin^{KK}.

4.3.4 Enzymatic characterization of monomeric chronophin

To investigate the effect of monomerization on the chronophin^{KK} mutant phosphatase activity, kinetic measurements were performed using pyridoxal 5'-phosphate (PLP) as a substrate of chronophin. The phosphate monoester hydrolysis was monitored colorimetrically by measuring free phosphate release using a modified malachite green assay. Figure 31 demonstrates that the catalytic activity of monomeric chronophin^{KK} is strongly reduced, while the homodimeric wild-type enzyme efficiently dephosphorylates PLP. The kinetic constants of the chronophin^{WT}- and chronophin^{KK}-catalyzed PLP hydrolysis are summarized in Table 37, showing that the impaired catalysis of chronophin^{KK} is mainly due to a ~65-fold increase in the K_m, whereas the v_{max} remains largely unaffected. This results in a drastic reduction of the chronophin^{KK} catalytic efficiency (k_{cat}/K_m) down to 3.53% compared to the wild-type protein.

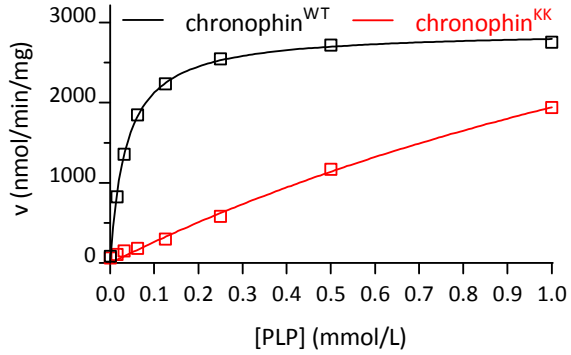

Figure 31. Kinetic analysis of the chronophin^{KK} phosphatase activity in comparison to chronophin^{WT}. The PLP dephosphorylation velocities (v) were determined as a function of substrate concentration. Purified, recombinant chronophin^{WT} or chronophin^{KK} (100nM per well) were incubated with the indicated concentrations of PLP ranging from 0-1mM in a total volume of 50µL. The reactions were stopped after 2min by addition of 100µL malachite green, the kinetics of inorganic phosphate release were measured at 620nm and quantified using a phosphate standard. The results represent mean values ± S.E.M. of three independent experiments performed with three independently purified batches of protein. The error bars are masked by the symbols.

Table 37. Kinetic constants of chronophin^{WT}- and chronophin^{KK}-catalyzed PLP hydrolysis. The PLP dephosphorylation velocities were measured as a function of substrate concentrations by incubating 100nM chronophin^{WT} or chronophin^{KK} with different concentrations of PLP ranging from 0-1mM in a total volume of 50µL. The reactions were stopped after 2min by addition of 100µL malachite green, the kinetics of inorganic phosphate release were measured at 620nm and quantified using a phosphate standard. The data shown are means ± S.E.M. of three independent experiments performed using three independently purified batches of proteins. K_m, Michaelis-Menten constant; v_{max}, maximum enzyme velocity; k_{cat}, turnover number; k_{cat}/K_m, specificity constant. The k_{cat} values were calculated from v_{max} using molecular masses of 31.828kDa for chronophin^{WT} and 31.942kDa for chronophin^{KK}.

	chronophin^{WT}	**chronophin^{KK}**
K_m (µM)	36.22 ± 1.15	2387 ± 492
v_{max} (nmol/min/mg)	2895 ± 21.19	6582 ± 1027
k_{cat} (s^{-1})	1.54 ± 0.01	3.50 ± 0.55
k_{cat}/K_m (s^{-1} M^{-1})	4.25×10^4	0.15×10^4

4.3.5 Isothermal titration calorimetry of BeF_3^- binding to chronophin^{KK} and chronophin^{WT}

The kinetic analysis of chronophin^{KK} revealed that the catalytic efficiency of the monomeric chronophin mutant is significantly reduced compared to the homodimeric wild-type enzyme. This result could be attributed particularly to a ~65-fold increase of the K_m-value of chronophin^{KK}, whereas the effect on the v_{max} was comparatively low (~2.3-fold increase). The K_m of an enzyme is highly dependent on the binding affinity of an enzyme towards the substrate, but also on the velocity of the reaction and the release of the product(s). To test whether the reduced enzymatic activity of chronophin^{KK} was due to impaired binding rather than due to lowered catalytic activity as a result of misfolding of the catalytic core, we analyzed the binding parameters of BeF_3^- interacting with chronophin^{WT} and chronophin^{KK} by isothermal titration calorimetry (ITC). We were not able to measure the binding of the substrate PLP, since the replacement of the essential cofactor Mg^{2+} by the catalytically inert Ca^{2+} was incomplete even at high Ca^{2+}-concentrations, resulting in residual heat release from substrate hydrolysis which made the interpretation of the binding data impossible.

Instead, we used BeF_3^-, a non-specific inhibitor of HAD phosphatases that structurally mimics their phosphoaspartate transition state [283]. Specifically, BeF_3^- acts as a phosphate analog bound to the active site aspartate and to the other catalytic core residues distributed over the highly conserved signature motifs I-IV, and it is also coordinated to the catalytically essential Mg^{2+} [283]. Functional studies have shown that BeF_3^- binding not only induces the same conformational changes as phosphorylation, but also leads to downstream signaling [284]. These characteristics make BeF_3^- ideally suited to probe the three-dimensional architecture of active site residues in HAD phosphatases [283, 285, 286].

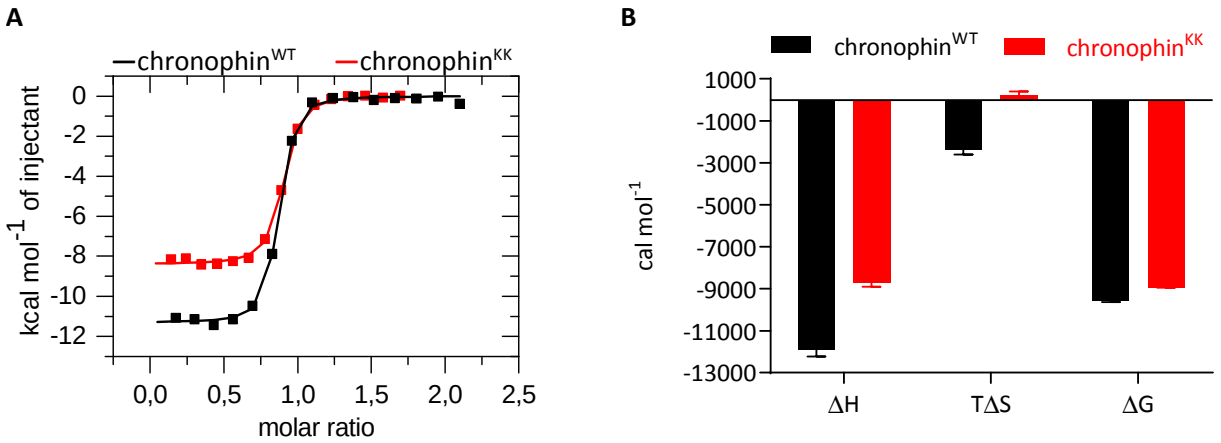

Figure 32. Isothermal titration calorimetry of BeF_3^- binding to chronophin^{WT} and chronophin^{KK}. A, Binding isotherms of BeF_3^- titrated into chronophin^{WT} (■) or chronophin^{KK} (■). Measured binding enthalpies are plotted as a function of the molar ratio of BeF_3^- to the respective chronophin variant. B, Thermodynamic profile of BeF_3^- binding to chronophin^{WT} or to chronophin^{KK}.

Figure 32A shows that the interaction of BeF_3^- with chronophin^{WT} and chronophin^{KK} can be optimally fitted to a one-site binding model, resulting in significantly different BeF_3^- dissociation constants (K_d) of 78.3 ± 13.35 nM for chronophin^{WT} and 215.3 ± 7.17 nM for chronophin^{KK}. The stoichiometry of the binding is 0.87 for chronophin^{WT} and 0.84 for chronophin^{KK}, suggesting that as expected one molecule BeF_3^- binds to one protein molecule. The deviation from the 1:1 binding ratio can be explained by inaccurate concentration determination of the samples or issues excluding a sub-population of the samples from binding, e.g. protein precipitation during the experiment. Interestingly, the quantity of released heat (ΔH) and the entropic contribution (ΔS) upon ligand binding differ significantly (Figure 32B), resulting in similar, though statistically significant different ΔG values, calculated as $\Delta G = \Delta H - T*\Delta S$, with T = 293.15 K. The binding constants including statistical analyses are summarized in Table 38.

Table 38. ITC derived binding constants of BeF_3^- binding to chronophin^{WT} or chronophin^{KK}. The data are mean values ± S.E.M. of three independent isothermal titration calorimetry experiments conducted with three independently purified batches of proteins. ΔH, enthalpy; T·ΔS, entropy; N, stoichiometry; ΔG, free Gibbs enthalpy; K_d, dissociation constant; n.d., not determined.

	chronophin^{WT}	**chronophin^{KK}**	***p*-value**
ΔH [cal·mol^{-1}]	-11920 ± 325	-8719 ± 196	0.0011
T·ΔS [cal·mol^{-1}]	-2368 ± 233	225 ± 177	0.0009
N	0.87 ± 0.03	0.84 ± 0.01	n.d.
ΔG [cal·mol^{-1}]	-9549 ± 95	-8945 ± 22	0.0034
K_d [nM]	78 ± 13	215 ± 7	0.0008

4.3.6 Structural comparison of murine chronophin^{WT} and chronophin^{KK}

The crystal structure of human chronophin has been solved in 2007 [94]. During this Ph.D. thesis work, I was able to solve the structure of the murine ortholog by crystallizing the recombinantly expressed and purified protein at ~10mg/mL in 0.1M imidazole (pH 8.0), 0.2M NaCl and 1M Na-tartrate; the cubic crystals appeared within 24 hours. Chronophin^{WT} crystallized in space group I23 and the dataset was collected at beamline 14.1 of the "Berlin Electron Storage Ring Society for Synchrotron Radiation" (BESSY, Berlin). The structure was solved by molecular replacement using the human ortholog (PDB code 2OYC) as search model, and subsequently refined to 2.2Å resolution with an R_{cryst} of 17.1% and an R_{free} of 20.7%. The data collection and refinement statistics of the chronophin^{WT} structure (PDB code 4BX3) are summarized in Table 39.

Murine chronophin and its human ortholog share a high degree of sequence homology (91.2% sequence identity), thus it is not surprising that the two crystal structures exhibit a high structural homology, as displayed in Figure 33. The overlay of murine and human chronophin shows almost perfect superposition, also displayed by an r.m.s.d. of ~0.6Å when all the Cα atoms of human (PDB code 2OYC) and murine (PDB code 4BX3) chronophin are aligned. The only exceptions are found in unstructured regions that often tend to be very flexible. Human chronophin is four amino acids longer than the murine ortholog. These additional residues are inserted in an unstructured loop that expands from Ala^{130} to Arg^{138} (Arg^{142} in human chronophin). Both, the human and the murine structures, show a conserved dimerization mode, mainly mediated by helices α6, α7 and also involving contacts to the substrate specificity loop.

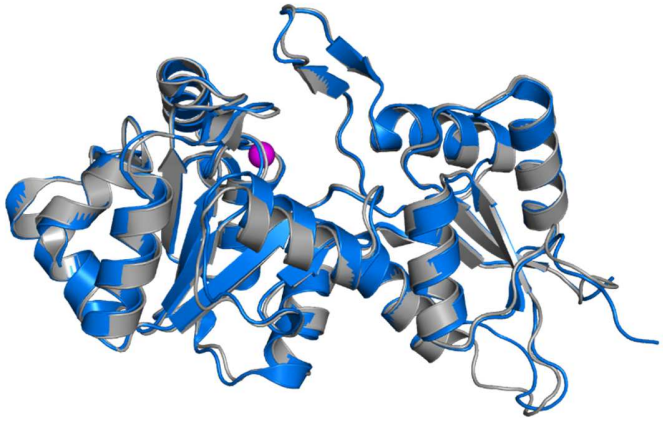

Figure 33. Superposition of murine and human chronophin. For simplification, only single protomers of the respective homodimeric proteins are displayed as cartoon representation. Murine chronophin (PDB code 4BX3) is shown in gray, human chronophin (PDB code 2OYC) in blue. The r.m.s.d. of the aligned Cα atoms is ~0.6Å. The position of the active site is indicated by the cofactor Mg^{2+} (magenta sphere).

Next, the structure of the monomeric mutant chronophin^{KK} was solved (together with C. Kestler), hoping to understand on a structural level, how dimerization of chronophin contributes to proper PLP-phosphatase function. For this, the monomeric mutant protein was expressed in *E. coli*, purified to homogeneity and crystallized at ~10mg/mL in 0.1M MES (pH 6.5) supplemented with 25% PEG MME 550. The crystals appeared after 1-2 days as thin plates that were clustered in most cases, excluding a majority of the crystals from diffraction experiments. A dataset of a single chronophin^{KK} crystal was collected at beamline 14.1 of the BESSY (Berlin). The protein crystallizes in space group P2 and was refined at 1.75Å resolution with an R_{cryst} of 19.1% and an R_{free} of 23.6% (for dataset and refinement statistics, see Table 39). An alignment of the wild-type protein and chronophin^{KK} revealed that the insertion of the $A^{194}K/A^{195}K$ double mutation in helix α7 of the dimer interface had no major impact on the fold of the protein (Figure 35A), additionally affirmed by an overall r.m.s.d. of ~0.48Å. The overall r.m.s.d. between the two protomers in the murine wild-type crystal structure is 0.32Å, suggesting that the mutations, resulting in a monomerization of chronophin, induce only minor structural rearrangements in chronophin. The only obvious difference between the two structures is the positioning of the substrate specificity loop that is tilted by ~25° towards the entrance of the active site in chronophin^{KK} compared to chronophin^{WT}, as measured between the Cα atoms of Asp^{182} and Pro^{187} of the respective molecules (see boxes in Figure

35A). This rearrangement of the substrate specificity loop results in a misplacement of His^{178}, a residue that has been shown to be of major importance for the coordination of the phosphatase's physiological substrate pyridoxal 5'-phosphate [94], as depicted in Figure 35B. This implies that the dimerization is crucial for the correct positioning of the substrate specificity loop, particularly due to the π-electron stacking of Trp^{177} and Arg^{185} of one protomer with Arg^{167} of the other protomer. This Arg^{167} additionally forms a hydrogen bond with the backbone carbonyl oxygen of Gly^{183} of this first protomer (Figure 35C). The abolishment of these interactions by monomerization of the physiological homodimer leads to a misplacement of the substrate specificity loop in chronophin^{KK}, causing a reorientation of the PLP-coordinating residue His^{178}, in turn resulting in a reduced PLP-phosphatase activity.

The missing interactions of the substrate specificity loop with the other protomer in the dimer might lead to a destabilization of this structural element. To test whether monomerization leads to an increased flexibility of the substrate specificity loop, the B-factors of residues Asp^{175} to Gly^{188} were analyzed. The B-factor, or temperature factor, is a measure of the positional uncertainty of each atom in the structure. The individual value increases with increasing thermal motion of the atoms, indicating flexibility of the structural element. Figure 34 shows that the individual B-factors of residue Asp^{175} to Gly^{188} (b_{res}), corrected for the average B-factor (b_{ave}) of the respective protein chain, do not deviate substantially between chronophin^{KK} and chronophin^{WT}, indicating that monomerization does not lead to increased flexibility of the substrate specificity loop.

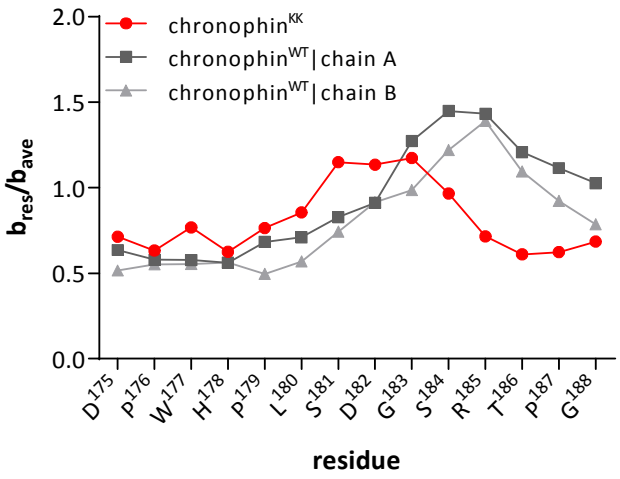

Figure 34. B-factor comparison of the chronophin^{KK} and the chronophin^{WT} substrate specificity loop. The individual B-factors (b_{res}) of residues D^{175} to G^{188} are shown as a quotient of the average B-factor (b_{ave}) of the respective protein to compensate for the resolution differences between the two structures.

To ascertain that monomerization has no effect on the orientation of the catalytic core residues of HAD motifs I-IV, the structures of chronophin^{WT} and chronophin^{KK} were compared with a chronophin^{WT} structure in complex with BeF_3^-, an unspecific HAD hydrolase inhibitor that mimics the phosphoaspartate transition state during catalysis [283]. Thus, BeF_3^- engages all catalytic core residues of the HAD signature motifs and the cofactor Mg^{2+} involved in substrate binding, showing them in their functional orientation. This makes BeF_3^- an ideal reporter for the structural integrity of HAD hydrolase active sites [283, 285, 286].

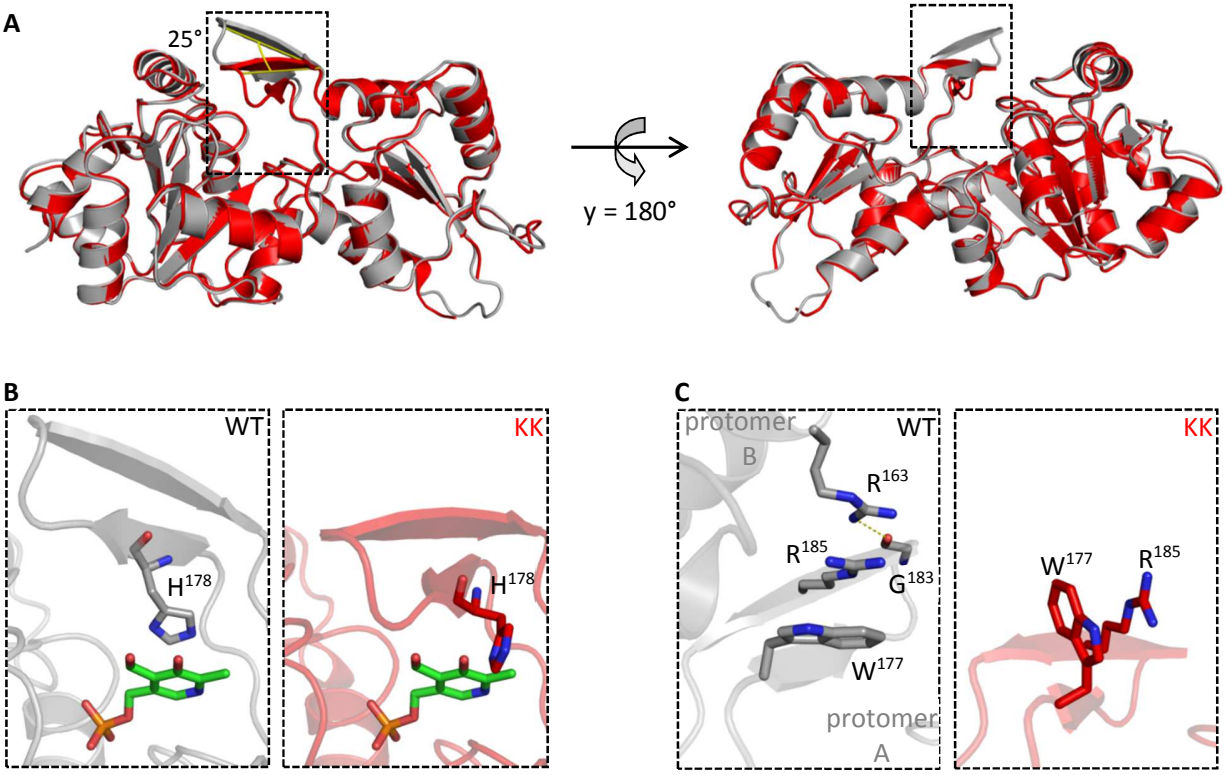

Figure 35. Structural comparison of murine chronophin^{WT} with the monomeric chronophin^{KK}. A, Cartoon representation of chronophin^{WT} (PDB code 4BX3, gray) and chronophin^{KK} (PDB code 4BX0, red) superimposed. The substrate specificity loop of chronophin^{KK} is tilted by ~25°, as measured between the Cα atoms of Asp^{182} and Pro^{187} of the respective molecules (see boxes). B, Detailed view of the substrate specificity loop with PLP (green) introduced from PDB code 2P69 for visualization purposes. The orientation of His^{178} in chronophin^{WT} (left panel, gray) allows the coordination of PLP by π-electron stacking of the histidine side chain with the pyridine ring of PLP. The misplacement of the substrate specificity loop in chronophin^{KK} (right panel, red) leads to a reorientation of His^{178} into a position with the imidazole side chain almost perpendicular to the pyridine ring of PLP. C, Back view of the substrate specificity loops shown in B reveals that in chronophin^{WT} (right panel, gray) Trp^{177} and Arg^{185} of protomer A stack together with Arg^{163} of protomer B. Arg^{163} additionally forms a hydrogen bond with the backbone carbonyl oxygen of Gly^{183} in protomer A. These interactions contribute to the homodimerization interface and are absent in the monomeric chronophin^{KK} (right panel, red).

For the structural analysis, recombinantly expressed and purified chronophin^{WT} was co-crystallized at ~10mg/mL with 1mM BeF_3^- in 0.1M imidazole (pH 8.0), 0.2M NaCl and 1M sodium-tartrate. The protein crystallized within 24 hours in a more rounded crystal form than the chronophin^{WT} crystals without BeF_3^-. A dataset was collected at the beamline 14.1 of the BESSY (Berlin). Chronophin^{WT} with bound BeF_3^- crystallized in space group I23, the structure was solved by molecular replacement using the human chronophin ortholog (PDB code 2OYC) as search model, and subsequently refined to 2.2Å resolution with an R_{cryst} of 16.8% and an R_{free} of 21.2%. The data collection and refinement statistics of the chronophin^{WT} structure with bound BeF_3^- (PDB code 4BX2) are summarized in Table 39.

Figure 36 depicts a superposition of chronophin^{WT}, chronophin^{WT} in complex with BeF_3^- and chronophin^{KK}, indicating that the catalytic core residues of the monomeric chronophin mutant as well as the essential cofactor Mg^{2+} are oriented correctly. This suggests that the reduced catalytic PLP-phosphatase activity (Figure 31, Table 37) and decreased binding of BeF_3^- (Figure 32, Table 38) of chronophin^{KK} is not a result of structural rearrangements in the catalytic site due to the introduced mutations, but rather an allosteric effect mediated by the dimerization that possibly diminishes the accessibility of the active site and leads to a mispositioning of the PLP-coordinating residue His^{178}.

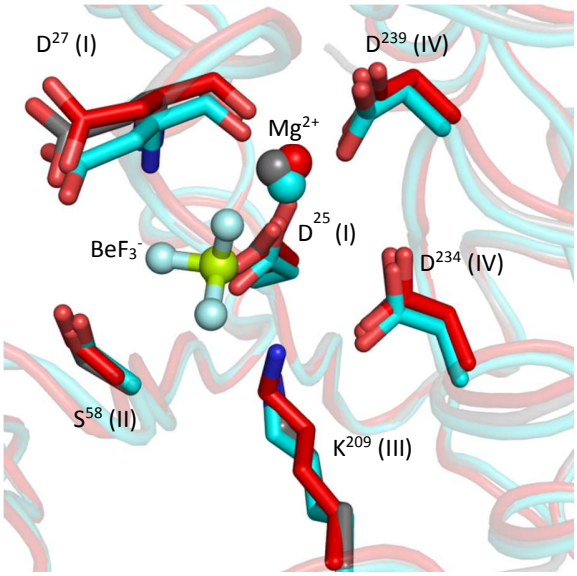

Figure 36. The catalytic core residues are unaltered by monomerization. Superposition of the catalytic core residues of chronophin^{WT} (gray, PDB code 4BX3), chronophin^{WT} in complex with BeF_3^- (cyan, PDB code 4BX2) and chronophin^{KK} (red, PDB code 4BX0) shows no substantial rearrangements in the catalytically essential HAD motifs I-IV.

Table 39. Chronophin data collection and refinement statistics.

Data collection	**chronophin^{WT}**	**chronophin^{WT} · BeF_3^-**	**chronophin^{KK}**
Wavelength (Å)	0.91841	0.91841	0.91841
Space group	I23	I23	P2
Unit cell parameters			
a, b, c (Å)	167.10, 167.10, 167.10	166.83, 166.83, 166.83	36.13, 91.82, 39.19
α, β, γ (°)	90.00, 90.00, 90.00	90.00, 90.00, 90.00	90.00, 98.28, 90.00
Resolution range (Å) [a]	44.659 - 2.193 (2.31 - 2.19)	44.587 - 2.193 (2.31 - 2.19)	33.32 - 1.75 (1.84 - 1.75)
R_{sym} [b]	0.082 (0.858)	0.116 (1.12)	0.093 (0.658)
$R_{p.i.m.}$ [c]	0.034 (0.358)	0.048 (0.472)	0.049 (0.347)
<I / sI> [d]	12.9 (2.2)	10.2 (1.8)	10.2 (2.3)
Completeness (%)	99.9 (99.7)	100 (100)	99.8 (99.9)
Multiplicity	6.8 (6.7)	6.7 (6.6)	3.5 (3.5)
Total reflections	269875	266023	89076
Unique reflections	39743 (5736)	39582 (5743)	25494 (3709)
Refinement			
Wilson B-factor (Å²)	47.02	41.096	19.09
Average B-factor (Å²)	48.38	45.53	28.6
macromolecules	48.69	45.80	27.99
solvent	40.58	39.17	34.24
R_{cryst} [e]	0.1707	0.1678	0.1913
R_{free} [e]	0.2067	0.2123	0.2363
Number of non H-atoms	4645	4676	2496
macromolecules	4453	4460	2247
ligands	14	28	7
water	178	188	242
R.m.s. deviations in			
bond lengths (Å)	0.015	0.014	0.005
bond angles (°)	1.640	1.567	1.006
planar groups (Å)	0.010	0.010	0.004
dihedral angles (°)	15.91	15.309	13.137
Coordinate error (Å) [f]	0.25	0.27	0.28
Ramachandran statistics [g]			
favored (%)	96.92	98.29	99.32
allowed (%)	2.22	1.54	0.34
outliers (%)	0.85	0.17	0.34
MolProbity clashscore [h]	9.83	11.83	11.63

[a] Numbers in parentheses refer to the respective highest resolution data shell in the data set.

[b] $R_{sym} = \Sigma_{hkl}\Sigma_i|I_i - < I >|/\Sigma_{hkl}\Sigma_i I_i$, where I_i is the i^{th} measurement, and $< I >$ is the weighted mean of all measurements of I.

[c] $R_{p.i.m.} = \Sigma_{hkl}\,(1/(n-1))^{1/2}\,\Sigma_i|I_i - < I >|/\Sigma_{hkl}\Sigma_i I_i$, where n is the multiplicity of the observed reflection.

[d] *<I /sigI>*: Indicates the average of the intensity divided by its S.D. value.

[e] $R_{cryst} = \Sigma|F_o - F_c|/\Sigma|F_o|$ where F_o and F_c are the observed and calculated structure factor amplitudes. R_{free}, same as R_{cryst} for 5% of the data randomly omitted from the refinement.

[f] Estimated coordinate error based on R_{free}.

[g] Ramachandran statistics indicate the fraction of residues in the favored, allowed and disallowed regions of the Ramachandran diagram, as defined by MolProbity [6].

[h] number of serious clashes per 1000 atoms (Reference: see [g]).

4.3.7 Dimerization as a potential general mechanism regulating the specificity of C2a-type HAD hydrolases

The previous results have shown that the homo-dimerization of chronophin is a prerequisite for proper enzymatic function, and the structural analysis revealed that the dimerization is crucial for the correct positioning of the substrate specificity loop, which harbors the PLP-coordinating His^{178} residue. In the monomeric mutant $chronophin^{KK}$, the substrate specificity loop is tilted by ~25°, resulting in reduced accessibility of the active site, poor coordination of PLP, and therefore in reduced catalytic activity towards this substrate and decreased affinity for BeF_3^-. Taken together with our bioinformatic analysis, which shows that all C2a subfamily HAD hydrolases are likely to form homo-dimers or homo-tetramers (dimers of dimers), the question arises whether the found mechanism of homophilic allosteric regulation is a unique feature of chronophin or if it is a general characteristic of C2a capped HAD hydrolases. To approach this question, a protein structure database search using the DALI server was conducted with human chronophin as query protein. The retrieved C2a subfamily members were cross-validated with the structures listed in Table 36, confirming that to date 16 structures of C2a capped HAD hydrolases are available in addition to human chronophin and the newly solved murine chronophin structure. Strikingly, all structures thus identified show a high degree of homology on the structural level (Figure 37), additionally indicated by the generally low r.m.s.d. values (Table 40), when the individual structure's Cα atoms are aligned with murine chronophin (PDB entry 4BX3). The sequence identities, however, are comparatively low and range from 16.1 to 28.3%, when compared to the murine chronophin sequence. The only exception is human chronophin, sharing 91.2% sequence identity with its murine ortholog.

Despite the low sequence identity, the mode of dimerization seems to be conserved in all C2a-capped HAD hydrolases, involving two homologous α-helices and a β-hairpin structure that resembles the substrate specificity loop of chronophin. According to the PDBePISA analysis, the buried surface area of the dimer interface covers ~1000Å² (Table 40). The detailed homo-dimer interfaces of the structurally characterized C2a capped HAD hydrolases are depicted in Figure 38, emphasizing the structural similarity of the C2a-type HAD hydrolase dimer interfaces. Two of the depicted structures (3RF6 and 2C4N) apparently contain an unstructured loop instead of a β-hairpin homologous to the substrate specificity loop of chronophin. A closer structural analysis revealed that the loops contain hydrogen bonds between the strands that are not adjacent to each other, hence they are not shown as β-sheets by the automatic secondary structure assignment of PyMol. However, all of the identified loops/β-hairpins participate in the dimer formation and might therefore be involved in the allosteric control of catalytic function and substrate specificity through dimerization.

Considering that all structurally characterized C2a-type HAD hydrolases are likely to form dimers (Table 40), and given the fact that all contain a structural element homologous to the substrate specificity loop of chronophin (Figure 6), one might conclude that dimerization is a prerequisite for proper enzymatic function, by ensuring correct positioning of specificity determinants through homo-dimerization.

Table 40. Oligomeric states of the structurally characterized C2a-type HAD hydrolases. The putative oligomeric state of the respective C2a-type HAD hydrolases including the buried surface areas and Δ^iG were calculated using the PDBe PISA online tool. [1]Δ^iG gives the solvation-free energy gain upon interface formation, calculated as the difference in total solvation energies of isolated and interfacing structures. Negative Δ^iG values indicate hydrophobic interfaces, or positive protein affinity. This value does not take the effect of satisfied hydrogen bonds and salt bridges across the interface into account [264]. [2]Values in italics correspond to possible tetramer interfaces. The shown r.m.s.d. values were calculated by aligning the Cα atoms of the respective structure with murine chronophin (PDB code 4BX3) in PyMol.

UniProtKG (PDB code)	organism	r.m.s.d. compared to 4BX3, [Å]	Dimer interface [Å²] (Δ^iG,[kcal/mol])[1,2]
Q96GD0 (2OYC)	*Homo sapiens*	0.67	1035.6 (-16.4)
Q9H008 (2X4D)	*Homo sapiens*	2.17	1306.8 (-17.9)
Q9H0R4 (3HLT)	*Homo sapiens*	2.47	1314.9 (-13.9)
P60487 (4BX3)	*Mus musculus*	-	992 (-14.7)
Q3UGR5 (2HO4)	*Mus musculus*	3.08	1299.5 (-13.6)
P36151 (3RF6)	*Saccharomyces cerevisiae*	10.61	1866.3 (-25.7)
O32125 (3PDW)	*Bacillus subtilis*	2.69	1202.7 (-15.3)
Q11S56 (2HX1)	*Cytophaga hutchinsonii ATCC 33406*	2.44	979.8 (-13.7)
			1273.2 (-5.2)
Q836C7 (1YV9)	*Enterococcus faecalis V583*	1.66	1151.2 (-12.2)
P0AF24 (2C4N)	*Escherichia coli K-12*	2.02	1097.3 (-23.8)
			1071.5 (-6.6)
L7N4Y2 (4I9F)	*Mycobacterium tuberculosis*	2.31	1146.3 (-19.6)
O59622 (1ZJJ)	*Pyrococcus horikoshii OT3*	1.78	1161.8 (-18.9)
Q8E044 (3EPR)	*Streptococcus agalactiae*	1.69	1142.6 (-12.9)
			1048.2 (-5.8)
Q8DTD6 (1WVI)	*Streptococcus mutans UA159*	1.94	1156.7 (-15.3)
			955.3 (-4.3)
Q97Q24 (1YDF)	*Streptococcus pneumoniae*	2.13	1079.6 (-12.7)
Q99ZW4 (1YS9)	*Streptococcus pyogenes*	1.67	1185.4 (-14.1)
			867.8 (-4.8)
Q9X264 (1VJR)	*Thermotoga maritima*	1.91	1032.5 (-14.7)
O29873 (3QGM)	*Archaeoglobus fulgidus*	1.71	1314.8 (-23.8)

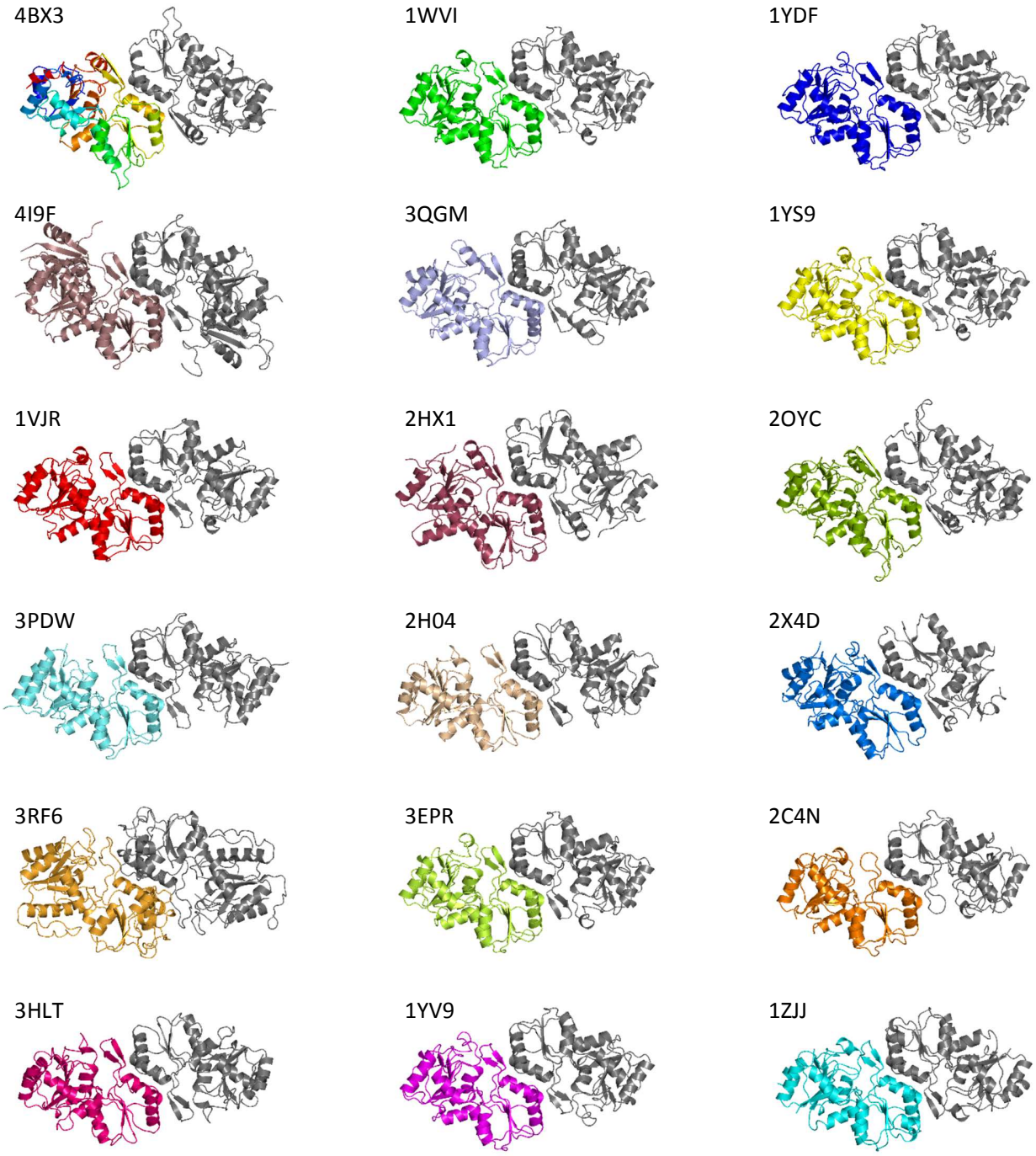

Figure 37. Overview of the structurally characterized C2a-type HAD hydrolases. The structures are shown in the same orientation as cartoon representations with one protomer colored, the other one in gray. 4BX3: chronophin/PDXP (M. musculus), 1WVI: putative phosphatase (S. mutans), 1YDF: hypothetical protein/HAD-like phosphatase (S. pneumoniae), 4I9F: glycerol-3-phosphate phosphatase (M. tuberculosis), 3QGM: p-nitrophenol phosphatase (A. fulgidus), 1YS9: hypothetical protein Spy1043 (S. pyogenes), 1VJR: p-nitrophenol phosphatase (T. maritima), 2HX1: possible sugar phosphatase (C. hutchinsonii), 2OYC: chronophin/PDXP (H. sapiens), 3PDW: putative p-nitrophenyl phosphatase (B. subtilis), 2H04: haloacid dehalogenase-like hydrolase domain containing protein2/HDHD2 (M. musculus), 2X4D: phospholysine/phosphohistidine inorganic pyrophosphate phosphatase/LHPP (H. sapiens), 3RF6: HAD-like phosphatase (S. cerevisiae), 3EPR: putative HAD superfamily hydrolase (S. agalactiae), 2C4N: NagD (E. coli), 3HLT: haloacid dehalogenase like hydrolase domain containing protein2/HDHD2 (H. sapiens) , 1YV9: HAD-like phosphatase (E. faecalis), 1ZJJ: hypothetical protein PH1952 (P. hyrokoshii).

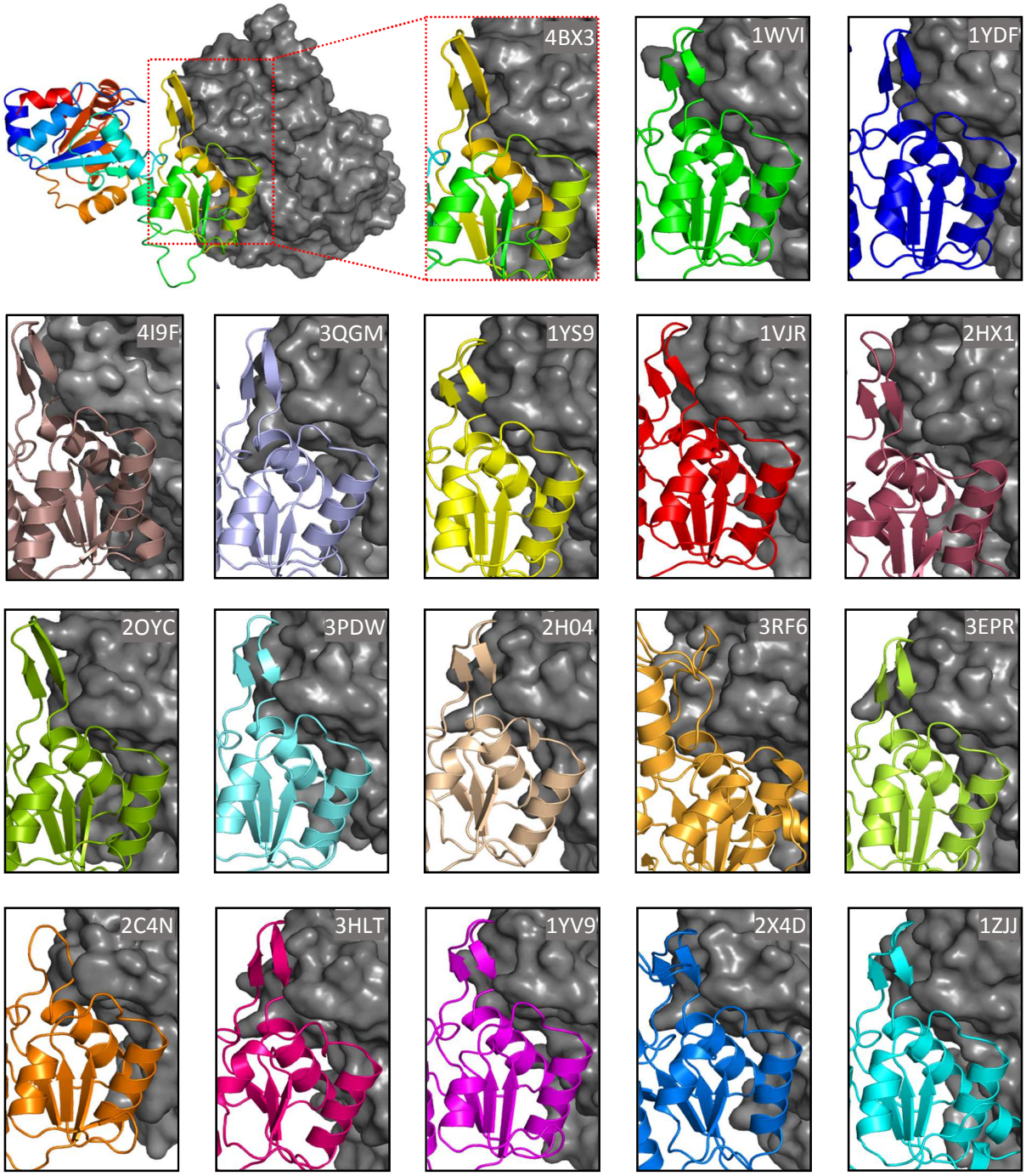

Figure 38. Homodimerization interfaces of C2α-type HAD hydrolases. One protomer of each dimer is shown as a cartoon representation colorcoded according to Figure 37, while the other protomer is shown as a gray surface representation. The dimer interface of the murine chronophin structure solved in this thesis (top left, PDB code 4BX3) is boxed in red, showing the position of the interface. All C2α-type hydrolase interfaces are composed of two α-helices and a β-hairpin, which resembles the substrate specificity loop in chronophin. This structural element is not shown in the structures 2C4N and 3RF6, because the residues participating in hydrogen bonding are not adjacent to each other, thus are not automatically assigned as β-hairpins. The PDB codes are indicated and the protein identities are given in Figure 37.

4.4 Determinants of substrate specificities in the C2a-type HAD hydrolases chronophin and AUM

This section addresses the question of whether the determinants for substrate specificity are solely located in the capping domain of the C2a-type HAD hydrolases. While the HAD hydrolase superfamily generally exhibits a low overall sequence identity [7], all family members show a structurally highly conserved catalytic core. This catalytic domain is composed of a Rossmann-fold that harbors the active site signature motifs and that coordinates the essential cofactor Mg^{2+}. These features are consistent with a highly conserved catalytic mechanism. The catalytic domain is equipped with additional inserts whose location, size and topology led to the classification into five structural HAD subfamilies [69]. These inserts, termed capping domains or caps, are thought to be pivotal for adding functionality and specificity to the catalytic domain. The uncapped C0 type HAD hydrolases for example have been shown to predominantly act on macromolecular substrates, as they exhibit an open, solvent accessible active site. Small molecules, however, can be utilized by this HAD subfamily if oligomerization leads to 'pseudocapping' of the active site [92]. In contrast, the capped hydrolases from the C1 and C2 subfamilies typically process low molecular weight substrates due to cap-mediated occlusion of the active site. Exceptions are proteins that are phosphorylated on their termini, such as cofilin 1, a protein substrate of chronophin [71], or the histone H2AX that is targeted by the Eyes absent homolog 1 (Eya1) phosphatase [287].

4.4.1 Generation of a hybrid protein consisting of the chronophin catalytic core and the AUM cap

In order to investigate the impact of the caps on C2a-type HAD hydrolase substrate specificity and selectivity, I generated an enzyme consisting of the catalytic core of murine chronophin equipped with the capping domain of murine AUM, an aspartate-based, ubiquitous, Mg^{2+}-dependent HAD phosphatase that has recently been identified in our group (gene annotation: phosphoglycolate phosphatase/PGP, [288]). AUM is the closest paralog of chronophin and the sequence similarity (42.7% identity, 26.5% similarity on amino acid level in the murine enzymes) is remarkably high for HAD hydrolases. This suggests a high structural homology. Nevertheless, the two enzymes have very different substrate specificities. AUM acts as a phospho-tyrosine phosphatase, and efficiently dephosphorylates adenosine and guanosine di-/tri-phosphates (ADP>ATP≈GTP≈GDP) as well as the generic phosphatase substrate *para*-nitrophenyl phosphate (*p*NPP) (Figure 40, [288]). Chronophin, in contrast, has so far been shown to exclusively

dephosphorylate phospho-serine/threonine residues [71, 168] and to specifically act on pyridoxal 5'-phosphate (PLP) (Figure 40, [70]). To test, whether replacing the chronophin cap with the AUM cap could interchange the respective protein's substrate preferences, the aforementioned hybrid protein termed "CAC" was generated, consisting of the murine chronophin catalytic core (chronophin residues 1-100 and 208-292) and the inserted capping domain of murine AUM (residues 114-233 of AUM). A sequence alignment of chronophin, the CAC hybrid protein and AUM is shown in Figure 39. The protein coding DNA sequence of this hybrid protein was cloned into the bacterial expression vector pETM-11 for recombinant expression as an N-terminally His_6-tagged fusion protein. The protein was recombinantly expressed in *E. coli* BL21(DE3) and purified to homogeneity for subsequent biochemical and structural analyses.

```
chronophin(M.m.) ---------MARCERLRGAALRDVLGQAQGVLFDCDGVLWNGERIVPGAPELLQRLARAG 51
CAC              ---------MARCERLRGAALRDVLGQAQGVLFDCDGVLWNGERIVPGAPELLQRLARAG 51
AUM(M.m.)        MAEAEAGGDEARCVRLSAERAKLLLAEVDTLLFDCDGVLWRGETAVPGAPETLRALRARG 60
                           *** ** .   : :*.:.: :*********.**  ****** *: *   *

chronophin(M.m.) KNTLFVSNNSRRARPELALRFARLGFAGLRA----EQLFSSALCAARLLRQRLSGPPDAS 107
CAC              KNTLFVSNNSRRARPELALRFARLGFAGLRA----EQLFSSALCAARLLRQRLAGVPDPK 107
AUM(M.m.)        KRLGFITNNSSKTRTAYAEKLRRLGFGGPVGPEAGLEVFGTAYCSALYLRQRLAGVPDPK 120
                 *.  *::*** ::*   * :: ****.*  .     ::*.:* *:*  *****:* ** .

chronophin(M.m.) GAVFVLGGEGLRAELRAAGLRLAGD---------------PGEDPRVRAVLVGYDEQFSF 152
CAC              --AYVLGSPALAAELEAVGVTSVGVGPDVLHGDGPSDWLAVPLEPDVRAVVVGFDPHFSY 165
AUM(M.m.)        --AYVLGSPALAAELEAVGVTSVGVGPDVLHGDGPSDWLAVPLEPDVRAVVVGFDPHFSY 178
                   .:***. .* ***.*.*:  .*                  :* ****:**:* :**:

chronophin(M.m.) SRLTEACAHLRDPDCLLVATDRDPWHPLSDGSRTPGTGSLAAAVETASGRQALVVGKPSP 212
CAC              MKLTKAVRYLQQPDCLLVGTNMDNRLPLENGRFIAGTGCLVRAVEMAAQRQADIIGKPSP 225
AUM(M.m.)        MKLTKAVRYLQQPDCLLVGTNMDNRLPLENGRFIAGTGCLVRAVEMAAQRQADIIGKPSR 238
                  :**:*  :*::******.*: *   **.:*    ***.*. *** *: *** ::****

chronophin(M.m.) YMFQCITEDFSVDPARTLMVGDRLETDILFGHRCGMTTVLTLTGVSSLEEAQAYLT---A 269
CAC              YMFQCITEDFSVDPARTLMVGDRLETDILFGHRCGMTTVLTLTGVSSLEEAQAYLT---A 282
AUM(M.m.)        FIFDCVSQEYGINPERTVMVGDRLDTDILLGSTCSLKTILTLTGVSSLEDVKSNQESDCM 298
                 ::*:*::::::.::* **:******:****:*  *.:.*:**********:.::

chronophin(M.m.) GQRDLVPHYYVESIADLMEGLED 292
CAC              GQRDLVPHYYVESIADLMEGLED 305
AUM(M.m.)        FKKKMVPDFYVDSIADLLPALQG 321
                  ::.:**.:**:*****: .*:
```

Figure 39. Sequence alignment of chronophin, the CAC hybrid and AUM. Identical sequences between chronophin and the CAC hybrid are highlighted in yellow, sequences that are identical between AUM and the CAC hybrid are shown in green. The boxed sequences indicate identical sequences in all three proteins at the edges of the cap that were used as insertion points for the AUM cap in chronophin. Identical residues in all three proteins are indicated as an asterisk (*), residues with highly similar properties are indicated with a colon (:) and a period (.) shows positions with only weakly similar properties.

4.4.2 Substrate specificities of chronophin, the CAC hybrid and AUM towards PLP and *p*NPP

The recombinantly expressed and purified chronophin, CAC hybrid and AUM (the latter kindly shared by A. Seifried) were tested against PLP and the generic phosphatase substrate *p*NPP, since assaying phosphatase activity with low molecular weight substrates is much more practicable, and the physiological substrate of AUM remains elusive to date.

In order to assess the PLP phosphatase activity, a modified malachite green assay was employed. For this, 100nM of the respective protein was incubated with 1mM PLP in a total volume of 50µL SEC buffer A. After 2 minutes, the reactions were stopped by the addition of 100µL Biomol Green and after 15 minutes the absorption was read at 620nm on an Envision 2104 multilabel microplate reader. Figure 40A shows that chronophin efficiently hydrolyses PLP, whereas almost no detectable PLP phosphatase activity is measurable for AUM and the CAC hybrid.

Next, the *p*NPP phosphatase activity of the three proteins was tested by adding *p*NPP (final concentration 1mM) to 100nM of the respective protein in a final volume of 100µL SEC buffer A. The generation of *para*-nitrophenol was determined after 20 minutes at 405nm using an Envision 2104 multilabel microplate reader. As show in Figure 40B, AUM readily dephosphorylates *p*NPP, while chronophin shows only low activity towards this artificial phosphatase substrate. The CAC hybrid shows only slightly increased activity compared to chronophin, implying that the generation of a hybrid protein, consisting of the chronophin catalytic domain equipped with the AUM capping domain could not transfer the AUM *p*NPP specificity to the chronophin catalytic domain.

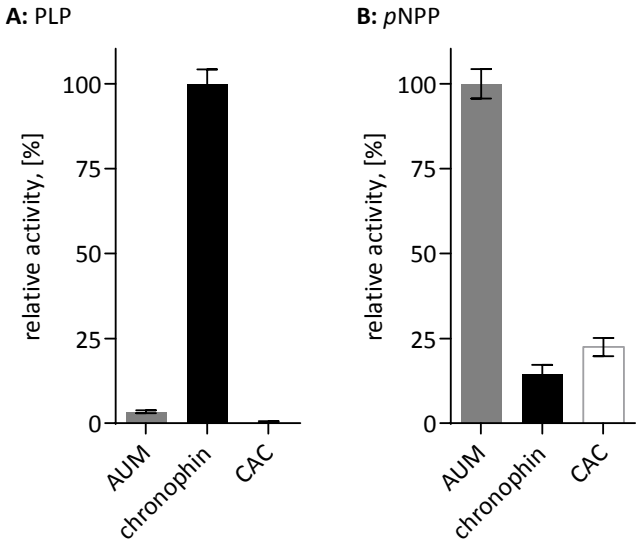

Figure 40. PLP and pNPP phosphatase activity of chronophin, the CAC hybrid and AUM. A, PLP dephosphorylation was measured by detecting the released free phosphate using a malachite green based assay. The values were normalized to the chronophin activity (100%). B, pNPP hydrolysis was monitored by measuring the para-nitrophenol accumulation at 405nm. The values were normalized to the AUM activity (100%).

Interestingly, the reciprocal experiments performed by A. Seifried, using a protein consisting of the AUM catalytic domain fused to the chronophin capping domain, referred to as the "ACA hybrid", led to an to a substantial PLP dephosphorylation, while the activity towards *p*NPP was considerably lowered, compared to AUM [288]. Here, the specificity of chronophin towards its physiological substrate PLP could

be transferred partially to the AUM catalytic domain by equipping it with the chronophin capping domain, supporting the hypothesis that critical determinants for substrate specificity are located in the capping domain of C2a-type HAD hydrolases. In contrast to this, the experiments with the CAC hybrid were conducted using the generic phosphatase substrate *p*NPP, thus the failure of the specificity-swap might be attributed to the fact that *p*NPP is an artificial substrate for AUM, not its physiological target.

4.4.3 Structural characterization of the CAC hybrid

In order to gain further insights into the differential substrate specificities of the closely related chronophin and AUM, X-ray crystallographic studies using the CAC hybrid were performed, since no structural information about AUM was available, and the protein failed to crystallize in our hands (for details, see thesis A. Seifried). For this, the recombinantly expressed and purified CAC hybrid was crystallized and crystals of the protein appeared after 2-3 days as thin plates. The majority of the crystals displayed high mosaicity when tested and were often twinned making the collection of a useful dataset impossible. Nonetheless, one of the many tested crystals could be used for dataset collection at the in-house X-ray system of the Rudolf Virchow Center. An additional dataset, which was collected at the BESSY (Berlin) did not show an increased resolution, thus the dataset from the in-house X-ray system was used for the solution of the structure. The protein crystallized in space group $P2_1$ with four molecules per asymmetric unit and was refined at 2.65Å resolution with an R_{cryst} of 19.8% and an R_{free} of 25.6%. The data collection and refinement statistics of the CAC hybrid (PDB code 4BKM) are summarized in Table 41.

A comparison of the newly solved structure of the CAC hybrid with the structure of murine chronophin reveals a high structural similarity between the two proteins. The overall r.m.s.d. of the aligned structures is ~1.0Å, a comparatively low value considering that every currently available structure of a C2a-type HAD hydrolase (besides human chronophin) has a higher r.m.s.d. value when aligned to murine chronophin (see Table 40). When the CAC hybrid domains taken from chronophin and AUM are compared separately with the respective domains of the murine chronophin structure, the r.m.s.d. values are even lower: ~0.4Å for the aligned catalytic domains, suggesting that the insertion of the AUM capping domain into the chronophin catalytic domain had no major impact on the folding of this domain, and ~0.6Å when only the capping domains are aligned. This observation that is not surprising when the previously described homology of C2a-type HAD hydrolases in general is taken into account (see Figure 37 and Figure 38). The discrepancy in the r.m.s.d. values of the isolated domains compared to the overall r.m.s.d. arises from the fact, that the CAC hybrid capping domain is rotated by ~6.5° (as determined using LSQKAB of the CCP4

program suite) with respect to the catalytic domain, when the murine chronophin structure and the CAC structure are superimposed using the catalytic domains only (Figure 41A). This differential relative orientation of the catalytic domain and the capping domain towards each other results in an altered position of the β-hairpin that corresponds to the substrate specificity loop of chronophin. The positioning of this loop is crucial for substrate specificity and accessibility of chronophin, as discussed in section 4.3.

Also, the previously found mode of dimerization of C2a-type HAD hydrolases is conserved in the CAC hybrid structure. Dimerization is entirely mediated by the (AUM) capping domain, and the dimer interface is composed of two α-helices that include interactions with the β-hairpin that has been described as the substrate specificity loop in chronophin (see Figure 6). An interface analysis using PDBePISA suggest that the protein is dimeric with an average dimer interface of 1518Å^2. The dimeric state of the protein is additionally confirmed by the size exclusion chromatography elution volume that corresponds to a calculated molecular mass of ~70kDa, while the monomeric protein has a theoretical molecular mass of 33.43kDa [288].

A striking structural difference between the capping domains of AUM, derived from the CAC hybrid, and chronophin is the existence of a prolonged loop, that is inserted between β-strands 2 and 3 of the capping domain, and that contains a short α-helical stretch (Figure 41). This loop is not present in chronophin and was termed transversal loop, since it extends from one protomer of a dimer into close proximity of the substrate specificity loop of the other protomer, partially occluding the active site entrance of the adjacent molecule. The position and conformation of this loop seems to be structurally conserved, as the superposition of the four molecules in the unit cell shows no obvious differences in the orientation of the loop. The presence of this loop might contribute to substrate specificity and selectivity.

Consistent with the structural conservation of C2a-type HAD hydrolase capping domains, these results show that the chronophin and the AUM capping domains display a high degree of structural homology. However, significant structural differences exist that might contribute to the respective protein's substrate specificity determinants, such as the transversal loop in AUM. In addition to these structural features, substrate specificity will be defined by particular residues that are located in close vicinity of the active site cleft, thus a detailed active site comparison was conducted. For this, a structure of human chronophin, which was co-crystallized with bound pyridoxal 5'-phosphate by replacing the cofactor Mg^{2+} with the catalytically inert Ca^{2+} (PDB code 2P69), was used to identify all residues within 5Å of PLP. The respective residues were then selected and compared within the murine chronophin and the CAC hybrid structure. The results are shown in Figure 42, displaying the identified residues of murine chronophin, the CAC hybrid and a superposition of both active sites. Remarkably, only few of the residues that are within 5Å of the

active site cavity differ between the two proteins. The residues of the catalytic domain are highly conserved between chronophin and AUM as they belong to the four HAD hydrolase signature motifs, and are responsible for catalysis rather than for substrate specificity. A difference between the AUM and chronophin catalytic core residues is Thr^{67} of motif 2 in AUM that is replaced by Ser^{58} in chronophin.

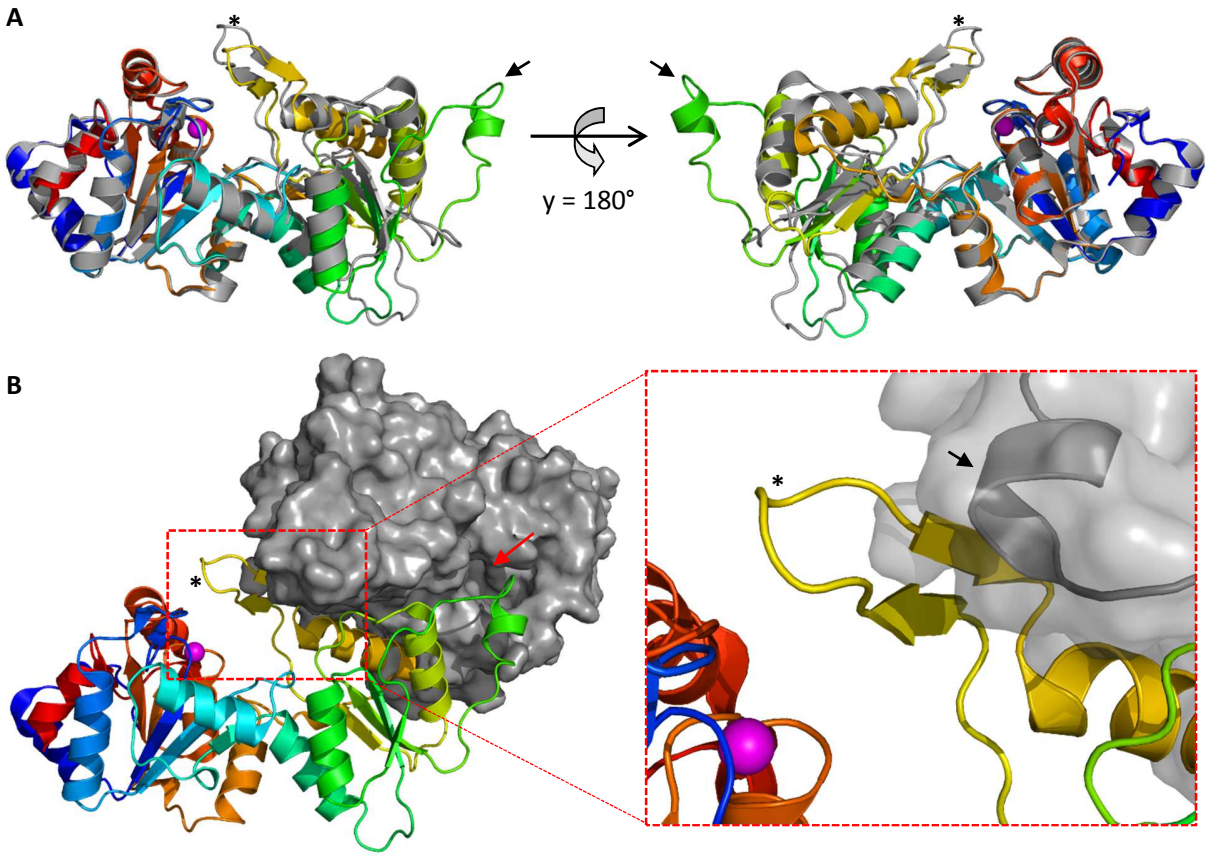

Figure 41. Structure of the CAC hybrid and comparison with murine chronophin. A, structure of the CAC hybrid (rainbow color) superpositioned with the murine chronophin (gray) structure. One protomer of each dimeric protein was aligned via the catalytic domains (Met^{1} to Leu^{95} and Pro^{212} to Leu^{291} in chronophin, Met^{1} to Leu^{95} and Pro^{225} to Leu^{303} in the CAC hybrid) indicating the different orientation of the catalytic domain towards the capping domain in the CAC hybrid, compared to chronophin. This leads to a shift in the positioning of the substrate specificity loop (*). The transverse loop of the CAC hybrid (AUM) cap is indicated by a black arrow. The position of the active site is indicated by the cofactor Mg^{2+} (magenta spheres). B, structure of the CAC hybrid homodimer. One protomer is shown as a ribbon representation (rainbow color), the other one as surface representation (gray). The transversal loops (black arrows) are positioned in close proximity of the active site entrances (red arrow) and the substrate specificity loop (, see detail). The transverse loop might thus be important for the accessibility of the active site cleft and substrate specificity.*

Nonetheless, the function of those residues is conserved, as they both function in the stabilization of the phospho-aspartate intermediate during catalysis [69]. Thus, the differences found in the capping domain are supposedly of particular importance for substrate specificity. The most striking difference is the presence of a leucine (Leu^{191}) in the CAC mutant (Leu^{204} in AUM) at the position of His^{178} of murine chronophin.

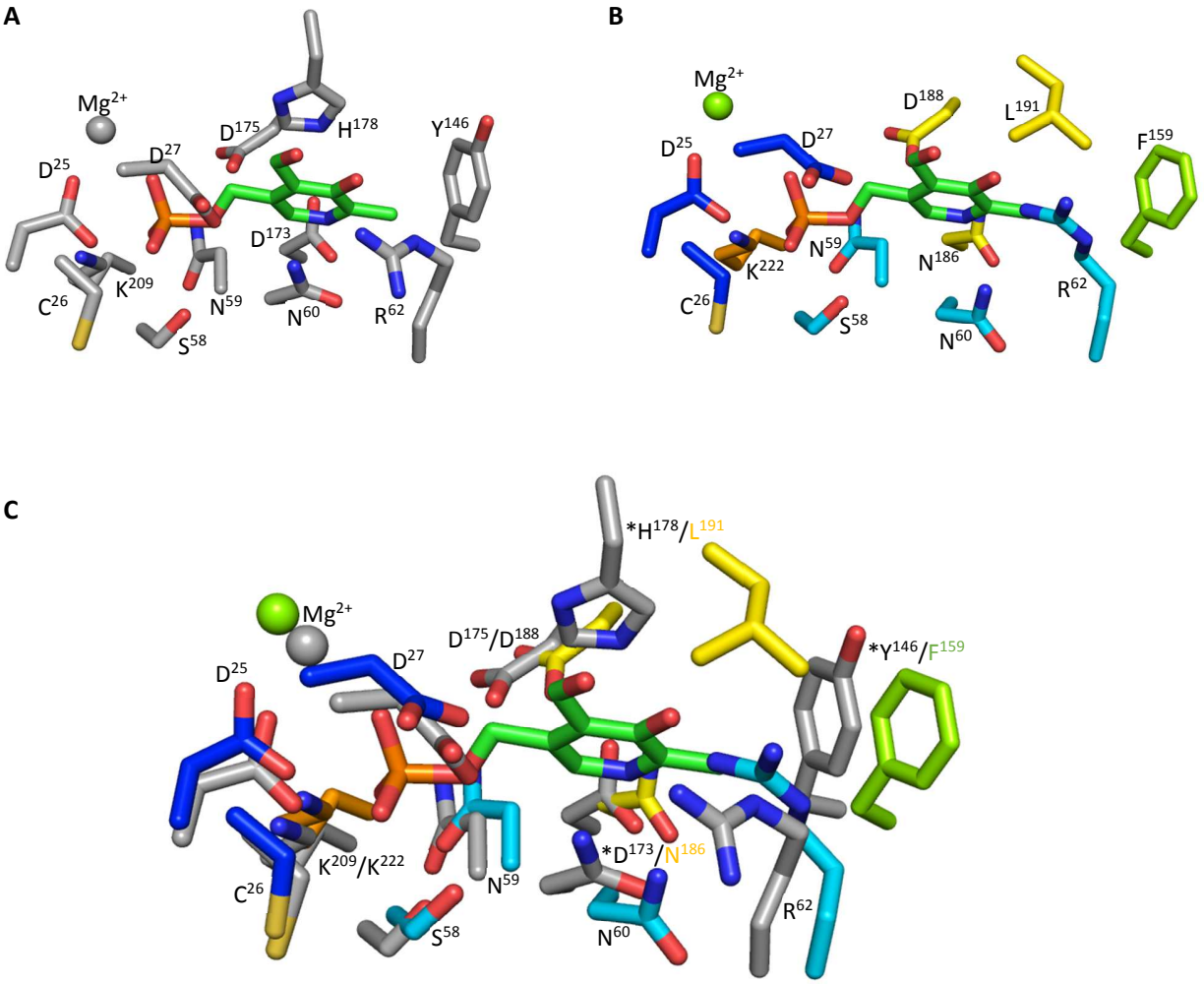

Figure 42. Active site comparison between the CAC hybrid and murine chronophin. Human chronophin residues within 5Å of PLP (PDB code 2P69) were identified and the respective side chains of murine chronophin (A) and the CAC hybrid (B) are displayed here. PLP (green) was modeled in according to the PLP-bound structure of human chronophin (PDB code 2P69) for better comparison. Conserved residues of the CAC hybrid catalytic core are shown in blue/cyan, whereas residues of the AUM capping domain are represented in green/yellow. C shows a superposition of the active site residues in the CAC hybrid (colored) and murine chronophin (gray). Residues that are not conserved are highlighted with an asterisk (*).

As stated before, this histidine residue has been shown to coordinate the pyridine ring of PLP, and thus substantially contributes to the substrate specificity of chronophin towards this small molecule. The presence of an aliphatic residue at the respective position impedes the coordination of PLP in the CAC

hybrid and in AUM, explaining their low activity towards this substrate. Importantly, A. Seifried could show that a single mutation of Leu^{204} in AUM to histidine (AUM^{L204H}) led to a significant PLP hydrolase activity of AUM while considerably reducing the *p*NPP phosphatase activity [288]. This finding implies that the β-hairpin that harbors His^{178} of murine chronophin (His^{182} in the human ortholog) and Leu^{204} in AUM, might generally be of importance for the substrate specificity of the C2a-type HAD hydrolase subfamily. An additional significant difference between the chronophin and the AUM cap is the presence of a charge-neutral residue (Asn^{186} in the CAC hybrid) at a position where chronophin exhibits the acidic Asp^{177}. Furthermore, the substitution of the less hydrophobic Tyr^{150} in chronophin by Phe^{159} in the CAC hybrid is worth mentioning.

Figure 43 shows a topological comparison of the active site clefts, indicating that the structural arrangements differ substantially between murine chronophin and the CAC hybrid. Whereas the active site entrance of chronophin is wide enough to easily accommodate PLP, the CAC hybrid active site entrance is much more constricted and does not offer sufficient space for the 3'-hydroxyl group of PLP, if positioned according to the PLP-bound structure of human chronophin (PDB code 2P69). In contrast to that, the pocket of the CAC hybrid seems to expand deeper into the capping domain of the protein.

Additionally, there is a channel connecting the active site cleft with the solvent and a hydrophobic cleft on the other side of the channel offering additional space for a potential substrate. This finding supports the hypothesis that the capping domain greatly contributes to substrate specificity, not only by harboring residues that coordinate the substrate, but also by providing the topological requirements for substrate binding.

Taken together, the results show that it was possible to successfully transfer the AUM capping domain onto the catalytic domain of chronophin, without structurally interfering with the catalytic domain. The high homology of the AUM cap compared to the C2a-type HAD hydrolase caps, and especially chronophin's capping domain, suggests that this domain is folded correctly as well, providing the first insights into the structure of AUM. Based on the structure of the CAC hybrid it was possible to compare the residues from the active site cavity and topologies with the AUM's closest paralog chronophin allowing to hypothesize on the importance of specific residues for substrate specificity. Importantly, only few residues within the cap portion of the active site cleft differ between chronophin and the AUM. However, the positioning of the substrate specificity loop and the transversal loop might be of importance for substrate specificity and selectivity as well.

Finally, the domain swap did not lead to the expected specificity swap, probably due to the low specificity of AUM towards the artificial phosphatase substrate *p*NPP.

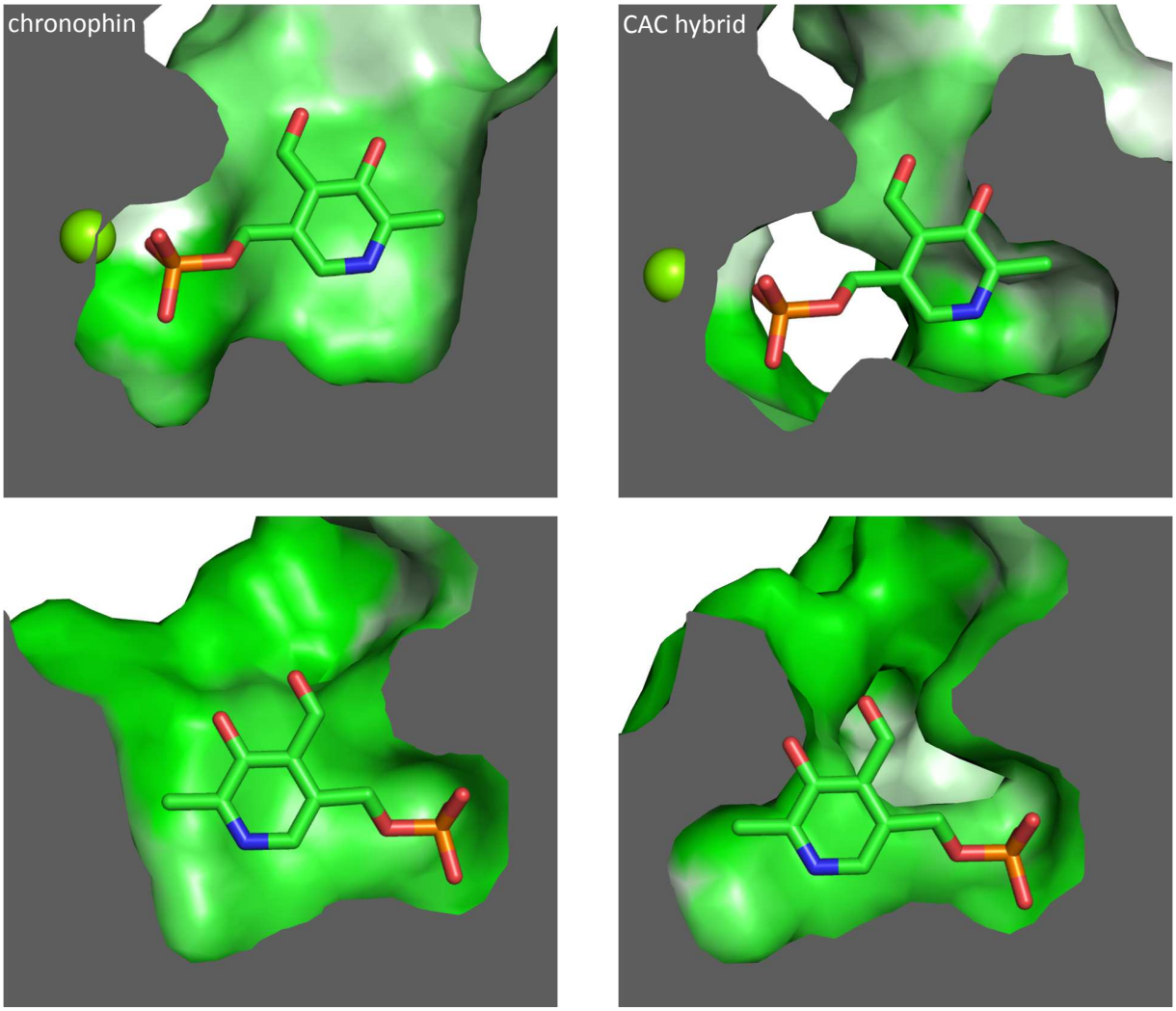

Figure 43. Active site topologies of the CAC hybrid and murine chronophin. The images shown provide a lateral view on the murine chronophin (left panels) and CAC hybrid (right panels) active site clefts. The protein surfaces were color-coded according to the Eisenberg hydrophobicity scale [3] with green being hydrophilic residues and white being hydrophobic residues. The cofactor Mg^{2+} is represented as a green sphere (top panels). PLP was modeled in according to the PLP-bound human chronophin structure (PDB code 2P69) for size comparison and simplified orientation. Top and bottom panels represent 180° rotations around the Y-axis. The interior of the proteins is colored in gray.

Table 41. Data collection and refinement statistics of the CAC hybrid (PDB code 4BKM).

Data collection		**Refinement**	
Wavelength (Å)	1.5418	Wilson B-factor (Å²)	50.0
Space group	P 2_1	Average B-factor (Å²)	86.9
Unit cell parameters		macromolecules	87.4
a, b, c (Å)	67.50, 91.96, 105.92	solvent	64.0
α, β, γ (°)	90, 90.2, 90	R_{cryst} [e]	0.1976 (0.2878)
Resolution range (Å) [a]	41.74 - 2.65 (2.79 - 2.65)	R_{free} [e]	0.2564 (0.3290)
R_{sym} [b]	0.125 (0.816)	Number of non H-atoms	9450
$R_{p.i.m.}$ [c]	0.070 (0.456)	macromolecules	9236
$\langle I / \sigma I \rangle$ [d]	6.6 (1.4)	ligands	12
Completeness (%)	96.2 (94.9)	water	202
Multiplicity	4.1 (4.1)	R.m.s. deviations in	
Total reflections	150275	bond lengths (Å)	0.004
Unique reflections	36203 (3531)	bond angles (°)	0.83
		planar groups (Å)	0.004
		dihedral angles (°)	13.54
		Coordinate error (Å) [f]	0.36
		Ramachandran statistics [g]	
		favored (%)	97.68
		allowed (%)	2.07
		outliers (%)	0.25
		MolProbity clashscore [h]	12.17

[a] Numbers in parentheses refer to the respective highest resolution data shell in the data set.

[b] $R_{sym} = \Sigma_{hkl}\Sigma_i |I_i - \langle I \rangle| / \Sigma_{hkl}\Sigma_i I_i$, where I_i is the i^{th} measurement, and $\langle I \rangle$ is the weighted mean of all measurements of I.

[c] $R_{p.i.m.} = \Sigma_{hkl} (1/(n-1))^{1/2} \Sigma_i |I_i - \langle I \rangle| / \Sigma_{hkl}\Sigma_i I_i$, where n is the multiplicity of the observed reflection.

[d] $\langle I / \sigma I \rangle$: Indicates the average of the intensity divided by its S.D. value.

[e] $R_{cryst} = \Sigma |F_o - F_c| / \Sigma |F_o|$ where F_o and F_c are the observed and calculated structure factor amplitudes. R_{free}, same as R_{cryst} for 5% of the data randomly omitted from the refinement.

[f] Estimated coordinate error based on R_{free}.

[g] Ramachandran statistics indicate the fraction of residues in the favored, allowed and disallowed regions of the Ramachandran diagram, as defined by MolProbity [6].

[h] number of serious clashes per 1000 atoms (Reference: see [g]).

4.5 Generation and characterization of chronophin-specific inhibitors

In our lab, we recently established conditional chronophin knock-out mouse lines, allowing us to investigate the effects of chronophin loss both on a biochemical and a physiological level. Importantly, we were able to show that pyridoxal 5'-phosphate (PLP) levels are dramatically increased in organs of whole-body chronophin knock-out mice, demonstrating that chronophin indeed functions as a physiological and non-redundant PLP phosphatase *in vivo* (unpublished data). In order to be able to acutely inhibit the phosphatase activity of chronophin in a pharmacological manner, we expanded this project towards the development of specific, low molecular weight chronophin inhibitors. As a first approach, we decided to generate active site-directed inhibitors based on the known structure of human chronophin in complex with its substrate PLP. The possibility of pharmacologically modulating a protein's function by specific inhibitors greatly increases the ability to investigate the physiological role of the respective protein, without possible compensatory effects upon genetic knock-out of a protein [289]. Thus, in collaboration with the group of Dr. M. Köhn from the EMBL Heidelberg, N. Jabari synthesized four potential chronophin inhibitors based on the structure of PLP (Figure 44). The effect of the compounds on the chronophin PLP-phosphatase activity were subsequently characterized biochemically in dose-response assays and in steady state kinetic assays, using recombinantly expressed and purified murine chronophin. These first-generation inhibitors showed moderate effects on the chronophin activity with IC_{50} values in the micromolar range. Additionally, co-crystallization studies were conducted resulting in an X-ray crystal structure of chronophin in complex with one of the inhibitors, so far.

This section comprises the results of the biochemical characterization and structural analysis of the chronophin inhibitors.

4.5.1 Generation of putative chronophin-specific inhibitors

The synthesis of the inhibitors was performed by N. Jabari in collaboration with the group of Dr. M. Köhn from the EMBL Heidelberg. The inhibitors are based on the structure of pyridoxal 5'-phosphate (PLP), a physiological substrate of chronophin. This was achieved by generating a non-hydrolysable substrate analog by replacing the phosphate moiety with a phosphonate. Because it is known that the 4'-position affects the kinetic constants of chronophin for its substrate [290], this position was either left unchanged (comprising an aldehyde function as in PLP), or substituted with an alcohol function. To test the effect of the altered bond length due to the exchange of the phosphate ester oxygen atom by a carbon atom in the

phosphonate, we decided to introduce a C-C double bond at the respective position in each set of inhibitors. The structures of PLP and the inhibitors are shown in Figure 44.

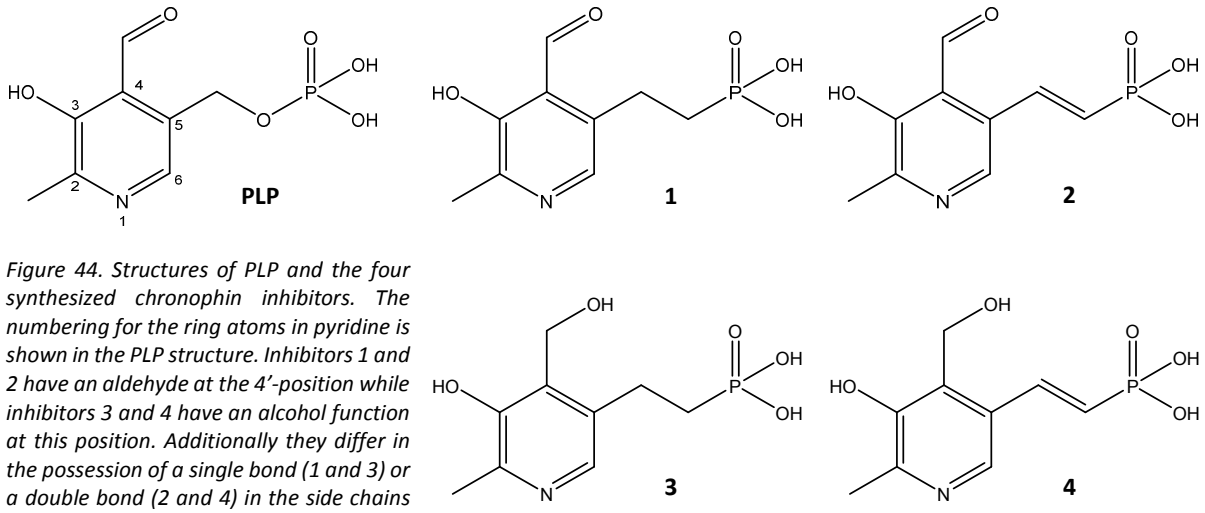

Figure 44. Structures of PLP and the four synthesized chronophin inhibitors. The numbering for the ring atoms in pyridine is shown in the PLP structure. Inhibitors 1 and 2 have an aldehyde at the 4'-position while inhibitors 3 and 4 have an alcohol function at this position. Additionally they differ in the possession of a single bond (1 and 3) or a double bond (2 and 4) in the side chains inserted at the 5'- position.

4.5.2 Biochemical characterization of the inhibitors

All four competitive chronophin inhibitors were characterized biochemically by N. Jabari in dose response assays and in steady state kinetic assays using recombinantly expressed and purified murine chronophin. All assays were performed in triplicates using three independently purified batches of chronophin. The preliminary dose-response assays clearly show that an aldehyde at the 4'-position leads to increased inhibition of chronophin, compared to the inhibitors substituted with an alcohol function at the 4'-position (Figure 45). The estimated half maximal inhibitory concentration (IC_{50}) of compounds 1 and 2 (aldehydes) towards chronophin is reached at ~300µM, while inhibitors 3 and 4 (alcohols) have a ~4.3-fold higher IC_{50} value of around 1.3mM (100nM chronophin/well tested with 20µM PLP). These values have to be considered as rough approximations of the actual IC_{50} values, since the assays were performed using only five inhibitor concentrations. For optimal fitting of the dose response curves, it is suggested to use at least 10 inhibitor concentrations (i.e. half-log dilutions) with half of the data points above and half below the IC_{50} [291]. Nevertheless, these preliminary results clearly show an increased inhibitory effect for the compounds substituted with an aldehyde at the 4'-position compared to the alcohol derivates. The presence of a C-C double bond in the 5'-position does not seem to have an effect on the affinity of the inhibitor.

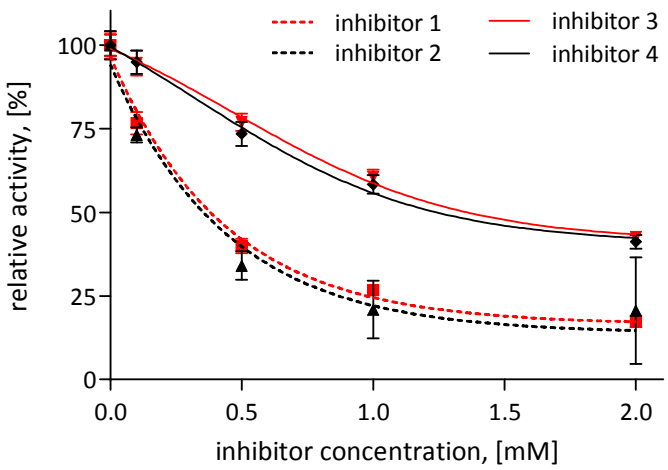

Figure 45. Dose-response curves for inhibitors 1-4. In vitro PLP phosphatase assays were performed in 96-well microtiter plates in a total volume of 50µL using 100nM chronophin per well and the indicated concentrations of the respective inhibitor. The reactions were started by the addition of 20µM PLP and stopped after 5 minutes by adding 100µL malachite green, released inorganic phosphate was measured at 620nm. The results represent mean values ± S.E.M. of three independently performed experiments using three purified batches of protein.

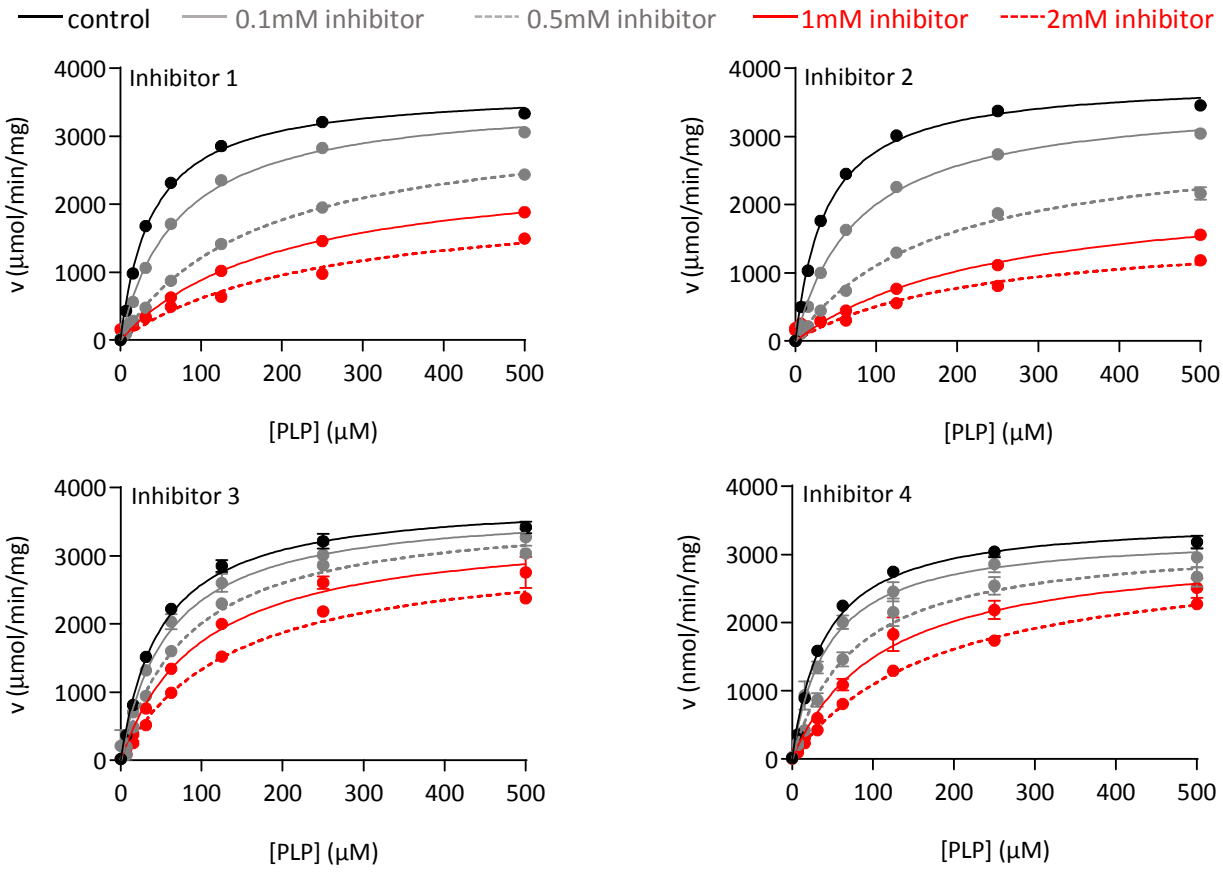

Figure 46. Steady-state kinetic measurement of chronophin with inhibitors. In vitro PLP phosphatase assays were performed in 96-well microtiter plates in a total volume of 50µL using 100nM chronophin per well. The enzyme was pre incubated with the indicated concentrations of the respective inhibitor (0-2mM). The reactions were subsequently started by the addition of PLP (final concentrations ranging from 0 – 500µM) and stopped after 2 minutes by the addition of 100µL malachite green. The kinetics of organic phosphate release were measured at 620nm and quantified using phosphate standard curves. The results represent mean values ± S.E.M. of triplicates performed with three independently purified batches of protein. The error bars are masked behind the symbols. Control measurements were performed in buffer without inhibitor.

As expected for a competitive chronophin inhibitor that is based on the structure of the substrate PLP, the kinetic constants derived from the steady state kinetic measurements show a strong increase in the K_m-values with increasing inhibitor concentrations, while the v_{max} values remain largely unaffected. The kinetic measurements are shown in Figure 46, the derived kinetic constants are summarized in Table 42.

Table 42. Kinetic constants of the chronophin-catalyzed PLP hydrolysis in the presence of inhibitors 1-4. The experiments were performed as described in the legend to Figure 46.

inhibitor	value	no inhibitor	0.1mM	0.5mM	1mM	2mM
1	v_{max}	3687 ± 43.6	3588 ± 44.6	3278 ± 78.6	2620 ± 85.7	2131 ± 161
	K_m	39.44 ± 1.65	71.95 ± 2.71	170.4 ± 9.59	196.9 ± 14.4	246.1 ± 38.7
2	v_{max}	3839 ± 49.0	3577 ± 55.1	2986 ± 99.3	2301 ± 163	1644 ± 238
	K_m	38.07 ± 1.74	78.33 ± 3.57	169.6 ± 13.3	248.4 ± 36.6	223.5 ± 70.0
3	v_{max}	3843 ± 70.0	3739 ± 159	3680 ± 70.6	3440 ± 140	3148 ± 101
	K_m	49.09 ± 3.00	59.40 ± 8.07	83.12 ± 4.64	97.56 ± 11.0	136.0 ± 10.9
4	v_{max}	3535 ± 66.2	3304 ± 121	3226 ± 151	3148 ± 195	3074 ± 206
	K_m	40.40 ± 2.66	44.28 ± 5.59	76.80 ± 10.7	111.8 ± 18.5	181.4 ± 28.0

4.5.3 Structural characterization of a chronophin-inhibitor 3 complex

In order to retrieve detailed information about the chronophin-inhibitor interactions on the atomic level, co-crystallization experiments of recombinantly expressed and purified murine chronophin with the four inhibitors were conducted. Several crystals of all inhibitors were obtained, but so far only one structure of chronophin in complex with inhibitor 3 contained electron density of the whole inhibitor. Here, chronophin was crystallized together with 5mM inhibitor 3. At 20°C, the cubic crystals appeared within hours after setting up the crystallization experiment. A dataset of the chronophin-inhibitor complex was collected at the in-house X-ray system of the Rudolf Virchow Center. The chronophin-inhibitor complex crystallized in space group I23 and was solved by molecular replacement using the previously solved structure of murine chronophin (PDB code 4BX3). The structure was subsequently refined to 2.75Å resolution with an R_{cryst} of 19.0% and an R_{free} of 24.7%. The data collection and refinement statistics of the chronophin structure in complex with inhibitor 3 are summarized in Table 43.

Figure 47 shows an overview of the structure of chronophin with the bound inhibitor 3 and a detailed view of the inhibitor bound to the enzyme's active site. The overall structure of murine chronophin remains unaltered by the binding of the ligand, indicated by an r.m.s.d. of 0.264Å, when the structure was aligned

with the previously solved murine chronophin apo-structure (PDB code 4BX3, this thesis). Thus, no open-close transition between the catalytic core and the capping domain is observable upon ligand binding.

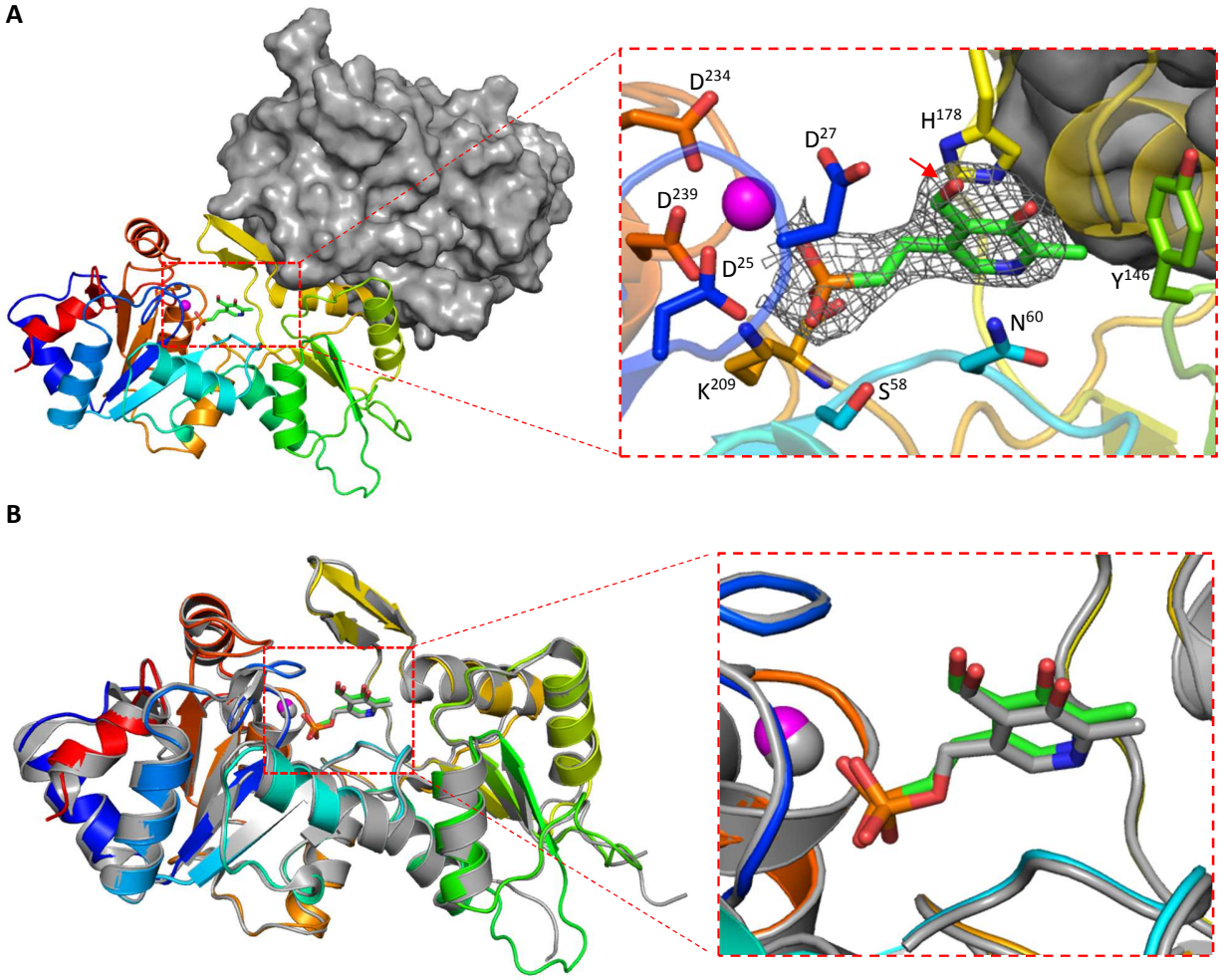

Figure 47. Structure of murine chronophin in complex with inhibitor 3. A, One protomer of chronophin is shown as a cartoon representation (rainbow color), the other protomer is depicted as a surface representation (gray). The inhibitor is shown in green and the cofactor Mg^{2+} as a magenta sphere. A detailed structure of the bound inhibitor and adjacent residues of the active site is shown in the boxed area. A hydrogen bond between the 4'-position of the inhibitor (red arrow) and Asn^{60} is probably responsible for the higher affinity of the aldehyde compounds compared to the alcohols. The refined $2F_o$-F_c electron density map of the inhibitor is contoured at an r.m.s.d. of 1. B, Structural comparison of murine chronophin in complex with inhibitor 3 (rainbow color) and human chronophin in complex with PLP (gray, PDB code 2CFT). The overall structure and the positioning of the ligands (boxed area; inhibitor 3: green, PLP: gray) are highly similar.

As expected for a PLP substrate analog, the coordination of the inhibitor within the protein strongly resembles the previously solved structures of human chronophin bound to PLP (PDB codes 2P69 and 2CFT, [94]). The closest residues to the 4'-position of the inhibitor are Asp^{27} (mean distance 3.75Å) and Asn^{60}

(mean distance 4.75Å). These distances are too far for hydrogen bonding, but could allow van der Waals interactions. However, an aldehyde group at the 4'-position of the inhibitor might be oriented differently and could be positioned in closer proximity to Asn^{60}, leading to the increased affinity and greater inhibitory effects, which have been observed in the enzymatic assays (see 4.5.2). Indeed, the distance between the 4'-aldehyde group of PLP and Asn60 of human chronophin (PDB code 2CFT) spans only 3.5Å, allowing the formation of a hydrogen bond and thereby explaining the supposedly higher affinity of the aldehyde compounds (inhibitors 1 and 2) compared to the alcohols (inhibitors 3 and 4), as measured by stronger inhibitory effects.

Table 43. Data collection and refinement statistics of the chronophin-inhibitor 3 structure.

Data collection		**Refinement**	
Wavelength (Å)	1.5418	Wilson B-factor (Å²)	67.02
Space group	I23	Average B-factor (Å²)	50.8
Unit cell parameters		macromolecules	50.9
a = b = c (Å)	166.81	solvent	35.5
α = β = γ (°)	90	R_{cryst} [e]	0.1895 (0.2628)
Resolution range (Å) [a]	32.71 - 2.75 (2.90 - 2.75)	R_{free} [e]	0.2466 (0.2902)
R_{sym} [b]	0.098 (0.952)	Number of non H-atoms	4486
$R_{p.i.m.}$ [c]	0.039 (0.380)	macromolecules	4403
$\langle I / \sigma I \rangle$ [d]	13.0 (1.9)	ligands	40
Completeness (%)	100 (100)	water	43
Multiplicity	7.3 (7.2)	R.m.s. deviations in	
Total reflections	147756	bond lengths (Å)	0.006
Unique reflections	20219 (2925)	bond angles (°)	0.932
		planar groups (Å)	0.004
		dihedral angles (°)	14.18
		Coordinate error (Å) [f]	0.34
		Ramachandran statistics [g]	
		favored (%)	98.44
		allowed (%)	0.87
		outliers (%)	0.69
		MolProbity clashscore [h]	8.02

[a] Numbers in parentheses refer to the respective highest resolution data shell in the data set.

[b] $R_{sym} = \Sigma_{hkl}\Sigma_i|I_i - \langle I \rangle|/\Sigma_{hkl}\Sigma_i I_i$, where I_i is the i^{th} measurement, and $\langle I \rangle$ is the weighted mean of all measurements of I.

[c] $R_{p.i.m.} = \Sigma_{hkl}\,(1/(n-1))^{1/2}\,\Sigma_i|I_i - \langle I \rangle|/\Sigma_{hkl}\Sigma_i I_i$, where n is the multiplicity of the observed reflection.

[d] $\langle I / \sigma I \rangle$: Indicates the average of the intensity divided by its S.D. value.

[e] $R_{cryst} = \Sigma|F_o - F_c|/\Sigma|F_o|$ where F_o and F_c are the observed and calculated structure factor amplitudes. R_{free}, same as R_{cryst} for 5% of the data randomly omitted from the refinement.

[f] Estimated coordinate error based on R_{free}.

[g] Ramachandran statistics indicate the fraction of residues in the favored, allowed and disallowed regions of the Ramachandran diagram, as defined by MolProbity [6].

[h] number of serious clashes per 1000 atoms (Reference: see [g]).

5 Discussion

5.1 The calcium and integrin binding protein 1 (CIB1) and calmodulin as chronophin interactors

Our group recently identified the calcium- and integrin binding protein 1 (CIB1) and calmodulin as interaction partners of the HAD phosphatase chronophin, and all three proteins were shown to interact with each other. CIB1 and calmodulin seemingly competed for binding to chronophin and, importantly, Ca^{2+}-ions were found to enhance the calmodulin/chronophin association, while the CIB1/calmodulin interaction was diminished. The interaction of CIB1 with chronophin, however, was not influenced by Ca^{2+}-ions (see Figure 15).

By employing chemical crosslinking, I could show in the present work that Ca^{2+} acts as a molecular switch that determines whether calmodulin or CIB1 associates with chronophin. When all three proteins together are subjected to formaldehyde crosslinking, CIB1 and chronophin preferentially interact in Ca^{2+}-free conditions, while the calmodulin/chronophin-complex is predominant in the presence of elevated Ca^{2+}-levels, suggesting that CIB1 and calmodulin are competing for the same or overlapping interaction sites on chronophin (see Figure 23). This is supported by the previously mapped interaction sites of CIB1 and chronophin, and the bioinformatically predicted calmodulin binding site on chronophin. We therefore hypothesize that under resting cell conditions and low intracellular Ca^{2+}-concentrations of approximately 100nM [292] a CIB1/chronophin association might be prevalent, while the 10- to 100-fold elevated Ca^{2+}-levels [292] that can occur during signaling lead to the formation of calmodulin/chronophin-complexes. It is possible that CIB1/chronophin and Ca^{2+}/calmodulin/chronophin fulfill different, currently unknown cellular functions. Calcium signaling can be restricted to narrow subcellular compartments [293], supporting the initial findings that chronophin is strictly regulated in a manner dependent on the spatiotemporal context [71].

The proposed Ca^{2+}-dependent switch of chronophin interactors resembles the regulation of the Ca^{2+}/calmodulin-dependent serine/threonine phosphatase calcineurin/PP2B. Calcineurin is an obligate, constitutive hetero-dimer composed of the catalytic subunit calcineurin A (CNA) and the regulatory subunit calcineurin B (CNB), which is structurally highly homologous to CIB1 [206]. The C-terminus of CNA contains a calmodulin binding site and an autoinhibitory domain that suppresses the phosphatase activity

at basal cellular Ca^{2+}-concentrations. At elevated Ca^{2+}-levels, calmodulin binds to CNA, displaces the autoinhibitory domain and fully activates the phosphatase [235, 258]. Although chronophin is structurally unrelated to calcineurin and the association of chronophin and CIB1 is supposedly dynamic, it is intriguing to speculate that chronophin might be another Ca^{2+}/calmodulin-regulated serine/threonine phosphatase besides calcineurin.

Ternary complexes, consisting of chronophin, CIB1 and calmodulin were never detected using chemical crosslinking, although they are hypothetically possible. Crosslinking is dependent on the presence and accessibility of suitable residues in the interacting interfaces, thus the absence of detectable cross-linked CIB1/calmodulin/chronophin-complexes might be attributed to the limitations of the method.

Other methods that were employed to investigate the binding of CIB1 and calmodulin to chronophin, such as isothermal titration calorimetry, analytical size exclusion chromatography, native PAGE, native agarose gel electrophoresis and analytical ultracentrifugation failed to detect interactions, indicating weak and/or transient binding of the proteins under the tested conditions. Although most published interactions involving calmodulin and CIB1 are of rather high affinity [216, 234, 294-296], there are also reports of weak and transient interactions with these proteins [297-299]. Transient protein-protein interactions (TPPIs) play an emerging role in cellular functions [300], and it has been shown that TPPIs often induce conformational changes in the respective protein [301, 302]. The interaction site of CIB1 on chronophin was experimentally mapped by yeast-two-hybrid screens to a loop just upstream of the capping domain, at the border between catalytic domain and capping domain. The binding of CIB1 (or Ca^{2+}-calmodulin) might therefore induce inter-domain movements in chronophin, as they have been reported for HAD-type phosphatases of other subfamilies [99, 100, 303]. These domain open-close-movements were implicated to be crucial for substrate binding and solvent inclusion/exclusion during catalysis. Domain movements in chronophin might therefore be necessary to facilitate the access of phosphorylated protein substrates into the deep catalytic pocket of the protein. This may be particularly relevant for proteins that are not phosphorylated at a terminal residue (as is the case for Ser^3-phosphorylated cofilin-1), such as the chronophin substrate SRC-3. While flexible phosphorylated termini of proteins might be able to access the catalytic site of capped HAD-type phosphatases [304], this seems unlikely for proteins phosphorylated at rigid structural elements, unless the access is facilitated by an opening of the catalytic cleft. The described calcium switch that determines whether CIB1 or calmodulin interacts with chronophin might therefore be important for discriminating between different phospho-protein substrates in a calcium-dependent manner. This hypothesis, however, is highly speculative, as the proposed mechanism of *extrinsic* regulation of HAD-type phosphatase domain movement has not been shown to date. Attempts to co-

crystallize the protein complexes failed, probably due to the transient character of the bimolecular interactions, and the enrichment of formaldehyde-crosslinked protein complexes did not yield enough protein for crystallization experiments (not shown). Thus, the biochemical and structural effects of CIB1 and calmodulin on chronophin remain elusive and deserve further study. The crosslinked complexes, however, could be used for future studies to experimentally verify the interaction sites of chronophin and CIB1 or calmodulin by employing mass spectrometry. This combination of methods has been successfully used to map protein-protein interfaces of complexes in solution [305].

The effect of CIB1 and calmodulin on the chronophin activity towards the known substrates pyridoxal 5'-phosphate (PLP) and serine^{3}-phosphorylated cofilin-1 were tested, showing no difference between chronophin alone and chronophin in the presence of the putative interactors CIB1 and calmodulin. Also, no changes in the phospho-peptide selectivity were found when a commercially available phospho-protein phosphatase substrate screen containing 360 known human phosphorylation sites was used. These results suggest that either the tested substrates were not the physiological targets of the respective complexes, that the complexes were missing additional subunits or other factors needed for proper function, or that the functions of the complexes are generally unrelated to the modulation of chronophin's substrate specificity and selectivity. CIB1 and calmodulin have been implicated in a variety of different cellular functions (see introduction), acting through a number of different mechanisms, including the introduction of conformational changes in the target proteins (i.e. displacement of an autoinhibitory domain), competition with other interactors, and scaffolding [256, 257, 259]. CIB1 has additionally been shown to mediate myristoylation-dependent membrane targeting [219, 233]. All these mechanisms potentially apply for the interaction with chronophin and will need further studies to elucidate how CIB1 and calmodulin influence the function of chronophin in cells. A. Hoffmann (this group), however, could not show a Ca^{2+}-dependent translocation of chronophin to the plasma membrane (see thesis A. Hoffmann).

The absence of *in vitro* phospho-cofilin phosphatase activity has been reported before for recombinantly expressed chronophin (unpublished data, A. Hoffmann). In fact, the dephosphorylation of serine^{3}-phosphorylated cofilin employing recombinantly expressed and purified chronophin has only been shown once, using GST-tagged human chronophin, which has been purified under denaturing conditions from bacterial inclusion bodies and subsequent refolding [71]. Other studies showing chronophin-specific cofilin dephosphorylation use proteins expressed in mammalian cells or rely on *in vivo* experiments [106, 194, 199]. This indicates that the protein used in the present work might lack post-translational modifications, interaction partners or was folded incorrectly. The chronophin crystal structures, however, are highly homologous to other structures of C2a-type HAD phosphatases, including prokaryotic enzymes

(see Figure 37), suggesting correct folding. The conformational changes needed for cofilin dephosphorylation might therefore be minimal. Minor changes in the structure of chronophin have been shown to greatly influence the phosphatase activity of this enzyme towards PLP (see 4.3 and 5.2), and might as well positively influence the ability of chronophin to dephosphorylate cofilin.

Although the *in vitro* studies failed to show effects of the newly identified chronophin interactors CIB1 and calmodulin on the tested substrates PLP and cofilin-1, Dr. Elisabeth Jeanclos in our group found that overexpression of CIB1 and chronophin leads to markedly decreased velocities of migrating cells. Importantly, the effect was dependent on the chronophin phosphatase activity, as no significant change in cell velocity was detected when using the phosphatase-dead mutant chronophin^{D25N}. Interestingly, simultaneous expression of calmodulin with CIB1 and chronophin effectively counteracted the reduced cell speed (not shown). These results indicate that CIB1 and calmodulin antagonistically participate in chronophin-dependent cell migration. Both, CIB1 and calmodulin, are known regulators of cofilin-mediated actin dynamics via LIM kinase 1 and slingshot (see introduction and [220, 241]), and both proteins have been implicated in the regulation of cell migration [220, 306]. The exact mechanism by which cell migration is regulated in this experimental setup remains unidentified, as no changes in the overall cofilin phosphocycling were detected. However, changes of the phospho-cofilin levels might occur at highly localized subcellular regions of actin dynamics during migration and escape the classical biochemical detection methods since the contribution to the overall phospho-cofilin pool is minor. Thus, these results do not exclude cofilin-1 as a target of the detected CIB1/calmodulin-regulated, chronophin-dependent effects on cell migration. Other substrates of the CIB1/chronophin- or calmodulin/chronophin-complexes remain possible as well, such as the known chronophin substrate steroid receptor coactivator 3 (SRC-3). The PAK1 dependent phosphorylation of a SRC-3 splice variant (SRC-3Δ4), for example, has recently been shown to promote cell migration in a focal adhesion kinase (FAK) mediated process [307].

5.2 The role of chronophin dimerization

In order to study the function of chronophin dimerization, we generated a monomeric variant of this phosphatase and studied the effects of monomerization on the chronophin activity towards pyridoxal 5'-phosphate (PLP) as a substrate. Both, homodimeric chronophin^{WT} and the monomeric chronophin point mutant were crystallized and structural analysis led to the discovery of a previously unknown mode of allosteric regulation of chronophin through a homophilic intermolecular interaction.

The formation of homo-dimers or higher order oligomers is a common phenomenon among proteins, providing them with structural advantages such as improved stability [308] and increased complexity, often mediating the regulation of enzymes [309], ion channels [310], receptors [311] and transcription factors [312]. This makes homo-oligomerization a commonly used modifier of a multitude of cellular processes like signaling, trafficking, metabolism, cell-cell-adhesion processes and gene expression. It has been suggested that the advantages of homo-oligomerization, compared to single-chain multidomain proteins are, that the association of identical single subunits into a larger functional unit helps to minimize the genome size, while at the same time facilitating quality control by simplified folding processes and exchangeability of the single subunits. Furthermore, the ability of homo-oligomers to associate and dissociate can be used as a regulatory concentration sensing mechanism [313-315]

Among 'classical' phosphatases, homo-dimerization is a known mechanism for activity regulation that underlies diverse modes of action. For receptor-like protein tyrosine phosphatases (RPTPs) such as PTPα, CD45, and SAP-1 it could be shown that dimerization negatively regulates catalytic activity by reciprocal occlusion of the catalytic sites [316, 317]. Dimerization itself might be regulated by ligand binding [16], or as shown for PTPα, by phosphorylation [318] and oxidative stress at elevated H_2O_2 levels [319]. In the case of PTPσ, dimerization could be identified as a factor that influences ligand binding and isoform specificity [320]. The *E. coli* alkaline phosphatase in contrast is an obligate dimer that loses catalytic activity and structural stability upon monomerization [321], indicating that oligomerization is potentially able to regulate phosphatase activity in a positive or negative manner.

Interestingly, a search for structures of haloacid dehalogenase-like hydrolases in the protein data base (PDB) revealed that out of the 175 unique entries with 90% sequence identity cutoff, that was used to reduce the number of multiple entries and mutant proteins, 100 (57%) hydrolases can be found that form homo-oligomers, compared to 73 (42%) structures assigned as monomers and two entries of hetero-oligomers (1%). Among the oligomeric HAD-like hydrolases, homo-dimers are the most abundant species (70%), followed by homo-tetramers (23%), homo-octamers (4%) and homo-trimers, homo-hexamers and

homo-dodecamers with one single entry each (1%). Although more than half of HAD-like hydrolases are homo-oligomers, there is not much known about the mechanistic reasons for the constitutive oligomerization of this class of enzymes. So far, the mechanisms and functions behind homo-oligomerization have only been studied for some members of the C0 and C1 subfamilies of HAD phosphatases. For example, structural analyses of the capless C0 phosphatase member KdsC from *E. coli* [322] revealed that tetramerization can be used for solvent exclusion, as each monomer acts as a cap for the adjacent molecule in the tetramer, thereby forming the active site pocket at the interface of two neighboring molecules. The *Haemophilus influenzae* C0-type phosphatase 8KDO [92] uses a similar tetramerization mechanism for 'pseudocapping'. In the case of the bifunctional T4 polynucleotide kinase/phosphatase PNKP, another member of the C0 subfamily of HADs, tetramerization is enabled by dimerization of the kinase domain and the phosphatase domain. It could be shown, that disruption of the phosphatase dimer-interface leads to ablation of phosphatase activity, since dimerization of this domain provides stability of the active site [323].

For members of the C1 subfamily of HAD hydrolases, several studies have addressed the relevance of homo-oligomerization. The native enzyme of the mammalian cytosolic 5'-nucleotidase (cN-II), for instance, forms tetramers. A dimeric mutant of this protein showed residual activity, whereas the monomer was completely inactive, making the changes of the oligomeric state of cN-II a possible mechanism to regulate the enzyme's specific activity [324]. The same applies for the *Haemophilus influenzae* (P4) acid phosphatase, where the dimerization appears to be important for catalysis, as intersubunit contacts stabilize the active site [325]. The soluble epoxide hydrolase 2 (sEH2) requires dimerization for hydrolase activity [326], although the exact mechanism is not yet clear. Taken together, these studies indicate that homo-oligomerization of HAD phosphatases is a common mechanism required for proper catalytic activity. The functions and mechanisms of C2 subfamily HAD hydrolase oligomerization, however, have not yet been investigated, although oligomerization seems to be particularly important in the C2a subfamily, the only group of HAD hydrolases in which - according to PDBePISA - all structurally characterized members form homo-oligomers.

Here, for the first time a monomeric mutant of a C2a-capped HAD was generated and subsequently compared biochemically and structurally to the wild-type enzyme. Based on the existing structure of human chronophin, we introduced a double mutation ($Ala^{194/195}Lys$) in the dimerization interface of the murine homolog using site directed mutagenesis (C. Kestler). The opposing positive charges of the lysines led to complete disruption of the dimerization, which could be clearly confirmed *in vitro* by analytical size exclusion chromatography, atomic force microscopy and analytical ultracentrifugation (see Figure 28 and

Figure 29). Pulldown assays using lysates from HEK293 cells overexpressing the respective proteins additionally confirmed the oligomeric states of wild-type chronophin and the mutant protein in cells (see Figure 30).

The monomeric variant of murine chronophin, termed chronophin^{KK}, displayed a strongly reduced catalytic activity when tested against the physiological substrate pyridoxal 5'-phosphate (PLP). Luckily, we were able to crystallize both, the murine wild-type protein and the monomeric mutant, allowing a structural comparison of both protein isoforms. The crystallographic models revealed that the overall structure of chronophin^{KK} was not altered by the introduced mutations that led to monomerization. The only significant difference was the positioning of the substrate specificity loop, which in chronophin^{WT} is held in place by interactions with the other protomer of the dimer. This β-hairpin harbors a histidine residue (His^{178}) that has been shown to be critical for the coordination of the pyridine ring in PLP [94]. We therefore concluded that the malpositioning of the substrate specificity loop in chronophin^{KK} leads to a drastic reduction of the binding affinity towards PLP, as confirmed experimentally by the dramatic rise in the K_m-value in the kinetic measurements, whereas the v_{max} remained largely unchanged (see Table 37). This was supported by detailed structural comparisons of the catalytic core residues of chronophin, which remained unaffected by the monomerization, when compared to the homodimeric wild-type protein in the absence or presence of BeF_3^- (see Figure 36). These data support the conclusion that the catalytic activity of chronophin *per se* remained unaltered by monomerization. Comparative isothermal titration calorimetric measurements of BeF_3^- binding to chronophin^{WT} and chronophin^{KK} showed that the binding affinity of chronophin^{KK} is significantly reduced, when compared to chronophin^{WT} (see Figure 32 and Table 38). As the BeF_3^--binding only represents interactions with the active site core residues, which are unaltered by monomerization as seen in the crystal structures, we hypothesize that the accessibility of the active site is reduced by occlusion as a result of the tilted substrate specificity loop.

In order to find out whether the mode of dimerization is a unique feature of chronophin or if this is a characteristic trait of C2a-capped HAD hydrolases in general, we analyzed all available structures of this HAD subfamily by performing a DALI structure similarity search using human chronophin (PDB code 2OYC) as a search model. The results were scanned manually for members of the C2a subfamily of HAD hydrolases, resulting in 16 highly homologous structures in addition to human chronophin and the newly solved structure of murine chronophin (see Table 40). Next, the oligomeric state of these 16 structures was determined employing the PDBePISA online tool with the outcome that every single one of these structures is a dimer with a buried surface area of ~1000 Å^2 at the dimer interface. Five of the analyzed proteins are likely to be tetramers. Interestingly, besides the generally high degree of structural homology,

there is a strong structural conservation of the dimer interface, which is in all cases composed of the equivalent helices in the capping domain as described for chronophin. In addition, the β-hairpin which has been identified to mediate substrate specificity in chronophin, is present in all C2a-capped HADs and participates in dimer formation (see Figure 38). These findings suggest that dimerization is a prerequisite for proper positioning of this particular loop that might likewise serve as a substrate specificity loop in other members of the C2a subfamily of HAD hydrolases. It thus appears probable that the homodimerization of C2a-type HAD phosphatases generally serves to hold the β-hairpin/potential substrate specificity loop in place.

It is intriguing to speculate, whether this mechanism is of physiological relevance in controlling the C2a subfamily activity through their intracellular concentration or post-translational modifications at the dimer-interface. Hypothetically, low protein concentrations or modifications at the interface, such as phosphorylations, would lead to dissociation of the respective dimers and a subsequent reduction of enzymatic activity.

The uncovered mechanism of allosteric activity regulation via dimerization also represents an interesting target for a pharmacological strategy to specifically reduce the C2a-type HAD hydrolase activity of enzymes playing a role in human disease. A novel type of synthetic, cell-permeable peptides, called stapled peptides, could be ideally suited for this purpose, as they are specifically designed to target protein-protein interaction sites (suggested by Dr. M. Köhn, EMBL Heidelberg). These bioactive peptides of 12 to 35 amino acids are locked in an α-helical conformation through the site-specific introduction of a chemical hydrocarbon brace (for more details see Figure 48). This modification greatly enhances the stability, cellular uptake through endocytic vesicle trafficking, proteolytic resistance, serum half-life and target affinity of the peptides, and has been successfully applied to disrupt protein-protein interfaces [327-329].

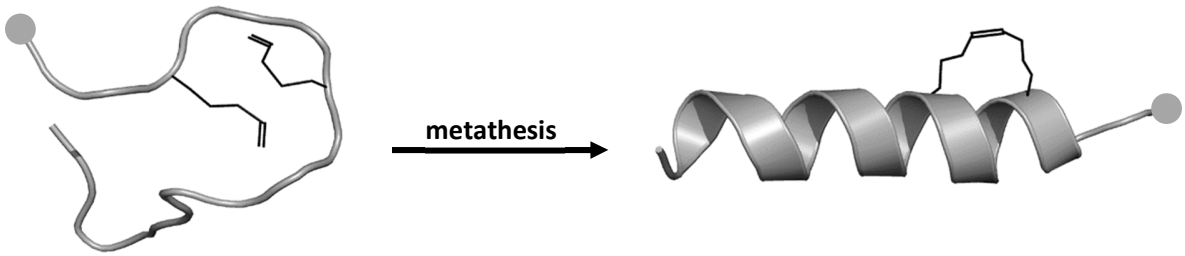

Figure 48. General strategy for the all-hydrogen stapling of peptides. A peptide containing two α-pentenyl-alanines at positions i and i+4 is synthesized using standard methods, such as the 9-fluorenylmethyloxycarbonyl assisted solid-phase peptide synthesis. The α-pentenyl-alanines serve as intramolecular cross-linkers, which are connected by ruthenium-catalyzed olefin metathesis [2]), covalently locking the peptide into a stable α-helical conformation. Variations of the α-alkyl-alanine positions on the same face of the helix, such as i and i+3 or i+7, can be employed by varying the stereochemistry and lengths of the cross-linker.

A method to assess the dimerization of HAD phosphatases, such as the soluble epoxide hydrolase 2 (sEH2), a C1 subfamily HAD hydrolase, has already been proposed [326]. The assay relies on a split firefly luciferase protein fragment-assisted complementation (SFL-PFAC) system, and could be used to screen the ability of stapled peptides to interfere with the dimer interface of C2a-type HAD phosphatases. Other protein-fragment complementation assays, such as the split green fluorescent protein (GFP) complementation assay, could be used as well. The principle of these assays is shown in Figure 49.

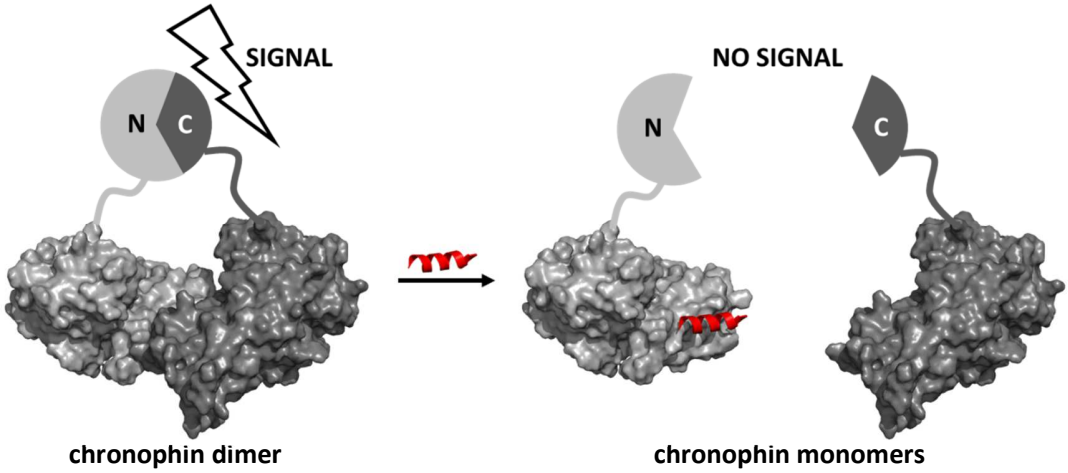

Figure 49. Principle of protein-fragment complementation assays. The assay relies on a reporter protein, which can be split into two parts. Here, N and C indicate the N- and C-terminus of the split protein. These two parts are fused to the interacting target proteins, or, as shown here, to the N-terminus of murine chronophin (PDB code 4BX3). Interaction of the target proteins reconstitutes the reporter protein, generating a detectable output, such as colorimetric or fluorescent signals. This assay could be used to screen for stapled peptides (red), which interfere with chronophin dimerization.

After successful screening for peptides, which compete with chronophin dimerization, other methods such as isothermal titration calorimetry and the established malachite green assay can be used to further characterize and evaluate the effects of the stapled peptides on chronophin.

Taken together, our results show that dimerization is a prerequisite for proper enzymatic function of chronophin, as the dimer interface involves intermolecular contacts to the substrate specificity loop. The exact positioning of this loop is required for correct PLP coordination and subsequent PLP hydrolysis. The introduction of a double mutant leading to monomerization of the enzyme caused a displacement of the aforementioned loop in the otherwise unaltered structure and this led to a drastically reduced enzymatic activity. The mode of interaction between the two protomers in chronophin is structurally highly conserved among all other structurally characterized members of the C2a HAD hydrolase subfamily, despite low sequence homologies. We therefore conclude that dimerization is essential for specific

enzyme activity in this subfamily of C2a-capped HAD hydrolases. Our results contribute to the mechanistic understanding of HAD structure-function relationships and specificity control, and may finally offer a possibility to specifically target these enzymes pharmacologically.

5.3 Determinants of substrate specificities in the C2a-type HAD hydrolases chronophin and AUM

Phosphatases acquired specificity using a variety of mechanisms. While most catalytic domains of the PPP family form substrate- and function-specific dimeric or trimeric holoenzymes, other protein phosphatase families, such as the PTPs or PPMs phosphatases, gained substrate specificity by fusing regulatory, scaffolding or targeting subunits in sequential order to the catalytic domains, yielding multidomain proteins (see introduction). In the case of HAD-type phosphatases, the structurally conserved catalytic Rossmann-fold core domain was accessorized by capping domain insertions at two distinct sites. Based on this domain architecture of HAD phosphatases, it has been suggested that the conserved Rossmann-fold catalytic domain of HAD phosphatases contains the residues to bind and hydrolyze the phosphate mono-ester, while the capping domain harbors the specificity determinants for the substrate's leaving group [68, 330]. Several X-ray crystallographic studies have already addressed the determinants of substrate specificity in the different HAD subfamilies, mostly investigating prokaryotic enzymes [95, 304, 331, 332]. However, the structure-function relationships of mammalian HAD-type phosphatases have not yet been fully explored.

In this thesis, the role of the capping domain in the C2a-type HAD hydrolase substrate specificity and selectivity was investigated by generating an enzyme consisting of the catalytic core of murine chronophin equipped the capping domain of the closest murine chronophin paralog AUM, an aspartate-based, ubiquitous, Mg^{2+}-dependent HAD phosphatase that has recently been identified and characterized in our group [288]. Despite the high similarity on the amino acid level (implying structural homology), both proteins exhibit very different substrate specificities. AUM has been shown to specifically dephosphorylate phospho-tyrosine residues, adenosine and guanosine di-/tri-phosphates (ADP>ATP≈GTP≈GDP) and the generic phosphatase substrate *para*-nitrophenyl phosphate (*p*NPP) [288]. Physiological substrates of AUM have not yet been identified. Chronophin, in contrast, has so far been shown to exclusively

dephosphorylate phospho-serine/threonine residues of proteins [71, 168] and to specifically act on phosphorylated vitamin B_6 derivatives, such as pyridoxal 5'-phosphate or pyridoxic acid 5'-phosphate [70].

In order to test, whether replacing the chronophin cap with the AUM cap could interchange the respective protein's substrate preferences, the aforementioned "CAC" termed hybrid protein was generated. The protein was recombinantly expressed, purified and tested for substrate selectivity using PLP and *p*NPP as substrates, showing that the CAC hybrid protein did not exhibit activity towards *p*NPP comparable to AUM (see Figure 40). This outcome was not surprising, as *p*NPP is an artificial phosphatase substrate and the determined K_m-value (3.13 ± 0.36mM, [288]) of AUM towards this substrate is indicative of a rather low specificity. This is comparable to results obtained for other protein phosphatases, which show apparent K_m-values for *p*NPP in a millimolar range [333, 334], while the HAD-type phosphotyrosine phosphatase eyes absent 3 (Eya3) displays a ~30-fold higher K_m [72]. Thus, the experiment may have succeeded by using a physiological (but yet unknown) AUM substrate. In contrast, the CAC-hybrid completely lost the ability to hydrolyze PLP, already indicating that substrate specificity determinants are located in the capping domain, assuming that the protein is correctly folded (see below). The reciprocal experiment, performed by A. Seifried (see [288] and thesis A. Seifried), successfully transferred part of chronophin's PLP specificity to AUM by fusing the chronophin cap to the AUM catalytic domain. This strongly supports the hypothesis of C2a subfamily capping domains as important factors determining substrate specificity, showing for the first time that domain swaps between two HAD-type phosphatase paralogs could, at least partially, interchange the respective enzyme's substrate preferences.

However, the binding of a substrate, and therefore the substrate specificity, cannot be regarded independently of the enzyme's catalysis, as expressed by the definition of the specificity constant k_{cat}/K_m. Thus, enzyme-specific differences in the binding of the phosphorous group to the catalytic core and the subsequent rate of substrate hydrolysis may exist, although the domain that harbors the four catalytic motifs is highly conserved among HAD-type hydrolases. Such differences could for example explain why the AUM catalytic domain equipped with the chronophin capping domain is not as efficient in hydrolyzing PLP as wild-type chronophin [288]. Indeed, A. Seifried performed mutational analyses of residues in the AUM catalytic core which affected the activity towards *p*NPP (see [288] and thesis of A. Seifried). The detailed structure-function relationships of these mutations currently remain unknown, since the structure of the AUM catalytic domain has not yet been solved. The codependence of the catalytic domain and the capping domain has not been investigated so far and would therefore be an interesting topic to study in the future.

The X-ray crystallographic structure determination of the CAC-hybrid allowed a detailed structural comparison of the two paralogous C2a-type HAD phosphatase caps of chronophin and AUM, furthermore providing the first available partial structure of AUM. The structural comparisons of the chronophin and AUM capping domains showed that the two proteins are indeed highly homologous, as expected from the sequence similarities. However, subtle differences could be revealed, which may be of importance for substrate selectivity, such as the topology of the active site, the existence of a transverse loop in AUM and the slightly different orientation of the catalytic domain towards the capping domain (see Figure 41). A combination of the structural comparison with the biochemical characterization of AUM performed by A. Seifried and evolutionary analyses of both proteins, performed in collaboration with Prof. J. Schultz, provided additional insights into HAD-type phosphatase specificity determinants and how the differences might have evolved [288].

A phylogenetic analysis revealed that chronophin and AUM evolved via gene duplication and subsequent neofunctionalization [288], a mechanism which has been proposed for the diversification of HAD-type hydrolases and other proteins in general [335, 336]. The evolutionary rate of the two genes could not be distinguished, therefore the determination of the ancestral gene was not possible. A more detailed analysis of the individual AUM and chronophin orthologs uncovered 16 positions of corresponding residues which are differently conserved in both orthologs (Table 44, [288]), and might therefore be specificity-determining positions. Interestingly, most of these positions are located in the capping domain (residues ~100-235 of AUM and ~85-210 of chronophin), supporting the hypothesis of a substrate recognition site which evolved independently of the catalytic site after genetic duplication, and led to neofunctionalization. Out of the differentially conserved positions, Leu^{204} in murine AUM and His^{178} in murine chronophin appeared to be of particular significance. His^{178} of murine chronophin is located in the protein's substrate specificity loop, and has previously been shown to be crucial for the coordination of PLP (see introduction and [94].). Importantly, a mutation exchanging Leu^{204} in AUM with a histidine residue reduced AUM's phosphatase activity towards *p*NPP down to ~63% and concomitantly increased the PLP phosphatase activity to a level similar to the hybrid protein consisting of the AUM catalytic core and the chronophin cap [288], confirming the importance of distinct, differently conserved residues within the capping domain for the determination of substrate specificity.

Table 44. Differently conserved sites between AUM and chronophin. Modified from [288]. The shown residues differ between the paralogs AUM and chronophin, but are conserved within the orthologs and therefore represent putative specificity-determining positions. Human and murine chronophin differ in the length of their amino acid sequence, therefore the deviant human positions are indicated in parentheses. The indicated positions in AUM are identical in the human and murine sequences of the protein. The respective amino acids found in the urochordate Ciona sp. are given for comparison with the sequence that predates the duplication event of a common ancestor gene. The Z-score is used to determine the significance of a local alignment with higher values indicating stronger conservation, compared to an average position in the alignment [337]

Amino acid and position in AUM	Amino acid and position in chronophin	Amino acid in *Ciona sp.*	Z-score
Leu^{204}	His^{178} (His^{182})	Met	6.88
Arg^{203}	Trp^{177} (Trp^{181})	Arg	6.58
Asn^{199}	Asp^{173} (Asp^{177})	Asn	6.56
Ala^{128}	Gly^{117}	Ala	6.55
Val^{244}	Ile^{218} (Ile^{222})	Ile	5.87
Asp^{263}	Glu^{237} (Glu^{241})	Asn	5.58
Tyr^{178}	Phe^{152} (Phe^{156})	Tyr	5.56
Cys^{217}	Ser^{191} (Ser^{195})	Cys	5.47
Thr^{101}	Ser^{88}	Thr	5.35
Lys^{72}	Arg^{63}	Lys	5.34
Leu^{268}	Phe^{242} (Phe^{246})	Phe	5.31
Val^{136}	Ala^{125}	Leu	5.00
Gly^{197}	Ala^{171} (Ala^{175})	Ala	4.96
Val^{169}	Leu^{143} (Leu^{147})	Leu	4.94
Ala^{226}	Ser^{200} (Ser^{204})	Ala	4.80
Gly^{100}	Ser^{87}	Ser	4.78

Other noteworthy differences are the charge neutral Asn^{199} and hydrophobic Lys^{72} in murine AUM, which correspond to the acidic Asp^{173} and positively charged Arg^{63} in murine chronophin, respectively. The side chains of these residues are directly oriented towards the active site cleft, and therefore influence its chemical properties, such as the hydrophobicity and the electrostatic environment. Theoretically, a very limited number of positions in the capping domain facing the active site cleft could be sufficient to create a vast amount of chemically and topologically differing binding pockets for the substrate leaving group. This raises the question whether the differently conserved amino acid positions found in chronophin and AUM are also conserved in other members of the C2a subfamily of HAD-type phosphatases, potentially allowing a prediction of the chemical properties of the substrate leaving group. For this, a detailed evolutionary analysis combined with structural comparisons of other C2a subfamily members and their orthologs in different species would be needed. Unfortunately, information regarding physiological substrates and the number of available structures of this class of enzymes is very limited.

A number of the differentially conserved positions in chronophin and AUM are located on the protein surface and appear to participate in the dimerization of the enzyme (Phe^{152}/Trp^{177}/Ser^{191}/Ser^{200} in murine chronophin and Tyr^{178}/Arg^{203}/Cys^{217}/Ala^{226} of murine AUM; see Figure 50). Dimerization has been shown to be important for chronophin activity by correctly positioning of the substrate specificity loop, thus allosterically regulating substrate specificity in this enzyme. In murine chronophin, the interaction of Trp^{178} with Arg^{185} and Arg^{163} of the other protomer seemed to be of particular importance for this mechanism. Similarly, in human AUM the differentially conserved Arg^{203}, which corresponds to Trp^{178} in murine chronophin, interacts with Gln^{189} and Gln^{227} of the other protomer in the dimer, possibly fulfilling the same function in correctly positioning the substrate specificity loop, and thereby supporting the hypothesis that dimerization is generally important for the proper function of C2a-type HAD phosphatases (see 4.3).

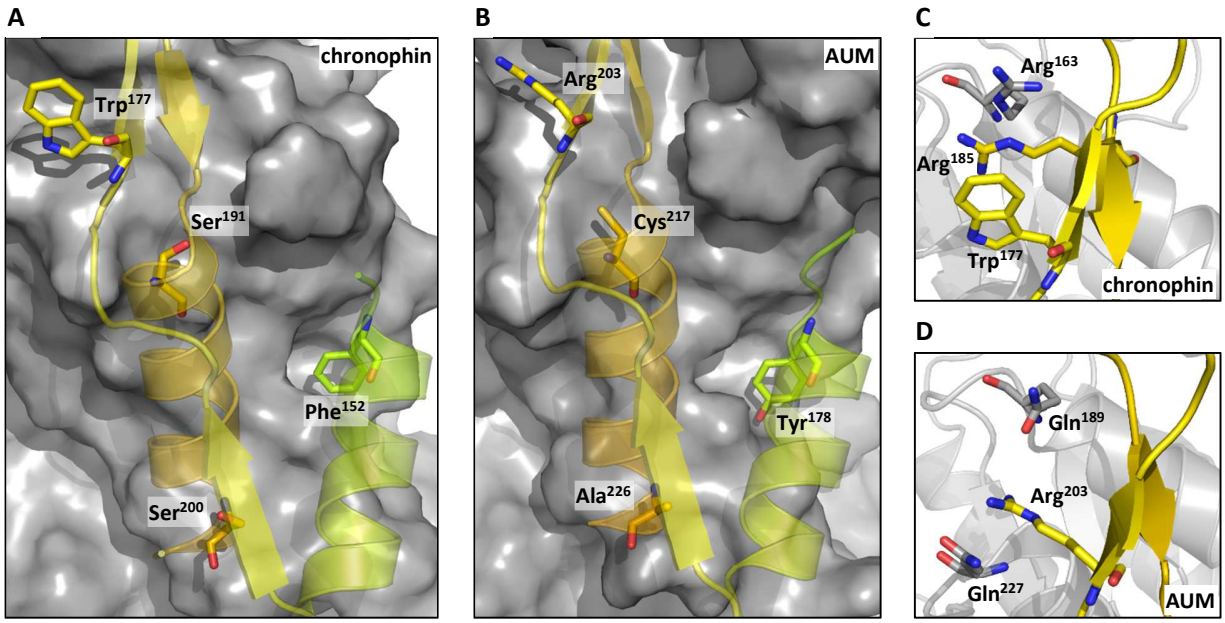

Figure 50. Differently conserved residues in the murine chronophin and AUM dimer interfaces. A and B show the dimer interfaces of murine chronophin and AUM, respectively. One protomer is shown as surface representation (gray), the other protomer is shown as transparent cartoon representation, with the differently conserved residues shown as sticks. The cartoon representations are reduced to the dimer interface for better visualization. C, The differently conserved residue Trp^{177} of chronophin has been shown to be important for the coordination of the substrate specificity loop (this thesis and [287]) by interacting with Arg^{185} and Arg^{163}, the latter of the other protomer in the dimer (shown in gray). Similarly, the corresponding conserved residue Arg^{203} in the AUM substrate specificity loop interacts with Gln^{189} and Gln^{227}, which are both located in the other protomer of the dimer (D, shown in gray). This interaction possibly serves for the correct positioning of the substrate specificity loop of AUM.

Three of the differently conserved residues are located on the protein surface (Gly^{117}/Ala^{125}/Glu^{237} in murine chronophin and Ala^{128}/Asp^{263}/Val^{136} in murine AUM) and might therefore participate in regulatory protein-protein interactions, while the remaining differently conserved residues are buried inside the protein, probably stabilizing the protein's structure.

Evolutionary analyses furthermore identified a set of residues that are highly conserved in one paralog, but show variability in the other [288]. In murine chronophin, three of the five sites are located on the surface (Arg^{13}/Arg^{74}/Glu^{83}) and might play a role in protein-protein interactions, while one is located at the dimer interface of the protein (Ala^{194}), and the last one is buried inside the protein (Ala^{92}). Interestingly, Arg^{74} is located next to the putative CIB1 interaction site, which has been mapped to residues 75-85 by employing yeast two-hybrid screens (see 1.5.3).

The residues, which were found to be conserved in AUM (Arg^{41}/Gly^{144}/Glu^{207}/Pro^{317}) are all located on the protein surface. However, Glu^{207} is of special interest as it is located on top of the substrate specificity loop and might therefore participate in the initial binding of AUM to its substrate.

Taken together, the combinatory approach employing biochemical characterization, mutational studies, domain swap experiments, evolutionary analyses [288] and the solution of the X-ray crystallographic structure of the CAC-hybrid (this thesis, part of [288]) greatly enhanced the understanding of substrate specificity determinants in the closely related paralogs chronophin and AUM. We could show that subtle differences in the capping domain of this structurally highly conserved subfamily of HAD phosphatases are decisive for non-overlapping substrate specificities, including the preference for serine/threonine- or tyrosine-phosphorylated proteins [288]. The differently conserved Leu^{204} in AUM and His^{178} in murine chronophin could be identified as a key residue in the determination of substrate specificity. This concept might be generally valid for members of the C2a-subfamily of HAD phosphatases and could therefore significantly contribute to the identification of substrates and the development of specific inhibitors.

5.4 Generation and characterization of chronophin inhibitors

Numerous HAD-type phosphatases are associated with pathological conditions including cancer, cardiovascular, metabolic and neurological disorders [7], and the emerging roles in human diseases make this class of enzymes interesting therapeutic targets for structure-based drug design. To date, the number of studies describing specific HAD phosphatase inhibitors is extremely limited. The results of these studies, however, appear to be promising starting points for a future *in vivo* use of HAD-type phosphatase inhibitors. For example, small molecular weight compounds inhibiting the human DNA-repair enzyme polynucleotide kinase/phosphatase (PNKP) are currently being studied for their potential to increase the sensitivity of human tumors to gamma-irradiation [338].

Additionally, a series of compounds could be identified, which specifically inhibit the eyes absent 2 (Eya2) phosphatase activity [339]. The Eya family of HAD phosphatases exhibit protein tyrosine phosphatase activity and are furthermore essential co-activators of the Six family of homeobox transcription factors [72, 97, 340]. Based on the role of Eya proteins for transformation, migration, invasion and metastasis of breast cancer cells [341-343], it is foreseeable that specific Eya inhibitors might be anti-tumorigenic and anti-metastatic, and could possibly sensitize cancer cells to DNA damage inducing therapies.

Inhibitors targeting the soluble epoxide hydrolase 2 (sEH2), which has recently been shown to dephosphorylate precursors of cholesterol biosynthesis besides hydrolyzing epoxyeicosatrienoic acids (lipid signaling molecules) [102, 344, 345], are being developed for the treatment of cardiovascular diseases and inflammatory disorders [344].

While most of the identified inhibitors were found by employing high throughput screens, some studies report the rational design of competitive HAD phosphatase inhibitors based on substrate analogs. For instance, the phosphoserine phosphatase (PSP) inhibitor 2-amino-3-phosphonopropionic acid (D- or L-AP3) is a non-hydrolysable analog of phosphoserine [346]. PSP catalyzes the final step of the phosphorylated pathway of L-serine biosynthesis [347], an important pathway in cell proliferation, making PSP inhibitors interesting compounds for cancer treatment [348]. The enantiomer D-AP3, however, shows only low inhibitory activity (IC_{50} 990µM) compared to other compounds, which were identified as uncompetitive PSP inhibitors, such as *p*-chloromercuriphenylsulfonic acid or glycerophosphorylcholine (IC_{50} 9.3µM or 18µM, respectively) [349].

Similarly, the trehalose-6-phosphate phosphatase (T6PP) of *Brugia malayi*, a nematode causing lymphatic filariasis, could be inhibited by the competitive, non-hydrolysable substrate analog trehalose 6-sulfate [350]. The accumulation of trehalose 6-phosphate has been shown to be toxic for the model nematode *Caenorhabditis elegans*, and T6PP is furthermore an essential enzyme in *Mycobacterium tuberculosis* [351, 352]. The inhibition of T6PP, which has no mammalian counterpart, might therefore be a basis for broad-range antihelmintic and antimycobacterial therapeutics.

In this thesis, for the first time chronophin inhibitors were characterized biochemically and structurally. The compounds are based on the structure of the phosphatase's low molecular weight substrate pyridoxal 5'-phosphate (PLP). For this, we replaced the 5'-phosphate group of PLP with a phosphonate. The 4'-position of the inhibitors pyridine ring was either substituted with an aldehyde, as in PLP, or an alcohol, as in pyridoxine 5'-phosphate (PNP). Furthermore, a double bond was introduced at the 5'-position of the pyridine ring in order to compensate the effect of the altered bond length due to the exchange of the phosphate ester oxygen atom by a carbon atom (see Figure 44). By employing dose-response assays and steady-state kinetic assays using PLP as a chronophin substrate, we could demonstrate that the double bond at the 5'-position had no impact on the potency of the inhibitors, while the existence of an aldehyde group at the 4'-position led to a ~4.3-fold decrease in the IC_{50}, compared to the alcohol compounds (see 4.5.2). These results are in line with the initial biochemical characterization of human chronophin as a PLP phosphatase, showing that the K_m for PLP (1.47µM) is lower than for PNP (5.19µM) [290], an indication of a higher affinity of chronophin towards PLP and structural analogs with an aldehyde at the 4'-position. I was able to solve the crystal structure of murine chronophin in complex with inhibitor 3, allowing a detailed analysis of the interaction. Based on this structure and the previously solved structure of human chronophin in complex with PLP [94], Asn^{60} could be identified as the residue that forms a hydrogen bond with the 4'-aldehyde in PLP or in inhibitors 1 and 2. This bond formation is not possible in compounds with alcohol substituents at the 4'-position, such as PNP or inhibitors 3 and 4, leading to a decreased binding affinity. Based on this information, we speculate that other substituents at this position of the inhibitors, which bring the aldehyde group or any other proton accepting functional group closer to Asn^{60}, might further increase the binding affinity of putative chronophin inhibitors. Additionally, the 4'-position substituents might influence the electron density of the pyridine ring, which interacts with $histidine^{178}$ of murine chronophin by π-electron stacking and therefore affect the inhibitor efficacies. An aldehyde group has a higher electronegativity than an alcohol group, thus attracts electrons from the pyridine ring stronger, possibly creating a more favorable environment for the stacking of π-electrons. In addition, it would be fascinating to investigate whether other aromatic residues, such as a

phenylalanine or tyrosine, would be as efficient in coordinating PLP or the inhibitors as the evolutionarily conserved histidine residue in the substrate specificity loop of chronophin.

The structure of murine chronophin in complex with inhibitor 3 solved in this work furthermore allowed us to speculate about other modifications of the inhibitors, which would ideally lead to higher efficacy and increased specificity. An inhibitor based on the structure of PLP might potentially target any PLP-dependent enzyme, and therefore unintentionally influence vital processes, such as the synthesis of neurotransmitters, glycogen breakdown, amino acid metabolism and heme synthesis [111-114, 116, 117]. Importantly, all known PLP-dependent enzymes coordinate the cofactor PLP via its aldehyde group at the 4'-position using a conserved mechanism [125, 126]. Thus, modifications at this position might exclude PLP-dependent enzymes from binding the inhibitor while at the same time increasing the affinity towards chronophin. A study in which PLP derivatives with varying functional groups at the 4'-position were tested as human chronophin substrates, indicates that substrates exhibiting negative charges/proton acceptors (aldehyde, carboxylic acid) at this position display significantly lower K_m-values and higher maximal velocities in kinetic studies than positively charged functional groups, such as the amino group in pyridoxamine 5'-phosphate. According to this study, PLP substituted with phenylalanine at the 4'-position (N-(5'-phospho-4'-pyridoxyl)phenylalanine) appears to be a better substrate than PNP, indicating that chronophin tolerates bulky substituents at this position, which could be used to improve the putative inhibitors [290].

The same study could show that modifications of arginines using phenylglyoxal (PG) led to the inactivation of chronophin, while PLP could protect the enzyme from PG inactivation. The authors therefore conclude that one or more arginines are involved in the binding of PLP [290]. Indeed, there are three arginines in the entrance of the active site. This positively charged region is an interesting target for the improvement of specific chronophin inhibitors, by replacing the 4'-position with negatively charged substituents long enough to access these arginines.

Increasing the specificity of the inhibitors towards chronophin and concomitantly decreasing the availability for other PLP-dependent enzymes should be the highest priority for future development and potential *in vivo* use of chronophin-specific inhibitors. However, other modifications of the existing chronophin inhibitors towards higher affinity are conceivable. For example, the use of other non-hydrolysable phosphate analogs with higher affinity towards the active site machinery of chronophin, such as sulfate, sulfonate or arsenate instead of a phosphonic acid. A difluoromethylphosphonate at the 5'-position could possibly form hydrogen bonds with serine[58] and backbone atoms of the catalytic domain, thus might lead to increased affinities. Also, replacements of the 2'-methyl group with other hydrophobic

substituents could be applicable in order to increase the hydrophobic interaction with tyrosine^{146} of the capping domain in murine chronophin (Tyr^{150} in the human ortholog). A selection of possible inhibitor modifications (suggested by Dr. D. Will, EMBL Heidelberg) is displayed in Figure 51.

The inhibitors characterized in this work are valuable tools for *in vitro* studies of chronophin. For example, investigations on the structure-function relationship of chronophin towards its substrate PLP will be greatly improved in the future. The inhibitors allow comparisons between wild-type chronophin and mutated versions, e.g. monomeric chronophin^{KK}, employing methods for direct affinity measurements, such as isothermal titration calorimetry, which could not be used with the substrate PLP.

However, a combination of the inhibitor modifications, leading to increased specificity and higher efficacy could ideally lead to the development of compounds for functional *in vivo* studies. We recently generated a chronophin knock-out mouse line and are currently investigating the effects of a chronophin loss on a biochemical and physiological level using this mouse model. Specific chronophin inhibitors would allow us to study the effects of chronophin loss in a more acute manner, without compensatory effects that often occur upon knock-out of a target protein [289]. Particularly, pathophysiological conditions, such as epilepsy, in which chronophin might play a role, would be of high interest [193-195], where the inhibition of chronophin might have positive effects on the outcome, implying a pharmacological use of chronophin-specific inhibitors. Interestingly, our characterization of chronophin knock-out mice revealed that chronophin functions as a non-redundant PLP phosphatase *in vivo*, showing significantly elevated PLP-levels in specific tissues, such as the brain, skeletal muscles and red blood cells. In other tissues, no differences could be detected compared to wild type animals (Dr. E. Jeanclos, data not shown). PLP has recently been shown to be beneficial in a number of cancers, such as colorectal tumors, non-small cell lung carcinomas (NSCLC) and breast cancer [353-356]. Importantly, elevated PLP-levels have been shown to sensitize NSCLC to apoptosis induced by physical and chemical stresses, including chemotherapeutics like cisplatin, positively influencing the disease progression in patients [354, 357]. The selective sensitization of tumors by promoting the apoptotic program of cells is also of great interest in radiation oncology [358].The positive effects of PLP on tumor progression and cancer therapy might be associated with the influence of PLP on the expression of p53. A recent preliminary study supports evidence that administration of pyridoxal increases the p21 gene expression via p53 activation in a number of human cancer cells and the mouse colon [359]. Both, the tumor suppressor protein p53 and the cyclin-dependent kinase inhibitor p21 can induce cellular growth arrest and mediate apoptosis [360, 361], and are therefore important targets for sensitizing tumors to chemo- or radiotherapy. In line with the aforementioned

studies, M. Schulze of our group could show that the experimental loss of chronophin by RNAi depletion in glioblastoma cells blocks *in vivo* tumor growth (see thesis M. Schulze).

In addition, preliminary results indicate that γ-aminobutyric acid (GABA)-levels are elevated in the brains of chronophin knock-out mice (Dr. E. Jeanclos, data not shown). GABA is the principal inhibitory neurotransmitter in the mammalian central nervous system and imbalanced GABA-levels, especially GABA-deficiencies, are associated with a number of neurological disorders, such as epileptic seizures, schizophrenia and anxiety disorders [362-364]. The concentration of GABA is regulated by the action of two PLP-dependent enzymes: the L-glutamic acid decarboxylase (GAD, two isoforms), which converts glutamate to GABA, and the GABA-aminotransferase (GABA-AT), which degrades GABA by transferring the GABA amino group onto 2-oxoglutarate yielding succinate semialdehyde and L-glutamate [365, 366]. Thus, GABA levels are directly PLP-dependent, and our data suggest that increased PLP-levels caused by chronophin knock-out subsequently lead to elevated GABA concentrations. Inhibiting chronophin might therefore be beneficial in in conditions caused by GABA deficiency. The biosynthesis of the neurotransmitters serotonin, dopamine, epinephrine and norepinephrine are also PLP-dependent, and it will be interesting to investigate the impact of chronophin loss on these important molecules.

Taken together these data suggest that pharmacological chronophin inhibition in order to acutely create elevated PLP-levels might be beneficial in certain pathophysiological conditions including cancer and several neurological disorders. The chronophin inhibitors presented in this work were biochemically characterized employing steady-state analyses and kinetic measurements, showing moderate inhibition with IC_{50}-values in the micromolar range and represent valuable tools for the future *in vitro* characterization of chronophin. These data, together with the crystal structure of murine chronophin in complex with inhibitor 3 solved in this thesis could be the basis for a rational drug design, finally leading to highly specific inhibitors with increased efficacy, which could be applied for *in vivo* studies of chronophin function or even serve as therapeutic agents. Another, different approach to specifically reduce the activity of chronophin has been proposed in this work: stapled peptides, which interfere with the chronophin dimerization might as well be used as molecular probes to investigate the role of this phosphatase *in vivo* (see 5.2). The generation, characterization and improvement of chronophin inhibitors is a fascinating topic, which should definitely be addressed in the future.

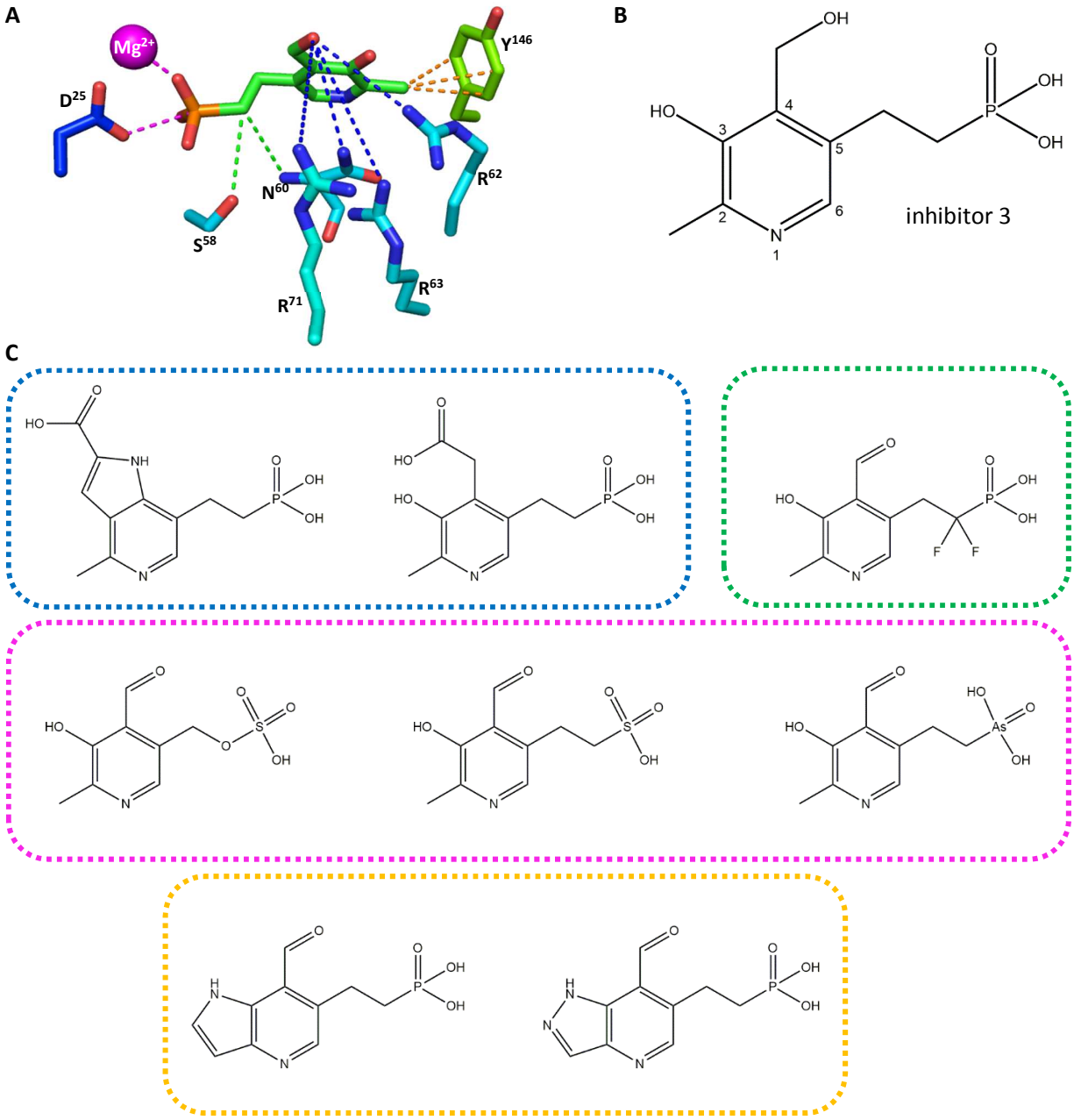

Figure 51. Possible modifications of chronophin inhibitors. A, Structure of inhibitor 3 with adjacent residues of murine chronophin, which might be targeted in order to increase the specificity and affinity of the existing inhibitors. Four different sites for possible modifications are given and indicated by color-coded dashed lines. B, Chemical structure of inhibitor 3, which has been co-crystallized with murine chronophin (this thesis). The atom numbers of the pyridine ring are given for facilitated understanding of the proposed modifications. C, The putative modifications of inhibitors are boxed in the color according to the modification site shown in the structure (A). Blue, Negatively charged substituents at the 4'-position of the pyridine ring might increase the affinity by interacting with Asn^{60}, Arg^{62}, Arg^{63} and/or Arg^{71}. This position has been shown to be crucial for the inhibitory efficacy of the tested inhibitors. As this position is used for covalent linkage by PLP-dependent enzymes (see 1.4.1), modifications of this site are thought to render the inhibitors inactive as a cofactor for those proteins. Green, The introduction of fluorines at the 5'-position might increase the affinity of the inhibitors by hydrogen bond formation to Ser^{58} and the backbone nitrogen of Asn^{60}. Magenta, Other non-hydrolizable phosphate analogs than a phosphonate group, such as sulfates, sulfonates or arsenates might increase the affinity of the inhibitors towards the active site machinery of chronophin. Orange, Substituents replacing the 2'-methyl group of the inhibitors might increase the hydrophobic interaction towards Tyr^{146}.

6 Apendix

6.1 Supplementary data

6.1.1 Thermofluor experiments

Thermofluor experiments were conducted in order to screen for optimal chronophin buffer conditions. The buffer screen (Table 45) revealed that all pH values in the range from pH 7 to pH 9 are equally well suited. Phosphate buffers showed exceptionally high melting temperatures due to the fact that free phosphate is able to bind the active site of chronophin and thereby to stabilize the protein. However, phosphate buffer cannot be used in phosphatase assays due to product inhibition and reactivity with malachite green.

Table 45. Thermofluor buffer screen of recombinantly expressed and purified murine chronophin. The shown melting temperatures (T_m) represent mean values of technical duplicates and are ordered from the lowest to the highest melting temperatures. The final buffer concentration in the screen was 50mM.

Buffer	**T_m [°C]**	**Buffer**	**T_m [°C]**
Na-Citrate pH 4	35	Tris pH 7.5	68
Na-Acetate pH 4.5	40	TAPS pH 8	68
Na-Cacodylate pH 5	48,5	CAPS pH 9.8	68
Na-Citrat pH 5	51	Na-Cacodylate pH 7	68,5
Na-Acetat pH 5.5	55	HEPES pH 7.5	68,5
Bis-Tris pH 6	59	CHES pH 9	68,5
Bis-Tris-Propane pH 6.5	60	Bis-Tris-Propane pH 8.5	69
Na-Citrate pH 6	61	PIPES pH 7.5	69
Imidazol pH 6.5	62	MOPS pH 7.5	69
Na-Cacodylate pH 6	64,5	HEPES pH 8	69
Bis-Tris pH 6.5	64,5	Bis-Tris-Propane pH 9.5	69,5
MOPS pH 6.5	65,5	Bicine pH 8	69,5
PIPES pH 6.5	66	Bicine pH 9	69,5
Na/K-PO_4 pH 4.5	66	Tris pH 8	69,5
Bis-Tris-Propane pH 7.5	66,5	Tris pH 9	69,5
Bis-Tris pH 7	67	TAPS pH 8.5	69,5
Imidazol pH 7.5	67	Bicine pH 8.5	70
HEPES pH 7	67	Tris pH 8.5	70
CHES pH 9.5	67,5	TAPS pH 9	70
PIPES pH 7	68	Na/K-PO_4 pH 5.5	71,5
MOPS pH 7	68	Na/K-PO_4 pH 8.5	75
TEA pH 7.4	**68**		

Therefore, triethanolamine at pH 7.4 was used as a buffer, as human chronophin has been characterized in this buffer before [70], allowing a direct comparison of kinetic constants due to similar buffer conditions.

Subsequently, a number of additives were tested. The results are summarized in Table 46, showing that sodium chloride slightly increases the melting temperature of chronophin, indicating a stabilization of the protein. Glycerol, β-mercaptoethanol and DMSO had no effect on the melting temperature of chronophin, while EDTA led to a significant decrease by complexing the essential cofactor Mg^{2+} of the protein. As expected, this leads to a destabilization of chronophin. Based on these results, the chronophin buffer was composed of 50mM TEA, 250mM NaCl and 5mM $MgCl_2$.

Table 46. Thermofluor additive screen of recombinantly expressed and purified murine chronophin. The final buffer concentration in these screens was 25mM TEA (pH 7.4). T_m, melting temperature.

Additive	**T_m [°C]**	**Additive**	**T_m [°C]**
no additive	67	50mM NaCl + 5mM ß-ME	68.00
50mM NaCl	69	50mM NaCl + 1mM EDTA	63.00
100mM NaCl	69	50mM NaCl + 1% (v/v) glycerol	67.00
200mM NaCl	69	50mM NaCl + 1% (v/v) DMSO	67.00
300mM NaCl	68		
400mM NaCl	68		
500mM NaCl	69		
1M NaCl	69		

6.1.2 CD-Spectroscopy

The conformational changes of CIB1 and calmodulin upon binding of calcium and magnesium were monitored using CD spectroscopy, in order to determine buffer conditions leading to full depletion of Ca^{2+}-ions or complete saturation with Ca^{2+}, respectively.

According to PDB file 1XO5, human CIB1 consists of 58% helices and 3% beta strands. Based on the high level of homology of ~93% sequence identity on amino acid level, one can assume that the human and murine orthologs show a high degree of homology on structural level as well. Figure 52A shows the CD-spectrum of murine CIB1 in 25mM TEA (pH 7.4) and 50mM NaCl, displaying minima at 208nm and 222nm, which are characteristic for α-helices, thus confirming that the protein is mostly helical. The addition of 1mM Ca^{2+} or 1mM Mg^{2+} resulted in only minor changes of the CD signal (2-4% at 208nm, ~2%

at 222nm), leading to the conclusion that CIB1 is almost saturated with magnesium and/or calcium even if the buffer was not supplemented with these ions. In contrast to this result, addition of 1mM EDTA or 1mM EGTA led to a strong decrease of the CD signal at 208nm and 222nm (~20% at 208nm, ~10% at 222nm), which therefore represents the conformation of apo-CIB1.

In order to further characterize the binding of Ca^{2+} to CIB1, CD-spectra at different Ca^{2+}-concentrations were recorded using apo-CIB1 that was purified in the presence of 10mM EGTA as described in the methods section (3.14.3). In the final purification step the buffer was exchanged to 25mM TEA and 50mM NaCl via size exclusion chromatography. Figure 52B shows that increasing Ca^{2+}-concentrations led to concomitantly increasing CD signals at 208nm and 222nm. Based on these results, I decided to use buffers supplemented with 1mM EGTA or 100µM Ca^{2+} in enzymatic assays, in order to produce Ca^{2+}-free or Ca^{2+}-saturated conditions, respectively. The same buffer conditions were applied to calmodulin, as similar results were obtained in CD-spectroscopic measurements (Figure 52C).

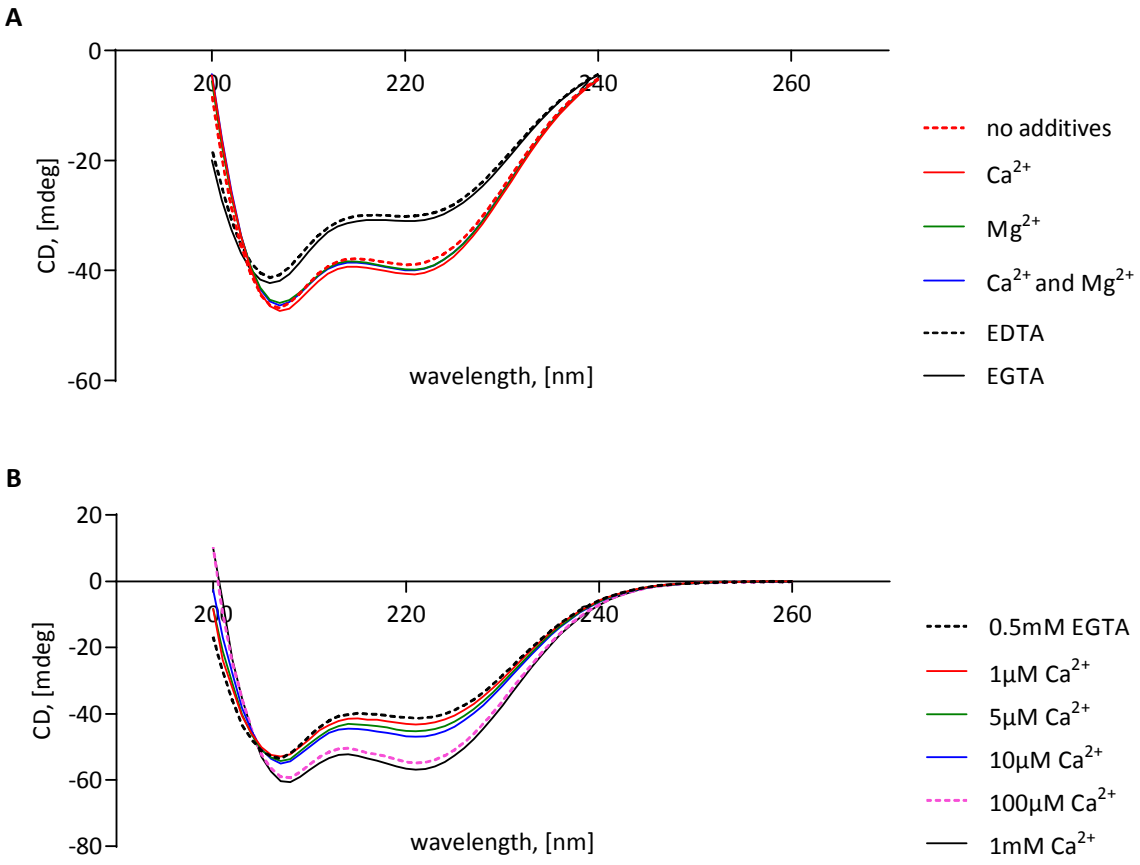

Figure legend on the next page.

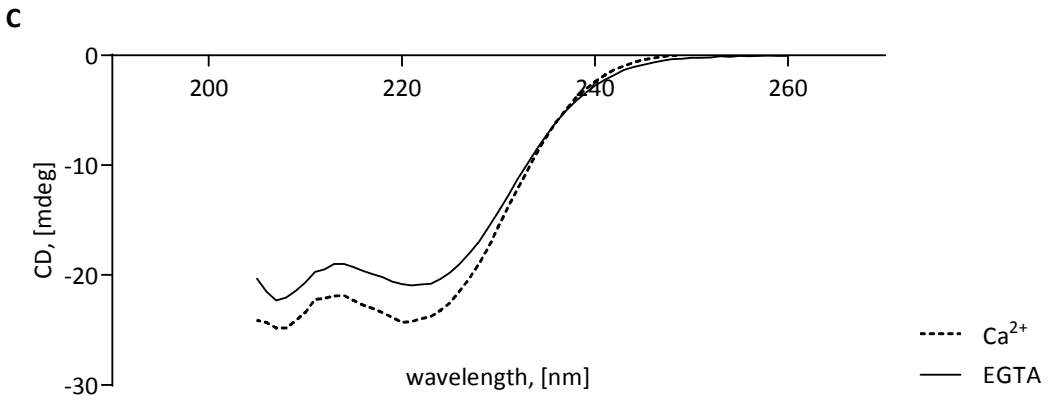

Figure 52. CD-spectroscopy of CIB1 and calmodulin. A, Effect of EGTA, EDTA, Ca^{2+} and Mg^{2+} on recombinantly expressed and purified CIB1 (final concentration 30µM). The protein was purified without using chelators, such as EDTA or EGTA. The sample buffer consisted of 25mM TEA NaCl (pH 7.4) and 50mM. The additives were used at final concentrations of 1mM. B, Effect of different Ca^{2+}-concentrations on recombinantly expressed CIB1 (final concentration 30µM), which was purified in the presence of EGTA. The sample buffer consisted of 25mM TEA (pH 7.4) and 50mM NaCl with the indicated concentrations of EGTA or Ca^{2+}. C, CD-spectra of recombinantly expressed and purified calmodulin (final concentration 10µM). The calmodulin sample buffer consisted of 50mM TEA (pH 7.4), 250mM NaCl, 5mM $MgCl_2$ supplemented with 25µM Ca^{2+} or 50µM EGTA.

6.2 Amino acids

The position of an amino acid within a protein sequence is given by superscript numbers.

Ala/A	Alanine
Arg/R	Arginine
Asn/N	Asparagine
Asp/D	Aspartic acid
Cys/C	Cysteine
Glu/E	Glutamic acid
Gln/Q	Glutamine
Gly/G	Glycine
His/H	Histidine
Ile/I	Isoleucine
Leu/L	Leucine
Lys/K	Lysine
Met/M	Methionine
Phe/F	Phenylalanine
Pro/P	Proline
Ser/S	Serine
Thr/T	Threonine
Trp/W	Tryptophan
Tyr/Y	Tyrosine
Val/V	Valine

6.3 Abbreviations

× *g*	Multiples of Earth's standard gravity (9.81m·s^{-2})
µg	Microgram
µL	Microliter
ADP	Adenosine diphosphate
ATP	Adenosine triphosphate
cm	Centimeter
CV	Column volume
ddH_2O	Double-distilled water
DNA	Deoxyribonucleic acid
dNTP	Deoxyribonucleotide
E. coli	*Escherichia coli*
GDP	Guanosine diphosphate
GTP	Guanosine triphosphate
IC_{50}	Half maximal inhibitory concentration
kb	Kilobases
K_d	Dissociation constant
kDa	Kilodalton
LB	Lysogeny broth
mA	Milliampere
min	Minute
mL	Milliliter
mM	Millimolar
MWCO	Molecular weight cut-off
ng	Nanogram
nm	Nanometer
nM	Nanomolar
OD_{600}	Optical density measured at a wavelength of 600nm
r.m.s.d.	Root mean square diviation
rpm	Rotations per minute
UV	Ultraviolet
WT	Wild-type

6.4 Figures

6.5 Tables

6.6 Literature

1. Albersen, M., et al., *The intestine plays a substantial role in human vitamin B6 metabolism: a Caco-2 cell model.* PLoS One, 2013. **8**(1): p. e54113.
2. Blackwell, H.E. and R.H. Grubbs, *Highly Efficient Synthesis of Covalently Cross-Linked Peptide Helices by Ring-Closing Metathesis.* Angewandte Chemie International Edition, 1998. **37**(23): p. 3281-3284.
3. Eisenberg, D., et al., *Analysis of membrane and surface protein sequences with the hydrophobic moment plot.* J Mol Biol, 1984. **179**(1): p. 125-42.
4. Liberti, S., et al., *HuPho: the human phosphatase portal.* FEBS J, 2013. **280**(2): p. 379-87.
5. Manning, G., et al., *The protein kinase complement of the human genome.* Science, 2002. **298**(5600): p. 1912-34.
6. Chen, V.B., et al., *MolProbity: all-atom structure validation for macromolecular crystallography.* Acta Crystallogr D Biol Crystallogr, 2010. **66**(Pt 1): p. 12-21.
7. Seifried, A., J. Schultz, and A. Gohla, *Human HAD phosphatases: structure, mechanism, and roles in health and disease.* FEBS J, 2013. **280**(2): p. 549-71.
8. Summers, K.C., et al., *Phosphorylation: the molecular switch of double-strand break repair.* Int J Proteomics, 2011. **2011**: p. 373816.
9. Karin, M. and T. Hunter, *Transcriptional control by protein phosphorylation: signal transmission from the cell surface to the nucleus.* Curr Biol, 1995. **5**(7): p. 747-57.
10. Liu, J. and A. Lin, *Role of JNK activation in apoptosis: a double-edged sword.* Cell Res, 2005. **15**(1): p. 36-42.
11. Shuai, K. and B. Liu, *Regulation of JAK-STAT signalling in the immune system.* Nat Rev Immunol, 2003. **3**(11): p. 900-11.
12. Bevan, P., *Insulin signalling.* J Cell Sci, 2001. **114**(Pt 8): p. 1429-30.
13. Lian, I., et al., *The role of YAP transcription coactivator in regulating stem cell self-renewal and differentiation.* Genes Dev, 2010. **24**(11): p. 1106-18.
14. Cohen, P., *The regulation of protein function by multisite phosphorylation--a 25 year update.* Trends Biochem Sci, 2000. **25**(12): p. 596-601.
15. Stenberg, K.A., P.T. Riikonen, and M. Vihinen, *KinMutBase, a database of human disease-causing protein kinase mutations.* Nucleic Acids Res, 2000. **28**(1): p. 369-71.
16. Tonks, N.K., *Protein tyrosine phosphatases: from genes, to function, to disease.* Nat Rev Mol Cell Biol, 2006. **7**(11): p. 833-46.
17. Lahiry, P., et al., *Kinase mutations in human disease: interpreting genotype-phenotype relationships.* Nat Rev Genet, 2010. **11**(1): p. 60-74.
18. Newman, R.H., et al., *Construction of human activity-based phosphorylation networks.* Mol Syst Biol, 2013. **9**: p. 655.
19. Ubersax, J.A. and J.E. Ferrell, Jr., *Mechanisms of specificity in protein phosphorylation.* Nat Rev Mol Cell Biol, 2007. **8**(7): p. 530-41.
20. Hunter, T. and B.M. Sefton, *Transforming gene product of Rous sarcoma virus phosphorylates tyrosine.* Proc Natl Acad Sci U S A, 1980. **77**(3): p. 1311-5.
21. Olsen, J.V., et al., *Global, in vivo, and site-specific phosphorylation dynamics in signaling networks.* Cell, 2006. **127**(3): p. 635-48.
22. Hanks, S.K. and T. Hunter, *Protein kinases 6. The eukaryotic protein kinase superfamily: kinase (catalytic) domain structure and classification.* FASEB J, 1995. **9**(8): p. 576-96.

23. Hanks, S.K., A.M. Quinn, and T. Hunter, *The protein kinase family: conserved features and deduced phylogeny of the catalytic domains.* Science, 1988. **241**(4861): p. 42-52.
24. Yang, J., et al., *Structural basis for substrate specificity of protein-tyrosine phosphatase SHP-1.* J Biol Chem, 2000. **275**(6): p. 4066-71.
25. Jia, Z., et al., *Structural basis for phosphotyrosine peptide recognition by protein tyrosine phosphatase 1B.* Science, 1995. **268**(5218): p. 1754-8.
26. Songyang, Z., et al., *Use of an oriented peptide library to determine the optimal substrates of protein kinases.* Curr Biol, 1994. **4**(11): p. 973-82.
27. Biondi, R.M. and A.R. Nebreda, *Signalling specificity of Ser/Thr protein kinases through docking-site-mediated interactions.* Biochem J, 2003. **372**(Pt 1): p. 1-13.
28. Holland, P.M. and J.A. Cooper, *Protein modification: docking sites for kinases.* Curr Biol, 1999. **9**(9): p. R329-31.
29. Bhattacharyya, R.P., et al., *Domains, motifs, and scaffolds: the role of modular interactions in the evolution and wiring of cell signaling circuits.* Annu Rev Biochem, 2006. **75**: p. 655-80.
30. Pawson, T. and J.D. Scott, *Signaling through scaffold, anchoring, and adaptor proteins.* Science, 1997. **278**(5346): p. 2075-80.
31. Howard, P.L., et al., *Redirecting tyrosine kinase signaling to an apoptotic caspase pathway through chimeric adaptor proteins.* Proc Natl Acad Sci U S A, 2003. **100**(20): p. 11267-72.
32. Disatnik, M.H., G. Buraggi, and D. Mochly-Rosen, *Localization of protein kinase C isozymes in cardiac myocytes.* Exp Cell Res, 1994. **210**(2): p. 287-97.
33. Draviam, V.M., et al., *The localization of human cyclins B1 and B2 determines CDK1 substrate specificity and neither enzyme requires MEK to disassemble the Golgi apparatus.* J Cell Biol, 2001. **152**(5): p. 945-58.
34. Miller, M.E. and F.R. Cross, *Distinct subcellular localization patterns contribute to functional specificity of the Cln2 and Cln3 cyclins of Saccharomyces cerevisiae.* Mol Cell Biol, 2000. **20**(2): p. 542-55.
35. Gao, Y., et al., *Myosin light chain kinase as a multifunctional regulatory protein of smooth muscle contraction.* IUBMB Life, 2001. **51**(6): p. 337-44.
36. Fischer, E.H., *Phosphorylase and the origin of reversible protein phosphorylation.* Biol Chem, 2010. **391**(2-3): p. 131-7.
37. Candas, D., et al., *CyclinB1/Cdk1 phosphorylates mitochondrial antioxidant MnSOD in cell adaptive response to radiation stress.* J Mol Cell Biol, 2013. **5**(3): p. 166-75.
38. Cukier, I.H., Y. Li, and J.M. Lee, *Cyclin B1/Cdk1 binds and phosphorylates Filamin A and regulates its ability to cross-link actin.* FEBS Lett, 2007. **581**(8): p. 1661-72.
39. Fluck, M., F.W. Booth, and M.N. Waxham, *Skeletal muscle CaMKII enriches in nuclei and phosphorylates myogenic factor SRF at multiple sites.* Biochem Biophys Res Commun, 2000. **270**(2): p. 488-94.
40. Hou, S.T., et al., *CaMKII phosphorylates collapsin response mediator protein 2 and modulates axonal damage during glutamate excitotoxicity.* J Neurochem, 2009. **111**(3): p. 870-81.
41. Meng, F., et al., *Autophosphorylated calcium/calmodulin-dependent protein kinase II alpha (CaMKII alpha) reversibly targets to and phosphorylates N-methyl-D-aspartate receptor subunit 2B (NR2B) in cerebral ischemia and reperfusion in hippocampus of rats.* Brain Res, 2003. **967**(1-2): p. 161-9.
42. Wang, W.Y., et al., *CaMKII phosphorylates a threonine residue in the C-terminal tail of Cav1.2 Ca(2+) channel and modulates the interaction of the channel with calmodulin.* J Physiol Sci, 2009. **59**(4): p. 283-90.
43. Ubersax, J.A., et al., *Targets of the cyclin-dependent kinase Cdk1.* Nature, 2003. **425**(6960): p. 859-64.

44. Cohen, P., *The structure and regulation of protein phosphatases.* Annu Rev Biochem, 1989. **58**: p. 453-508.
45. Hubbard, M.J. and P. Cohen, *On target with a new mechanism for the regulation of protein phosphorylation.* Trends Biochem Sci, 1993. **18**(5): p. 172-7.
46. Moorhead, G.B., et al., *Evolution of protein phosphatases in plants and animals.* Biochem J, 2009. **417**(2): p. 401-9.
47. Duan, G., X. Li, and M. Kohn, *The human DEPhOsphorylation database DEPOD: a 2015 update.* Nucleic Acids Res, 2014.
48. Das, A.K., et al., *Crystal structure of the protein serine/threonine phosphatase 2C at 2.0 A resolution.* EMBO J, 1996. **15**(24): p. 6798-809.
49. Strater, N., et al., *Crystal structure of a purple acid phosphatase containing a dinuclear Fe(III)-Zn(II) active site.* Science, 1995. **268**(5216): p. 1489-92.
50. Shi, Y., *Serine/threonine phosphatases: mechanism through structure.* Cell, 2009. **139**(3): p. 468-84.
51. Eichhorn, P.J., M.P. Creyghton, and R. Bernards, *Protein phosphatase 2A regulatory subunits and cancer.* Biochim Biophys Acta, 2009. **1795**(1): p. 1-15.
52. Seshacharyulu, P., et al., *Phosphatase: PP2A structural importance, regulation and its aberrant expression in cancer.* Cancer Lett, 2013. **335**(1): p. 9-18.
53. Cohen, P.T., *Protein phosphatase 1--targeted in many directions.* J Cell Sci, 2002. **115**(Pt 2): p. 241-56.
54. Peti, W., A.C. Nairn, and R. Page, *Structural basis for protein phosphatase 1 regulation and specificity.* FEBS J, 2013. **280**(2): p. 596-611.
55. Zhang, W. and L. Shi, *Evolution of the PPM-family protein phosphatases in Streptomyces: duplication of catalytic domain and lateral recruitment of additional sensory domains.* Microbiology, 2004. **150**(Pt 12): p. 4189-97.
56. Travis, S.M. and M.J. Welsh, *PP2C gamma: a human protein phosphatase with a unique acidic domain.* FEBS Lett, 1997. **412**(3): p. 415-9.
57. Rodriguez, P.L., *Protein phosphatase 2C (PP2C) function in higher plants.* Plant Mol Biol, 1998. **38**(6): p. 919-27.
58. Ofek, P., et al., *Cell cycle regulation and p53 activation by protein phosphatase 2C alpha.* J Biol Chem, 2003. **278**(16): p. 14299-305.
59. Tsukamoto, T., et al., *Cloning and characterization of two human cDNAs encoding the mRNA capping enzyme.* Biochem Biophys Res Commun, 1998. **243**(1): p. 101-8.
60. Maehama, T., G.S. Taylor, and J.E. Dixon, *PTEN and myotubularin: novel phosphoinositide phosphatases.* Annu Rev Biochem, 2001. **70**: p. 247-79.
61. Hnia, K., et al., *Myotubularin phosphoinositide phosphatases: cellular functions and disease pathophysiology.* Trends Mol Med, 2012. **18**(6): p. 317-27.
62. Egloff, M.P., et al., *Crystal structure of the catalytic subunit of human protein phosphatase 1 and its complex with tungstate.* J Mol Biol, 1995. **254**(5): p. 942-59.
63. Yuvaniyama, J., et al., *Crystal structure of the dual specificity protein phosphatase VHR.* Science, 1996. **272**(5266): p. 1328-31.
64. Barford, D., A.J. Flint, and N.K. Tonks, *Crystal structure of human protein tyrosine phosphatase 1B.* Science, 1994. **263**(5152): p. 1397-404.
65. Alonso, A., et al., *Protein tyrosine phosphatases in the human genome.* Cell, 2004. **117**(6): p. 699-711.
66. Akiva, E., et al., *The Structure-Function Linkage Database.* Nucleic Acids Res, 2014. **42**(Database issue): p. D521-30.
67. Allen, K.N. and D. Dunaway-Mariano, *Phosphoryl group transfer: evolution of a catalytic scaffold.* Trends Biochem Sci, 2004. **29**(9): p. 495-503.

68. Allen, K.N. and D. Dunaway-Mariano, *Markers of fitness in a successful enzyme superfamily.* Curr Opin Struct Biol, 2009. **19**(6): p. 658-65.
69. Burroughs, A.M., et al., *Evolutionary genomics of the HAD superfamily: understanding the structural adaptations and catalytic diversity in a superfamily of phosphoesterases and allied enzymes.* J Mol Biol, 2006. **361**(5): p. 1003-34.
70. Fonda, M.L., *Purification and characterization of vitamin B6-phosphate phosphatase from human erythrocytes.* J Biol Chem, 1992. **267**(22): p. 15978-83.
71. Gohla, A., J. Birkenfeld, and G.M. Bokoch, *Chronophin, a novel HAD-type serine protein phosphatase, regulates cofilin-dependent actin dynamics.* Nat Cell Biol, 2005. **7**(1): p. 21-9.
72. Tootle, T.L., et al., *The transcription factor Eyes absent is a protein tyrosine phosphatase.* Nature, 2003. **426**(6964): p. 299-302.
73. Bernstein, N.K., et al., *The molecular architecture of the mammalian DNA repair enzyme, polynucleotide kinase.* Mol Cell, 2005. **17**(5): p. 657-70.
74. Kim, Y., et al., *A conserved phosphatase cascade that regulates nuclear membrane biogenesis.* Proc Natl Acad Sci U S A, 2007. **104**(16): p. 6596-601.
75. Rinaldo-Matthis, A., et al., *Crystal structure of a human mitochondrial deoxyribonucleotidase.* Nat Struct Biol, 2002. **9**(10): p. 779-87.
76. Johnson, K.R., et al., *Role of human sphingosine-1-phosphate phosphatase 1 in the regulation of intra- and extracellular sphingosine-1-phosphate levels and cell viability.* J Biol Chem, 2003. **278**(36): p. 34541-7.
77. Sigal, Y.J., M.I. McDermott, and A.J. Morris, *Integral membrane lipid phosphatases/phosphotransferases: common structure and diverse functions.* Biochem J, 2005. **387**(Pt 2): p. 281-93.
78. Li, J., et al., *Crystal structures and biochemical studies of human lysophosphatidic acid phosphatase type 6.* Protein Cell, 2013. **4**(7): p. 548-61.
79. Jefferson, A.B., et al., *Signaling inositol polyphosphate-5-phosphatase. Characterization of activity and effect of GRB2 association.* J Biol Chem, 1997. **272**(9): p. 5983-8.
80. Pyne, S., et al., *Lipid phosphate phosphatases and lipid phosphate signalling.* Biochem Soc Trans, 2005. **33**(Pt 6): p. 1370-4.
81. Kai, M., et al., *Cloning and characterization of two human isozymes of Mg2+-independent phosphatidic acid phosphatase.* J Biol Chem, 1997. **272**(39): p. 24572-8.
82. Hooks, S.B., S.P. Ragan, and K.R. Lynch, *Identification of a novel human phosphatidic acid phosphatase type 2 isoform.* FEBS Lett, 1998. **427**(2): p. 188-92.
83. Noakes, C.J., G. Lee, and M. Lowe, *The PH domain proteins IPIP27A and B link OCRL1 to receptor recycling in the endocytic pathway.* Mol Biol Cell, 2011. **22**(5): p. 606-23.
84. Mao, Y., et al., *A PH domain within OCRL bridges clathrin-mediated membrane trafficking to phosphoinositide metabolism.* EMBO J, 2009. **28**(13): p. 1831-42.
85. Bessman, M.J., D.N. Frick, and S.F. O'Handley, *The MutT proteins or "Nudix" hydrolases, a family of versatile, widely distributed, "housecleaning" enzymes.* J Biol Chem, 1996. **271**(41): p. 25059-62.
86. McLennan, A.G., *The Nudix hydrolase superfamily.* Cell Mol Life Sci, 2006. **63**(2): p. 123-43.
87. Mildvan, A.S., et al., *Structures and mechanisms of Nudix hydrolases.* Arch Biochem Biophys, 2005. **433**(1): p. 129-43.
88. Ren, L., et al., *Substrate specificity of protein tyrosine phosphatases 1B, RPTPalpha, SHP-1, and SHP-2.* Biochemistry, 2011. **50**(12): p. 2339-56.
89. Selner, N.G., et al., *Diverse levels of sequence selectivity and catalytic efficiency of protein-tyrosine phosphatases.* Biochemistry, 2014. **53**(2): p. 397-412.
90. Peisach, E., et al., *X-ray crystal structure of the hypothetical phosphotyrosine phosphatase MDP-1 of the haloacid dehalogenase superfamily.* Biochemistry, 2004. **43**(40): p. 12770-9.

91. Galburt, E.A., et al., *Structure of a tRNA repair enzyme and molecular biology workhorse: T4 polynucleotide kinase.* Structure, 2002. **10**(9): p. 1249-60.
92. Lu, Z., et al., *Structure-function analysis of 2-keto-3-deoxy-D-glycero-D-galactonononate-9-phosphate phosphatase defines specificity elements in type C0 haloalkanoate dehalogenase family members.* J Biol Chem, 2009. **284**(2): p. 1224-33.
93. Nguyen, H.H., et al., *Structural determinants of substrate recognition in the HAD superfamily member D-glycero-D-manno-heptose-1,7-bisphosphate phosphatase (GmhB).* Biochemistry, 2010. **49**(6): p. 1082-92.
94. Almo, S.C., et al., *Structural genomics of protein phosphatases.* J Struct Funct Genomics, 2007. **8**(2-3): p. 121-40.
95. Lahiri, S.D., et al., *Analysis of the substrate specificity loop of the HAD superfamily cap domain.* Biochemistry, 2004. **43**(10): p. 2812-20.
96. Lu, Z., D. Dunaway-Mariano, and K.N. Allen, *HAD superfamily phosphotransferase substrate diversification: structure and function analysis of HAD subclass IIB sugar phosphatase BT4131.* Biochemistry, 2005. **44**(24): p. 8684-96.
97. Rayapureddi, J.P., et al., *Eyes absent represents a class of protein tyrosine phosphatases.* Nature, 2003. **426**(6964): p. 295-8.
98. Dai, J., et al., *Analysis of the structural determinants underlying discrimination between substrate and solvent in beta-phosphoglucomutase catalysis.* Biochemistry, 2009. **48**(9): p. 1984-95.
99. Zhang, G., et al., *Kinetic evidence for a substrate-induced fit in phosphonoacetaldehyde hydrolase catalysis.* Biochemistry, 2002. **41**(45): p. 13370-7.
100. Fieulaine, S., et al., *The structure of a cyanobacterial sucrose-phosphatase reveals the sugar tongs that release free sucrose in the cell.* Plant Cell, 2005. **17**(7): p. 2049-58.
101. Pandya, C., et al., *Structure-guided approach for detecting large domain inserts in protein sequences as illustrated using the haloacid dehalogenase superfamily.* Proteins, 2014.
102. Newman, J.W., et al., *The soluble epoxide hydrolase encoded by EPXH2 is a bifunctional enzyme with novel lipid phosphate phosphatase activity.* Proc Natl Acad Sci U S A, 2003. **100**(4): p. 1558-63.
103. Rebay, I., S.J. Silver, and T.L. Tootle, *New vision from Eyes absent: transcription factors as enzymes.* Trends Genet, 2005. **21**(3): p. 163-71.
104. Zheng, H., et al., *Cloning and characterization of a novel RNA polymerase II C-terminal domain phosphatase.* Biochem Biophys Res Commun, 2005. **331**(4): p. 1401-7.
105. Csaki, L.S. and K. Reue, *Lipins: multifunctional lipid metabolism proteins.* Annu Rev Nutr, 2010. **30**: p. 257-72.
106. Huang, T.Y., et al., *Chronophin mediates an ATP-sensing mechanism for cofilin dephosphorylation and neuronal cofilin-actin rod formation.* Dev Cell, 2008. **15**(5): p. 691-703.
107. Zoudilova, M., et al., *beta-Arrestins scaffold cofilin with chronophin to direct localized actin filament severing and membrane protrusions downstream of protease-activated receptor-2.* J Biol Chem, 2010. **285**(19): p. 14318-29.
108. Jang, Y.M., et al., *Human pyridoxal phosphatase. Molecular cloning, functional expression, and tissue distribution.* J Biol Chem, 2003. **278**(50): p. 50040-6.
109. Cho, H.-J. and B.-S. Kang, *Closed Conformation of a Human Phosphatase, Chronophin under the Reduced Condition.* Journal of Life Science, 2008. **18**(4): p. 585-589.
110. Percudani, R. and A. Peracchi, *A genomic overview of pyridoxal-phosphate-dependent enzymes.* EMBO Rep, 2003. **4**(9): p. 850-4.
111. Awapara, J., R.P. Sandman, and C. Hanly, *Activation of DOPA decarboxylase by pyridoxal phosphate.* Arch Biochem Biophys, 1962. **98**: p. 520-5.
112. Baxter, C.F. and E. Roberts, *The gamma-aminobutyric acid-alpha-ketoglutaric acid transaminase of beef brain.* J Biol Chem, 1958. **233**(5): p. 1135-9.

113. Schirch, V. and D.M. Szebenyi, *Serine hydroxymethyltransferase revisited.* Curr Opin Chem Biol, 2005. **9**(5): p. 482-7.
114. Raboni, S., et al., *The molecular pathway for the allosteric regulation of tryptophan synthase.* Biochim Biophys Acta, 2003. **1647**(1-2): p. 157-60.
115. Bettati, S., et al., *Role of pyridoxal 5'-phosphate in the structural stabilization of O-acetylserine sulfhydrylase.* J Biol Chem, 2000. **275**(51): p. 40244-51.
116. Palm, D., et al., *The role of pyridoxal 5'-phosphate in glycogen phosphorylase catalysis.* Biochemistry, 1990. **29**(5): p. 1099-107.
117. Ferreira, G.C., P.J. Neame, and H.A. Dailey, *Heme biosynthesis in mammalian systems: evidence of a Schiff base linkage between the pyridoxal 5'-phosphate cofactor and a lysine residue in 5-aminolevulinate synthase.* Protein Sci, 1993. **2**(11): p. 1959-65.
118. Combs, G.F., *The vitamins : fundamental aspects in nutrition and health*. 3rd ed. 2008, Amsterdam ; Boston: Elsevier Academic Press. xix, 583 p.
119. Zhang, X.H., et al., *Vitamin B6 and colorectal cancer: current evidence and future directions.* World J Gastroenterol, 2013. **19**(7): p. 1005-10.
120. Hvas, A.M., et al., *Vitamin B6 level is associated with symptoms of depression.* Psychother Psychosom, 2004. **73**(6): p. 340-3.
121. Mills, P.B., et al., *Epilepsy due to PNPO mutations: genotype, environment and treatment affect presentation and outcome.* Brain, 2014.
122. Lin, P.T., et al., *Low pyridoxal 5'-phosphate is associated with increased risk of coronary artery disease.* Nutrition, 2006. **22**(11-12): p. 1146-51.
123. Booth, C.C. and M.C. Brain, *The absorption of tritium-labelled pyridoxine hydrochloride in the rat.* J Physiol, 1962. **164**: p. 282-94.
124. Merrill, A.H., Jr., et al., *Metabolism of vitamin B-6 by human liver.* J Nutr, 1984. **114**(9): p. 1664-74.
125. Denesyuk, A.I., et al., *Functional attributes of the phosphate group binding cup of pyridoxal phosphate-dependent enzymes.* J Mol Biol, 2002. **316**(1): p. 155-72.
126. Toney, M.D., *Controlling reaction specificity in pyridoxal phosphate enzymes.* Biochim Biophys Acta, 2011. **1814**(11): p. 1407-18.
127. Blanchoin, L., et al., *Actin dynamics, architecture, and mechanics in cell motility.* Physiol Rev, 2014. **94**(1): p. 235-63.
128. Pollard, T.D., et al., *Actin and myosin biochemistry in relation to cytokinesis.* Ann N Y Acad Sci, 1990. **582**: p. 120-30.
129. Mooren, O.L., B.J. Galletta, and J.A. Cooper, *Roles for actin assembly in endocytosis.* Annu Rev Biochem, 2012. **81**: p. 661-86.
130. Adamo, J.E., G. Rossi, and P. Brennwald, *The Rho GTPase Rho3 has a direct role in exocytosis that is distinct from its role in actin polarity.* Mol Biol Cell, 1999. **10**(12): p. 4121-33.
131. Frank, D.J., T. Noguchi, and K.G. Miller, *Myosin VI: a structural role in actin organization important for protein and organelle localization and trafficking.* Curr Opin Cell Biol, 2004. **16**(2): p. 189-94.
132. Schutt, C.E. and U. Lindberg, *Actin as the generator of tension during muscle contraction.* Proc Natl Acad Sci U S A, 1992. **89**(1): p. 319-23.
133. Bamburg, J.R., et al., *ADF/Cofilin-actin rods in neurodegenerative diseases.* Curr Alzheimer Res, 2010. **7**(3): p. 241-50.
134. Wang, W., R. Eddy, and J. Condeelis, *The cofilin pathway in breast cancer invasion and metastasis.* Nat Rev Cancer, 2007. **7**(6): p. 429-40.
135. Smoyer, W.E. and P. Mundel, *Regulation of podocyte structure during the development of nephrotic syndrome.* J Mol Med (Berl), 1998. **76**(3-4): p. 172-83.
136. Zheng, B., et al., *Nuclear actin and actin-binding proteins in the regulation of transcription and gene expression.* FEBS J, 2009. **276**(10): p. 2669-85.

137. Chua, B.T., et al., *Mitochondrial translocation of cofilin is an early step in apoptosis induction.* Nat Cell Biol, 2003. **5**(12): p. 1083-9.
138. Han, L., et al., *Direct stimulation of receptor-controlled phospholipase D1 by phospho-cofilin.* EMBO J, 2007. **26**(19): p. 4189-202.
139. Kim, J.H., et al., *Phospholipase D1 regulates cell migration in a lipase activity-independent manner.* J Biol Chem, 2006. **281**(23): p. 15747-56.
140. Vartiainen, M.K., et al., *The three mouse actin-depolymerizing factor/cofilins evolved to fulfill cell-type-specific requirements for actin dynamics.* Mol Biol Cell, 2002. **13**(1): p. 183-94.
141. Tahtamouni, L.H., et al., *Non-overlapping activities of ADF and cofilin-1 during the migration of metastatic breast tumor cells.* BMC Cell Biol, 2013. **14**: p. 45.
142. Estornes, Y., et al., *Differential involvement of destrin and cofilin-1 in the control of invasive properties of Isreco1 human colon cancer cells.* Int J Cancer, 2007. **121**(10): p. 2162-71.
143. Gurniak, C.B., E. Perlas, and W. Witke, *The actin depolymerizing factor n-cofilin is essential for neural tube morphogenesis and neural crest cell migration.* Dev Biol, 2005. **278**(1): p. 231-41.
144. Hotulainen, P., et al., *Actin-depolymerizing factor and cofilin-1 play overlapping roles in promoting rapid F-actin depolymerization in mammalian nonmuscle cells.* Mol Biol Cell, 2005. **16**(2): p. 649-64.
145. Galkin, V.E., et al., *Remodeling of actin filaments by ADF/cofilin proteins.* Proc Natl Acad Sci U S A, 2011. **108**(51): p. 20568-72.
146. Prochniewicz, E., et al., *Cofilin increases the torsional flexibility and dynamics of actin filaments.* J Mol Biol, 2005. **353**(5): p. 990-1000.
147. Andrianantoandro, E. and T.D. Pollard, *Mechanism of actin filament turnover by severing and nucleation at different concentrations of ADF/cofilin.* Mol Cell, 2006. **24**(1): p. 13-23.
148. Yeoh, S., et al., *Determining the differences in actin binding by human ADF and cofilin.* J Mol Biol, 2002. **315**(4): p. 911-25.
149. Hawkins, M., et al., *Human actin depolymerizing factor mediates a pH-sensitive destruction of actin filaments.* Biochemistry, 1993. **32**(38): p. 9985-93.
150. Yonezawa, N., E. Nishida, and H. Sakai, *pH control of actin polymerization by cofilin.* J Biol Chem, 1985. **260**(27): p. 14410-2.
151. Bernstein, B.W., et al., *Intracellular pH modulation of ADF/cofilin proteins.* Cell Motil Cytoskeleton, 2000. **47**(4): p. 319-36.
152. Pavlov, D., et al., *Severing of F-actin by yeast cofilin is pH-independent.* Cell Motil Cytoskeleton, 2006. **63**(9): p. 533-42.
153. Frantz, C., et al., *Cofilin is a pH sensor for actin free barbed end formation: role of phosphoinositide binding.* J Cell Biol, 2008. **183**(5): p. 865-79.
154. Leyman, S., et al., *Unbalancing the phosphatidylinositol-4,5-bisphosphate-cofilin interaction impairs cell steering.* Mol Biol Cell, 2009. **20**(21): p. 4509-23.
155. Pope, B.J., et al., *Solution structure of human cofilin: actin binding, pH sensitivity, and relationship to actin-depolymerizing factor.* J Biol Chem, 2004. **279**(6): p. 4840-8.
156. Pfannstiel, J., et al., *Human cofilin forms oligomers exhibiting actin bundling activity.* J Biol Chem, 2001. **276**(52): p. 49476-84.
157. Klemke, M., et al., *Oxidation of cofilin mediates T cell hyporesponsiveness under oxidative stress conditions.* Immunity, 2008. **29**(3): p. 404-13.
158. Bamburg, J.R., *Proteins of the ADF/cofilin family: essential regulators of actin dynamics.* Annu Rev Cell Dev Biol, 1999. **15**: p. 185-230.
159. Toshima, J., et al., *Cofilin phosphorylation and actin reorganization activities of testicular protein kinase 2 and its predominant expression in testicular Sertoli cells.* J Biol Chem, 2001. **276**(33): p. 31449-58.

160. Scott, R.W. and M.F. Olson, *LIM kinases: function, regulation and association with human disease.* J Mol Med (Berl), 2007. **85**(6): p. 555-68.
161. Ambach, A., et al., *The serine phosphatases PP1 and PP2A associate with and activate the actin-binding protein cofilin in human T lymphocytes.* Eur J Immunol, 2000. **30**(12): p. 3422-31.
162. Niwa, R., et al., *Control of actin reorganization by Slingshot, a family of phosphatases that dephosphorylate ADF/cofilin.* Cell, 2002. **108**(2): p. 233-46.
163. Barisic, S., et al., *Phosphorylation of Ser 402 impedes phosphatase activity of slingshot 1.* EMBO Rep, 2011. **12**(6): p. 527-33.
164. Huet, G., et al., *Actin-regulated feedback loop based on Phactr4, PP1 and cofilin maintains the actin monomer pool.* J Cell Sci, 2013. **126**(Pt 2): p. 497-507.
165. Soosairajah, J., et al., *Interplay between components of a novel LIM kinase-slingshot phosphatase complex regulates cofilin.* EMBO J, 2005. **24**(3): p. 473-86.
166. Ahmed, T., et al., *A PAK4-LIMK1 pathway drives prostate cancer cell migration downstream of HGF.* Cell Signal, 2008. **20**(7): p. 1320-8.
167. Kaji, N., et al., *Cell cycle-associated changes in Slingshot phosphatase activity and roles in cytokinesis in animal cells.* J Biol Chem, 2003. **278**(35): p. 33450-5.
168. Li, C., et al., *Essential phosphatases and a phospho-degron are critical for regulation of SRC-3/AIB1 coactivator function and turnover.* Mol Cell, 2008. **31**(6): p. 835-49.
169. Mangelsdorf, D.J., et al., *The nuclear receptor superfamily: the second decade.* Cell, 1995. **83**(6): p. 835-9.
170. Lonard, D.M. and B.W. O'Malley, *The expanding cosmos of nuclear receptor coactivators.* Cell, 2006. **125**(3): p. 411-4.
171. Anzick, S.L., et al., *AIB1, a steroid receptor coactivator amplified in breast and ovarian cancer.* Science, 1997. **277**(5328): p. 965-8.
172. Liao, L., et al., *Molecular structure and biological function of the cancer-amplified nuclear receptor coactivator SRC-3/AIB1.* J Steroid Biochem Mol Biol, 2002. **83**(1-5): p. 3-14.
173. Suen, C.S., et al., *A transcriptional coactivator, steroid receptor coactivator-3, selectively augments steroid receptor transcriptional activity.* J Biol Chem, 1998. **273**(42): p. 27645-53.
174. Xu, J., et al., *The steroid receptor coactivator SRC-3 (p/CIP/RAC3/AIB1/ACTR/TRAM-1) is required for normal growth, puberty, female reproductive function, and mammary gland development.* Proc Natl Acad Sci U S A, 2000. **97**(12): p. 6379-84.
175. Louie, M.C., et al., *ACTR/AIB1 functions as an E2F1 coactivator to promote breast cancer cell proliferation and antiestrogen resistance.* Mol Cell Biol, 2004. **24**(12): p. 5157-71.
176. Yan, J., et al., *Steroid receptor coactivator-3 and activator protein-1 coordinately regulate the transcription of components of the insulin-like growth factor/AKT signaling pathway.* Cancer Res, 2006. **66**(22): p. 11039-46.
177. Werbajh, S., et al., *RAC-3 is a NF-kappa B coactivator.* FEBS Lett, 2000. **485**(2-3): p. 195-9.
178. Arimura, A., et al., *The transcriptional co-activator p/CIP (NCoA-3) is up-regulated by STAT6 and serves as a positive regulator of transcriptional activation by STAT6.* J Biol Chem, 2004. **279**(30): p. 31105-12.
179. Qin, L., et al., *The AIB1 oncogene promotes breast cancer metastasis by activation of PEA3-mediated matrix metalloproteinase 2 (MMP2) and MMP9 expression.* Mol Cell Biol, 2008. **28**(19): p. 5937-50.
180. Yu, C., et al., *An essential function of the SRC-3 coactivator in suppression of cytokine mRNA translation and inflammatory response.* Mol Cell, 2007. **25**(5): p. 765-78.
181. Kuang, S.Q., et al., *AIB1/SRC-3 deficiency affects insulin-like growth factor I signaling pathway and suppresses v-Ha-ras-induced breast cancer initiation and progression in mice.* Cancer Res, 2004. **64**(5): p. 1875-85.

182. Ma, G., et al., *SRC-3 has a role in cancer other than as a nuclear receptor coactivator.* Int J Biol Sci, 2011. **7**(5): p. 664-72.
183. Chen, H., et al., *Regulation of hormone-induced histone hyperacetylation and gene activation via acetylation of an acetylase.* Cell, 1999. **98**(5): p. 675-86.
184. Ferry, C., et al., *Cullin 3 mediates SRC-3 ubiquitination and degradation to control the retinoic acid response.* Proc Natl Acad Sci U S A, 2011. **108**(51): p. 20603-8.
185. Feng, Q., et al., *Signaling within a coactivator complex: methylation of SRC-3/AIB1 is a molecular switch for complex disassembly.* Mol Cell Biol, 2006. **26**(21): p. 7846-57.
186. Amazit, L., et al., *Regulation of SRC-3 intercompartmental dynamics by estrogen receptor and phosphorylation.* Mol Cell Biol, 2007. **27**(19): p. 6913-32.
187. Chen, H., et al., *Nuclear receptor coactivator ACTR is a novel histone acetyltransferase and forms a multimeric activation complex with P/CAF and CBP/p300.* Cell, 1997. **90**(3): p. 569-80.
188. Naeem, H., et al., *The activity and stability of the transcriptional coactivator p/CIP/SRC-3 are regulated by CARM1-dependent methylation.* Mol Cell Biol, 2007. **27**(1): p. 120-34.
189. Font de Mora, J. and M. Brown, *AIB1 is a conduit for kinase-mediated growth factor signaling to the estrogen receptor.* Mol Cell Biol, 2000. **20**(14): p. 5041-7.
190. Osborne, C.K., et al., *Role of the estrogen receptor coactivator AIB1 (SRC-3) and HER-2/neu in tamoxifen resistance in breast cancer.* J Natl Cancer Inst, 2003. **95**(5): p. 353-61.
191. Wu, R.C., et al., *Regulation of SRC-3 (pCIP/ACTR/AIB-1/RAC-3/TRAM-1) Coactivator activity by I kappa B kinase.* Mol Cell Biol, 2002. **22**(10): p. 3549-61.
192. Wu, R.C., et al., *Selective phosphorylations of the SRC-3/AIB1 coactivator integrate genomic reponses to multiple cellular signaling pathways.* Mol Cell, 2004. **15**(6): p. 937-49.
193. Kim, J.E., et al., *Potential role of pyridoxal-5'-phosphate phosphatase/chronopin in epilepsy.* Exp Neurol, 2008. **211**(1): p. 128-40.
194. Kim, J.E., et al., *Pyridoxal-5'-phosphate phosphatase/chronophin induces astroglial apoptosis via actin-depolymerizing factor/cofilin system in the rat brain following status epilepticus.* Glia, 2010. **58**(16): p. 1937-48.
195. Kim, J.E., et al., *Pyridoxal-5'-phosphate phosphatase/chronophin inhibits long-term potentiation induction in the rat dentate gyrus.* Hippocampus, 2009. **19**(11): p. 1078-89.
196. Luttrell, L.M. and R.J. Lefkowitz, *The role of beta-arrestins in the termination and transduction of G-protein-coupled receptor signals.* J Cell Sci, 2002. **115**(Pt 3): p. 455-65.
197. Pierce, K.L. and R.J. Lefkowitz, *Classical and new roles of beta-arrestins in the regulation of G-protein-coupled receptors.* Nat Rev Neurosci, 2001. **2**(10): p. 727-33.
198. DeWire, S.M., et al., *Beta-arrestins and cell signaling.* Annu Rev Physiol, 2007. **69**: p. 483-510.
199. Zoudilova, M., et al., *Beta-arrestin-dependent regulation of the cofilin pathway downstream of protease-activated receptor-2.* J Biol Chem, 2007. **282**(28): p. 20634-46.
200. Eckl, J.M. and K. Richter, *Functions of the Hsp90 chaperone system: lifting client proteins to new heights.* Int J Biochem Mol Biol, 2013. **4**(4): p. 157-65.
201. Pearl, L.H. and C. Prodromou, *Structure and mechanism of the Hsp90 molecular chaperone machinery.* Annu Rev Biochem, 2006. **75**: p. 271-94.
202. Garcia-Cardena, G., et al., *Dynamic activation of endothelial nitric oxide synthase by Hsp90.* Nature, 1998. **392**(6678): p. 821-4.
203. Holt, S.E., et al., *Functional requirement of p23 and Hsp90 in telomerase complexes.* Genes Dev, 1999. **13**(7): p. 817-26.
204. Pearl, L.H., *Hsp90 and Cdc37 -- a chaperone cancer conspiracy.* Curr Opin Genet Dev, 2005. **15**(1): p. 55-61.
205. Pratt, W.B. and D.O. Toft, *Regulation of signaling protein function and trafficking by the hsp90/hsp70-based chaperone machinery.* Exp Biol Med (Maywood), 2003. **228**(2): p. 111-33.

206. Gentry, H.R., et al., *Structural and biochemical characterization of CIB1 delineates a new family of EF-hand-containing proteins.* J Biol Chem, 2005. **280**(9): p. 8407-15.
207. Armacki, M., et al., *A novel splice variant of calcium and integrin-binding protein 1 mediates protein kinase D2-stimulated tumour growth by regulating angiogenesis.* Oncogene, 2014. **33**(9): p. 1167-80.
208. Shock, D.D., et al., *Calcium-dependent properties of CIB binding to the integrin alphaIIb cytoplasmic domain and translocation to the platelet cytoskeleton.* Biochem J, 1999. **342 Pt 3**: p. 729-35.
209. Saito, T., et al., *Structure, expression profile, and chromosomal location of a mouse gene homologous to human DNA-PKcs interacting protein (KIP) gene.* Mamm Genome, 1999. **10**(3): p. 315-7.
210. Sobczak, A., et al., *Calcium-binding calmyrin forms stable covalent dimers in vitro, but in vivo is found in monomeric form.* Acta Biochim Pol, 2005. **52**(2): p. 469-76.
211. Yamniuk, A.P., et al., *Auxiliary Ca2+ binding sites can influence the structure of CIB1.* Protein Sci, 2009. **18**(5): p. 1128-34.
212. Vallar, L., et al., *Divalent cations differentially regulate integrin alphaIIb cytoplasmic tail binding to beta3 and to calcium- and integrin-binding protein.* J Biol Chem, 1999. **274**(24): p. 17257-66.
213. Hollenbach, A.D., et al., *The EF-hand calcium-binding protein calmyrin inhibits the transcriptional and DNA-binding activity of Pax3.* Biochim Biophys Acta, 2002. **1574**(3): p. 321-8.
214. White, C., et al., *CIB1, a ubiquitously expressed Ca2+-binding protein ligand of the InsP3 receptor Ca2+ release channel.* J Biol Chem, 2006. **281**(30): p. 20825-33.
215. Kauselmann, G., et al., *The polo-like protein kinases Fnk and Snk associate with a Ca(2+)- and integrin-binding protein and are regulated dynamically with synaptic plasticity.* EMBO J, 1999. **18**(20): p. 5528-39.
216. Naik, M.U., et al., *Calcium-dependent inhibition of polo-like kinase 3 activity by CIB1 in breast cancer cells.* Int J Cancer, 2011. **128**(3): p. 587-96.
217. Haataja, L., et al., *The small GTPase Rac3 interacts with the integrin-binding protein CIB and promotes integrin alpha(IIb)beta(3)-mediated adhesion and spreading.* J Biol Chem, 2002. **277**(10): p. 8321-8.
218. Naik, M.U. and U.P. Naik, *Calcium-and integrin-binding protein regulates focal adhesion kinase activity during platelet spreading on immobilized fibrinogen.* Blood, 2003. **102**(10): p. 3629-36.
219. Stabler, S.M., et al., *A myristoylated calcium-binding protein that preferentially interacts with the Alzheimer's disease presenilin 2 protein.* J Cell Biol, 1999. **145**(6): p. 1277-92.
220. Leisner, T.M., et al., *Essential role of CIB1 in regulating PAK1 activation and cell migration.* J Cell Biol, 2005. **170**(3): p. 465-76.
221. Naik, M.U. and U.P. Naik, *Calcium- and integrin-binding protein 1 regulates microtubule organization and centrosome segregation through polo like kinase 3 during cell cycle progression.* Int J Biochem Cell Biol, 2011. **43**(1): p. 120-9.
222. Yuan, W., et al., *CIB1 is essential for mouse spermatogenesis.* Mol Cell Biol, 2006. **26**(22): p. 8507-14.
223. Zayed, M.A., et al., *Tumor growth and angiogenesis is impaired in CIB1 knockout mice.* J Angiogenes Res, 2010. **2**: p. 17.
224. Zayed, M.A., et al., *CIB1 regulates endothelial cells and ischemia-induced pathological and adaptive angiogenesis.* Circ Res, 2007. **101**(11): p. 1185-93.
225. Denofrio, J.C., et al., *Characterization of calcium- and integrin-binding protein 1 (CIB1) knockout platelets: potential compensation by CIB family members.* Thromb Haemost, 2008. **100**(5): p. 847-56.
226. Heineke, J., et al., *CIB1 is a regulator of pathological cardiac hypertrophy.* Nat Med, 2010. **16**(8): p. 872-9.

227. Sun, W., et al., *Calcium- and integrin-binding protein-1 is down-regulated in the sperm of patients with oligoasthenozoospermia : CIB1 expression in patients with oligoasthenozoospermia.* J Assist Reprod Genet, 2014. **31**(5): p. 541-7.
228. Sutcliffe, J.G., et al., *Peripheral reduction of beta-amyloid is sufficient to reduce brain beta-amyloid: implications for Alzheimer's disease.* J Neurosci Res, 2011. **89**(6): p. 808-14.
229. Yamniuk, A.P., et al., *Metal ion binding properties and conformational states of calcium- and integrin-binding protein.* Biochemistry, 2004. **43**(9): p. 2558-68.
230. Yamniuk, A.P., et al., *Domain stability and metal-induced folding of calcium- and integrin-binding protein 1.* Biochemistry, 2007. **46**(24): p. 7088-98.
231. Levitsky, D.O. and M. Takahashi, *Interplay of Ca2+ and Mg2+ in Sodium-Calcium Exchanger and in Other Ca2+-Binding Proteins: Magnesium, Watchdog That Blocks Each Turn if Able.* Sodium Calcium Exchange: A Growing Spectrum of Pathophysiological Implications, 2013. **961**: p. 65-78.
232. Yamniuk, A.P. and H.J. Vogel, *Calcium- and magnesium-dependent interactions between calcium- and integrin-binding protein and the integrin alphaIIb cytoplasmic domain.* Protein Sci, 2005. **14**(6): p. 1429-37.
233. Jarman, K.E., et al., *Translocation of sphingosine kinase 1 to the plasma membrane is mediated by calcium- and integrin-binding protein 1.* J Biol Chem, 2010. **285**(1): p. 483-92.
234. Yamniuk, A.P., H. Ishida, and H.J. Vogel, *The interaction between calcium- and integrin-binding protein 1 and the alphaIIb integrin cytoplasmic domain involves a novel C-terminal displacement mechanism.* J Biol Chem, 2006. **281**(36): p. 26455-64.
235. Rusnak, F. and P. Mertz, *Calcineurin: form and function.* Physiol Rev, 2000. **80**(4): p. 1483-521.
236. Chin, D. and A.R. Means, *Calmodulin: a prototypical calcium sensor.* Trends Cell Biol, 2000. **10**(8): p. 322-8.
237. Bkaily, G. and N. Sperelakis, *Calmodulin is required for a full activation of the calcium slow channels in heart cells.* J Cyclic Nucleotide Protein Phosphor Res, 1986. **11**(1): p. 25-34.
238. Marone, G., et al., *Possible role of calmodulin in human inflammatory reactions.* Monogr Allergy, 1983. **18**: p. 290-9.
239. Racioppi, L. and A.R. Means, *Calcium/calmodulin-dependent protein kinase kinase 2: roles in signaling and pathophysiology.* J Biol Chem, 2012. **287**(38): p. 31658-65.
240. Villar-Palasi, C., D.L. Oshiro, and R.H. Kretsinger, *Interaction of calmodulin and glycogen phosphorylase.* Biochim Biophys Acta, 1983. **757**(1): p. 40-6.
241. Zhao, J.W., et al., *Regulation of cofilin activity by CaMKII and calcineurin.* Am J Med Sci, 2012. **344**(6): p. 462-72.
242. Wang, Y., F. Shibasaki, and K. Mizuno, *Calcium signal-induced cofilin dephosphorylation is mediated by Slingshot via calcineurin.* J Biol Chem, 2005. **280**(13): p. 12683-9.
243. Schmalzigaug, R., Q. Ye, and M.W. Berchtold, *Calmodulin protects cells from death under normal growth conditions and mitogenic starvation but plays a mediating role in cell death upon B-cell receptor stimulation.* Immunology, 2001. **103**(3): p. 332-42.
244. Nyegaard, M., et al., *Mutations in calmodulin cause ventricular tachycardia and sudden cardiac death.* Am J Hum Genet, 2012. **91**(4): p. 703-12.
245. Marsman, R.F., et al., *A mutation in CALM1 encoding calmodulin in familial idiopathic ventricular fibrillation in childhood and adolescence.* J Am Coll Cardiol, 2014. **63**(3): p. 259-66.
246. Crotti, L., et al., *Calmodulin mutations associated with recurrent cardiac arrest in infants.* Circulation, 2013. **127**(9): p. 1009-17.
247. Kursula, P., *Crystallographic snapshots of initial steps in the collapse of the calmodulin central helix.* Acta Crystallogr D Biol Crystallogr, 2014. **70**(Pt 1): p. 24-30.
248. Rhoads, A.R. and F. Friedberg, *Sequence motifs for calmodulin recognition.* FASEB J, 1997. **11**(5): p. 331-40.

249. Jin, H., et al., *Effect of apocalmodulin on recombinant human brain glutamic acid decarboxylase.* J Neurochem, 2005. **92**(4): p. 739-48.
250. Schumacher, M.A., et al., *Structure of the gating domain of a Ca2+-activated K+ channel complexed with Ca2+/calmodulin.* Nature, 2001. **410**(6832): p. 1120-4.
251. Majava, V. and P. Kursula, *Domain swapping and different oligomeric States for the complex between calmodulin and the calmodulin-binding domain of calcineurin a.* PLoS One, 2009. **4**(4): p. e5402.
252. Tidow, H. and P. Nissen, *Structural diversity of calmodulin binding to its target sites.* FEBS J, 2013. **280**(21): p. 5551-65.
253. Fallon, J.L., et al., *Structure of calmodulin bound to the hydrophobic IQ domain of the cardiac Ca(v)1.2 calcium channel.* Structure, 2005. **13**(12): p. 1881-6.
254. Dagher, R., et al., *A general strategy to characterize calmodulin-calcium complexes involved in CaM-target recognition: DAPK and EGFR calmodulin binding domains interact with different calmodulin-calcium complexes.* Biochim Biophys Acta, 2011. **1813**(5): p. 1059-67.
255. Haiech, J., C.B. Klee, and J.G. Demaille, *Effects of cations on affinity of calmodulin for calcium: ordered binding of calcium ions allows the specific activation of calmodulin-stimulated enzymes.* Biochemistry, 1981. **20**(13): p. 3890-7.
256. Pitt, G.S., et al., *Molecular basis of calmodulin tethering and Ca2+-dependent inactivation of L-type Ca2+ channels.* J Biol Chem, 2001. **276**(33): p. 30794-802.
257. Hoeflich, K.P. and M. Ikura, *Calmodulin in action: diversity in target recognition and activation mechanisms.* Cell, 2002. **108**(6): p. 739-42.
258. Ye, Q., et al., *Structural basis of calcineurin activation by calmodulin.* Cell Signal, 2013. **25**(12): p. 2661-7.
259. Yamniuk, A.P., M. Rainaldi, and H.J. Vogel, *Calmodulin has the Potential to Function as a Ca-Dependent Adaptor Protein.* Plant Signal Behav, 2007. **2**(5): p. 354-7.
260. Collaborative Computational Project, N., *The CCP4 suite: programs for protein crystallography.* Acta Crystallogr D Biol Crystallogr, 1994. **50**(Pt 5): p. 760-3.
261. Emsley, P. and K. Cowtan, *Coot: model-building tools for molecular graphics.* Acta Crystallogr D Biol Crystallogr, 2004. **60**(Pt 12 Pt 1): p. 2126-32.
262. Holm, L. and P. Rosenstrom, *Dali server: conservation mapping in 3D.* Nucleic Acids Res, 2010. **38**(Web Server issue): p. W545-9.
263. Battye, T.G., et al., *iMOSFLM: a new graphical interface for diffraction-image processing with MOSFLM.* Acta Crystallogr D Biol Crystallogr, 2011. **67**(Pt 4): p. 271-81.
264. Krissinel, E. and K. Henrick, *Inference of macromolecular assemblies from crystalline state.* J Mol Biol, 2007. **372**(3): p. 774-97.
265. Adams, P.D., et al., *PHENIX: a comprehensive Python-based system for macromolecular structure solution.* Acta Crystallogr D Biol Crystallogr, 2010. **66**(Pt 2): p. 213-21.
266. Evans, P., *Scaling and assessment of data quality.* Acta Crystallogr D Biol Crystallogr, 2006. **62**(Pt 1): p. 72-82.
267. Schuck, P., *Size-distribution analysis of macromolecules by sedimentation velocity ultracentrifugation and lamm equation modeling.* Biophys J, 2000. **78**(3): p. 1606-19.
268. Lehman, I.R., *DNA ligase: structure, mechanism, and function.* Science, 1974. **186**(4166): p. 790-7.
269. Laemmli, U.K., *Cleavage of structural proteins during the assembly of the head of bacteriophage T4.* Nature, 1970. **227**(5259): p. 680-5.
270. Schagger, H., *Tricine-SDS-PAGE.* Nat Protoc, 2006. **1**(1): p. 16-22.
271. Diederichs, K. and P.A. Karplus, *Improved R-factors for diffraction data analysis in macromolecular crystallography.* Nat Struct Biol, 1997. **4**(4): p. 269-75.
272. Weiss, M., *Global indicators of X-ray data quality.* Journal of Applied Crystallography, 2001. **34**(2): p. 130-135.

273. McCoy, A.J., et al., *Phaser crystallographic software.* J Appl Crystallogr, 2007. **40**(Pt 4): p. 658-674.
274. Brunger, A.T., *Free R value: cross-validation in crystallography.* Methods Enzymol, 1997. **277**: p. 366-96.
275. Moriarty, N.W., R.W. Grosse-Kunstleve, and P.D. Adams, *electronic Ligand Builder and Optimization Workbench (eLBOW): a tool for ligand coordinate and restraint generation.* Acta Crystallogr D Biol Crystallogr, 2009. **65**(Pt 10): p. 1074-80.
276. Adams, P.D., et al., *The Phenix software for automated determination of macromolecular structures.* Methods, 2011. **55**(1): p. 94-106.
277. Nadeau, O.W. and G.M. Carlson, *Protein Interactions Captured by Chemical Cross-linking: One-Step Cross-linking with Formaldehyde.* CSH Protoc, 2007. **2007**: p. pdb prot4634.
278. Peeraer, Y., et al., *How calcium inhibits the magnesium-dependent enzyme human phosphoserine phosphatase.* Eur J Biochem, 2004. **271**(16): p. 3421-7.
279. Coburn, S.P., J.D. Mahuren, and T.R. Guilarte, *Vitamin B-6 content of plasma of domestic animals determined by HPLC, enzymatic and radiometric microbiological methods.* J Nutr, 1984. **114**(12): p. 2269-73.
280. Albersen, M., et al., *Vitamin B-6 vitamers in human plasma and cerebrospinal fluid.* Am J Clin Nutr, 2014. **100**(2): p. 587-592.
281. Kestler, C., et al., *Chronophin dimerization is required for proper positioning of its substrate specificity loop.* J Biol Chem, 2014. **289**(5): p. 3094-103.
282. Pandya, C., et al., *Consequences of domain insertion on sequence-structure divergence in a superfold.* Proc Natl Acad Sci U S A, 2013. **110**(36): p. E3381-7.
283. Cho, H., et al., *BeF(3)(-) acts as a phosphate analog in proteins phosphorylated on aspartate: structure of a BeF(3)(-) complex with phosphoserine phosphatase.* Proc Natl Acad Sci U S A, 2001. **98**(15): p. 8525-30.
284. Zhao, X., et al., *Crystal structure of a complex between the phosphorelay protein YPD1 and the response regulator domain of SLN1 bound to a phosphoryl analog.* J Mol Biol, 2008. **375**(4): p. 1141-51.
285. Roberts, A., et al., *YbiV from Escherichia coli K12 is a HAD phosphatase.* Proteins, 2005. **58**(4): p. 790-801.
286. Jung, S.K., et al., *Crystal structure of ED-Eya2: insight into dual roles as a protein tyrosine phosphatase and a transcription factor.* FASEB J, 2010. **24**(2): p. 560-9.
287. Cook, P.J., et al., *Tyrosine dephosphorylation of H2AX modulates apoptosis and survival decisions.* Nature, 2009. **458**(7238): p. 591-6.
288. Seifried, A., et al., *Evolutionary and structural analyses of mammalian haloacid dehalogenase-type phosphatases AUM and chronophin provide insight into the basis of their different substrate specificities.* J Biol Chem, 2014. **289**(6): p. 3416-31.
289. Gu, Z., et al., *Role of duplicate genes in genetic robustness against null mutations.* Nature, 2003. **421**(6918): p. 63-6.
290. Gao, G.J. and M.L. Fonda, *Kinetic analysis and chemical modification of vitamin B6 phosphatase from human erythrocytes.* J Biol Chem, 1994. **269**(10): p. 7163-8.
291. Brooks, H.B., et al., *Basics of Enzymatic Assays for HTS*, in *Assay Guidance Manual*, G.S. Sittampalam, et al., Editors. 2004: Bethesda (MD).
292. Clapham, D.E., *Calcium signaling.* Cell, 2007. **131**(6): p. 1047-58.
293. Naraghi, M. and E. Neher, *Linearized buffered Ca2+ diffusion in microdomains and its implications for calculation of [Ca2+] at the mouth of a calcium channel.* J Neurosci, 1997. **17**(18): p. 6961-73.
294. Fischer, R., J. Julsgart, and M.W. Berchtold, *High affinity calmodulin target sequence in the signalling molecule PI 3-kinase.* FEBS Lett, 1998. **425**(1): p. 175-7.
295. Yamada, M., et al., *The calmodulin-binding domain in the mouse type 1 inositol 1,4,5-trisphosphate receptor.* Biochem J, 1995. **308 (Pt 1)**: p. 83-8.

296. Quintana, A.R., et al., *Kinetics of calmodulin binding to calcineurin.* Biochem Biophys Res Commun, 2005. **334**(2): p. 674-80.
297. Kajio, H., et al., *A low-affinity Ca2+-dependent association of calmodulin with the Rab3A effector domain inversely correlates with insulin exocytosis.* Diabetes, 2001. **50**(9): p. 2029-39.
298. Taiakina, V., et al., *The calmodulin-binding, short linear motif, NSCaTE is conserved in L-type channel ancestors of vertebrate Cav1.2 and Cav1.3 channels.* PLoS One, 2013. **8**(4): p. e61765.
299. Freeman, T.C., Jr., et al., *Identification of novel integrin binding partners for calcium and integrin binding protein 1 (CIB1): structural and thermodynamic basis of CIB1 promiscuity.* Biochemistry, 2013. **52**(40): p. 7082-90.
300. Perkins, J.R., et al., *Transient protein-protein interactions: structural, functional, and network properties.* Structure, 2010. **18**(10): p. 1233-43.
301. Nooren, I.M. and J.M. Thornton, *Diversity of protein-protein interactions.* EMBO J, 2003. **22**(14): p. 3486-92.
302. Janin, J., R.P. Bahadur, and P. Chakrabarti, *Protein-protein interaction and quaternary structure.* Q Rev Biophys, 2008. **41**(2): p. 133-80.
303. Dai, J., et al., *Conformational cycling in beta-phosphoglucomutase catalysis: reorientation of the beta-D-glucose 1,6-(Bis)phosphate intermediate.* Biochemistry, 2006. **45**(25): p. 7818-24.
304. Lu, Z., D. Dunaway-Mariano, and K.N. Allen, *The X-ray crystallographic structure and specificity profile of HAD superfamily phosphohydrolase BT1666: comparison of paralogous functions in B. thetaiotaomicron.* Proteins, 2011. **79**(11): p. 3099-107.
305. Rappsilber, J., *The beginning of a beautiful friendship: cross-linking/mass spectrometry and modelling of proteins and multi-protein complexes.* J Struct Biol, 2011. **173**(3): p. 530-40.
306. Wang, H., et al., *Interaction between p68 RNA helicase and Ca2+-calmodulin promotes cell migration and metastasis.* Nat Commun, 2013. **4**: p. 1354.
307. Long, W., et al., *SRC-3Delta4 mediates the interaction of EGFR with FAK to promote cell migration.* Mol Cell, 2010. **37**(3): p. 321-32.
308. Neet, K.E. and D.E. Timm, *Conformational stability of dimeric proteins: quantitative studies by equilibrium denaturation.* Protein Sci, 1994. **3**(12): p. 2167-74.
309. Mazurek, S., *Pyruvate kinase type M2: a key regulator of the metabolic budget system in tumor cells.* Int J Biochem Cell Biol, 2011. **43**(7): p. 969-80.
310. Littler, D.R., et al., *The intracellular chloride ion channel protein CLIC1 undergoes a redox-controlled structural transition.* J Biol Chem, 2004. **279**(10): p. 9298-305.
311. Canals, M., et al., *Adenosine A2A-dopamine D2 receptor-receptor heteromerization: qualitative and quantitative assessment by fluorescence and bioluminescence energy transfer.* J Biol Chem, 2003. **278**(47): p. 46741-9.
312. Amoutzias, G.D., et al., *Choose your partners: dimerization in eukaryotic transcription factors.* Trends Biochem Sci, 2008. **33**(5): p. 220-9.
313. Hashimoto, K., et al., *Caught in self-interaction: evolutionary and functional mechanisms of protein homooligomerization.* Phys Biol, 2011. **8**(3): p. 035007.
314. Mei, G., et al., *The importance of being dimeric.* FEBS J, 2005. **272**(1): p. 16-27.
315. Marianayagam, N.J., M. Sunde, and J.M. Matthews, *The power of two: protein dimerization in biology.* Trends Biochem Sci, 2004. **29**(11): p. 618-25.
316. Chin, C.N., J.N. Sachs, and D.M. Engelman, *Transmembrane homodimerization of receptor-like protein tyrosine phosphatases.* FEBS Lett, 2005. **579**(17): p. 3855-8.
317. Walchli, S., X. Espanel, and R. Hooft van Huijsduijnen, *Sap-1/PTPRH activity is regulated by reversible dimerization.* Biochem Biophys Res Commun, 2005. **331**(2): p. 497-502.
318. Bilwes, A.M., et al., *Structural basis for inhibition of receptor protein-tyrosine phosphatase-alpha by dimerization.* Nature, 1996. **382**(6591): p. 555-9.

319. van der Wijk, T., et al., *Redox-regulated rotational coupling of receptor protein-tyrosine phosphatase alpha dimers.* J Biol Chem, 2003. **278**(16): p. 13968-74.
320. Lee, S., et al., *Dimerization of protein tyrosine phosphatase sigma governs both ligand binding and isoform specificity.* Mol Cell Biol, 2007. **27**(5): p. 1795-808.
321. Boulanger, R.R., Jr. and E.R. Kantrowitz, *Characterization of a monomeric Escherichia coli alkaline phosphatase formed upon a single amino acid substitution.* J Biol Chem, 2003. **278**(26): p. 23497-501.
322. Biswas, T., et al., *The tail of KdsC: conformational changes control the activity of a haloacid dehalogenase superfamily phosphatase.* J Biol Chem, 2009. **284**(44): p. 30594-603.
323. Zhu, H., et al., *Structure-function analysis of the 3' phosphatase component of T4 polynucleotide kinase/phosphatase.* Virology, 2007. **366**(1): p. 126-36.
324. Spychala, J., et al., *ATP and phosphate reciprocally affect subunit association of human recombinant High Km 5'-nucleotidase. Role for the C-terminal polyglutamic acid tract in subunit association and catalytic activity.* Eur J Biochem, 1999. **259**(3): p. 851-8.
325. Felts, R.L., et al., *Structure of recombinant Haemophilus influenzae e (P4) acid phosphatase reveals a new member of the haloacid dehalogenase superfamily.* Biochemistry, 2007. **46**(39): p. 11110-9.
326. Nelson, J.W., et al., *Soluble epoxide hydrolase dimerization is required for hydrolase activity.* J Biol Chem, 2013. **288**(11): p. 7697-703.
327. Verdine, G.L. and G.J. Hilinski, *Stapled peptides for intracellular drug targets.* Methods Enzymol, 2012. **503**: p. 3-33.
328. Blackwell, H.E., et al., *Ring-closing metathesis of olefinic peptides: design, synthesis, and structural characterization of macrocyclic helical peptides.* J Org Chem, 2001. **66**(16): p. 5291-302.
329. Schafmeister, C.E., J. Po, and G.L. Verdine, *An All-Hydrocarbon Cross-Linking System for Enhancing the Helicity and Metabolic Stability of Peptides.* Journal of the American Chemical Society, 2000. **122**(24): p. 5891-5892.
330. Lahiri, S.D., et al., *Diversification of function in the haloacid dehalogenase enzyme superfamily: The role of the cap domain in hydrolytic phosphoruscarbon bond cleavage.* Bioorg Chem, 2006. **34**(6): p. 394-409.
331. Daughtry, K.D., et al., *Structural basis for the divergence of substrate specificity and biological function within HAD phosphatases in lipopolysaccharide and sialic acid biosynthesis.* Biochemistry, 2013. **52**(32): p. 5372-86.
332. Huang, H., et al., *Divergence of structure and function in the haloacid dehalogenase enzyme superfamily: Bacteroides thetaiotaomicron BT2127 is an inorganic pyrophosphatase.* Biochemistry, 2011. **50**(41): p. 8937-49.
333. Takai, A. and G. Mieskes, *Inhibitory effect of okadaic acid on the p-nitrophenyl phosphate phosphatase activity of protein phosphatases.* Biochem J, 1991. **275 (Pt 1)**: p. 233-9.
334. Zhuo, S., et al., *Expression, purification, crystallization, and biochemical characterization of a recombinant protein phosphatase.* J Biol Chem, 1993. **268**(24): p. 17754-61.
335. Aravind, L., et al., *Trends in protein evolution inferred from sequence and structure analysis.* Curr Opin Struct Biol, 2002. **12**(3): p. 392-9.
336. Lynch, M. and A. Force, *The probability of duplicate gene preservation by subfunctionalization.* Genetics, 2000. **154**(1): p. 459-73.
337. Mazin, P.V., et al., *An automated stochastic approach to the identification of the protein specificity determinants and functional subfamilies.* Algorithms Mol Biol, 2010. **5**: p. 29.
338. Freschauf, G.K., et al., *Identification of a small molecule inhibitor of the human DNA repair enzyme polynucleotide kinase/phosphatase.* Cancer Res, 2009. **69**(19): p. 7739-46.
339. Krueger, A.B., et al., *Identification of a selective small-molecule inhibitor series targeting the eyes absent 2 (Eya2) phosphatase activity.* J Biomol Screen, 2013. **18**(1): p. 85-96.

340. Li, X., et al., *Eya protein phosphatase activity regulates Six1-Dach-Eya transcriptional effects in mammalian organogenesis.* Nature, 2003. **426**(6964): p. 247-54.
341. Fu, J., et al., *miR-30a suppresses breast cancer cell proliferation and migration by targeting Eya2.* Biochem Biophys Res Commun, 2014. **445**(2): p. 314-9.
342. Farabaugh, S.M., et al., *Eya2 is required to mediate the pro-metastatic functions of Six1 via the induction of TGF-beta signaling, epithelial-mesenchymal transition, and cancer stem cell properties.* Oncogene, 2012. **31**(5): p. 552-62.
343. Pandey, R.N., et al., *The Eyes Absent phosphatase-transactivator proteins promote proliferation, transformation, migration, and invasion of tumor cells.* Oncogene, 2010. **29**(25): p. 3715-22.
344. EnayetAllah, A.E., et al., *Opposite regulation of cholesterol levels by the phosphatase and hydrolase domains of soluble epoxide hydrolase.* J Biol Chem, 2008. **283**(52): p. 36592-8.
345. Morisseau, C. and B.D. Hammock, *Impact of soluble epoxide hydrolase and epoxyeicosanoids on human health.* Annu Rev Pharmacol Toxicol, 2013. **53**: p. 37-58.
346. Hawkinson, J.E., M. Acosta-Burruel, and P.L. Wood, *The metabotropic glutamate receptor antagonist L-2-amino-3-phosphonopropionic acid inhibits phosphoserine phosphatase.* Eur J Pharmacol, 1996. **307**(2): p. 219-25.
347. Collet, J.F., et al., *Human L-3-phosphoserine phosphatase: sequence, expression and evidence for a phosphoenzyme intermediate.* FEBS Lett, 1997. **408**(3): p. 281-4.
348. Possemato, R., et al., *Functional genomics reveal that the serine synthesis pathway is essential in breast cancer.* Nature, 2011. **476**(7360): p. 346-50.
349. Hawkinson, J.E., et al., *Novel phosphoserine phosphatase inhibitors.* Eur J Pharmacol, 1997. **337**(2-3): p. 315-24.
350. Farelli, J.D., et al., *Structure of the trehalose-6-phosphate phosphatase from Brugia malayi reveals key design principles for anthelmintic drugs.* PLoS Pathog, 2014. **10**(7): p. e1004245.
351. Kormish, J.D. and J.D. McGhee, *The C. elegans lethal gut-obstructed gob-1 gene is trehalose-6-phosphate phosphatase.* Dev Biol, 2005. **287**(1): p. 35-47.
352. Woodruff, P.J., et al., *Trehalose is required for growth of Mycobacterium smegmatis.* J Biol Chem, 2004. **279**(28): p. 28835-43.
353. Galluzzi, L., et al., *Effects of vitamin B6 metabolism on oncogenesis, tumor progression and therapeutic responses.* Oncogene, 2013. **32**(42): p. 4995-5004.
354. Galluzzi, L., et al., *Prognostic impact of vitamin B6 metabolism in lung cancer.* Cell Rep, 2012. **2**(2): p. 257-69.
355. Lurie, G., et al., *Prediagnostic plasma pyridoxal 5'-phosphate (vitamin b6) levels and invasive breast carcinoma risk: the multiethnic cohort.* Cancer Epidemiol Biomarkers Prev, 2012. **21**(11): p. 1942-8.
356. Larsson, S.C., N. Orsini, and A. Wolk, *Vitamin B6 and risk of colorectal cancer: a meta-analysis of prospective studies.* JAMA, 2010. **303**(11): p. 1077-83.
357. Galluzzi, L., et al., *Vitamin B6 metabolism influences the intracellular accumulation of cisplatin.* Cell Cycle, 2013. **12**(3): p. 417-21.
358. Bernier, J., E.J. Hall, and A. Giaccia, *Radiation oncology: a century of achievements.* Nat Rev Cancer, 2004. **4**(9): p. 737-47.
359. Zhang, P., et al., *Vitamin B(6) activates p53 and elevates p21 gene expression in cancer cells and the mouse colon.* Oncol Rep, 2014. **31**(5): p. 2371-6.
360. Amundson, S.A., T.G. Myers, and A.J. Fornace, Jr., *Roles for p53 in growth arrest and apoptosis: putting on the brakes after genotoxic stress.* Oncogene, 1998. **17**(25): p. 3287-99.
361. Gartel, A.L. and A.L. Tyner, *The role of the cyclin-dependent kinase inhibitor p21 in apoptosis.* Mol Cancer Ther, 2002. **1**(8): p. 639-49.
362. Wong, C.G., T. Bottiglieri, and O.C. Snead, 3rd, *GABA, gamma-hydroxybutyric acid, and neurological disease.* Ann Neurol, 2003. **54 Suppl 6**: p. S3-12.

363. Aroniadou-Anderjaska, V., F. Qashu, and M.F. Braga, *Mechanisms regulating GABAergic inhibitory transmission in the basolateral amygdala: implications for epilepsy and anxiety disorders.* Amino Acids, 2007. **32**(3): p. 305-15.
364. Treiman, D.M., *GABAergic mechanisms in epilepsy.* Epilepsia, 2001. **42 Suppl 3**: p. 8-12.
365. Erlander, M.G., et al., *Two genes encode distinct glutamate decarboxylases.* Neuron, 1991. **7**(1): p. 91-100.
366. Storici, P., et al., *Crystal structure of GABA-aminotransferase, a target for antiepileptic drug therapy.* Biochemistry, 1999. **38**(27): p. 8628-34.

C Affidavit

I hereby declare that my thesis entitled

"Biochemical and Structural Characterization of Chronophin"

is the result of my own work. I did not receive any help or support from commercial consultants. All sources and/or materials applied are listed and specified in the thesis.

Furthermore, I confirm that this thesis has not yet been submitted as part of another examination process neither in identical nor similar form.

Würzburg.....
Date Signature

D Publications and conference contributions

Research articles

1. Kestler C* and **Knobloch G***, Tessmer I, Jeanclos E, Schindelin H, Gohla A (2014) Chronophin dimerization is required for proper positioning of its substrate specificity loop. *J. Biol Chem.* 289, 3094-3103
2. Seifried A, **Knobloch G**, Duraphe PS, Segerer G, Manhard J, Schindelin H, Schultz J, Gohla A (2014) Evolutionary and Structural Analyses of Mammalian Haloacid Dehalogenase-type Phosphatases AUM and Chronophin Provide Insight into the Basis of Their Different Substrate Specificities. *J. Biol. Chem.* 289, 3416-3431
3. **Knobloch G*** and Jeanclos E*, Hoffmann A, Fedorchenko O, Odersky A, Lamprecht AK, Schindelin H, Gohla A. CIB1 and Ca^{2+}-Calmodulin Are Competing Interactors of Chronophin: Potential Switch Mechanism to Regulate Chronophin Phosphatase Specificity. (Submitted)
4. **Knobloch G**, Jabari N, Schindelin H, Köhn M, Gohla A. Synthesis, Biochemical and Structural Characterization of Chronophin specific Inhibitors as a Model for Structure Based Drug Design on HAD hydrolases. (In preparation)

*equal contribution

Oral presentations

Date	Organizer and meeting title	Title
Sept. 2010	Annual Retreat of the Rudolf Virchow Center	"Biochemical and Structural Basis of Chronophin activation"
Feb. 2014	Rudolf Virchow Center Symposium	"Chronophin Dimerization is Required for Substrate Specificity"
Sept. 2014	Annual Retreat of the Rudolf Virchow Center	"Generation and Characterization of Chronophin Inhibitors"

Poster presentations

Date	Organizer and meeting title	Title
Jul. 2010	International Meeting of the DGZ on Actin Dynamics	"Identification and Characterization of a Ca^{2+}-dependent Chronophin Phosphatase Complex"
Jul. 2011	EMBO Conference on Protein Phosphatases	"Biochemical Basis of Chronophin Activation"
Nov. 2011	Annual Retreat of the Rudolf Virchow Center	"Biochemical Basis of Chronophin Activation"
Oct. 2013	Annual Retreat of the Rudolf Virchow Center	"The Role of Chronophin Dimerization"

E Curriculum vitae

F Acknowledgements

Foremost, I would like to express my gratitude to my primary supervisor Prof. Dr. Antje Gohla for the opportunity to work in her group and for the continuous support during my PhD thesis. Thank you!

Special thanks also to my second supervisor Prof. Dr. Hermann Schindelin for introducing me into the field of structural biology, and the constant help solving the structures I presented in this thesis.

I would also like to thank my third supervisor Dr. Katrin Heinze for the discussions in our meetings and the supervision of my thesis.

I am very grateful to the members of the Gohla group for the great discussions, the help in the laboratory and the nice working atmosphere. Thanks to Dr. Elisabeth Jeanclos, Dr. Annegrit Seifried, Gabriela Segerer, Kerstin Hadamek, Angelika Keller and the former members Simon Vogel, Beate Vogt, Markus Schulze and Karina Lamprecht and Ambrish Saxena.

Special thanks to Christian Kestler, who worked with me on the chronophin-monomer project, and to Nauras Jabari, who synthesized the chronophin inhibitors and contributed to the inhibitor project.

I also thank Dr. Ingrid Tessmer for performing the AFM experiments and for helping with the AUC measurements, and thereby contributing to the chronophin-monomer manuscript.

I would also like to thank our collaborators from the EMBL Heidelberg: Dr. Maja Köhn for the great contributions to the inhibitor project and to Dr. David Will for suggesting possible inhibitor modifications.

Finally, I would like to thank all members of the Schindelin and Kisker groups in the department for structural biology at the Rudolf Virchow Center for their help in the laboratory.

I dedicate this work to my family.